

UC Davis

UC Davis Electronic Theses and Dissertations

Title

Structural Disorders of 3D Epitaxial PbSe Quantum Dot Superlattices

Permalink

<https://escholarship.org/uc/item/4807s023>

Author

Chu, Xiaolei

Publication Date

2022

Peer reviewed|Thesis/dissertation

Structural Disorders of 3D epitaxial PbSe Quantum Dot Superlattices

By

XIAOLEI CHU
DISSERTATION

Submitted in partial satisfaction of the requirements for the degree of

DOCTOR OF PHILOSOPHY

in

Materials Science and Engineering

in the

OFFICE OF GRADUATE STUDIES

of the

UNIVERSITY OF CALIFORNIA

DAVIS

Approved:

Adam Moulé, Chair

Yayoi Takamura

Jiandi Wang

Committee in Charge

2022

Copyright © 2022 by

Xiaolei Chu

All rights reserved.

CONTENTS

List of Figures	vi
List of Tables	xxi
Abstract	xxii
Acknowledgments	xxiii
1 Motivation & Overview	1
1.1 Motivation	2
1.2 Overview	2
2 Introduction	5
2.1 Quantum Dot Solids	6
2.1.1 Synthesis and Properties	6
2.1.2 Structural Defects in QD SLs	8
2.2 Electron Tomography	10
2.2.1 Basic Principals	10
2.2.2 Conventional ET	12
2.2.3 full-tilt ET	13
2.2.4 Limitations of ET	14
3 Structural Characterization of Superlattice Disorder of PbSe epi-SLs by Electron Tomography	16
3.1 Preface	17
3.2 Introduction	17
3.3 Experimental	19
3.3.1 Materials	19
3.3.2 Quantum Dot Sythesis	20
3.3.3 Substrate preparation	21

3.3.4	Superlattice fabrication	21
3.3.5	Basic characterization	22
3.3.6	Grazing incidence small-angle X-ray scattering	22
3.3.7	Tomography needle sample preparation	22
3.3.8	HAADF-STEM Electron Tomography	23
3.3.9	Mobility Simulation	24
3.4	Results and Discussion	27
3.4.1	SL Unit Cell and Disorder	28
3.4.2	Characterization of Neck Disorder	32
3.4.3	Charge Transport Simulation	37
3.5	Conclusion	39
3.6	Conflicts of Interest	41
3.7	Acknowledgments	41

4 Near-Atomic Electron Tomography Study on the Orientation Disorder of PbSe

	epi-SLs	47
4.1	Preface	48
4.2	Introduction	48
4.3	Methods	50
4.3.1	Tomography needle sample preparation	50
4.3.2	HAADF-STEM Electron Tomography	51
4.3.3	Determination of QD positions and SL vectors	51
4.3.4	Calculating optimal AL orientation from SL basis matrix	52
4.3.5	Determination of atomic lattice orientation from measurement	53
4.3.6	Characterization of AL orientation transformation	54
4.3.7	Orientation correlation matrix and von Neumann entropy	55
4.4	Results	57
4.4.1	The relationship between AL orientation and SL structure	60
4.4.2	Anisotropic orientation disorder	64

4.4.3	Effect of interfaces	67
4.5	Conclusion	68
4.6	Supporting Information	69
4.7	Acknowledgments	69
4.8	Conflicts of Interest	70
5	Comparison of Structural Disorder in 2D and 3D PbSe Quantum Dot Superlattice	74
5.1	Preface	75
5.2	Introduction	75
5.3	Experimentals	77
5.3.1	Materials	77
5.3.2	Quantum dot synthesis	77
5.3.3	Fabrication of multilayer QD superlattices	78
5.3.4	Fabrication of monolayer QD superlattices for STEM experiments	78
5.3.5	Electron Tomography	79
5.3.6	STEM-HAADF Analysis	79
5.4	Results and Discussion	79
5.5	Conclusion	86
5.6	Acknowledgement	86
5.7	Supporting Information	86
6	Unfinished Work	87
6.1	Preamble	88
6.2	Electron Tomography Study on the Phase distribution of PCE11-PCBM Organic Bulk Heterojunctions	88
6.3	Three Dimensional Geometric Phase Analysis	94
6.3.1	Introduction	94
6.3.2	Methodology	95
6.3.3	2D GPA Analysis on Superlattices	97

A	Supporting information for “Structural Characterization of Superlattice Disorder of PbSe epi-SLs by Electron Tomography”	102
B	Supporting information for “Near-Atomic Electron Tomography Study on the Orientation Disorder of PbSe epi-SLs”	119
B.1	Sample Preparation and Tomography Reconstruction	120
B.2	Tomogram Analysis	121
B.2.1	Determination of QD positions and SL vectors	121
B.2.2	Calculating optimal AL orientation from SL basis matrix	122
B.2.3	Experimental Determination of 3D atomic lattice orientation	124
B.2.4	Characterization of AL orientation transformation	126
B.2.5	Orientation correlation matrix and von Neumann entropy	127
B.3	Crystal Stacking	131
B.4	Grazing Incidence X-ray Diffraction	131

LIST OF FIGURES

2.1	The ideal perfect structure versus the real structure of QD SLs and the impact from structural imperfection on the energetic landscape. Adapted from ref[?] .	7
2.2	The ideal perfect structure versus the real structure of QD SLs and the impact from structural imperfection on the energetic landscape.	8
2.3	Several types of intra-grain structural defects in epi-SLs. The upper left image is adapted from [?]	9
2.4	A comparison of different 2D and 3D characterization techniques and the accessible information on the structure of QD SLs.	10
2.5	A diagram showing the principals of ET work flow. A tilt-series of STEM images are collected under a series of tilting angles of the sample. The tilt-series is then aligned and reconstructed by a particular method. The resulted reconstruction can be subsequently analyzed with image processing techniques.	11
2.6	The missing-wedge effect. When tilting angle range is limited in ET, the shape of the reconstructed object is elongated and the boundary is blurred. Adapted from [?]	12
2.7	An overview of the various 3D characterization techniques and their applicable sample size and spatial resolution.	14
3.1	Fabrication of the PbSe QD epi-superlattice tomography sample. (a) Sample fabrication. (b) Plan-view and cross-section SEM images of a different region of the epi-SL film. The film is a polycrystalline SL with SL grains of two different in-plane orientations, previously assigned to the $(100)_{SL}$ and $(01\bar{1})_{SL}$ projections of a distorted simple cubic SL.[31] Most of the SL grains in this image have a $(100)_{SL}$ orientation. The dashed yellow line encircles a $(01\bar{1})_{SL}$ -oriented grain. Scale bars are 100 nm. (c) HAADF-STEM image of the needle-shaped tomography sample with disc-shaped epi-SL layer and all layers labeled. Scale bar is 50 nm.	20

- 3.2 The epi-SL tomogram and QD positions. (a) Top, (b) bottom, (c) cross-section, and (d) perspective views of the tomogram of the epi-SL film. The color scale denotes the normalized electron density in units of e^-/nm^3 . Dashed lines represent grain boundaries between the three SL grains (labeled grain I, II, and III). The scale bar is 40 nm. (e) Perspective image of the center of mass coordinates of all QDs in the sample. Each QD is represented by a sphere with a diameter of 1 nm (for ease of viewing). The QDs are color coded according to their location in grain I (blue), grain II (green), or grain III (red). The scale bar is 20 nm. (f) Exploded view of the seven QD layers of the sample to illustrate the internal structure of the epi-SL film. Each QD is represented by a 6 nm diameter sphere (Fig. S6). Layer 1 (L1) is the top layer of the originally floating film (at the QD/gas interface), while layer 7 (L7) is the bottom layer of the film (at the liquid/QD interface). The QDs are color coded according to panel e. (f-g) Representative monolayers in grain I separated along direction x and y, representing SL lattice planes of (f)(100)_{SL} and (g)(010)_{SL}. 28
- 3.3 Analysis of the QD necks. (a) A slice of the tomogram through the middle of L4, showing in-plane necks between the QDs. (b) Heat map of the total number of necks for each QD in L4. The color scale is labeled. (c) Heat map of the average neck diameter for each QD in L4, including both in-plane and out-of-plane necks. The color scale is labeled. (d) Magnified isosurface views of two regions of the sample to illustrate typical neck polydispersity (narrow, wide, and missing necks) and a highly-fused pair of QDs (inset). The green dots denote the CoM of each QD. (e) Histograms of neck number for all QDs in grain I, II and III (inclusive of L1-7, not just L4). The solid curves are fitted beta distributions. (f) Corresponding histograms of average neck diameter. Fitting beta distributions are shown as solid curves. See Fig. S15 for histograms of the diameter of every neck in each grain. 32

- 3.4 Correlation of neck number with nearest neighbor QD positional disorder. (a) Histograms of NN distance (d_{NN}) at each neck number for all of the QDs in grains I and II. Overlaid red curves are Gaussian fits. (b) Plot of the average NN distance (\bar{d}_{NN}) versus neck number. (c) Plot of the standard deviation of the NN distance (σ_d) and the normalized standard deviation of the NN distance ($\bar{\sigma}_d = \sigma_d/\bar{d}_{\text{NN}}$) versus neck number. $\bar{\sigma}_d$ is a measure of the local disorder that is independent of differences in unit cell size. 34
- 3.5 Transport simulation results. (a-c) Perspective views of the three types of simulated samples. (a) The tomography sample (trimmed from a disc into a cuboid). Grains I, II, and III are labeled. (b) A monocrystalline epi-SL. (c) A bicrystalline epi-SL. The monocrystalline and bicrystalline epi-SLs were generated using the lattice parameters, QD size distribution, QD positional disorder and neck statistics of grain I. The bicrystalline samples are bisected by a plane of missing necks (a necking grain boundary), which limits transport across this plane to hopping. Virtual electrical contacts are placed at the left and right sides of each sample. All simulation boxes are approximately $92 \times 92 \times 39$ nm. (d) Comparison of the calculated electron mobility of the tomography sample (dashed red line), monocrystalline epi-SLs (blue bars) and bicrystalline epi-SLs (gray bars). The horizontal error bar represents the error in the mobility estimate for the tomography sample. Overlaid black curves are Gaussian fits of the histograms. The mobility for the monocrystalline and bicrystalline samples is 4.25 ± 1.25 cm²/Vs and 3.28 ± 0.8 cm²/Vs, respectively. 38

4.1 SEM, STEM images and tomographic reconstruction of the PbSe SLs. a) SEM image of a region of interest within a $(100)_{SL}$ -oriented SL grain. The dashed circle denotes the approximate site where the cylindrical tomography sample initially located in the film. b) SEM image of the FIB-prepared needle sample. c) HAADF-STEM image of the PbSe epi-SL tomography sample. d) A perspective view of the entire tomogram and a zoom-in view of one of the QDs showing 3D near-atomic details. The color scale denotes the normalized electron density in units of e^-/nm^3 . The presented Cartesian axes are pre-defined reference coordinates systems with \vec{z}^* being the film normal direction. e) The 1D power spectra of the Fourier transformations of the experimental reconstruction and the simulated reconstruction. The dashed lines denotes the PbSe Bragg peaks of $\{111\}_{AL}$, $\{200\}_{AL}$ and $\{220\}_{AL}$ with corresponding d-spacing of 3.52 Å, 3.05 Å and 2.16 Å. Embedded in the panel is the visualization of the 3D power spectrum of the experimental reconstruction with arrows annotating the $\{200\}_{AL}$ Bragg spots. 56

4.2 The interpretation of the tomogram with data visualization. a) Exploded view of the cube-stick representation of selected $(001)_{SL}$ layers (C1, C3, C5, C7 and C9) from the original tomogram. The coordinates and orientations of the cube reflect the actual relative positions and atomic orientation of the QDs. The color scale of the cubes denotes the magnitude of the differences ($L_{2,2}$ distance) between the predicted optimal orientation R_{mono}^{AL} and the measured orientation R_i^{AL} . The presence/absence of the sticks represents characterized neck or missing-neck scenarios for the morphological coupling of neighboring QDs. The diameter of the sticks corresponds to the diameters of the necks. The color scale of the sticks denotes the experimental orientation differences between the connected QDs. (b-d) Plan-views of the cube-stick representations of C1 (b), C5 (c) and C9 (d) overlaid on top of the raw tomographic slices (thickness of 2 nm around vertical layer center-of-mass) of the corresponding layers. The top panels are the side-views. (e) Gaussian-mixture-modeling of positional distribution of the QD CoMs along the film normal (\vec{z}^*) direction. C1 is at the liquid-film interface with ethylene glycol and C9 is the film-gas interface during film synthesis. 58

4.3 AL/SL relationship. a) AL/SL lattice vector distributions encompassing $[100]_{AL}$ (green), $[010]_{AL}$ (blue), $[001]_{AL}$ (red), $[100]_{SL}$ (lime), $[010]_{SL}$ (cyan) and $[001]_{SL}$ (pink). The star points denote the calculated optimal AL orientation R_{mono}^{AL} . The diamond points on the enlarged patches are AL vectors averaged over each layers. b) Schematics showing the difference between a nonoptimal AL/SL configuration and the corresponding optimal AL/SL configuration in which the summation of the cofacial $\{100\}_{AL}$ area is maximized under the given SL lattice angles. The solid vectors denote the nonorthogonal SL basis matrix R^{SL} and are identical between nonoptimal and optimal configurations. The dashed vectors represent the orthogonal AL basis R^{AL} . c-d) Pearson correlation matrix of R_i^{AL} (c) and R_i^{SL} (d). The color scale of each element in the matrices denotes the 2D correlation coefficient between the basis matrices of an arbitrary pair of QDs. The rows/columns are grouped by layer and the order follows ascending layer indices. Within each group, the elements are randomly reshuffled to exclude potential unintended grouping effect. 60

4.4 Anisotropic orientation disorder. a) Schematic showing the AL misorientation between nearest neighboring QDs. b) Scatter plot and linear regression of $\vec{\delta}_{ij}$ as a linear combination of \vec{a}_i , \vec{b}_i and \vec{c}_i . c) Histograms of magnitudes of misorientation gradient θ_{ij} (rad per SL spacing) along different SL directions. d) Histograms of $|\vec{a}_i \cdot \vec{\xi}_{ij}|$ showing distinct tilt/twist misorientation characteristics along different SL direction. 64

4.5 Effects of interfaces on orientational entropy and neck disorder. a) Vertical variations of in-layer component of misorientation gradient magnitude θ_{ij} (blue) and orientational entropy (orange) over each $(001)_{SL}$ (C) layers. b) Vertical variations of the alignment between determined common rotational axis $\vec{\xi}_{ij}$ and local rotation axis, averaged over each C layers. c) Vertical variation of neck diameters. 67

5.1	Structural analysis of monolayer PbSe QD epi-SLs. (a) STEM-HAADF images of QDs with one, two, three, and four necks. Inset FFT images show the corresponding orientations of the atomic lattice for indicated zone axis. (b) Large area HAADF image of 2D PbSe QDs epi-SL. Overlaid model indicates square lattice symmetry. (c-d) FFT image of HAADF in b indicating the atomic (100) and super lattice (10) symmetry. (e) Optimum QDs with epitaxial necking (encircled with yellow dashed line) is highlighted. (f) Variation of QDs (red) and neck (blue) size in epi-SL presented with overlaid model. (g) QDs (encircled with yellow line) and the missing necks (denoted with red disk) shown. 25% of the necks are missing in the epi-SL. (h) Distribution of the QDs according to their number of necking indicated with color coded overlay showing QDs with one (purple), two (green), three (red), four (yellow) necks.	80
5.2	Structural analysis of multilayer (3D) PbSe QD epi-SLs. (a) SEM image of a QD epi-SL showing a boundary of two crystal plane orientation. Overlay model shows surface orientation of epi-SL. (b) HIM image shows periodic registry between inter layers in (100) orientation. Overlay model shows the twin boundary angled 70 degrees. Inset 3D model presents the distorted cubic structure of the PbSe QDs epi-SL. (c) HAADF image shows the cross section of the QD epi-SL on APT post.	82
5.3	(a) Tomography analysis of PbSe QD epi-SL consist of three grains presented with yellow reconstruction (1 nm resolution) and the highly ordered grain presented with green reconstruction in (b). This reconstruction does not present the size dispersion of the QDs, nor the necking, but shows the location of the QDs in the 3D epi-SL as obtained from center-of-mass analysis. 3D sample grouped into three sets of 2D plane defined as (001) being lateral layers in (c) , (010) in (d) and (100) in (e) being vertical layers (grouped) denoted with blue, red, and brown accordingly.	83

5.4	Structural analysis of PbSe QD epi-SLs. (a) Histogram of QDs and neck's diameter show similar distribution for all layers. (b) QDs sorted according to their number of intraplane necking shows similar trend. (c) QDs deviate from their lattice points by increase in missing number of necking for all planes. (d) Interplanar distance increases by missing necks for 3D lateral layers while subtle change seen for 3D vertical layers. (e) Inter QDs distance increases by increasing intraplanar necking. (f) While the average QDs size is increasing by necking, the opposite trend is observed for size of the neck in (g). The relative change of neck size vs QDs size as a function of necking shown in (h) indicates inverse relation.	85
6.1	Phase behaviour and solid state microstructure of PCE11:PCBM blend films. a, Chemical structures of PCBM and PCE11. b, Non-equilibrium phase diagram of the PCE11:PCBM system deduced from DSC first heating thermograms, obtained at 10°C/min, of high-temperature drop-cast samples. A eutectic behaviour is found with a eutectic composition around 75-80 %wt PCE11 and a eutectic temperature around 252 °C. The black crosses represent the cold-crystallisation temperature, as deduced by a line drawn tangential to the thermograms to intercept the onset of the heat-flow slope variation. c, Cross-section HRSEM BSE micrographs of spin-coated (top row) and wire-bar coated (bottom row) PCE11:PCBM films of different blend compositions, after exposure to 80 cycles of DEZ and water at 60 °C, showing selective deposition of ZnO in the PCE11-rich domains (bright contrast). In contrast, PCBM-rich domains inhibit ZnO deposition, and, thus, are characterized by dark contrast. The selective “staining” of PCE11-rich domains by ZnO in the VPI process effectively maps the phase separation as well as the size- and spatial distribution of the donor- and acceptor-rich domains in PCE11:PCBM blend films. The scale bar for all the micrographs is 300 nm.	89

6.2	Tomographic reconstruction of selected PCE11:PCBM BHJs films from TEM-STEM tilt-series showing the 3D-spatial distribution of PCE11-rich domains (green), PCBM-rich domains (red) and the interface between them (yellow).	92
6.3	Two-dimensional GPA analysis on PbSe epi-SLs. (a) Contrast-enhanced SEM image of the surface of the epi-SLs. (b) FFT of the image with different Bragg spots segmented. (c) The Bragg-filtered image with respect to the $(100)_{SL}$ d-spacing and (d) $(010)_{SL}$ d-spacing	96
6.4	Strain and displacement of SLs. (a) Map of shear strain τ_{ab} . (b) The displacement vector field with white arrows representing the direction of the displacement and the underlying color scale represents the magnitude of the local SL displacement. (c) Map of normal strain ϵ_{aa} and (d) Map of normal strain ϵ_{bb} .	97
6.5	3D GPA processing of a tomogram.	98
6.6	Slice view of the tomogram before and after the GPA processing. Panels in the first column are slices of the original tomogram. Panels in the second column are from Bragg-filtered tomogram. The third column includes phase maps and the fourth column includes phase shift maps.	99
6.7	Detection of dislocation lines. (a) Phase shift map. (b) Processed with phase variance algorithms. The bright spots are where phase singularities (dislocation cores) are found. (c) 3D map of (001) misfit dislocation line colored in blue and the surface of the bulk material is colored in gold. (d) (010) misfit dislocation line.	100
A.1	UV-vis extinction spectrum of colloidal PbSe QDs dispersed in tetrachloroethylene. The average QD diameter (6.4 nm) and standard deviation (0.3 nm) was determined using the empirical relationship by Moreels et al.	104

A.2	Steps of FIB tomography needle preparation. (a) The region of interest (ROI) is selected. (b) After carbon and platinum deposition, a wedge is FIB milled and attached to a lift-out probe by ion beam welding. (c) The wedge is transferred to the tip of a sample holder for needle tomography samples. (d-e) The wedge is FIB milled into a needle shape. (f) HAADF-STEM image of the finished needle, with layers labeled.	105
A.3	Six of the 181 images of the HAADF-STEM tilt-series, with tilt angles labeled.	106
A.4	The entire projection tilt series set is obtained by merging two separately acquired tilt series. Since the ex-situ rotation angle of the holder is not precisely controlled, there is a redundant portion in tilt series 2 that repeats some of the tilt angles that are already sampled in tilt series 1. This overlapped portion is determined by monitoring the standard deviation of the intensity distribution of each image. This value varies as the sample is projected at different tilt angles. The overlapped portion is removed from series 2 and the non-redundant images are attached after series 1 to make the whole tilt series for tomographic reconstruction. The two sharp peaks occur at tilt angles for which the SL axes are inadvertently aligned along the electron beam direction.	107

A.5 (a) To conduct Fourier Shell Correlation, the 2D projection images are split into two subsets, with odd-indexed images in one set and even-indexed images in the other. This is to ensure that both subsets are mutually exclusive but still cover the entire tilt angle range. The halves are independently aligned and reconstructed using SIRT and the spatial frequency information is extracted through 3D Discrete Fourier Transformation of the half reconstructions for evaluating correlation.⁴ (b) Fourier Shell Correlation data between the two reconstructed halves as illustrated in Fig. S5a. In the “masked” data, the voxel intensity is set to zero if it is $\geq 2\sigma$ from the mean of the Gaussian-fit intensity distribution of the QDs in the reconstruction. The FSC threshold value is selected to be 0.143.⁶ When the correlation is above the threshold, the orthogonal reconstructions share common structural features that stand out from random noise at the corresponding spatial frequency $f_c = 0.77\text{nm}^{-1}$. Thus the resolution of the half reconstruction is $r_c = 1/f_c = 1.3\text{ nm}$. The other set was reconstructed using the non-linear anisotropic diffusion filter and does not exhibit significant decrease of the resolution. The resolution of the full data set with both odd and even indexed images evaluated to be $r_c = 1/(2f_c) = 0.65\text{ nm}$. 108

A.6 The diameter of the QDs is determined by analyzing conventional STEM images of the SLs. (a) A program is used to isolate each QD from its connected neighbors and calculate the effective diameter of the dot. The scale bar is 20 nm. (b) The result of QD size distribution from image analysis. The red line is a Gaussian fit to the histogram. 109

A.7 (a) Grazing incidence small-angle X-ray scattering pattern of the film used in this study, overlaid with calculated diffraction patterns from (100)- and (01 $\bar{1}$)-oriented epi-SL planes (the most prominent SL orientations) with SL unit cell lattice parameters $a = 6.6\text{ nm}$ and $\alpha = 99^\circ$. (b) Model of the epi-SL showing fusion along PbSe{100}. Additional details of the structure can be found in Ref 6. 109

A.8	Proposed mechanism for SL structure transition from grain II to grain I. The SL structure in the far left end (region 1) undergoes a slight tilt of 15 degrees from near-perfect $(011)_{SL}$ orientation as the structure propagates to the right into region 2. A glide of $(100)_{SL}$ plane occurs in between region 2 and 3 that can be effectively considered as if the orientation of SL changes 90 degrees counter-clockwise. Such process may potentially also alter the β angle, explaining our statistics shown in Table 1.	110
A.9	Plan-view SEM images of grain boundaries of the SL sample, showing the structure of these GBs. (a) A tricrystalline region that is similar to the tomography sample. (b) Corrugated grain boundaries between $(100)_{SL}$ -oriented and $(011)_{SL}$ -oriented grains. Scale bars are 100 nm.	110
A.10	Regional slices of the tomogram showing arrangements of the QDs and the necks in grain I (i,ii) and II (iii,iv). The bisecting planes are annotated as plane (i-iv) which indicated the position of the respective slices and also represent different lattice planes indexed in the corresponding small panels for different grains. Plane (i) and (iii) are parallel to each other, as well as plane (ii) and (iv). All panels share the same scale bar.	111
A.11	The epi-SL can be reconstructed with QDs represented by spheres of identical size positioned according to the CoM data. (b) Perspective and (c) cross-sectional views of the sample with the QDs represented by perfect spheres. (a,d) Labeling conventions for assigning lattice parameters to grain I and II, respectively. Red planes correspond to the 100 facets.	111
A.12	Histograms of SL lattice parameters in grain I, including (a-c) lattice angles α , β and γ , and (d-f) lattice spacing a, b and c.	112
A.13	Histograms of SL lattice parameters in grain II, including (a-c) lattice angles α , β and γ , and (d-f) lattice spacing a, b and c.	112

A.14	An illustration of how the neck diameter is determined. In (a), two necked QDs are shown in iso-surface form. A plane is generated such that it is perpendicular to the vector between the centers of mass of the necked QDs. This plane is then allowed to slide along this vector to locate the minimum area of the neck. (b) Image of this plane at the neck minimum. Using a threshold value (the same value for the masking reconstruction in Fig. S5), (b) is reduced to (c) to estimate the neck shape and area. The neck diameter is calculated as the effective diameter of the neck area.	113
A.15	Histograms of diameters of each individual neck characterized from each of the three grains. Zero diameter represents a “missing neck”.	113
A.16	Heat maps of the neck number for each QD in the sample. Each circle represents a QD in L1-7.	114
A.17	Heat maps of the average neck diameter for each QD in the sample. Each circle represents a QD in L1-7.	115
A.18	(a) Average neck diameter as a function of neck number for each QD in grains I, II, and III. Error bars denote one standard deviation. (b) Average neck number for each QD layer in the tomogram. Layer 1 is the top of the epi-SL (QD/gas interface) and Layer 7 is the bottom of the epi-SL (QD/liquid interface). (c) Average neck diameter for each QD layer.	115
A.19	(a-c) Separate 3D Fourier transformations of (a) grain I, (b) grain II and (c) grain III. (d) Fourier Shell Intensity comparison between the three grains. Both grain I and grain II show structural features at high spatial frequency, while grain III lacks fine feature at sub-QD length scales (< 6 nm).	116
A.20	Radial distribution of (a) average neck diameter and (b) average neck number. .	117
A.21	Radial distribution of (a) average neck diameter and (b) average neck number. .	117
B.1	SEM images of the region of interest (ROI) within a single grain. The Au marker array are deposited onto the substrate before stamping the film. The markers are used to relocate ROI after depositing carbon on top of the film. . .	122
B.2	Selected HAADF projection images from the tilt-series.	123

B.3	An exemplary STEM projection image showing atomic details.	128
B.4	EDX measurement of PbSe section on the tomography needle.	129
B.5	QD center-of-mass distributions along different SL direction: $[001]_{SL}(b)$, $[010]_{SL}(c)$ and $[100]_{SL}(c)$	130
B.6	Slices of $(001)_{SL}$ layers from the raw reconstruction.	131
B.7	Slices of $(100)_{SL}$ (A) layers from the raw reconstruction.	132
B.8	Slices of $(010)_{SL}$ (B) layers from the raw reconstruction.	132
B.9	Local tomographic slices showing 3D atomic details with a resolution of ~ 0.2 nm.	133
B.10	The iterative process of QD center-of-mass determination.	134
B.11	(a) SL spacings distributions. (b) Mean SL spacings over different $[100]_{SL}$ layers.	135
B.12	Vector field maps for the orientation of the QDs. The positions of each arrow represent the actual positions of the QD. The directions of the arrows repre- sent the vector directions of the corresponding atomic lattice and superlattice vectors. Plots in the first column just show the AL vectors while plots in the second column show both AL and SL vectors.	136
B.13	The glyph-stick visualization of the structural information.	137
B.14	The glyph-stick visualization of all $(001)_{SL}$ planes (C1-C9).	138
B.15	The glyph-stick visualization of selected $(100)_{SL}$ planes (A5 – B10). (a) per- spective side views. (b) orthogonal views.	139
B.16	The glyph-stick visualization of selected $(010)_{SL}$ planes (B5 – B10). (a) or- thogonal views. (b) perspective side views.	140

B.17	Pearson cross-correlation matrices for R_i^{AL} grouping by $[001]_{SL}$ (first column), $[100]_{SL}$ (second column) and $[010]_{SL}$ (third column) layers. The first row are raw PCMs and the second rows are block averaged. The elements in the PCMs are the cross-correlation coefficients of the orientation basis matrices $corr(R_i^{AL}, R_j^{AL})$ between a pair of QD i and j. The elements are arranged in groups following ascending $[001]_{SL}$ (C) layer indices. Within each group, the order of QDs is reshuffled to exclude potential unwanted grouping effect from other SL directions. Comparing PCMs of each SL direction, we see that the orientation gradient is unique in $[001]_{SL}$	141
B.18	Vector field of measured AL and calculated AL with/without global monocystal assumption. (a,b) $[001]_{AL}$, (c,d) $[010]_{AL}$ and (e,f) $[100]_{AL}$	142
B.19	(a-c) PCMs of R_i^{SL} , R_i^{AL} (experimental) and \hat{R}_i^{AL} (polycrystal prediction). The outliers related with C8 in (a) come from this layer's high density of missing dots. (d) PCM intensity profiles. Three observations can be distilled from the comparisons of the PCMs shown. (1) The R_i^{AL} PCM shares similarity with the R_i^{SL} PCM, indicating that the AL orientation is systematically determined by the SL structure. The differences are that any change in the AL appear to be smoother than change in the SL. (2) The roughness of \hat{R}_i^{AL} PCM indicates the short-range AL coherence is worse than experimental measurements, indicating that AL is inert to local SL randomness and minimization of AL misalignment is preferred for the system. (3) The diagonal block color scale is a qualitative indicator of the orientational entropy of each $[001]_{SL}$ layers.	143
B.20	Predicted optimal AL/SL configurations based on SL angles.	144

LIST OF TABLES

3.1	Lattice constants of SL grains I and II as determined from statistical analysis of the tomogram. GISAXS data is from refrence 31	30
3.2	Neck statistics.	36
A.1	Preliminary Profilometer thickness measurements of thin films deposited from same processing conditions and at the time the NR films were made.	103

ABSTRACT

Structural Disorders of 3D epitaxial PbSe Quantum Dot Superlattices

Quantum dots (QDs) are novel building blocks that feature size-tunable and unique photophysical properties. The interactions (e.g., electronic, excitonic, magnonic) in self-assembled QD superlattices (SLs) can be tuned by changing particle size, size distribution, shape, inter-particle spacing, structural ordering, surface chemistry and defects, making QD solids an exciting playground for mesoscale science. To date, the properties of QD-made devices have been limited by the relatively high energetic and spatial disorder of the coupling pattern of QDs, inhibiting the emergence of new collective mesoscale behavior. However, rational improvements in film synthesis relies on comprehensive understanding of the 3D structure that current studies have yet been able to present with conventional 2D diffraction and imaging techniques. In this dissertation, I demonstrate the use of full-tilt Electron Tomography based on High Angular Annular Dark Field (HAADF) Scanning Transmission Electron Microscopy (STEM) images in generating quantitatively interpretable digital reconstruction of the QD SLs. With sufficient spatial resolution of under 0.4 nm over a volume containing $\sim 10^3$ QDs, both superlattice and atomic lattice structural order and morphological information are obtained through real and reciprocal space calculations. This allows hierarchal analyses on the spatial variations of and correlations among different structural features. These new knowledges enable new understandings of the QD oriented-attachment mechanism and provide rational guidance to film quality refining.

ACKNOWLEDGMENTS

I would like to deliver my deepest gratitude to my advisor Dr. Adam Moulé for the guidance, support and encouragement he has been offering me for the last five and a half years of my PhD study. I joined the Moule Group without a slight bit of experience in Electron Microscopy and Adam paid lots of attention on ensuring that I get proper mentorship. Adam has played a role more than an academic supervisor but also a source of emotional support and he has the genuine care for his students' personal career development. His openness and optimism towards questioning and challenges made effortless communications between him and me. It is also my privilege to have Dr. Yayoi Takamura and Dr. Jiandi Wang as my thesis committee members. I owe a deep sense of gratitude to Dr. Takamura for her support and advices on helping me pass my candidate exam.

It is my genuine pleasure to work with my fellow colleagues in the Moule lab. They are the most friendly and helpful peers and we had a wonderful time working, learning and enjoying life together. I would like to particularly thank Dr. Fei Wu and Dr. Hamed Heidari for being great mentors and friends to me as they helped introducing me into Electron Microscopy and onboarding me on several projects in the beginning of my PhD study. I also want to thank Tucker Murrey, Goktug Gonel, Makena Dettmann and Meghna Jha for giving enlightening opinions and ideas in the countless discussions that happened during the years. I am extremely thankful to our long-term collaborators including Alex Abelson, Caroline Qian and Prof. Matt Law from UC-Irvine and Davis Unruh, Chase Hansen and Prof. Gergely Zimanyi from Physics Department at UC-Davis. Alex and Caroline are always responsive and reliable when I need support on sample preparation. They showed great hospitality every time I visited UCI. I want to thank Prof. Getti Frey and Artem Levitsky from Technion for hosting me when I visited Israel as a visiting student.

Last but not the least, I owe my gratitude to my parents, my sister and my friends back in home China. My presences were not there when they had their big moments in their own lifes. Never, do they hesitate to offer their spiritual company, care and love to me in times of uncertainty, depression and social isolation. I could not imagine to make it all through without their supports.

Chapter 1

Motivation & Overview

1.1 Motivation

Recent synthetic advances have enabled the creation of novel supercrystal materials with emergent collective electrical, optical and mechanical properties.[128, 105, 38, 109, 16] Structural imperfections at the atomic and nanoscale limit the expression of quantum mechanical properties.[132, 99] Therefore, techniques for characterizing the atomic structure of supercrystals are vital for obtaining a sufficient understanding of synthesis/structure/property relationships to make higher-performance materials for applications. In spite of many advances in diffraction and real space imaging, [32, 114, 87], it remains exceedingly difficult to characterize multicrystalline 3D materials at atomic resolution over mesoscopic length scales. Here, we use electron tomography and combined real and inverse space analysis to determine the structure of a 105 nm³ disc of a multilayer epitaxially-fused PbSe quantum dot (QD) superlattice (epi-SL) with near atomic resolution. Epi-SLs are predicted to demonstrate quantum effects, including multiple exciton generation and mini-band formation between groups of QDs. [68, 51, 74, 93] Previous structural studies on PbX QDs relied on diffraction measurements that averaged data over many QDs, [126, 10, 50] scanning electron microscopy (SEM) imaging of surfaces of multi-layer SL samples, [41] and scanning transmission electron microscopy (STEM) imaging for 2D QD SL samples. [114, 87, 131] Diffraction showed that on average the atomic lattice (AL) and SL structures are aligned. [1] However, 3D epi-SLs have been shown to form distorted cubic cells with a systematic AL/SL misalignment, unlike the more energetically optimal structure in 2D. Electron tomography imaging is already able to show grain boundaries in the 3D epi-SLs and determine individual QD positions in 3D space, but limited resolution and reconstruction artifacts have prevented a complete understanding of the coupled AL/SL structure. [25, 102]

1.2 Overview

In this dissertation, I introduced the technique of mesoscale electron tomography to investigate the translational, orientational and morphological defects of 3D epi-SLs.

In Chapter 2, a brief scientific background is given to layout fundamental understanding of the nature of the quantum-dot superlattice materials, including their synthesis, structure imper-

fections, properties etc. A short review of various structural characterization techniques is also given in this Chapter to answer the question that why ET is needed for the purpose of studying 3D structure of QD SLs in this dissertation. Lastly in this chapter, a basic introduction to the technical principals of ET is provided.

In Chapter 3, a multi-grain 3D PbSe epi-SLs sample is analyzed with through full-tilt electron tomographic reconstruction. This tomogram provides (i) sufficiently high spatial resolution (0.65 nm) to accurately determine the position and size/shape of the QDs and their necks and (ii) sufficiently large volume ($4.3 \times 10^5 \text{ nm}^3$) to enable meaningful statistical analysis of structural disorder in the sample. In testing correlations between neck number, neck diameter, inter-QD distance, and QD location in the film, we discovered a strong association between neck number and both the average and standard deviation of the nearest neighbor QD distance, demonstrating that QDs with more necks tend to have more ordered local environments. Achieving more complete, uniform necking will require fabrication of more perfect oleate-capped SLs and greater control of the kinetics of the phase transition from the oleate-capped SL to the epi-SL. This work sets a baseline for the quantitative structural characterization of 3D QD epi-SLs for elucidating processing/structure/property relationships and guiding the fabrication of increasingly perfect structure.

In Chapter 4, a single-grain region from a 3D epitaxially-connected PbSe QD SL film is characterized with full-tilt ET with a spatial resolution of 3.1 Å which allows for accurate determinations of the 3D SL position together with AL orientation of each of the 633 QDs. We show that the AL orientation variation over the entire sample is not random but suggests a characteristic rotation axis of $[\bar{1}20]_{AL}$ shared by the majority of QD pairs of non-trivial orientation difference. This effect results in a major contribution from out-of-plane tilting to the overall orientation disorder. We are also able to mathematically describe and statistically validate the relationship between the atomic lattice (AL) orientation and the superlattice structure (SL), in which the AL forms the nearest orthogonal basis to the SL. We show that the AL orientation collectively adapts to a small systematic shear distortion of the SL structure without significantly breaking the short-range atomic alignment. This publication addresses the importance of regulating mid- to long-range SL order to minimize orientation disorder within a single grain.

The ET data permits determination of 3D structural attributes that are spatially coupled and thus allows extraction of knowledge that are typically inaccessible with other structural characterization techniques. We believe that the experimental and analytical approach presented in this publication can be applied to other hard materials of complex structure for studying 3D spatial dependency of atomic to nanoscale structural features within a $\sim 10^2$ nm length scale.

During my PhD, I also co-authored a paper in which I conducted ET study on the 3D phase morphology of PCE11:PCBM organic bulk heterojunction films as organic photovoltaic (OPV) devices. This measurement provides supporting evidence to the scanning calorimetry (DSC), vapor phase infiltration (VPI) and transient absorption spectroscopy (TAS) measurements (DSC-VPI-TAS) which together are advocated to be a potential method for fast-screening OPV blends based on their microscopic phase distribution that determines the efficiency in charge transport. Additionally, I have also worked on developing multi-scale Geometric Phase Analysis(GPA) methods for both 2D and 3D epi-SLs structures. Through this technique, auxiliary images such as local periodicity, displacement vector field, phase shift, strain field and pseudo-atomic reconstruction can be generated from the original tomogram. These analyses grant access to the rich structural information that are hidden in the tomogram that is often hard to interpret at its original form. An algorithm is developed to identify phase singularities in a slice-by-slice manner in the phase shift volume to detect dislocation lines in the atomic lattices in the tomogram. This work has potential impact on quantitative analysis of high-resolution atomic tomographic reconstructions. The above content is included in Chapter 6.

Chapter 2

Introduction

2.1 Quantum Dot Solids

2.1.1 Synthesis and Properties

Typically, quantum dots (QDs) or nanocrystals refers to nanosized crystals of group II-VI, III-VI and IV-VI semiconductors that are in the size of 2-20 nm. Colloidal QDs can be dispersed in solvents or form into solid-state material through solution-based fabrication techniques. It is well known that monodisperse QDs capped with their native long-chain organic ligands (e.g., oleic acid) readily form superlattice structures (SLs) upon drying from common solvents, but these SLs are electrically insulating because their long, insulating ligands offer negligible QD coupling. Recently, it was discovered that replacement of these long ligands by certain ultrashort ligands such as SCN^- , HCOO^- , or ethanedithiol can cause the QDs within the insulating SL to rearrange and partially fuse (usually along their 100 facets) into coherent, single-crystalline, and inherently conductive SL grains typically $10^2 \sim 10^3$ nm in diameter. The QDs within these SLs are crystallographically connected yet retain their quantum confinement. The ligand stripping can also be realized through thermal desorption [106] or exposure to light. [117] The optical and electrical properties of QD SLs are largely dependent on the composition, size, and shape and are therefore essential nanoscale building blocks for fabricating mesoscale materials that exhibit emergent and programable collective properties. For example, the interdot distance dictates the interaction between the electronic wavefunctions of the QDs. As the interdot distance decreases, electrons can transport between neighboring dots at a faster rate. [83] Therefore, ligand stripping and exchange increases QD coupling for improved charge transport and shifts the energy levels and energy gap of the QD solids, thus enabling bandgap engineering of QD materials for device integration.

A grand challenge in mesoscience is to achieve the delocalization of electronic wavefunctions and formation of bulk-like electronic bands (“mini-bands”) in highly-ordered, highly-coupled solids composed of nanoscale building blocks. High-quality 3D QD superlattices material is considered to be promising candidates in achieving delocalized transport. The 3D PbSe epi-SLs studied in this dissertation are QDs epitaxially interconnected (necked or partially fused) to form three-dimensional porous single crystals.[43, 11] These “confined-but-connected” or “epitaxially-fused” QD SLs (epi-SLs) feature exceptional coupling and spatial

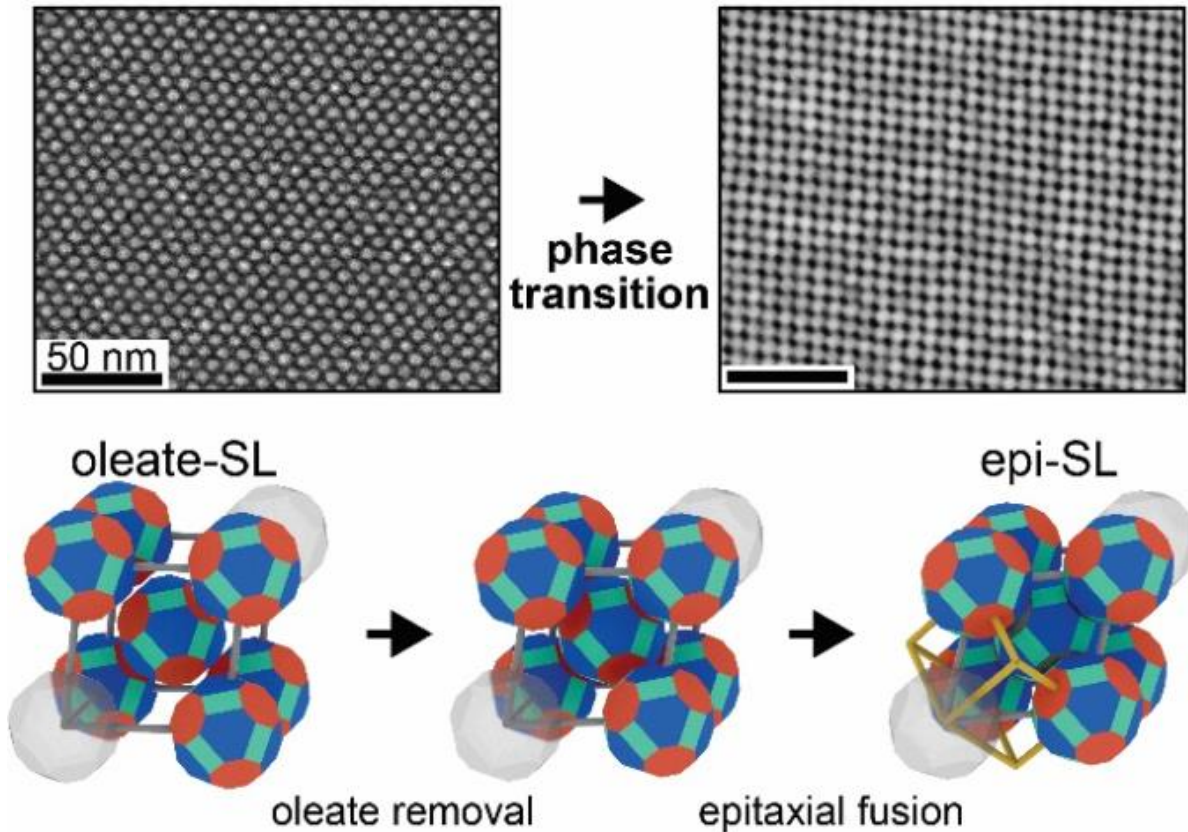


Figure 2.1. The ideal perfect structure versus the real structure of QD SLs and the impact from structural imperfection on the energetic landscape. Adapted from ref[1]

order and are therefore promising systems for mini-band formation.

In the preparation of this material, it is shown that the oleate-capped SL adopts a remarkable rhombohedrally-distorted body-centered cubic unit cell in which the QDs are rotationally aligned in 3D such that each QD is surrounded by six nearest neighbors with cofacial 100 facets (Fig. 2). This structure pre-positions the QDs for facile epitaxial fusion of their 100 surfaces to form a distorted simple cubic epi-fused superlattice with unprecedented spatial order in three dimensions. The phase transition from the oleate-capped SL to epi-SL occurs by nearly-pure translational motion and a slight rotation ($\sim 10^\circ$) of each QD, avoiding the need for large coordinated QD rotations that would likely increase spatial disorder and defects.

The electron and excitonic interaction between QDs in the self-assembled solids can be tuned by changing QD size, size distribution, shape, inter-QD spacing, spatial ordering, surface chemistry, and QD-QD bridging, making QD solids an exciting playground for mesoscale sci-

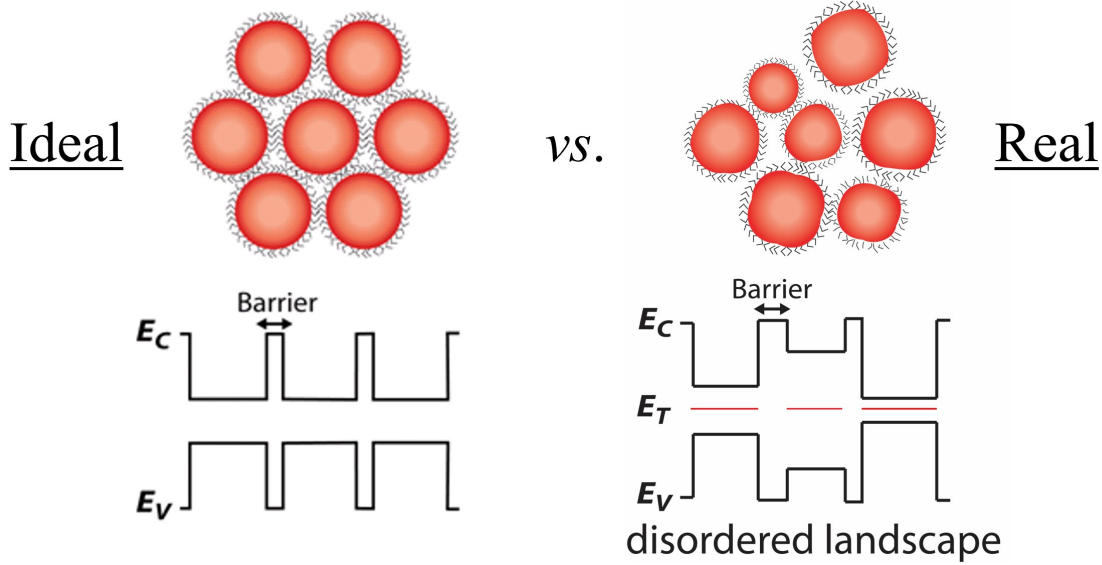


Figure 2.2. The ideal perfect structure versus the real structure of QD SLs and the impact from structural imperfection on the energetic landscape.

ence. However, A related challenge in mesoscience is to map the 3D structure of mesomaterials from the atomic to macro scale in order to understand their structure-property relationships.

2.1.2 Structural Defects in QD SLs

The structural perfection of the epi-SL is determined by two factors: (i) the structural perfection of the parent oleate-capped SL and (ii) the kinetics of the phase transition. Clearly, the spatial order of the epi-SL cannot be better than the spatial order of the parent oleate-capped SL. Using large-grain oleate-capped SLs made by slow evaporation, we have produced epi-SLs with lateral grain sizes up to $\sim 5\mu\text{ m}$ (100 nm film thickness), which facilitates single-grain transport measurements (see below) While a large epi-SL grain size is important, several types of intra-grain structural defects conspire to degrade spatial order within the grains, destroy mini-bands, and localize charge carriers. A subset of the possible defects includes variations in QD and neck size and shape, missing necks, misaligned QDs (edge dislocations, screws, and jitter), larger-scale wave-like variations in QD position (“meander”) that result from flow of the QD film on the liquid surface, and variations in the surface coverage of ligands, ions, and traps, all of which will scatter carriers and disrupt SL periodicity to some degree. Fig 2.3 shows a subset of the possible defects, which include variations in QD and neck size and shape, missing necks, misaligned QDs (edge dislocations, screws,

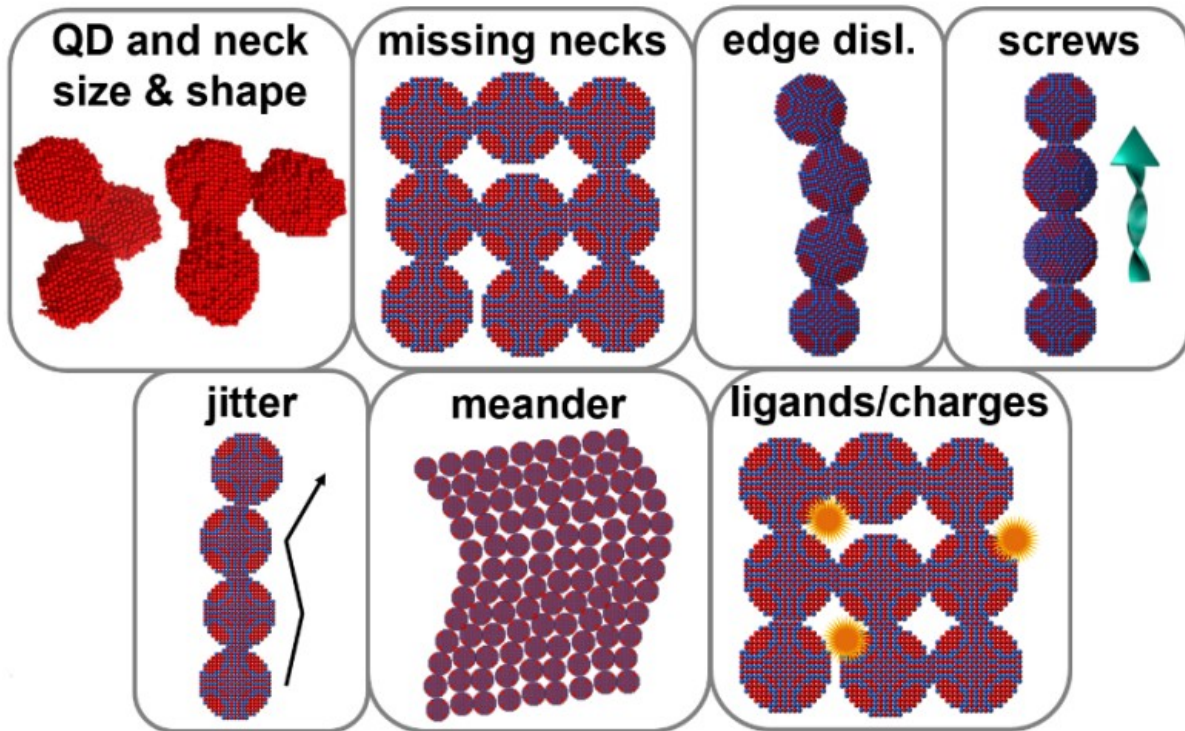


Figure 2.3. Several types of intra-grain structural defects in epi-SLs. The upper left image is adapted from [50]

and jitter), larger-scale wave-like variations in QD position (“meander”) that result from flow of the QD film on the liquid surface, and variations in the surface coverage of ligands, ions, and traps, all of which will scatter carriers and disrupt SL periodicity to some degree. Most of these defects have been observed in 2D epiSLs (QD monolayers), which are easy to image by conventional TEM. [43, 11, 132, 44, 109, 14, 139, 50, 125, 138, 120, 8, 124] Transport measurements of 2D epi-SLs show that carriers are localized, and several groups have identified the missing necks as the primary cause of carrier localization in these materials.[132, 44] The majority of existing studies on the structural characterization of epi-SLs have been focused on 2D films. For example, neck connectivity and projected neck size in 2D epi-SLs have been directly imaged by (S)TEM,[132, 44, 8] and the three-dimensional structure of these necks was deduced from single images by high-angle annular dark-field (HAADF) STEM atom counting reconstruction.[50] To date, structural characterization of 3D epi-SLs has been almost exclusively limited to X-ray scattering and conventional electron microscopy imaging/diffraction methods,[11, 1, 111, 131] neither of which can visualize the intra-grain neck network or in-

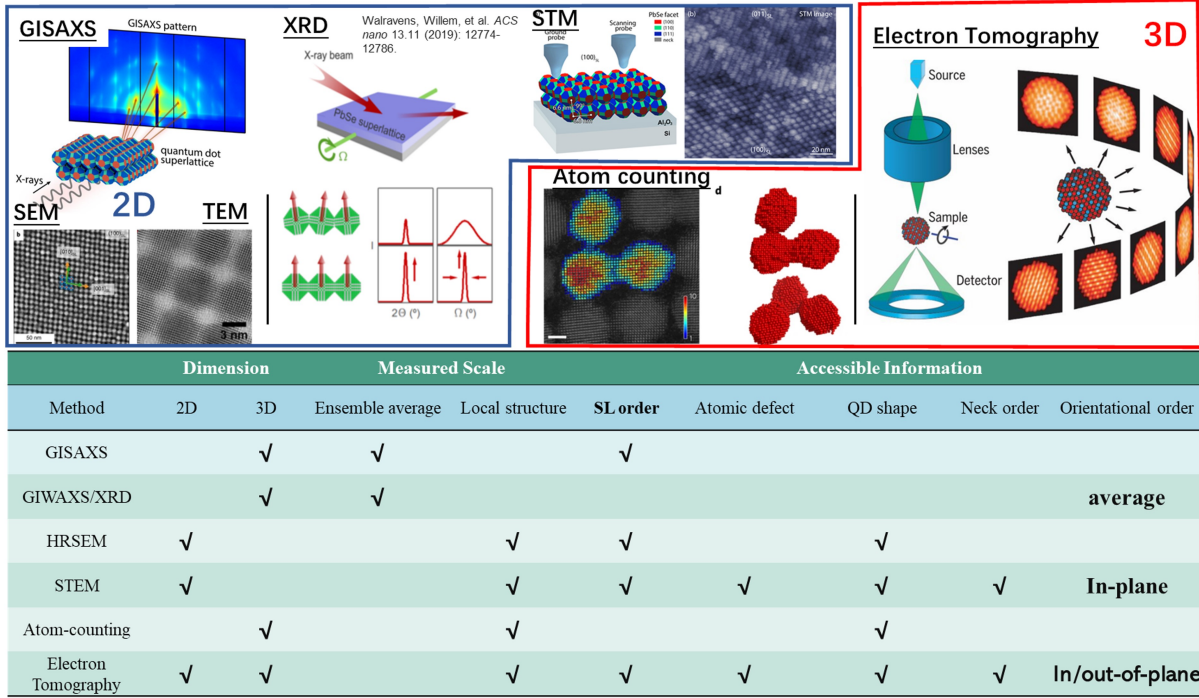


Figure 2.4. A comparison of different 2D and 3D characterization techniques and the accessible information on the structure of QD SLs.

ternal structural defects that are so important for understanding carrier delocalization in these materials.

In contrast to 2D epi-SLs, 3D epi-SLs have received much less attention because they are harder to make and characterize.[11, 111, 131, 102]Figure X summarizes a set of both 2D and 3D characterization techniques which are compared in terms of accessible information that are most important to the study of 3D epi-SLs. It is concluded that that ET is a suitable tool to resolve the multi-scale structural characterization problem associated to this material.

2.2 Electron Tomography

2.2.1 Basic Principals

At a fundamental level, any tomographic reconstruction is an reversed operation of creating a series of projections of an object. The projection is dictated, in its simplest form, by Radon's transformation such as

$$Rf(L) = \int_L f(x,y) |dx| |dy| \quad (2.1)$$

where L is an arbitrary transmitted line passing through function $f(x,y)$ and $Rf(L)$ is the corresponding Radon transformation. Alternatively, the projection problem is often express in an simple algebraic form as

$$m = Ax \tag{2.2}$$

where m represents the projections, A being the projecting operator and x is the original object. While m is known and A can or cannot be inferred, any reconstruction method looks into solving x through an optimization approach such that

$$\tag{2.3}$$

The solution of this inverse problem can be performed either in an analytical or iterative way. Figure 2.5 shows the basic principle of ET. A series of images of the object is acquired with TEM by tilting the sample over a range of degrees. The tilting axis is usually perpendicular to the electron beam direction. Proper alignment of the images should be conducted to compensate translate shift and any other image transformation (rotate, shear, scale, etc.) due to stage unstability and imperfect perpendicularity of the sample rotation axis to the beam. The aligned tilt series is then used as input for obtaining the reconstruction.

The respective tilt series should contain projections from a desirable high tilt-angle range, at best at least 180° , which is required to potentially obtain an unique solution of the inverse problem.[92] Additionally, the imaging conditions and magnification should always be chosen considering the Nyquist-Shannon sampling theorem [62]and the Crowther criterion[27] dependent from the sample thickness and the desired resolution. The Nyquist-Shannon sampling theorem says that the sampling frequency need to be at least two times larger than the highest frequency in the original signal [18].

The tilting angle range of the tilt-series is an important factor dictating the quality of the final reconstruction. In fact, the solution of the inverse problem is theoretically unique only when the angle sampling range is 180° . However, full-tilt range projection acquisition is not commonly implemented because it needs a specialized holder subjective to the design of the microscope used.

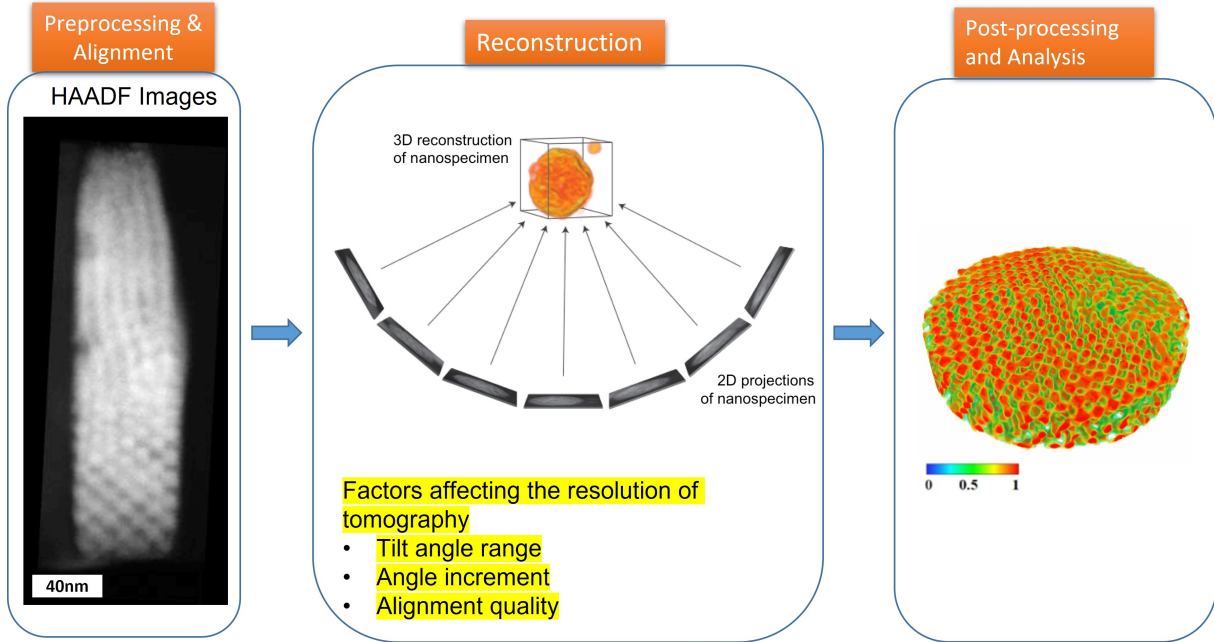


Figure 2.5. A diagram showing the principals of ET work flow. A tilt-series of STEM images are collected under a series of tilting angles of the sample. The tilt-series is then aligned and reconstructed by a particular method. The resulted reconstruction can be subsequently analyzed with image processing techniques.

2.2.2 Conventional ET

Naturally, the reconstructed solution we obtain from the inversed projection problem is perfect because projections are mere samplings of the original 3D object. In practice of Electron Tomography, the range of tilting is often restricted to single-axis $\pm 60-70^\circ$. At a higher tilting, the geometry of a slab sample casts shadows of high-surface-profile features onto the area of interest. Even the sample is perfectly flat, the increasing effective thickness inevitably leads to deterior signal-to-noise ratio at high angles. Additionally, the mechanical limitation of the goniometer often sets a tilting limitation of less than 60 degrees. These restrictions imposes the so-called "missing-wedge" effect in most conventional ET practices that are limited in tilting range. This effect is essentially caused by missing component in the Fourier space and imposes a real-space elongation and blurring of the intensity profile of the reconstructed object in the beam direction. The elongation effect can be quantified as

$$e = \sqrt{\frac{\alpha + \sin \alpha \cdot \cos \alpha}{\alpha - \sin \alpha \cdot \cos \alpha}} \quad (2.4)$$

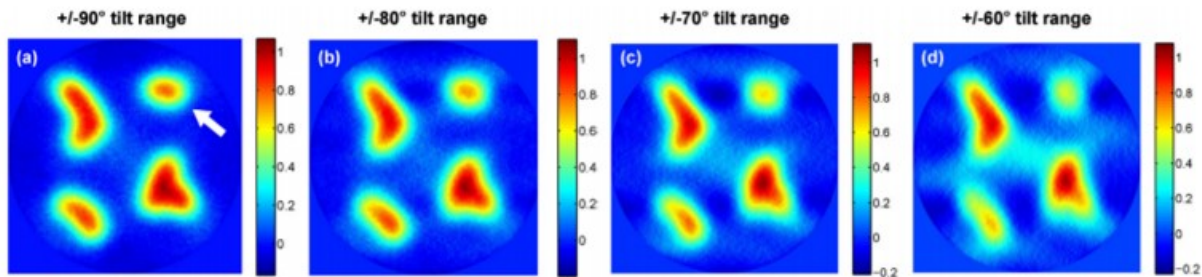


Figure 2.6. The missing-wedge effect. When tilting angle range is limited in ET, the shape of the reconstructed object is elongated and the boundary is blurred. Adapted from [76]

where α is the maximum tilt angle. Alternatively, dual-axis ET can be implemented by acquiring two consecutive tilt-series against two, usually perpendicular rotation axes. Beside conventional single-axis ET it is possible to perform dual-axis ET [86] (not applied in this work) comprising the acquisition of two subsequently acquired tilt series with perpendicular tilt axes. This extension reduces the missing wedge down to a missing pyramid of information in Fourier space. Despite the resolution improvement compared to single-axis practice, dual-axis ET has its disadvantages in requiring a double-tilt holder with high tilt-range capability in both axes and the post-processing of dual-axis tilt-series is much more challenging.

2.2.3 full-tilt ET

A full-tilt ET indicates that the sample are free to tilt $0 - 360^\circ$ in the microscope, producing a tilt-series without miss-sampling angles. In practice, a 180° tilt-series is sufficient to include complete reciprocal-space information to avoid missing-wedge effect since any angle beyond 180° is essentially a flipped copy of a previous projection within the $0 \sim 180^\circ$ range. To ensure stable SNR throughout the tilt-series acquisition, this technique requires a rod-like sample with nearly constant thickness and geometry at any tilting condition. [64, 137, 70, 12, 65] This can be realized with focused-ion-beam sample preparation provided by a dual-beam scanning electron microscope. The details of the FIB preparation technique are introduced in Chapter 3, 4 and 5.

In this work, we use an on-axis rotation tomography holder (Fischione model 2050) for full-tilt ET experiments which enables a rotation of the specimen around the main pole axis in a range of 180° with tilt increments of usually $1-2^\circ$ depending on the microscope goniometer configuration. Full-tilt ET produces higher amount of projections used for the reconstruction to increases the SNR of the reconstruction under same imaging conditions. Studies have shown

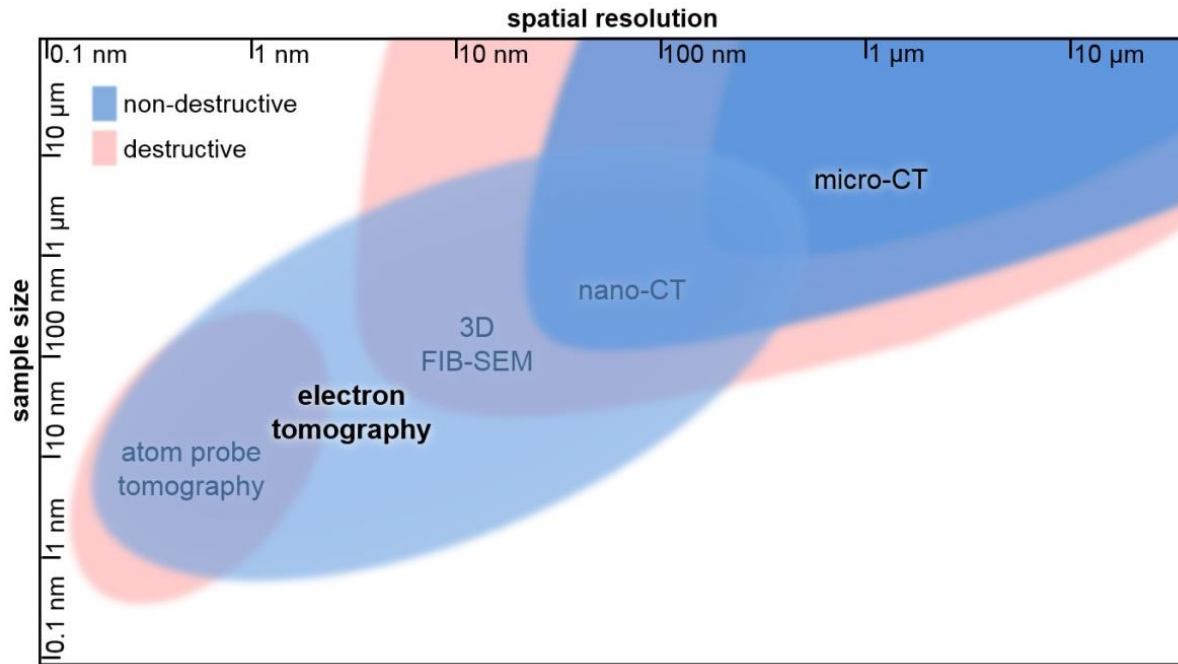


Figure 2.7. An overview of the various 3D characterization techniques and their applicable sample size and spatial resolution.

that full-tilt ET under HAADF mode results more realistic object surface profile and density profile for materials with internal structures (such as pores), compared to conventional method. [64, 12, 73]. The available equipment required that the acquisition of a 180° tilt series needed to be performed in two steps by acquiring two subsequent tilt series, which were afterwards merged to one full tilt series. In this work, each tilt series was acquired in a tilt-angle range of $\pm 55^\circ$ (using the microscope goniometer) with the 0° tilt position of both tilt series 90° tilted towards each other (realized by manually tilting the rod axis inside the sample holder). Using an overlap of a certain tilt range between both tilt series, usually facilitates to merge and align them to their common tilt axis.

2.2.4 Limitations of ET

There are different techniques existing to obtain 3D structural information of materials in nano- or micro-scale. Figure 2.7 gives an overview over the major techniques with their accessible sample sizes and spatial resolutions. ET covers a broad range of sample volumes from about $\sim 1\mu m^3$ down to about $\sim 1nm^3$ with spatial resolutions down to sub-nanometer. These dimensions cannot be accessed by other non-destructive tomography techniques like micro-CT and

nano-CT. Similar, if not lower spatial resolution can be attained by atom-probe tomography or 3D FIB-SEM but these are destructive techniques. Recent developments in ET show 3D atomic resolution.[108, 136] Such high resolution usually requires prior knowledge about the crystal structure of the analyzed material, and the sampling region is only a few nanometer in size. This implies that the resolution is highly coupled with sampling volume size in ET. The higher is resolution required the smaller the sampling size is. This may make the result not statistically representative of the studied material. A solution is to bridge ET's result with other structure resolving techniques for correlative investigations. For example, the combination of ET and micro-CT (Figure 2.7) can access large volumes and detailed, high-resolution information at the same time [17, 116, 98]. Another limiting factor of ET is that it does not give information about chemistry. Nevertheless, the principle of ET can be extended to more advanced spectroscopy tomography technique such as EDS tomography and EELS tomography.[66, 40] Because ET is a non-destructive technique, continuative experiments can be conducted for temporal analysis(e.g., chemical analysis, high-resolution (S)TEM imaging or in situ experiments) after tilt-series acquisition.

Chapter 3

Structural Characterization of Superlattice Disorder of PbSe epi-SLs by Electron Tomography

3.1 Preface

In this chapter, I am reprinting an article I wrote on how to fabricate multilayered semiconducting polymer films; DOI: 10.1039/C8TC05652H. Many organic electronic devices require vertically layered structures to operate. This manuscript demonstrates an additive solution process for depositing multiple layers of semiconducting polymer (SP) films by controlling film solubility with molecular dopants. During multi-layer deposition the bottom layers are exposed to a series of solvent environments that swell the SP films. We use neutron reflectometry (NR) to quantify the film thickness change and solvent content during solvent exposure in a single poly-3-hexylthiophene (P3HT) layer. The film thickness increases by 40-80% with exposure to good solvents. Four layer thin-films composed of alternating protonated and deuterated P3HT layers were additively coated from solution. NR measurements reveal high individual layer purity and that extensive solvent soaking induces no mixing between layers. Finally, two-point conductivity measurements demonstrate that P3HT:P3HT layer interfaces have no effect on vertical conductivity. This facile process enables additive layering of mutually soluble SP films and can be used to design novel electronic device architectures.

3.2 Introduction

Colloidal semiconductor quantum dots (QDs) exhibit intriguing photophysical properties relevant to next-generation solar cells,[101, 110, 20, 69] field-effect transistors,[60, 97] photodetectors[72, 3] and lasers.[31, 23] While improvements in QD processing, electronic performance and stability are ongoing, the use of QDs in many optoelectronic devices is limited by poor charge transport relative to bulk semiconductors. Poor transport is in part caused by energetic disorder arising from variations in QD size, spacing and other types of spatial disorder.[83, 132, 53] Epitaxially-fused PbX (X = Se, S) QD superlattices (epi-SLs) consist of PbX QDs that are arranged in a periodic lattice and epitaxially interconnected (necked or partially fused) to form a porous single crystal of “confined-but-connected” QDs. Epi-SLs promise to combine the tunable optical properties and processability of QDs with the high-efficiency band-like transport of bulk semiconductors.[89] However, charge transport studies have so far failed to demonstrate band-like transport in epi-SLs, probably because structural defects from the atomic scale to the

mesoscale disrupt the SL periodicity and localize charge carriers.[61, 11]

Making PbX QD epi-SLs with larger lateral grain sizes is important for reducing the density of inter-grain structural defects (*e.g.*, grain boundaries, amorphous regions, and voids), but it is the several types of intra-grain defects that conspire to degrade spatial order within the grains, destroy mini-bands, and prevent the emergence of delocalized states.[61, 53, 132] Intra-grain defects include variations in QD and neck size and shape, missing necks, missing QDs (vacancies), misaligned QDs (edge dislocations, screws dislocations, and zig-zag jitter), larger-scale wave-like oscillations in QD position that result from flow of the QD film on the liquid surface (meander), and variations in the surface coverage of ligands, ions, and traps, all of which will scatter carriers and disrupt SL periodicity to some degree. Most of these defects have been observed in 2D epi-SLs (QD monolayers), which are readily imaged by conventional transmission electron microscopy (TEM) and scanning transmission electron microscopy (STEM).[43, 11, 132, 44, 109, 14, 139, 50, 125, 138, 120, 8, 124] Transport measurements of 2D epi-SLs show that carriers are localized, and several groups have proposed that missing necks are a primary cause of carrier localization in these materials.[132, 44] Furthermore, the electronic coupling of necked QDs is expected to be sensitive to neck polydispersity (length, width, atomic coherence, and faceting) and the number of nearest neighbor QDs.[132]

While 2D epi-SLs can be structurally characterized using traditional electron microscopy, imaging the internal details of 3D epi-SLs is more challenging.[35, 5, 50, 111] Neck connectivity and projected neck size in 2D epi-SLs have been directly imaged by (S)TEM,[132, 44, 8] and the three-dimensional structure of these necks was deduced from single images by high-angle annular dark-field (HAADF) STEM atom counting reconstruction.[50] To date, structural characterization of 3D epi-SLs has been almost exclusively limited to X-ray scattering and conventional electron microscopy imaging/diffraction methods,[11, 1, 111, 131] neither of which can visualize the intra-grain neck network or internal structural defects that are so important for understanding carrier delocalization in these materials. Electron tomography (ET) is a suitable tool for the near-atomistic structural characterization of 3D epi-SLs. The Vanmaeklebergh group has previously used ET to establish the basic unit cell of non-fused 3D binary[47, 15] and ternary[42] QD SLs, 2D honeycomb epi-SLs,[14] and thin multilayer honeycomb epi-SLs.[102]

Savitzky *et al.* reported a tomogram of a fused 3D PbS QD SL made at high pressure, but no assessment of necks or structural defects was presented.[112]

Here we report an in-depth and quantitative structural analysis of a 3D PbSe QD epi-SL using electron tomography. We show that with a full-tilt HAADF ET reconstruction of a disc-shaped epi-SL film (120 nm in diameter \times 38 nm tall), we are able to achieve sufficient spatial resolution (0.65 nm) to determine the position of all 1,846 QDs and the size and shape of all necks in the sample. From the center-of-mass coordinates of the QDs, we find that the sample consists of three SL grains and assign the unit cell and in-plane crystallographic orientation of each grain as well as the 3D structure of the grain boundaries. The epi-SL grains have a distorted simple cubic structure with lattice parameters in agreement with our previous results.[1] Maps of the neck locations and diameters reveal that the sample has an average of 3.7 necks per QD (giving an overall network connectivity of 72%) and an average neck diameter of 4.1 nm (64% of the QD diameter). The three grains show similar distributions of neck number (necks per QD) but very different distributions of average neck diameter, reflecting significant inhomogeneity between the adjacent grains. We discover a weak positive correlation between neck number and diameter and a strong negative correlation between neck number and both the average and standard deviation of the nearest neighbor QD distance, indicating that QDs with more necks tend to have more ordered local environments. Kinetic Monte Carlo charge transport simulations show that the SL grain boundaries have little impact on carrier mobility because the three grains are interconnected by many necked QDs. Our statistical analysis of this relatively disordered polycrystalline sample utilizes electron tomography to understand structure/property relationships and may help to achieve mini-band formation in more perfect 3D PbX QD epi-SLs.

3.3 Experimental

3.3.1 Materials

Lead oxide (PbO, 99,999%), oleic acid (OA, technical grade, 90%), diphenylphosphine (DPP, 98%), 1-octadecene (ODE, 90%), ethylene glycol (EG, 99.8%, anhydrous), acetonitrile (99.99%, anhydrous), hexanes (\geq 99%, anhydrous), toluene (99.8%, anhydrous), (3-mercaptopropyl)trimethoxysilane

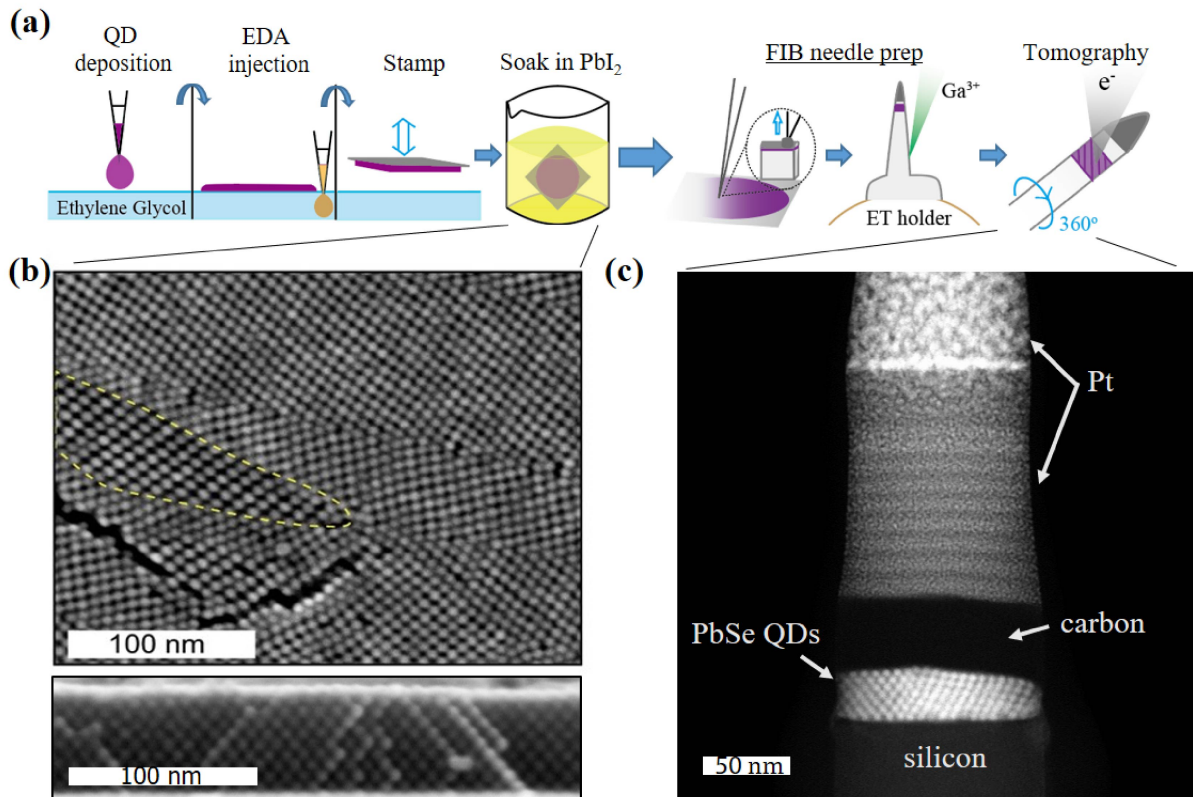


Figure 3.1. Fabrication of the PbSe QD epi-superlattice tomography sample. (a) Sample fabrication. (b) Plan-view and cross-section SEM images of a different region of the epi-SL film. The film is a polycrystalline SL with SL grains of two different in-plane orientations, previously assigned to the $(100)_{\text{SL}}$ and $(01\bar{1})_{\text{SL}}$ projections of a distorted simple cubic SL.[1] Most of the SL grains in this image have a $(100)_{\text{SL}}$ orientation. The dashed yellow line encircles a $(01\bar{1})_{\text{SL}}$ -oriented grain. Scale bars are 100 nm. (c) HAADF-STEM image of the needle-shaped tomography sample with disc-shaped epi-SL layer and all layers labeled. Scale bar is 50 nm.

(3-MPTMS, 95%), and N,N-dimethylformamide (DMF, 99.8%, anhydrous) were purchased from Sigma Aldrich and used as received. Trioctylphosphine (TOP, technical grade, $\approx 90\%$) and selenium (99.99%) were acquired from Fluka and mixed for 24 hours to form a 1 M TOP-Se stock solution. Ethylenediamine (EDA, $\approx 98.0\%$, anhydrous) was purchased from TCI and mixed with acetonitrile in a 1:1 volume ratio to make a 7.5 M EDA stock solution.

3.3.2 Quantum Dot Synthesis

PbSe QDs were synthesized and purified using standard air-free techniques. PbO (1.50 g), OA (5.00 g), and ODE (10.00 g) were mixed and degassed in a three-neck round-bottom flask at room temperature. The mixture was heated to 120 °C under vacuum to form dissolved $\text{Pb}(\text{OA})_2$

and dry the solution. After 1 hour at 120 °C, the Pb(OA)₂ solution was heated to 180 °C under argon flow and 9.5 mL of a 1 M solution of TOP-Se containing 200 μL of DPP was rapidly injected into this hot solution. An immediate darkening of the solution was observed, and the QDs were grown for 105 seconds at ~160 °C. The reaction was quenched with a liquid nitrogen bath and injection of 10 mL of anhydrous hexanes. QD purification and SL fabrication were performed in glove boxes with ≤ 0.5 ppm O₂ content. The QDs were purified by two rounds of precipitation/redispersion using ethanol/hexane and stored as a powder in the glove box.

3.3.3 Substrate preparation

A single-side polished Si substrate was cleaned using 10 minutes of sonication in acetone, Millipore water, and then isopropanol, followed by drying in a stream of flowing air. The cleaned substrate was immersed in a 100 mM solution of 3-MTPMS in toluene for 1 hour to functionalize its native SiO_x surface for improved epi-SL adhesion, then rinsed with neat toluene and dried in flowing air.

3.3.4 Superlattice fabrication

An oleate-capped superlattice was prepared in the glovebox by drop casting 70 μL of a 4 g/L dispersion of PbSe QDs in hexanes onto 6 mL of ethylene glycol (EG) in a Teflon well (3.5 × 5 × 1 cm). After depositing the QD solution, the well was immediately covered with a glass slide. The hexane evaporated over 30 minutes, resulting in a smooth, dry QD film floating on the EG surface. The glass slide was then removed and 0.1 mL of a 7.5 M solution of ethylenediamine in acetonitrile was slowly injected (5-10 sec) into the EG under the QD film using a 500 μL Hamilton syringe. After 30 seconds of exposure to EDA, the resulting epi-SL film was stamp transferred to the Si substrate using a vacuum wand, rinsed vigorously with acetonitrile and dried under flowing N₂. The epi-SL film was then immediately immersed in a 10 mM solution of PbI₂ in DMF for 5 minutes, rinsed thoroughly with acetonitrile and dried under flowing N₂. This procedure is nearly identical to the one used in our previous report[1] and yields epi-SL films with the same SL unit cell, grain size, and homogeneity, including degree of QD necking, coverage of the substrate, and density of cracks. However, the films for tomography studies are somewhat thinner (40 nm vs. 50-80 nm) and have a higher density of intra-grain

extended defects (e.g., partial twins) because they were prepared in a glove box with a higher O₂ concentration (5 ppm vs. ~0.1 ppm).

3.3.5 Basic characterization

Optical absorbance measurements of QDs dispersed in TCE were performed with a PerkinElmer Lambda 950 spectrophotometer. Neat TCE served as the background for the solution measurements. Scanning electron microscopy was performed on both an FEI Magellan 400L XHR SEM operating at 10 kV and 25-50 pA and a JEOL JEM-2800 TEM (with a secondary electron detector) operated in STEM mode with a 1.0 nm probe size.

3.3.6 Grazing incidence small-angle X-ray scattering

GISAXS measurements were performed on Beamline 7.3.3 of the Advanced Light source (ALS) at Lawrence Berkeley National Laboratory using 10 keV monochromatic X-rays ($\lambda = 1.24 \text{ \AA}$) with an energy bandwidth of 1%. For GISAXS measurements, SL films were prepared on Si substrates and transported with the QD suspensions to the ALS under nitrogen to minimize air exposure prior to measurement. However, measurements were performed in air. A Dectris Pilatus 2M detector with a pixel size of $0.172 \times 0.172 \text{ mm}$ and 1475×1679 pixels was used to record the 2D scattering patterns. A silver behenate standard was used to determine the sample-to-detector distance and beam center. Exposure times ranged from 0.2 to 30 s. The grazing angle of incidence was varied from 0.2° to 0.3° . Manual pattern fitting was performed using the IndexGIXS software package provided by Detlef Smilgies of the Cornell High Energy Synchrotron Source. The critical angles of the films were fit empirically (0.195° for the oleate-capped SLs and 0.21° for the epi-SLs) to capture the breadth of the Yoneda band.

3.3.7 Tomography needle sample preparation

An area of the epi-SL film suitable for FIB milling was located by SEM and tagged with a Pt fiducial marker deposited by electron-beam induced deposition (EBID) in an FEI Quanta 3D FEG DualBeam microscope. The sample was then coated with 50 nm of carbon using the pulse plasma mode of a Leica ACE200 evaporator and returned to the DualBeam for FIB milling, lift-out, and final needle preparation. Prior to milling, a $\sim 200 \text{ nm}$ Pt capping layer was deposited onto the carbon-coated sample by EBID, followed by an additional $\sim 2000 \text{ nm}$ of Pt deposited

by ion beam induced deposition (IBID). The carbon layer serves primarily to enhance STEM imaging contrast by separating the epi-SL layer from the high-Z protective Pt capping layer. The area of interest was then FIB milled into a wedge shape ($10\ \mu\text{m} \times 6\ \mu\text{m} \times 2\ \mu\text{m}$), lifted-out with an OmniProbe 400 nanomanipulator, ion welded to the tip of a sample holder for needle tomography samples (Single Point Tip, Hummingbird Scientific), and FIB milled again into a $\sim 130\ \text{nm}$ diameter needle (Fig. S2). Milling was performed in several stages. The wedge was first milled into a pillar shape ($1\ \mu\text{m}$ diameter) using a $0.3\ \text{nA}$ ion beam at a $30\ \text{keV}$ accelerating voltage, then thinned to a $\sim 200\ \text{nm}$ diameter needle using $50\ \text{pA}$ at $16\ \text{keV}$. Finally, a 5 minute ion beam shower ($25\ \text{pA}$ at $5\ \text{keV}$) was employed to sharpen the needle to $\sim 130\ \text{nm}$ and remove surface damage. The finished needle contained a disc-shaped epi-SL layer ($38\ \text{nm}$ tall $\times 128\ \text{nm}$ in diameter) for tomographic analysis.

3.3.8 HAADF-STEM Electron Tomography

The needle sample was mounted on the rotation axis of a Hummingbird Scientific single-tilt tomography holder (1000 Series) and imaged in a double aberration corrected JEOL JEM-ARM 300F TEM operated at $300\ \text{keV}$ in STEM mode ($\sim 25\ \text{mrad}$ semi-convergence angle). Two series of images were acquired, with HAADF and bright-field data recorded simultaneously ($2\text{k} \times 2\text{k}$ images) at each tilt angle. The first series consisted of 145 HAADF images spanning tilt angles over -78 to 67 degrees in 1 degree steps. The sample was then removed from the microscope, manually rotated on the sample holder by 86 degrees, and re-imaged from -68 to 78 degrees in 2 degree steps (resulting in 73 additional images). All 2D and 3D image processing was conducted in MATLAB unless otherwise noted. The two tilt-series were then merged using cross-correlation comparison (Fig. S4). The merged tilt-series include 181 images covering tilt angles from 0° to 226° . The image stack was then aligned vertically (along the rotation axis) by iteratively shifting the images to maximize the value of the 2D normalized cross-correlation function between adjacent images in the stack. Pixels outside of the epi-SL film were excluded from this cross-correlation calculation in order to maximize the quality of the vertical image alignment. Horizontal alignment of the images (normal to the rotation axis) was accomplished by converting each image to a 1D intensity profile and shifting the images to maximize the match between the 1D curves. The aligned image stack was then processed through two iter-

ations of a Wiener image filter to remove noise. Tomographic reconstruction was carried out on the aligned and de-noised tilt-series using 200 iterations of the simultaneous iterative reconstruction technique (SIRT) in the ASTRA toolbox.[119, 122] The raw reconstructed volume consisted of $2048 \times 2048 \times 700$ voxels with edge lengths of 1 Å. The spatial resolution of this reconstruction was evaluated by the Fourier shell correlation (FSC) method to be 6.5 Å (Fig. S5).

The raw reconstruction was processed in two different ways. For analysis of the QD necks, the reconstruction was simply smoothed by a nonlinear anisotropic diffusion filter. Image processing for analysis of the QD positions was more involved. The raw tomogram was first filtered with a morphological 3D top-hat filter to minimize reconstruction intensity attenuation and enhance contrast. A top-hat filter was used to retain edge contrast instead of the more common Fourier filter[21] because Fourier filtering would erroneously remove necks between QDs and other important structural features present in the raw tomogram. To better emphasize the QD positions, the filtered tomogram was convolved with a spherical 6.0 nm diameter QD kernel with a homogeneous intensity profile to obtain a 3D map of normalized cross-correlation (NCC) coefficients indicating the center of mass of each QD in the sample. Use of the 6.0 nm QD template is justified by the analysis of the average QD size and polydispersity from conventional dark-field STEM images (pixel size of 0.2 nm) of a different area of the same sample (Fig. S6). Prior to data analysis, the outer 6 nm of the cylinder-shaped tomogram was digitally removed to exclude QDs near the surface of the sample that were potentially deformed by the FIB milling process. To automate the measurement of neck dimensions, a script was written that defines a plane normal to each inter-QD axis and slides this plane along the axis to locate the minimum neck area. The neck diameter was then determined as the diameter of a circle of the same area.

3.3.9 Mobility Simulation

Mobility simulations were performed utilizing the Hierarchical Nanoparticle Transport Simulator (HiNTS) kinetic Monte Carlo code, developed by some of us previously.[121, 104] HiNTS simulates transport by developing several modeling layers and then integrating them into a hierarchical scheme. After the energetics of the individual QDs is computed by *ab initio* methods,

the QD-to-QD transitions of the charges are described by the following two mechanisms:

(1) Miller-Abrahams single phonon-assisted hopping between nearest neighbor QDs:

$$\Gamma_{i \rightarrow j} = \begin{cases} \nu g_{ij} \beta_{ij} \exp\left(\frac{-\Delta E_{ij}}{k_b T}\right) & \text{if } \Delta E_{ij} > 0, \\ \nu g_{ij} \beta_{ij} & \text{if } \Delta E_{ij} \leq 0 \end{cases} \quad (3.1)$$

where ν is a suitably chosen prefactor, g_{ij} is the product of the initial density of states on QD_i and the final density of states on QD_j, β_{ij} is the tunneling amplitude evaluated using the WKB approximation as $\beta_{ij} = \exp\left(-2\Delta x \sqrt{\frac{-m^*(E_i + E_j)}{\hbar^2}}\right)$, where Δx is the minimal surface separation of the QDs, m^* is the effective mass of electrons in the barrier, and E_i and E_j are the energy levels of QD_i and QD_j. ΔE_{ij} is the total energy difference associated with an electron transitioning from QD_i to QD_j: $\Delta E_{ij} = \Delta E_{ij}^{band} + \Delta E_{ij}^{charging} + \Delta E_{ij}^{voltage}$, where ΔE_{ij}^{band} is calculated using the one-electron band energies of the QDs determined by *ab initio* methods,[63] $\Delta E_{ij}^{charging}$ is calculated using the charging energies of the QDs as determined by a hybrid empirical-perturbative method,[34] and $\Delta E_{ij}^{voltage}$ is the energy difference due to the applied voltage. In general, the QD-QD hopping can be nearest neighbor or farther neighbor, variable range hopping. Either hopping process can involve an elastic reorganization of the QD atoms, the Marcus process, or not, the Miller-Abrahams process. Finally, the long-range part of the Coulomb interaction may or may not be included. Of the eight possible combinations, for example, [56] investigated the intriguing process of variable range hops with long-range Coulomb interactions and the Marcus reorganization process. HiNTS is capable of accommodating any of these eight combinations. We chose the simplest Miller-Abrahams process because both variable range hops and Marcus processes have been shown to become important only at low temperatures, whereas our experiments were performed at room temperature. Indeed, experiments on QD lattices regularly report the standard activated, Miller-Abrahams temperature dependence around room temperature.[135]

(2) Tunneling through the neck of epitaxially-fused QDs:

$$\Gamma_{i \rightarrow j} = \begin{cases} \frac{2\pi}{\hbar} |t|^2 g_{ij} \exp\left(\frac{-\Delta E_{ij}}{k_b T}\right) & \text{if } \Delta E_{ij} > OE, \\ \frac{2\pi}{\hbar} |t|^2 g_{ij} & \text{if } \Delta E_{ij} \leq OE \end{cases} \quad (3.2)$$

where $|t|$ is the QD-QD tunneling matrix element, and OE is an overlap energy. This transition channel represents that when a neck is formed between two QDs, their electronic states overlap and therefore hybridize. This hybridization induces a perturbation of the energy levels of the individual QDs, which we model by an overlap energy OE that is proportional to the neck diameter. The electronic states of those pairs of QDs whose energy level difference is less than OE : $\Delta E_{ij} \leq OE$, hybridize to such a degree that they support a metallic QD_i-to-QD_j transition instead of a hopping one, paving the way toward the formation of a mini-band. The tunneling matrix element $|t|$ depends on the wavefunction overlap between the necked QDs. For its calculation, we adopt the approximation of Fu *et al.*: [48]

$$|t| = \frac{9\hbar^2 n \rho^3}{m^* d^2} \quad (3.3)$$

where n is the average electron volume density of the two quantum dots, ρ is the neck radius, m^* is the effective electron mass, and d is average QD diameter. HiNTS simulates nearest neighbor transitions and interactions, it does not include transitions to and interaction with farther neighbors.

On the next HiNTS modeling layer, a superlattice of QDs, or epi-SL, is constructed. Simulations were performed on three types of epi-SL samples. To begin with, the replica of the tomography sample was generated using the experimentally determined center-of-mass coordinates, QD diameters, and neck map. This tomography sample included all three SL grains. Since the circular shape and uneven periphery of the tomography sample would make it harder to set up controlled transport simulations, QDs at the periphery of the sample were removed to reduce the simulation volume to the well-defined central cuboid of the tomography sample. To develop a comparative analysis of the transport of this tomography sample, we next generated two ensembles of over a thousand samples each to form a comparison basis. The first ensemble consisted of monocrystalline epi-SLs with the lattice parameters and neck statistics of grain I of the tomogram. The second ensemble consisted of bicrystalline epi-SLs with the same lattice parameters and neck statistics of grain I, but bisected by a plane of missing necks normal to the transport direction to create a necking grain boundary. The QDs in the latter two types of samples were assigned a diameter and lattice displacement vector according to the experimentally-determined Gaussian distributions.

Electron transport was simulated by first randomly placing electrons on QDs to fill the samples with a predetermined density of electrons. Based on our previous work, we chose the electron density to be 0.5 electrons per QD, remaining far from commensuration to avoid Coulomb blockade effects.[121] A small voltage of 1 mV was then applied across electrical contacts on opposite sides of each sample to induce electron transport. Periodic boundary conditions were used. Throughout the simulation, we checked and ensured that the current-voltage characteristic stayed in the linear regime. Finally, the mobility was determined according to the following equation:

$$\mu = \frac{\text{electrons collected at drain electrode} \times l}{\text{total number of electrons} \times t \times E} \quad (3.4)$$

where l is the length of simulation box normal to the electrodes, t is the simulation time, and E is the applied electric field. The transport across every sample in both ensembles was simulated.

3.4 Results and Discussion

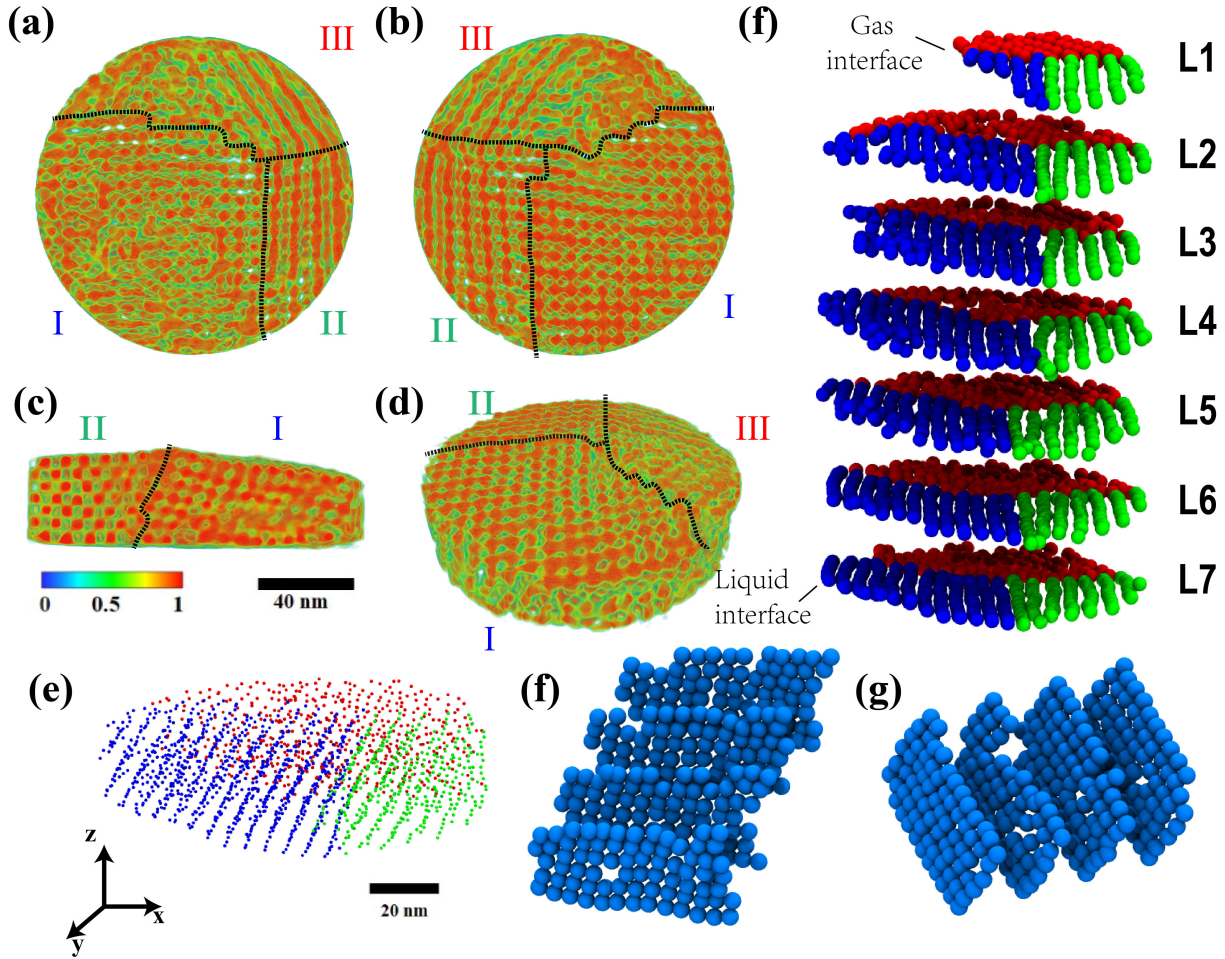


Figure 3.2. The epi-SL tomogram and QD positions. (a) Top, (b) bottom, (c) cross-section, and (d) perspective views of the tomogram of the epi-SL film. The color scale denotes the normalized electron density in units of e^-/nm^3 . Dashed lines represent grain boundaries between the three SL grains (labeled grain I, II, and III). The scale bar is 40 nm. (e) Perspective image of the center of mass coordinates of all QDs in the sample. Each QD is represented by a sphere with a diameter of 1 nm (for ease of viewing). The QDs are color coded according to their location in grain I (blue), grain II (green), or grain III (red). The scale bar is 20 nm. (f) Exploded view of the seven QD layers of the sample to illustrate the internal structure of the epi-SL film. Each QD is represented by a 6 nm diameter sphere (Fig. S6). Layer 1 (L1) is the top layer of the originally floating film (at the QD/gas interface), while layer 7 (L7) is the bottom layer of the film (at the liquid/QD interface). The QDs are color coded according to panel e. (f-g) Representative monolayers in grain I separated along direction x and y, representing SL lattice planes of (f)(100)_{SL} and (g)(010)_{SL}.

3.4.1 SL Unit Cell and Disorder

Oleate-capped PbSe QDs with a diameter of 6.4 ± 0.3 nm were used to fabricate a 3D polycrystalline epi-SL film via self-assembly and ligand exchange on a liquid ethylene glycol substrate

(Fig. 3.1a and Methods).[11, 43, 36, 37] After triggering epitaxial fusion of the QDs with 1,2-ethylenediamine, the epi-SL film was stamped onto a silicon substrate, immersed in a solution of PbI_2 to remove additional oleate ligands, and milled by focused ion beam (FIB) into a 128 nm diameter disc embedded in a nanoscale needle for full-tilt electron tomography studies (Fig. 1a). Scanning electron microscopy (SEM) images of the epi-SL film and the finished tomography needle are presented in Fig. 1b and 1c, respectively. An optical extinction spectrum of the QDs in solution and additional details about the preparation of the tomography sample are provided in the Supporting Information (Figs. S1-S2).

We acquired a $\pm 113^\circ$ single-axis tilt-series of 181 images of the sample using high-angle annular dark-field scanning transmission electron microscopy (HAADF-STEM) in a double aberration-corrected microscope (see Methods and Figs. S3-S4). Tomographic reconstruction of the sample was accomplished using the SIRT algorithm after careful image alignment and noise filtering. The final tomogram (Fig. 3.2a and Movie S1) has a spatial resolution of 6.5 Å (~ 1 unit cell of PbSe) as determined by the Fourier shell correlation (FSC) method (Fig. S5). This resolution is sufficient to unambiguously identify the center of mass (CoM) coordinates of all 1,846 QDs in the sample volume, as illustrated in Fig. 3.2e-f.

The CoM data were used to determine the size, shape, crystallographic orientation, and lattice parameters of the constituent SL grains as well as the presence of inter-grain defects (grain boundaries, amorphous domains, voids) and intra-grain defects. Visual inspection of Fig. 3.2 shows that the sample is seven QD layers thick and consists of three cylindrical sector-shaped (pie slice) SL grains that meet at a grain boundary triple junction near the center of the tomogram (dashed lines in Fig. 3.2a-d). While it is possible to assign the SL grain crystallography *a priori* from the CoM coordinates, we utilized the known unit cell of similarly-prepared PbSe QD epi-SLs[1] (distorted simple cubic with $a = 6.6 \pm 0.2$ nm and $\alpha = 99 \pm 2^\circ$; Fig. S7) to help interpret the tomogram. Grain I has a square-like lattice of QDs in each QD layer parallel to the substrate, so it is assigned as a $(100)_{\text{SL}}$ -oriented SL grain, which is the most common grain orientation in this sample (see Fig. 1b). Grains II and III have 1D chains of QDs in each layer parallel to the substrate, with an average QD spacing of a along the chains and $\sqrt{2}a$ between the chains. This arrangement is consistent with the $(01\bar{1})_{\text{SL}}$ projection of the dis-

Table 3.1. Lattice constants of SL grains I and II as determined from statistical analysis of the tomogram. GISAXS data is from refrence **31**.

Grain	a/nm	b/nm	c/nm	α	β	γ
I	6.4 ± 0.6	6.4 ± 0.6	5.9 ± 0.7	$102 \pm 8^\circ$	$95 \pm 7^\circ$	$96 \pm 7^\circ$
II	6.3 ± 0.6	6.5 ± 0.6	6.2 ± 0.7	$103 \pm 9^\circ$	$107 \pm 5^\circ$	$97 \pm 7^\circ$
GISAXS		6.6 ± 0.2			$99 \pm 2^\circ$	

torted simple cubic SL unit cell, so grains II and III are assigned as $(01\bar{1})_{\text{SL}}$ -oriented SL grains (again, see Fig. 3.1b). Grains II and III intersect at a planar coherent twin boundary indexed as $39^\circ[001],(010)$ (most easily seen in Fig. 3.2a-b). Between grains I and II, it is harder to define a grain boundary interface as we observe in Fig. 3.2c a relatively smooth change in the $[001]_{\text{SL}}$ lattice vector from grain II on the left side to grain I on the right side. A possible mechanism for such an inter-grain orientational transition is proposed in Fig. S8 involving a small rotation and a subsequent glide of the $(100)_{\text{SL}}$ plane. Grains I and III meet at a highly-corrugated boundary. All three grain boundaries are normal or nearly normal to the substrate and span the entire thickness of the QD film. SEM images of similar grain boundaries are presented in Fig. S9. In Fig. 3.2f-h, we show representative separated layers in grain I along all three SL lattice vectors showing QD vacancies and dislocations from different perspectives. The randomness in the QD positional order is shown to occur in all directions. We also note that there is no significant difference in the vacancy rate for layers normal to different lattice vectors. Several slice views of the tomogram taken at different angles are shown in Fig. S10 emphasizing the orientational differences between SL unite cells of grain I and II and also how the lateral and vertical monolayers are connected through necks. See Movies S2 and S3 for additional continuous slices of this sample.

We determined the lattice parameters of grains I and II by compiling nearest-neighbor QD distances and bond angles from the CoM data (see Fig. S11 for labeling conventions). Grain III was excluded from this analysis due to its poor spatial order. Histograms of the QD distances and angles (Figs. S12-S13) show Gaussian distributions with average and standard deviation values summarized in Table 1. The lattice constants of grains I and II are in good agree-

ment with the unit cell parameters of similar epi-SL films derived from ensemble GISAXS measurements,[1] so we conclude that these epi-SLs have essentially the same crystal structure, validating the recent GISAXS results. However, grains I and II also exhibit broad distributions of distances and angles indicative of a relatively large amount of positional disorder, as is apparent from Fig. 3.2. The spatial order of this sample is likely limited by the structural disorder of the original oleate-capped SL, the presence of several nearby grain boundaries, variability in QD neck number and diameter (*vide infra*), and (possibly) mechanical strain caused by sample preparation. Two additional aspects of the data are noteworthy. First, while grains I and II have very similar triclinic unit cells, they differ slightly in their β angle (Table 1). Such grain-to-grain variability is expected in polycrystalline SLs due to local differences in grain nucleation and growth, especially when the SL grains are small and experience non-uniform stress. Electron tomography is one of the few techniques capable of detecting such minute structural differences between individual QD SL grains. Second, grain I is slightly compressed along the film normal, which is shown in Fig. 3.2g-h in the c direction compared to Fig. 3.2f. This is commonly seen for nanocrystal films prepared by solvent evaporation.[130, 55, 115, 39]

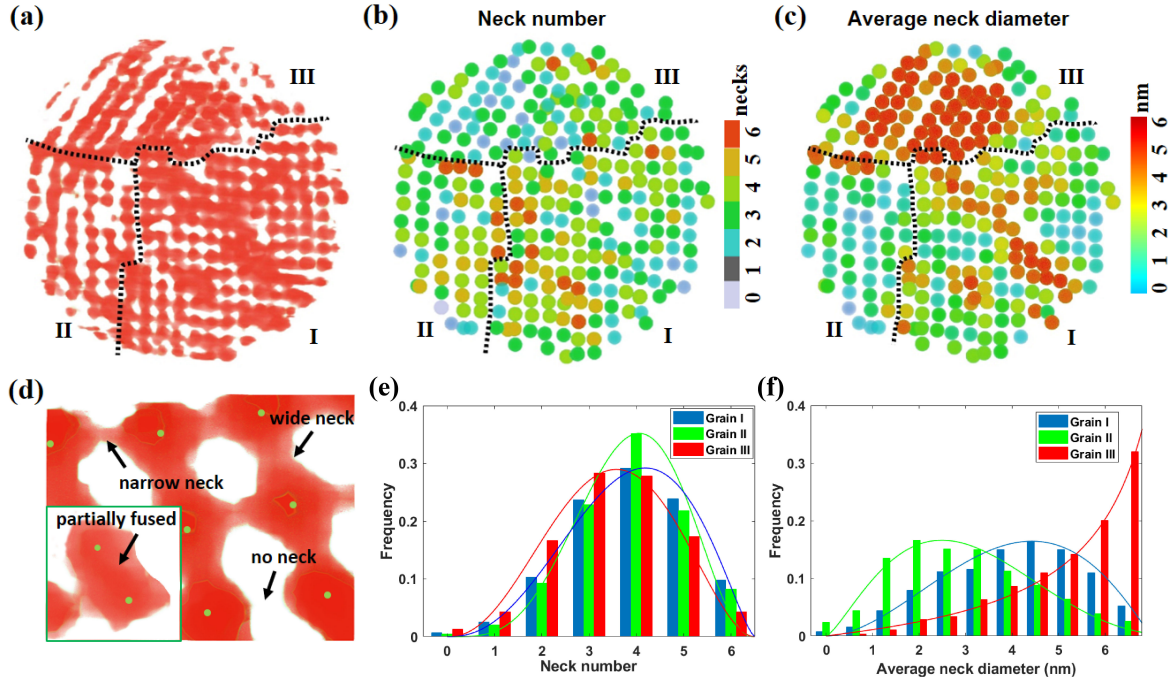


Figure 3.3. Analysis of the QD necks. (a) A slice of the tomogram through the middle of L4, showing in-plane necks between the QDs. (b) Heat map of the total number of necks for each QD in L4. The color scale is labeled. (c) Heat map of the average neck diameter for each QD in L4, including both in-plane and out-of-plane necks. The color scale is labeled. (d) Magnified isosurface views of two regions of the sample to illustrate typical neck polydispersity (narrow, wide, and missing necks) and a highly-fused pair of QDs (inset). The green dots denote the CoM of each QD. (e) Histograms of neck number for all QDs in grain I, II and III (inclusive of L1-7, not just L4). The solid curves are fitted beta distributions. (f) Corresponding histograms of average neck diameter. Fitting beta distributions are shown as solid curves. See Fig. S15 for histograms of the diameter of every neck in each grain.

3.4.2 Characterization of Neck Disorder

In addition to the positions of the QDs, the tomogram provides rich information about the crystalline connections (necks) between the QDs. Previous TEM studies have shown that the QDs in these SLs are epitaxially fused across their $\{100\}$ facets.[50, 111, 87, 131, 124, 129] The epitaxial necks likely dictate the strength and uniformity of electronic coupling within the epi-SLs,[83] so mapping the location and size of the necks is essential for understanding and optimizing the electronic properties of these materials. Electron tomography can directly visualize the necks and map the 3D neck network inside each SL grain. Fig. 3.3a shows a slice of the tomogram through the middle of L4 with the necks between the QDs clearly visible. We

implemented an automated program to measure the cross-sectional area of every neck in the sample and assign each an effective diameter (Fig. S14). In our approach, any connection with an area smaller than the tomogram spatial resolution (0.43 nm^2 , or about one PbSe unit cell) was considered to be absent (a “missing neck”). An example of a missing neck is shown in Fig. 3.3d.

Heat maps of the average neck diameter and the total number of necks for each QD in L4 are presented in Fig. 3.3b-c. Maps for all seven layers of the sample are compiled in Figs. S16 and S17. The 1,846 QDs in the sample have a maximum of 4,865 possible epitaxial necks (considering the six $\{100\}$ facets of each QD and sample edge effects, vacancies, and voids). We observe a total of 3,471 necks, giving an overall network connectivity of 71%, well above the bond percolation threshold (p_c) of 25% for simple cubic lattices.[127] This estimate of neck connectivity is conservative because, as mentioned above, any neck smaller than the tomogram resolution (≤ 3 Pb atoms wide) is not counted by our algorithm. Overall, the average number of necks per QD is 3.7 and the average neck diameter is 4.1 nm (64% of the QD diameter). Table 2 summarizes the neck statistics for the sample.

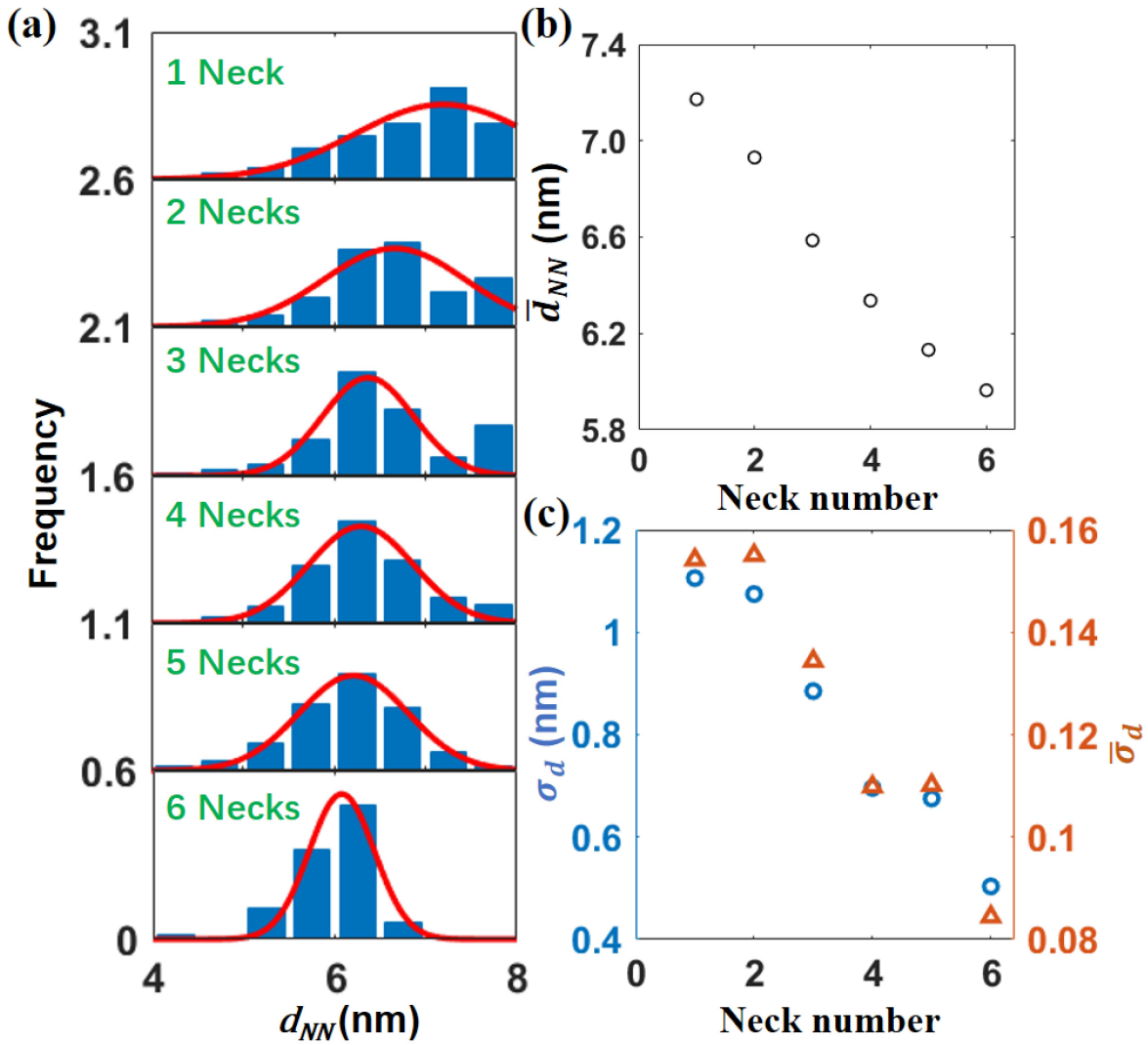


Figure 3.4. Correlation of neck number with nearest neighbor QD positional disorder. (a) Histograms of NN distance (d_{NN}) at each neck number for all of the QDs in grains I and II. Overlaid red curves are Gaussian fits. (b) Plot of the average NN distance (\bar{d}_{NN}) versus neck number. (c) Plot of the standard deviation of the NN distance (σ_d) and the normalized standard deviation of the NN distance ($\bar{\sigma}_d = \sigma_d/\bar{d}_{NN}$) versus neck number. $\bar{\sigma}_d$ is a measure of the local disorder that is independent of differences in unit cell size.

Figs. 3.3e and f show histograms of neck number and diameter for the three epi-SL grains in this sample. The neck number for all three grains follows a beta distribution (solid curves) with a peak at 3.5-4 necks per QD. Grain I has the largest fraction of QDs with high connectivity (five and six necks), while grain II has the largest fraction of QDs with intermediate connectivity (four necks) and the smallest fraction of QDs with low connectivity (three or fewer necks).

Overall, grains I and II are quite similar with respect to neck number. In contrast, grain III has much poorer neck connectivity than grains I and II, with the smallest fraction of high-connectivity QDs and the largest fraction of low-connectivity QDs. Grain III is also dominated by QDs with very large neck diameters (see the J-shaped distribution in Fig. 3.3f). The low neck number and large fraction of heavily-fused QDs contribute to the poor spatial order of grain III. The average neck diameters of grains I and II also follow a beta distribution and are similarly polydisperse. These two beta distributions (grain I: $\alpha = 2.90$, $\beta = 2.25$; grain II: $\alpha = 2.10$, $\beta = 3.18$) are approximately mirror images of each other (Fig. 3.3f). Grain I has a larger fraction of thicker necks (>4 nm) while grain II has a larger fraction of thinner necks (<4 nm). The reason for these differences in neck diameter and number in adjacent epi-SL grains is unclear, but probably related to variability in the spatial order of the parent oleate-capped SL and the kinetics of the epi-SL phase transition. We attempted to determine a correlation between neck number and diameter to measure whether the number of necks on each QD determined the neck thickness. Supporting Information Fig. S18a shows this correlation for the full sample and for each of the grains, indicating little correlation between the number of necks and the neck thickness for each QD, but also clearly showing that the average neck thickness is consistent throughout the grain regardless of the number of necks. Understanding the origin of such differences between grains will require systematic study of many tomograms to establish statistical relationships.

We also measured whether there are trends in the necking that depend on the position of the layer within the SL. Fig. S18b-c plot the average neck number and diameter for each of the seven QD layers of the film. We find that the neck number is essentially constant in the middle five QD layers of grains I and II, while the neck number is significantly lower in grain III. However, there is a reduced neck number in L1 (the top of the film) for grains I-III and L7 (the bottom of the film) for grain II and III, despite taking into account edge effects. We conclude that the top and bottom monolayers of the epi-SL tend to have fewer necks per QD. For all three grains, the neck diameter is smaller in L1 and L7 and increases in the middle of the film (Fig. 3.4c). Interestingly, while neck number and neck thickness are not in general correlated, the number and thickness of necks is lower at the QD/liquid and QD/gas interfaces, which suggests that out-of-plane forces from adjacent layers are important for necking forma-

Table 3.2. Neck statistics.

Parameter	Grain I	Grain II	Grain III	Total
number of QDs	903	389	554	1846
QD number density (nm^{-3}) $\times 10^3$	3.9	3.7	3.5	3.7(3.5*)
space filling fraction	0.53	0.51	0.48	0.51
possible necks	2343	1028	1494	4865
observed necks	1760	774	959	3493
connectivity	75%	75%	64%	72%
average number of necks	3.8	4.0	3.4	3.7
average neck diameter(nm)	4.0	3.5	5.0	4.1

* from reference 31.

tion and order. One might also expect to observe a monotonic decrease in neck number and diameter along the film normal due to ligand (glycoxide and oleate) concentration gradients since the ligands diffuse into the SL from the QD/liquid interface. Our neck diameter profile suggests that no such concentration gradients exist in this sample, in agreement with recent infrared spectroscopy measurements showing homogeneous ligand exchange in films of similar thickness.[1]

We also explored the relationship between neck number and the local spatial order of the epi-SL. In the ideal averaged epi-SL unit cell (Fig. S7), each QD is necked to six nearest neighbors (NNs) located at a common center-to-center distance and fixed lattice angles. In contrast, QDs in real epi-SLs have distributions of neck number, NN distance, and lattice angles. These distributions provide a measure of the local (nanoscale) spatial disorder of the QD array. We reasoned that the distribution of NN distances and lattice angles should depend strongly on neck number because necks can form over only a narrow range of QD positions. Thus, QDs with high (low) connectivity should have more (less) ordered local environments. To assess the impact of neck number on local spatial order, we compiled histograms of the nearest neighbor distance (d_{NN}) as a function of neck number for all of the QDs in grains I and II (Fig. 3.4a).

Grain III was again excluded from analysis due to its poor order. We find that as neck number increases, the average NN distance (\bar{d}_{NN}) and standard deviation of the distance (σ_d) decrease in a linear fashion. As Fig. 3.4b and c shows, \bar{d}_{NN} decreases from ~ 7.2 nm for QDs with one neck to ~ 6.0 nm for QDs with six necks, while σ_d decreases from 1.1 nm to 0.5 nm (a 55% reduction). Although this simple metric is limited to NNs and neglects the propagation of disorder across longer length scales,[111] it demonstrates the importance of neck connectivity to the structural order of QD epi-SLs: high neck number is associated with high local spatial order. Future tomograms of more perfect monocrystalline samples will be used to map, understand, and ultimately minimize the multiscale spatial disorder of these QD solids.

3.4.3 Charge Transport Simulation

Charge transport in the above characterized epi-SL tomography sample was simulated with the HiNTS code. As described in the Methods section, the simulated tomography sample was generated using the QD CoM coordinates and neck network of the experimental tomogram and trimmed into a cuboid shape with electrodes on opposite faces (Fig. 3.5a). In this geometry, electrons must cross the grain boundary between grains I and II, or I and III, to traverse the sample. The tomogram shows that grains I, II, and III are connected by many necks across these grain boundaries. The mobility of the tomography sample was found to be ~ 4.6 cm²/Vs (Fig. 3.5d).

To probe the relative importance of the necking versus the conventional SL grain boundaries, and the disorder for the electron transport across the tomography sample, mobility simulations were also performed on the two ensembles of its monocrystalline and bicrystalline analogues. First, we compared the mobility of the tomography sample to that of the ensemble of monocrystalline (single-grain) epi-SLs with the same lattice parameters and neck statistics as grain I (Fig. 3.5b). Relative to the monocrystalline samples, the tomography sample has three grains separated by SL grain boundaries, but these grain boundaries are bridged by a large number of inter-QD necks. In spite of these differences, visibly the tomography sample's mobility remains typical of the mobility distribution of the ensemble of monocrystalline epi-SLs, as shown in the upper panel of Fig. 3.5d. Next, we also calculated the carrier mobilities of the ensemble of bicrystalline (double-grain) epi-SLs, generated by removing a bisecting plane of

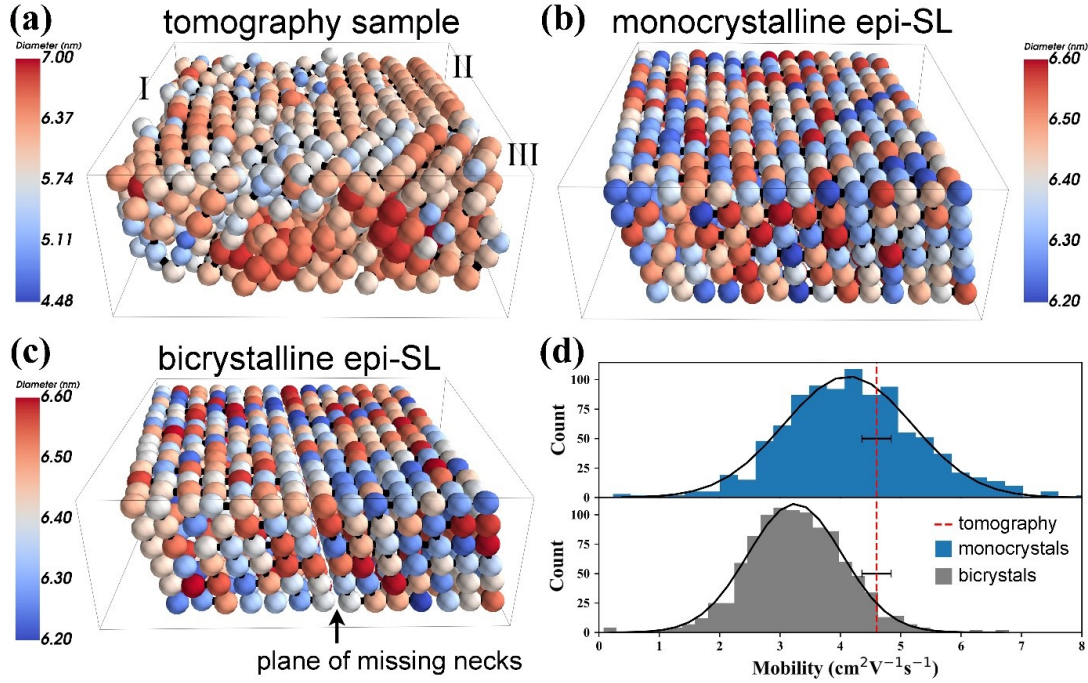


Figure 3.5. Transport simulation results. (a-c) Perspective views of the three types of simulated samples. (a) The tomography sample (trimmed from a disc into a cuboid). Grains I, II, and III are labeled. (b) A monocrystalline epi-SL. (c) A bicrystalline epi-SL. The monocrystalline and bicrystalline epi-SLs were generated using the lattice parameters, QD size distribution, QD positional disorder and neck statistics of grain I. The bicrystalline samples are bisected by a plane of missing necks (a necking grain boundary), which limits transport across this plane to hopping. Virtual electrical contacts are placed at the left and right sides of each sample. All simulation boxes are approximately $92 \times 92 \times 39$ nm. (d) Comparison of the calculated electron mobility of the tomography sample (dashed red line), monocrystalline epi-SLs (blue bars) and bicrystalline epi-SLs (gray bars). The horizontal error bar represents the error in the mobility estimate for the tomography sample. Overlaid black curves are Gaussian fits of the histograms. The mobility for the monocrystalline and bicrystalline samples is 4.25 ± 1.25 cm²/Vs and 3.28 ± 0.8 cm²/Vs, respectively.

necks from the monocrystalline samples (Fig. 3.5c). Electrons can move across this “necking grain boundary” only by hopping, which is significantly slower than direct tunneling through necks. We find that the computed average mobility decreases by $\sim 25\%$ as a consequence of splitting the neck network in twain (lower panel of Fig. 3.5d). Visibly, the introduction of the necking grain boundary makes the tomography sample’s mobility largely inconsistent with the bicrystalline mobility distribution.

The most natural explanation of these results is that the mobility in these strongly disordered epi-SLs is primarily determined by transport across the inter-QD neck network, while SL grain

boundaries impact the mobility only to a limited degree as long as inter-QD necks continue to connect the SL grains across the SL grain boundary with a reasonable density. The tomography sample falls into this category: this explains why its mobility is consistent with the mobility distribution of the monocrystalline samples. In contrast, when a sample is bisected with a neck grain boundary, so that the two neck-grains cease to be connected by inter-QD necks, electrons are forced to thermally hop across no-neck boundaries rather than tunnel through necks, thereby reducing the mobility by a substantial amount. Our analysis suggests that the formation of necks between QDs across conventional SL grain boundaries is an efficient way to substantially increase carrier transport across those grain boundaries. Strategies to enhance the mobility in SLs were already discussed in earlier works, wherein the importance of reducing the disorder of SLs to form mini-bands was emphasized.[84] A key message of the present paper is that the mobility of QD SLs can also be substantially improved by forming sample-spanning neck networks. In a single-grain sample, charge transport should be improved by regulating intra-grain necking conditions such as decreasing neck size dispersity and increasing connectivity. This is particularly true for QD SL based photovoltaics, where the charge carriers are collected along the through-plane (film normal) direction of the multilayer instead of in-plane direction. We did observe a higher through-plane connectivity of QDs in Grain I and the voltage was accordingly applied in the same direction for the simulations. However, further investigations should be conducted to look into the effect of the degree of anisotropy of connectivity on the mobility, and will more rely on structural statistics from single-grain tomography samples, which is beyond the scope of this paper.

3.5 Conclusion

We analyzed a full-tilt electron tomographic reconstruction of a disc-shaped region of a 3D epitaxially-connected PbSe QD SL film. This tomogram provides (i) sufficiently high spatial resolution (0.65 nm) to accurately determine the position and size/shape of the QDs and their necks and (ii) sufficiently large volume ($4.3 \times 10^5 \text{ nm}^3$) to enable meaningful statistical analysis of structural disorder in the sample. We showed that the sample consists of three SL grains and assigned the unit cell and in-plane crystallographic orientation of each grain as well as the

structure of the three grain boundaries. Maps of the neck locations and diameters revealed that the sample has an average of 3.7 necks per QD (overall network connectivity of 71%) and an average neck diameter of 4.1 nm (64% of the QD diameter). In testing correlations between neck number, neck diameter, inter-QD distance, and QD location in the film, we discovered a strong association between neck number and both the average and standard deviation of the nearest neighbor QD distance, demonstrating that QDs with more necks tend to have more ordered local environments. Achieving more complete, uniform necking will require fabrication of more perfect oleate-capped SLs and greater control of the kinetics of the phase transition from the oleate-capped SL to the epi-SL.

We also simulated the combined nearest-neighbor hopping/tunneling transport in this SL film. Simulations of monocrystalline and bicrystalline analogues showed that SL grain boundaries have limited impact on the electron mobility as long as the grains remain interconnected by necked QDs that form percolating neck networks. An encouraging message of this result is that high mobilities can still be achieved in QD SLs even if they have a high density of grain boundaries, and thus small grain sizes, by increasing the QD attachment density, or neck connectivity, across the SL grain boundaries. To complete the picture, it is natural to expect that once the neck networks connect most of the QDs of the epi-SL to the point that carriers delocalize into mini-bands, further mobility enhancements can be achieved by reducing the density of conventional SL grain boundaries as well.

Our study sets a baseline for the quantitative structural characterization of 3D QD epi-SLs. Looking forward, electron tomography will likely be an important tool for elucidating processing/structure/property relationships and guiding the fabrication of increasingly perfect 3D epi-SLs. Higher-quality epi-SLs will in turn encourage more in-depth analysis of the tomograms, particularly with regard to disorder across length scales longer than those emphasized in this paper.[111] Finally, we note that improving the tomogram resolution by a factor of two would allow visualization of QD facets and atomic-scale defects such as edge dislocations,[126] thereby providing a comprehensive near-atomistic picture of the 3D structure of these mesoscale QD films.

3.6 Conficts of Interest

There are no conficts of interest to declare.

3.7 Acknowledgments

This work was supported by the UC Office of the President under the UC Laboratory Fees Research Program Collaborative Research and Training Award LFR-17-477148. We thank Jian-Guo Zheng for assistance with FIB sample preparation and Toshihiro Aoki with help with TEM. Electron microscopy was performed at the user facilities of the UC Irvine Materials Research Institute (IMRI). The GISAXS measurements used resources of the Advanced Light Source at Lawrence Berkeley National Laboratory.

Chapter 4

Near-Atomic Electron Tomography Study on the Orientation Disorder of PbSe epi-SLs

4.1 Preface

In this chapter, we discuss the application of near-atomic electron tomography measurement on characterizing multi-scale structural disorder of a single-grain PbSe epi-SLs. Quantum materials exhibit unique macroscopic properties that depend on nanoscopic arrangements of atoms with local quantum mechanical behavior. Self-assembly of colloidal quantum dots (QDs) into three dimensional epitaxially-fused superlattices (epi-SLs) offers a pathway to delocalized states and mini-band charge transport, but is limited by disorder. Here, we present the use of direct and reciprocal space electron tomography for the structural characterization of PbSe QD-epi-SLs with 3D mesoscale dimensions. Analysis of QD size, position, connectivity, and atomic lattice (AL) orientation in multilayer samples reveals how structural disorder is propagated through 100's hundreds of crystalline interfaces. Correlation analysis across the sample reveals that mesoscale disorder is driven by mismatch between the triclinic SL and rock salt AL. Orientation disorder through layers is driven by heterogeneous interface forces during self-assembly.

4.2 Introduction

Advances in chemical, physical and mechanical synthetic methods have enabled assembly of novel super-crystal materials with emergent collective nano-to-mesoscopic electrical, optical and mechanical properties. Atomic scale and nano-scale structural imperfections limit the expression of quantum mechanical properties. Therefore, mapping of different structural features is vital for rational feedback to synthesis practices and lead to a systematic understanding of structure/property relationships. In spite of many advances in diffraction and real space imaging, it has not been possible to simultaneously characterize multicrystalline 3D materials with atomic resolution over mesoscopic length scales. Here we present the use electron tomography reconstructions over a volume of roughly 10^5nm^3 with near atomic resolution over 633 PbSe quantum dots (QDs) in a super-lattice (SL) by using combined real and inverse space analysis.

Recent hardware and software developments in electron-based imaging and diffraction have led to multiple mapping techniques that are suitable for different scenarios. Electron-Back-Scattered-Diffraction (EBSD) is usually applied in sub-micron scale for inter-grain misorienta-

tion characterization.[103, 71, 19] Conducting 3D EBSD usually requires Focused-Ion-Beam (FIB), laser or mechanical induced sample-sectioning which induce less resolution control in the sectioning direction.[103, 19] Nanobeam diffraction or 4D-STEM allows fast mapping of atomic orientation from reciprocal space directly onto real space with pixel resolution identical to the corresponding STEM image. However, since the obtained diffraction patterns are reduced to 2D, 4D-STEM is limited to 2D materials or 3D materials with insignificant orientation gradient in the zone-axis. The application of phase retrieval strategy allows for the capture of real-space information from electron diffraction with astonishing sub-Angstrom resolution in ptychography experiments but its vertical resolution is currently still severely limited. Dark-Field-Electron-Tomography (DT-ET) provides full access to the Z-contrast information of a 3D volume in real space and is therefore a suitable tool for structural characterization of thick samples (≥ 100 nm). The resolution of ET is typically inversely dependent on the volume of examination. Cutting-edge ET studies are able to resolve atomic positions with a sub-angstrom precision for single crystal or amorphous nanoparticles of 6~10 nm in diameter ($\geq 500nm^3$). For the purpose of mapping both atomic and nanoscale features, we herein present an electron tomography reconstructions of a volume of roughly 10^5nm^3 with near atomic resolution for the 3D mapping of atomic orientation as well as other nanoscale structural features for a total amount of sampled 633 PbSe QD SLs.

Here we study 3D epi-SL of PbSe because this system has demonstrated quantum effects including multiple exciton generation and mini-band formation between groups of QDs.[1] Complex structural disorder has been characterized on 2D epi-SLs films[87, 49, 131, 126, 132] including shear, tensile and bending atomic defects at the interdot connections that are associated with misorientations between individual QDs.[114] McCray et al. further observed larger out-of-plane misorientation than in-plane misorientation and is attributed to the interfacial energetics.[87] The understanding gained from study of 2D films are hardly transferrable to 3D films due to a more complicated self-assembly mechanism.[2] 3D epi-SLs form distorted cubic structures that are further away from the energetically optimal structure (i.e. simple cubic) compared to the often more closely squared cell in 2D cases.[2, 99, 25, 124]

we have previously demonstrated using ET[25] for characterization and mapping of 3D

PbSe epi-SLs'. We imaged 1365 QDs in a 7-layer epi-SP including the position and connectivity of epitaxial bridges, but could not resolve the orientation of individual particles within the lattice. Here we resolve atomic orientation using Fourier analysis of atomic clusters,[28] enabling characterization of the orientation of each QD in addition to the real space determination of QD position and connectivity.

Multiscale mappings of these features shows significantly higher variations in AL orientation, SL parameters and neck conditions in the film normal direction, which are likely an result of both detailed SL growth kinetics and interfacial conditions.[24] The effects of the presence of interfaces are also reflected in suppressing the SL transnational disorder and the AL orientational entropy, practically undermining the credibility of 2D analysis on accessing the film quality. Additionally, our analysis on lattice vector distributions suggest a AL/SL relationship such that the AL orientation is determined by pre-conditioned SL angles and cell orientation and adapts to systematic change of SL structure for maximizing $[100]_{AL}$ co-facial contact area within a distorted cubic cell. These results have shown 3D structural heterogeneities that are tied to synthesis conditions and provide insights in identifying the root causes to different structural disorders for better synthesis optimization.

4.3 Methods

4.3.1 Tomography needle sample preparation

An area of the epi-SL film suitable for FIB milling was located by SEM and several images of different magnifications were taken with the pre-deposited Au arrays as fiducial markers for later relocating the area of interest. The sample was then coated with 50 nm of carbon using the pulse plasma mode of a Leica ACE200 evaporator and returned to an FEI Quanta 3D FEG DualBeam microscope for FIB milling, lift-out, and final needle sample preparation. Prior to milling, a ~ 200 nm Pt capping layer was deposited onto the carbon-coated sample by EBID, followed by an additional ~ 2000 nm of Pt deposited by ion beam induced deposition (IBID). The carbon layer serves primarily to enhance STEM imaging contrast by separating the epi-SL layer from the high-Z protective Pt capping layer. The area of interest was then FIB milled into a wedge shape ($10 \mu\text{m} \times 6 \mu\text{m} \times 2 \mu\text{m}$), lifted-out with an OmniProbe 400 nanomanipulator,

ion welded to the tip of a 1-mm-diameter post for an on-axis rotation tomography sample holder (Fischione Model 2050), and FIB milled again into a ~ 60 nm diameter needle (Fig. S2). Milling was performed in several stages. The wedge was first milled into a pillar shape (1 μm diameter) using a 0.3 nA ion beam at a 30 keV accelerating voltage, then thinned to a ~ 200 nm diameter needle using 50 pA at 16 keV. Finally, a 5 minute ion beam shower (25 pA at 5 keV) was employed to sharpen the needle to ~ 60 nm and remove surface damage. The finished needle contained a disc-shaped epi-SL layer (38 nm tall \times 60 nm in diameter) for tomographic analysis.

4.3.2 HAADF-STEM Electron Tomography

We mounted the needle sample on a Fischione Model 2050 single-tilt tomography holder. HAADF images ($4\text{k} \times 4\text{k}$) were then acquired in a JEOL JEM-ARM 300F TEM operated at 300 KeV in STEM mode. The projection stack consisted of 124 images spanning tilt angles over 0 to 193 degrees in roughly 1.5 degree steps. Full-tilt projection image acquisition is conducted because of low tolerance of missing-wedge artifact that potentially introduces smearing of the edge profile in the less-sampled direction, causing artificial attachments between QDs. The image stack is then sequentially aligned based on center-of-mass and common-line approaches.[ref] All 2D and subsequent 3D image processing were conducted in MATLAB unless otherwise noted. The aligned stack was further processed by matching histogram of every two consecutive images to compensate for the brightness instability and then denoised via a Wiener filter for 2 iterations. Tomographic reconstruction was conducted on subsequently using 200 iterations of simultaneous iterative reconstruction technique (SIRT) in the ASTRA Tool box.[122] The raw reconstruction was downsized so that it consisted of $2048 \times 2048 \times 700$ voxels with edge lengths of 0.38 Å. The downsized reconstruction was smoothed with nonlinear anisotropic diffusion filtering for subsequent structural information measurements. The spatial resolution of this reconstruction was evaluated to be 3.1 Å by comparing the Fourier power spectra between the actual and the simulated reconstructions.[R]

4.3.3 Determination of QD positions and SL vectors

The coordinates of the QDs determines the local superlattice vectors and the collective positions determines the representative super lattice unit cell structure for the examined sample. The QD

positions are determined by an Iterative Digital Image Correlation (IDIC) method. First, a cubic subvolume (V_s) containing a representative complete sample QD (usually a volume of $301 \times 301 \times 301$ pixels) is extracted from the entire tomogram V via common volume slicing. A cross-correlation 3D convolution operation is conducted upon the original tomogram using V_s as the convolution kernel. Then 3D local maxima are searched for pooling candidate QD centroids. An Otsu-threshold [ref] cutoff is then applied to screen out unlikely candidate centroids of small correlations and result a centroid set $\{r_c\}$. We then sample a set of subvolumes of the same size as V_s around each centroid in $\{r_c\}$ and calculate the average with equal weights. This is again averaged with previous sample QD V_s to generate a new sample volume V_s' for the next round of convolution. This process is iterated until the number of QD centroids converges and the mean-square-error cannot be improved further. The entire process usually converges within 15 iterations regardless of the initial QD sample we choose, as indicated in Figure Sxyz. With the pre-knowledge of cubic-like SL structure, the determination of superlattice vectors begins by pooling the 6 nearest neighbors (NNs) for each QD centroid in the final $\{r_c\}$. Considering not all QDs (peripherals) have 6 $\{100\}_{SL}$ NNs, a cut-off maximum distance of 9 nm is used to ensure the sampling is constrained to $\{100\}_{SL}$ neighbors and a minimum amount of $\{100\}_{SL}$ neighbors. Next, an unsupervised K-MEANS clustering is applied to the NN set to determine the representative $\{100\}_{SL}$ vectors. The average SL unit cell parameters are then calculated with the centroids of the determined clusters.

4.3.4 Calculating optimal AL orientation from SL basis matrix

First, the SL basis matrix is expressed as

$$R_i^{SL} = \begin{bmatrix} A_x^* & A_y^* & A_z^* \\ B_x^* & B_y^* & B_z^* \\ C_x^* & C_y^* & C_z^* \end{bmatrix}_i \quad (4.1)$$

where $[A_x^*, A_y^*, A_z^*]$ is the normalized local $[100]_{SL}$ vector $\vec{A}_i/|\vec{A}_i|$ for QD i and similarly for other matrix components.

The corresponding optimal AL orientation assumes an orthonormal 3D basis \hat{R}_i^{AL} that is

nearest to R_i^{SL} in terms of $L_{2,2}$ distance.

$$\hat{R}_i^{AL} = \{\operatorname{argmin}_R \|R - R_i^{SL}\| \cap R^T R = I\} \quad (4.2)$$

\hat{R}_i^{AL} can be numerically solved by singular value decomposition (SVD) such that,

$$R_i^{SL} = U\Sigma V^T \quad (4.3)$$

$$\hat{R}_i^{AL} = UV^T \quad (4.4)$$

While \hat{R}_i^{AL} can change for different SLs as R_i^{SL} changes locally, a global enforcement of strict mono-crystallinity can be implemented to obtain a different solution \hat{R}_{mono}^{AL} . Alternatively, assumptions of bi-crystal or tri-crystal can be made in which orientations are fixed within designated subsets of SLs from the entire sampled. We have compared these solutions with experimental measurement $\{R_i^{AL}\}$ and summarized the results in table S.XYZ.

4.3.5 Determination of atomic lattice orientation from measurement

First, a $301 \times 301 \times 301$ ($\sim 1500 \text{ nm}^3$) cubic subvolume V_0 is extracted from the reconstruction around the center of mass of a specific QD of interest. This size is taken so that it is big enough to include one QD but not too big to include multiple QDs. The volume is then convoluted with a gaussian mask F placed at the center to suppress potential unwanted signals from adjacent QDs. The intensity profile of the filtered volume V is described as following

$$V(\vec{r}) = V_0(\vec{r}) \cdot F(\vec{r}) \quad (4.5)$$

$$F(\vec{r}) = \exp\left(-\frac{\vec{r}^2}{2\sigma^2}\right) \quad (4.6)$$

where σ is usually taken to be the diameter ($\sim 6 \text{ nm}$) of the QD of interest. We next obtain the reciprocal power volume $\hat{V}(\vec{k})$ following Discrete-Fast-Fourier-Transformation (DFFT) such that

$$\hat{V}(\vec{k}) = \log \left| \iiint V(\vec{r}) \exp(-2\pi i \vec{k} \cdot \vec{r}) d\vec{r} \right| \quad (4.7)$$

The FFT power volume is treated with a band-pass filter to remove information outside of desired spatial frequency ranged within $2 \sim 4 \text{ nm}^{-1}$, in which we shall find the $\{110\}$ and $\{200\}$ PbSe diffraction peaks. The resulted volume is binarized with a threshold equals to

75% of the maximum power. A Density-Based Spatial Clustering of Applications with Noise (DBSCAN) algorithm is applied to the thresholded volume to detect diffraction Bragg spots as voxel clusters and remove noises. Then a Gaussian Mixture Model (GMM) clustering is applied with initial guesses of cluster centroids obtained from the DBSCAN. The resulting fitted GMM model takes the form as

$$P(\vec{k}) = \sum_N \frac{w_i}{2\pi|\Sigma_i|} \exp\left\{-\frac{1}{2}(\vec{k} - \vec{\mu}_i)^T \Sigma_i^{-1} (\vec{k} - \vec{\mu}_i)\right\} \quad (4.8)$$

where N is the number of clusters, w_i is the weight for each cluster and Σ_i is the covariance matrix. The cluster centroids $\vec{\mu}_i$ in the reciprocal space from GMM model are considered as the centroids of the Bragg Spots of Pb lattices resolved from the original reconstruction. The real space lattice vectors are then calculated as

$$\vec{g}_i = \frac{\vec{\mu}_i}{|\vec{\mu}_i|^2} \quad (4.9)$$

The calculated atomic lattices vector \vec{g}_i are classified into $[200]_{AL}(\vec{a})$, $[020]_{AL}(\vec{b})$ and $[002]_{AL}(\vec{c})$ vectors based on their general directions with respect to the reference cartesian axes of the global reconstruction volume.

With the AL vectors characterized, the orientation of a QD in 3D cartesian space can be expressed as

$$R_i^{AL} = \begin{bmatrix} a_x^* & a_y^* & a_z^* \\ b_x^* & b_y^* & b_z^* \\ c_x^* & c_y^* & c_z^* \end{bmatrix}_i \quad (4.10)$$

where $\vec{a}_i^* = (a_x^*, a_y^*, a_z^*)_i$ corresponds to the unit basis vector $[200]_{AL}$ measured from WFFT and similarly for the other AL vectors. Since R_i are numerically derived, the orthogonality of the matrix is not strictly ensured. Therefore, matrix regularization is conducted via finding the closest orthogonal matrix to enforce mutual orthonormality among the basis vectors in R_i^{AL} . The mean error between raw R_i^{AL} and regularized R_i^{AL} is evaluated to be 0.2%.

4.3.6 Characterization of AL orientation transformation

The orientation difference between QD i and QD j are described by a single-axis rigid body rotation transformation vector $\vec{\delta}_{ij}$,

$$\vec{\delta}_{ij} = \varepsilon_{ij} \vec{\xi}_{ij} \quad (4.11)$$

where ε_{ij} is the magnitude of the rotation and $\vec{\xi}_{ij}$ is the unit vector defining the rotation axis, which are calculated as following,

$$T_{ij}\vec{\xi}_{ij} = \vec{\xi}_{ij} \quad (4.12)$$

$$\varepsilon_{ij} = \arccos\left(\frac{\text{trace}(T_{ij}) - 1}{2}\right) \quad (4.13)$$

$$T_{ij} = \frac{R_j^{AL}}{R_i^{AL}} \quad (4.14)$$

T_{ij} is the rotational transformation matrix between orientation R_i^{AL} and R_j^{AL} , and $\vec{\xi}_{ij}$ is obtained through solving the eigen vector for T_{ij} with a corresponding eigenvalue of 1. $\vec{\xi}_{ij}$ can then be rewritten as a linear combination of local AL basis vectors such that

$$\vec{\xi}_{ij} = l \frac{\vec{a}_i^* + \vec{a}_j^*}{|\vec{a}_i^* + \vec{a}_j^*|} + m \frac{\vec{b}_i^* + \vec{b}_j^*}{|\vec{b}_i^* + \vec{b}_j^*|} + n \frac{\vec{c}_i^* + \vec{c}_j^*}{|\vec{c}_i^* + \vec{c}_j^*|} \quad (4.15)$$

The coefficients l, m and n are used to find major rotation axis using linear regression.

4.3.7 Orientation correlation matrix and von Neumann entropy

The Pearson correlation matrix K for the orientation of QDs are constructed such that for each element in K,

$$K_{ij} = \text{corr}(R_i, R_j) \quad (4.16)$$

The von Neumann entropy of a group of QDs' orientational states is derived such that

$$S_I = -k_B \text{trace}(\rho_I \ln \rho_I) \quad (4.17)$$

$$\rho_I = \frac{K_{II}}{N} \quad (4.18)$$

where I is the group index for a particular layer, K_{II} is the diagonal blocks in the Pearson correlation matrices representing the intra-group correlation submatrices for group I and N is the dimension of K_{II} . Note that here the ln is a matrix natural logarithmic operator instead of an elementwise operator.

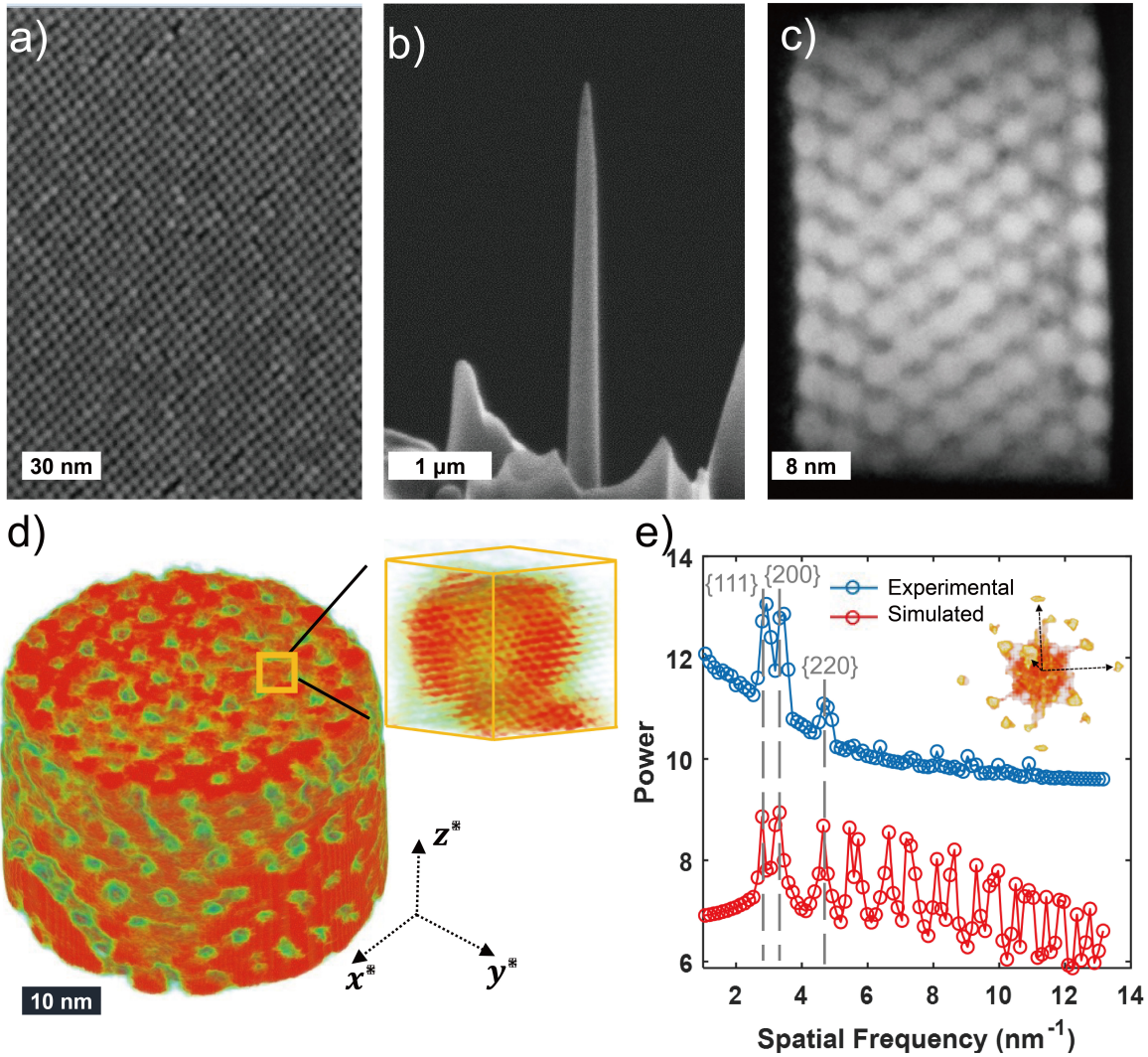


Figure 4.1. SEM, STEM images and tomographic reconstruction of the PbSe SLs. a) SEM image of a region of interest within a $(100)_{SL}$ -oriented SL grain. The dashed circle denotes the approximate site where the cylindrical tomography sample initially located in the film. b) SEM image of the FIB-prepared needle sample. c) HAADF-STEM image of the PbSe epi-SL tomography sample. d) A perspective view of the entire tomogram and a zoom-in view of one of the QDs showing 3D near-atomic details. The color scale denotes the normalized electron density in units of e^-/nm^3 . The presented Cartesian axes are pre-defined reference coordinates systems with \vec{z}^* being the film normal direction. e) The 1D power spectra of the Fourier transformations of the experimental reconstruction and the simulated reconstruction. The dashed lines denotes the PbSe Bragg peaks of $\{111\}_{AL}$, $\{200\}_{AL}$ and $\{220\}_{AL}$ with corresponding d-spacing of 3.52 Å, 3.05 Å and 2.16 Å. Embedded in the panel is the visualization of the 3D power spectrum of the experimental reconstruction with arrows annotating the $\{200\}_{AL}$ Bragg spots.

4.4 Results

The ET reconstruction features a cylindrical QD SL sample with a diameter of 60 nm and a thickness of ~ 40 nm, as shown in Fig. 4.1c-d. We identify 633 QDs forming a total of 9 lateral layers (zone axis of $[001]_{SL}$). One of the primary structural measurements from the reconstruction is the QD positions, which define the local SL order and collectively determine a representative SL unit cell for this single grain. We consider the position of each QD as its center-of-mass (CoM) that can be found by iteratively convoluting the reconstruction with a sample QD extracted from the original reconstruction volume (SI Fig. XYZ). We use the unit vectors connecting CoMs of neighboring QDs to derive local SL basis vectors \vec{A}_i^* ($[100]_{SL}$), \vec{B}_i^* ($[010]_{SL}$) and \vec{C}_i^* ($[001]_{SL}$). Vector field graphs (SI Fig. XYZ) can be generated to visualize the SL structure variations throughout the measured volume. Another important structural measurement is the orientation of the QDs given the near atomic resolution of the reconstruction. Fig. 4.1e shows the 1D power spectrum of the reconstruction, compared to the spectrum of a simulated reconstruction filled with Pb lattices (space group F23) according to perfect PbSe rocksalt crystal structure [6] convoluted with a Gaussian blurring function to incorporate the effect of instrumental instabilities. The inset shows the corresponding 3D power spectrum with $\{200\}_{AL}$ Bragg spots annotated. The experimental 1D power spectrum indicates adequately high signal-noise ratio at the spatial frequency corresponding to PbSe $d_{200} = 3.05$ Å. This spatial resolution is conservatively confirmed by measuring FWHMs of the point spread functions of several randomly selected atomic features in the volume.(SI Fig. XYZ)[88] This resolution is sufficient to allow us to determine the local 3D AL orientations of individual QDs with an angular resolution of 0.05 rad. Specifically, the AL orientation of each QD is determined by applying local Windowed-FFT(WFFT) and identifying the $(100)_{AL}$, $(010)_{AL}$ and $(001)_{AL}$ Bragg spots in the reciprocal space, referring in real space to a set of three mutually orthonormal AL basis vectors forming a matrix $R_i^{AL} = [\vec{a}_i, \vec{b}_i, \vec{c}_i]$, where i refers to the index of a QD. Similarly, vector field graphs(SI Fig. XYZ) can be used to observe the atomic orientation change over space. Another commonly used approach to determine crystal orientation from 2D and 3D TEM/STEM measurements is the Geometric Phase Analysis (GPA) method.[58, 52] GPA is particularly useful for obtaining relative lattice orientation differences in a tensor field form

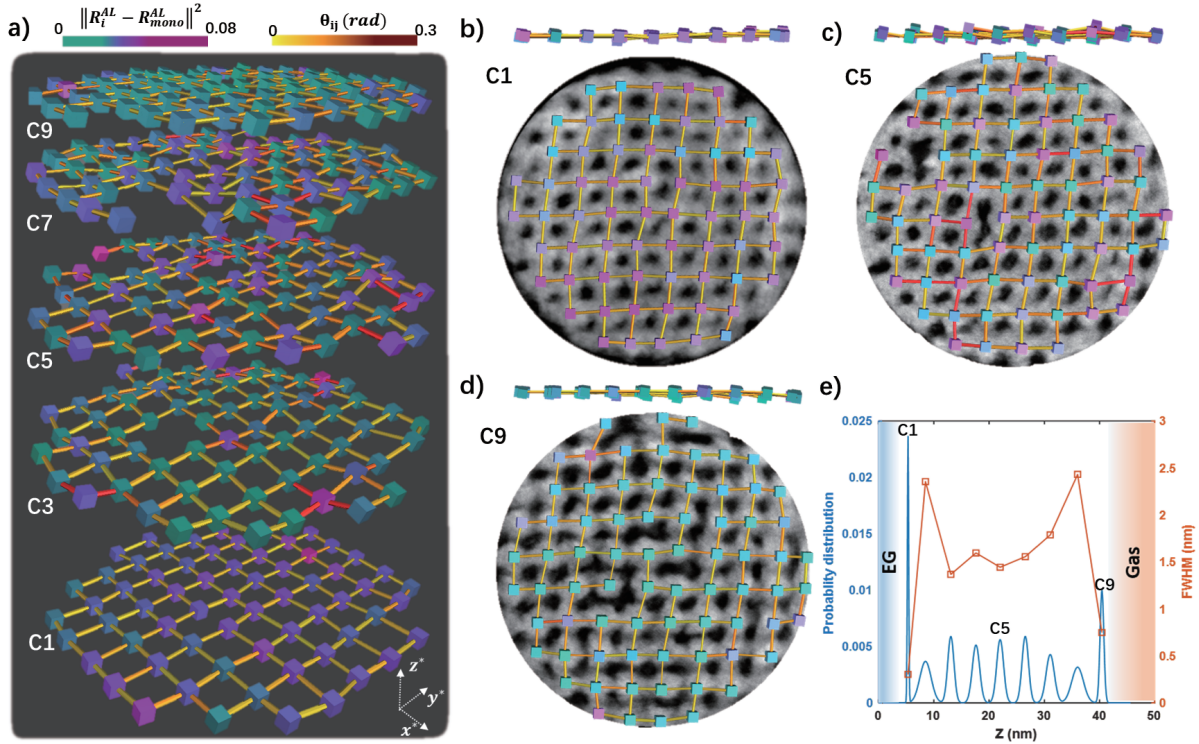


Figure 4.2. The interpretation of the tomogram with data visualization. a) Exploded view of the cube-stick representation of selected $(001)_{SL}$ layers (C1, C3, C5, C7 and C9) from the original tomogram. The coordinates and orientations of the cube reflect the actual relative positions and atomic orientation of the QDs. The color scale of the cubes denotes the magnitude of the differences ($L_{2,2}$ distance) between the predicted optimal orientation R_{mono}^{AL} and the measured orientation R_i^{AL} . The presence/absence of the sticks represents characterized neck or missing-neck scenarios for the morphological coupling of neighboring QDs. The diameter of the sticks corresponds to the diameters of the necks. The color scale of the sticks denotes the experimental orientation differences between the connected QDs. (b-d) Plan-views of the cube-stick representations of C1 (b), C5 (c) and C9 (d) overlaid on top of the raw tomographic slices (thickness of 2 nm around vertical layer center-of-mass) of the corresponding layers. The top panels are the side-views. (e) Gaussian-mixture-modeling of positional distribution of the QD CoMs along the film normal (z^*) direction. C1 is at the liquid-film interface with ethylene glycol and C9 is the film-gas interface during film synthesis.

from the vectorial displacement field when there is no need to couple the orientation to other structural feature. However, since our subsequent analyses are heavily relied on correlating AL orientations to other attributes such as positions and SL vectors, we instead use a direct WFFT method.[29]

With the spatially coupled SL and AL information characterized, we convert the reconstruction layer-by-layer into a much more interpretable cube-stick representation shown in Fig. 4.2b-

d as examples. Each cube represents the 3D position of one QD and the sticks represent detected oriented attachments between the QDs. The orientation of the cubes also reflect the actual 3D atomic orientation R_i^{AL} of each respective QD, determined from the WFFT of the associated local space (see SI for method). There are three additional quantitative structural attributes of interest being encoded into the scale of the size and color of the sticks and color of the cubes, corresponding to neck size, magnitude of nearest-neighbor misorientation (or magnitude of atomic misalignment) and magnitude of deviation from optimal AL orientation respectively, all of which will be discussed in detail in the later sections. A full list of raw tomogram slices and corresponding cube-stick visualization can be found in SI Fig. X-Y. Here, a qualitatively observation of Fig. 4.2 reveals multiple aspects of structural disorders including translational disorder in the positions of the QDs, missing dots (point defects), variation in QD orientations, missing neck and variation in neck sizes. The translational disorder is particularly more significant in the film normal direction when we compare the top and bottom layers with other bulk layers, which appears wavier than the former. This is also demonstrated in the comparison of the side views of three selected layers (C1,C5 and C9) in the top panels of Fig. 4.2b-d. A Gaussian mixture model is used to fit the vertical QD CoMs distribution in Fig. 4.2e. We see that the peaks are much narrower for the layers at the liquid/film and gas/film interfaces with peak full-widths-at-half-maximums (FWHMs) respectively calculated to be 0.1 nm and 0.4 nm, while the middle layers all have FWHMs above 0.6 nm. This mass distribution profile is unique for $(001)_{SL}$ planes compared to other SL directions shown in SI Fig. XYZ. This potentially indicate the translational SL order is affected by the presence of the interfaces. Missing-dot defects are commonly seen from SEM images for QD SLs. Here, we showed internal point defects manifesting either as missing of entire QDs or presence of partial QDs (Fig. 4.2c) at the corresponding lattice points. We consider the partial QDs as point defects and exclude them from further analysis because their shape significantly deviate from the regular QDs with a over 50% volumetric loss and their orientation can not be sampled accordingly. Layer C8 shows a particularly larger point defect density of 19.7% compared to other layers (0~3%) but does not affect the integrity of its adjacent layers.

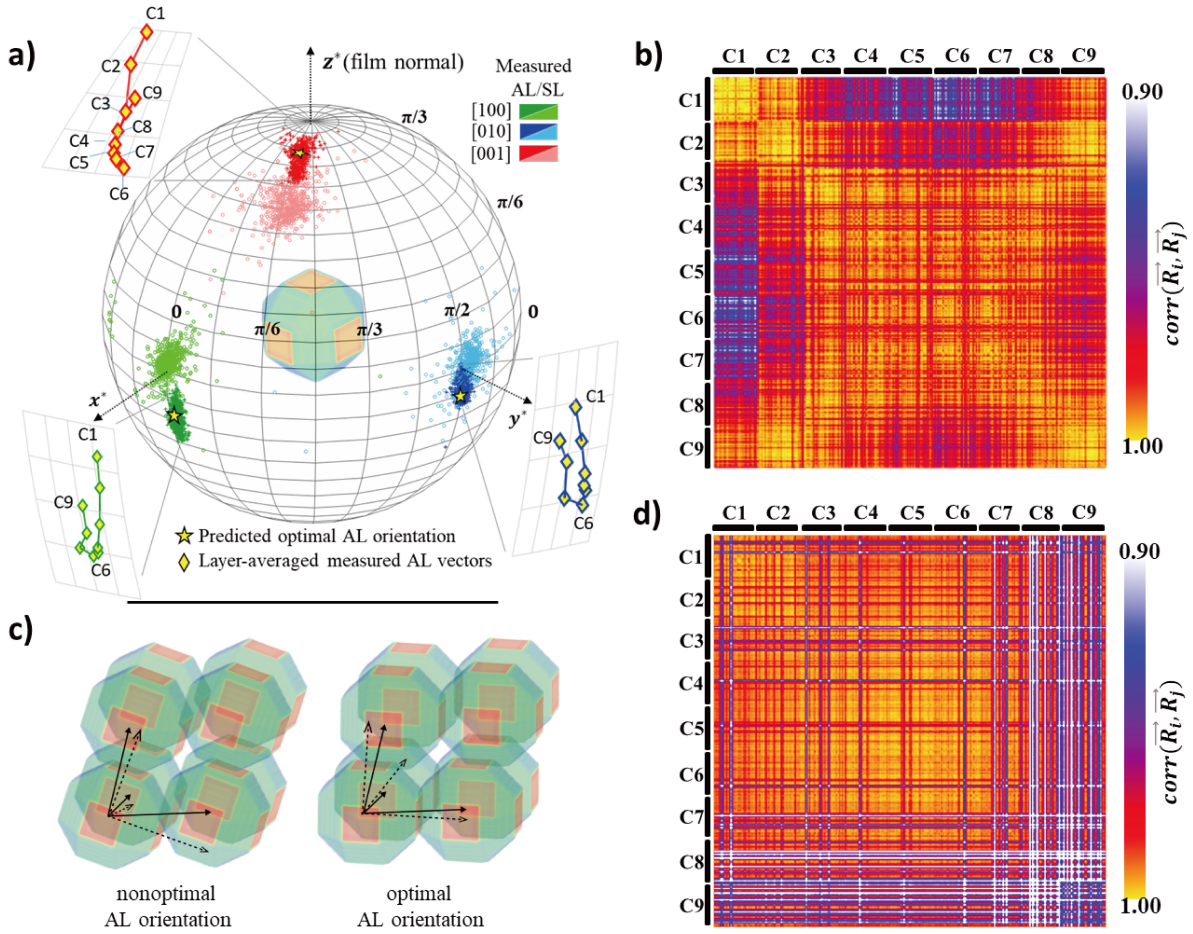


Figure 4.3. AL/SL relationship. a) AL/SL lattice vector distributions encompassing $[100]_{AL}$ (green), $[010]_{AL}$ (blue), $[001]_{AL}$ (red), $[100]_{SL}$ (lime), $[010]_{SL}$ (cyan) and $[001]_{SL}$ (pink). The star points denote the calculated optimal AL orientation R_{mono}^{AL} . The diamond points on the enlarged patches are AL vectors averaged over each layers. b) Schematics showing the difference between a nonoptimal AL/SL configuration and the corresponding optimal AL/SL configuration in which the summation of the cofacial $\{100\}_{AL}$ area is maximized under the given SL lattice angles. The solid vectors denote the nonorthogonal SL basis matrix R^{SL} and are identical between nonoptimal and optimal configurations. The dashed vectors represent the orthogonal AL basis R^{AL} . c-d) Pearson correlation matrix of R_i^{AL} (c) and R_i^{SL} (d). The color scale of each element in the matrices denotes the 2D correlation coefficient between the basis matrices of an arbitrary pair of QDs. The rows/columns are grouped by layer and the order follows ascending layer indices. Within each group, the elements are randomly reshuffled to exclude potential unintended grouping effect.

4.4.1 The relationship between AL orientation and SL structure

To better illustrate the three-dimensional statistical AL orientation and SL structural information, we cast the AL and SL vectors of each dot together onto a unit vector sphere surface shown in

Fig. 4.3a. The distribution of the AL vectors represents the variation of atomic crystallographic orientations of the dots, and the SL vector distributions represent the variations in SL angles and orientations with respect to the reference axes. The AL vectors are also averaged over $[001]_{SL}$ layers and shown as diamond points on the enlarged surface patches over the sphere. The depicted rather continuous trajectory of cross-layer orientation change can be described by a counter-clockwise tilting starts from L1 following a rotation axis relatively more aligned with y^* . The tilting reaches a maximum at L6, and then rotates backward toward L9, resulting a slit-like overall distribution for the AL vectors. The shape and direction of the AL distribution implies a larger contribution from out-of-plane(layer) tilting than in-plane(layer) spinning to the overall orientation variation. Similar observations are reported for 2D epi-SLs.[R] Among the three basis AL vectors, $(001)_{AL}$ exhibits the largest range of tilting (~ 0.2 rad in average) across the layers, with 0.12 rad and 0.09 rad for $(010)_{AL}$ and $(100)_{AL}$ respectively, as shown in SI Fig. XYZ. The same behavior is found for in-layer orientation variation, judging from the fact that the magnitude of tilting uncertainty is significantly smaller for $(100)_{AL}$ compared to the other two.(SI.XYZ) This hints that the QDs might share a common rotation axis leading to a similar reorientation behavior. The determination of a characteristic rotational axis will be discussed in a later section. To better capture the orientation change over space, we construct a 633×633 Pearson Cross-Correlation Matrix (PCM) as Fig. 4.3b, in which each element is the cross-correlation coefficient of the orientation basis matrices $corr(R_i^{AL}, R_j^{AL})$ between a pair of QD i and j. The elements are arranged in groups following ascending $[001]_{SL}$ (C) layer indices. Within each group, the order of QDs is reshuffled to exclude potential unwanted grouping effect from other SL directions. The exhibited heterogeneity of the PCM is unique in $[001]_{SL}$ compared to other SL directions (SI Fig. XYZ). First, We observe higher correlations in diagonal blocks than their adjacent off-diagonal blocks, which represent auto-layer and nearest inter-layer orientation correlation respectively. This is true for most of the layers as indicated in the block-averaged PCM in SI Fig. XYZ. It indicates lower in-layer orientational dispersion than between-layers, possibly due to a larger orientation gradient along the $[001]_{SL}$.

Different from the AL vector, the SL vector data indicates a clear triclinicity of the superlattice unit cell structure. The average SL lattice spacings are characterized to be $A = 6.2 \pm 0.6$

nm, $B = 6.0 \pm 0.4$ nm and $C = 5.6 \pm 0.8$ nm, and lattice angles to be $\alpha = 76.1^\circ$, $\beta = 61.9^\circ$ and $\gamma = 96.3^\circ$. For a particular QD, we quantify its local SL structure by defining SL basis matrix $R_i^{SL} = [\vec{A}^*, \vec{B}^*, \vec{C}^*]_i$, which is similar to R_i^{AL} but nonorthogonal. The mismatches between the AL and SL basis vectors are apparent in Fig. 4.3, with mean angular mismatch calculated as $[100]_{AL} \angle [100]_{SL} = 17.4^\circ$, $[010]_{AL} \angle [010]_{SL} = 8.4^\circ$ and $[001]_{AL} \angle [001]_{SL} = 17.3^\circ$. The AL/SL mismatch is a known feature for 3D PbSe epi-SLs[2] with reported unit cell structures varying from simple cubic to different degrees of distortion toward triclinicity. This is potentially a result of varying ligand coverage density that effectively change the shapes of the QDs in different studies.[refs(nano ring paper)] However, the relationship between the SL structure and the embedded AL orientation is not fully understood. Specifically, for a given distorted cubic cell, the orientation can be theoretically taken with quite a large degree of orientation freedom, as shown in Fig. 4.3c, provided that the $\{100\}_{AL}$ facets have maintained connection with each other.

Here, we note that a minimum amount of AL/SL mismatch is topologically inherent in a triclinic SL cell. In other words, for any specific distorted cubic basis R_i^{SL} , there exists an QD orientation configuration R_i^{AL} that matches R_i^{SL} to the best extent, hence maximizing the co-facial attachment area between the $\{100\}_{AL}$ facets, resulting an energetic favorable outcome. This is mathematically equivalent to finding the unique "nearest orthogonal matrix" for a non-orthogonal matrix in linear algebra. Therefore, given the measured $\{R_i^{SL}\}$ distribution in Fig. 4.3a, we calculate the optimal orientation R_{mono}^{AL} that minimizes the sum of $L_{2,2}$ (Frobenius) distance $\sum ||R_{mono}^{AL} - R_i^{SL}||^2$ by assuming perfect AL monocrystallinity. This calculation is numerically done via matrix singular value decomposition. The calculated orientation basis are shown as yellow stars in Fig. 4.3a, agreeing very well with the measured data with an mean angular difference of 1.4° or a mean $L_{2,2}$ error of 1.9%. A similarly accurate prediction is made based on the a separate tomography sample with a different SL structure and yields an mean angular difference of 1.7° (SI.XYZ) from measured AL vectors. The R_{mono}^{AL} configuration suggests the minimization the AL/SL mismatch under the condition of introducing no extra atomic misaligned energy. On the other hand, if no constraint on monocrystallinity is assumed, that is, a necessary amount of atomic misalignment is allowed to ensure the lowest possible

AL/SL mismatch based on the measured SL configuration, the corresponding optimal orientation configuration $\{\hat{R}_i^{AL}\}$ is solved by minimizing $\sum \|\hat{R}_i^{AL} - R_i^{SL}\|^2$. For both $\{R_i^{AL}\}$ and R_{mono}^{AL} , we show their 3D orientation maps in SI Fig. XYZ overlaid on top of $\{R_i^{AL}\}$ for comparison. The short-range AL coherence of $\{\hat{R}_i^{AL}\}$ is worse than the experimental measurement $\{R_i^{AL}\}$, judging from the exceeding roughness of the PCM of $\{\hat{R}_i^{AL}\}$ in SI Fig. XYZ. Indeed, the mean $L_{2,2}$ difference between $\{R_i^{AL}\}$ and $\{\hat{R}_i^{AL}\}$ is 4.1%, which is higher than that between $\{R_i^{AL}\}$ and R_{mono}^{AL} . This result implies that the QD orientation is statistically dependent on the SL structure but rather inert to the local SL randomness. Another evidence is that the significantly larger missing dot density in C7 does not significantly disrupt the local AL orientation. However, we do observe a systematic albeit small orientation change of at the interfaces, which could be tied to the shearing that seemingly also affects the SL.

To further study this, we construct another PCM matrix for $\{R_i^{SL}\}$ in Fig. 4.3d similar to that of $\{R_i^{AL}\}$. The PCM shows an increasing dissimilarity of local SL structure between QDs in the bulk and those close to the interfaces. This is also characterized in SI Fig. XYZ as a systematic increase of α and β SL lattice angles indicating a in-plane(layer) shearing effect that leads to a less distorted cell at the interfaces. The comparison of the two PCMs, showing similar patterns of overall heterogeneity but different levels of smoothness, has confirmed that the AL orientation adapts to systematic changes of SL but is rather insensitive to short-range SL randomness. Based on the proposed AL/SL relationship, we also show in SI Fig. XYZ a variety of SL cells from cubic to triclinic created from different sets of lattice angles, based on which the AL orientations are calculated to complete each model. This finding may potentially simplify the crystalgraphic characterization of PbSe SLs samples and inspire designs of new nanocrystal systems.

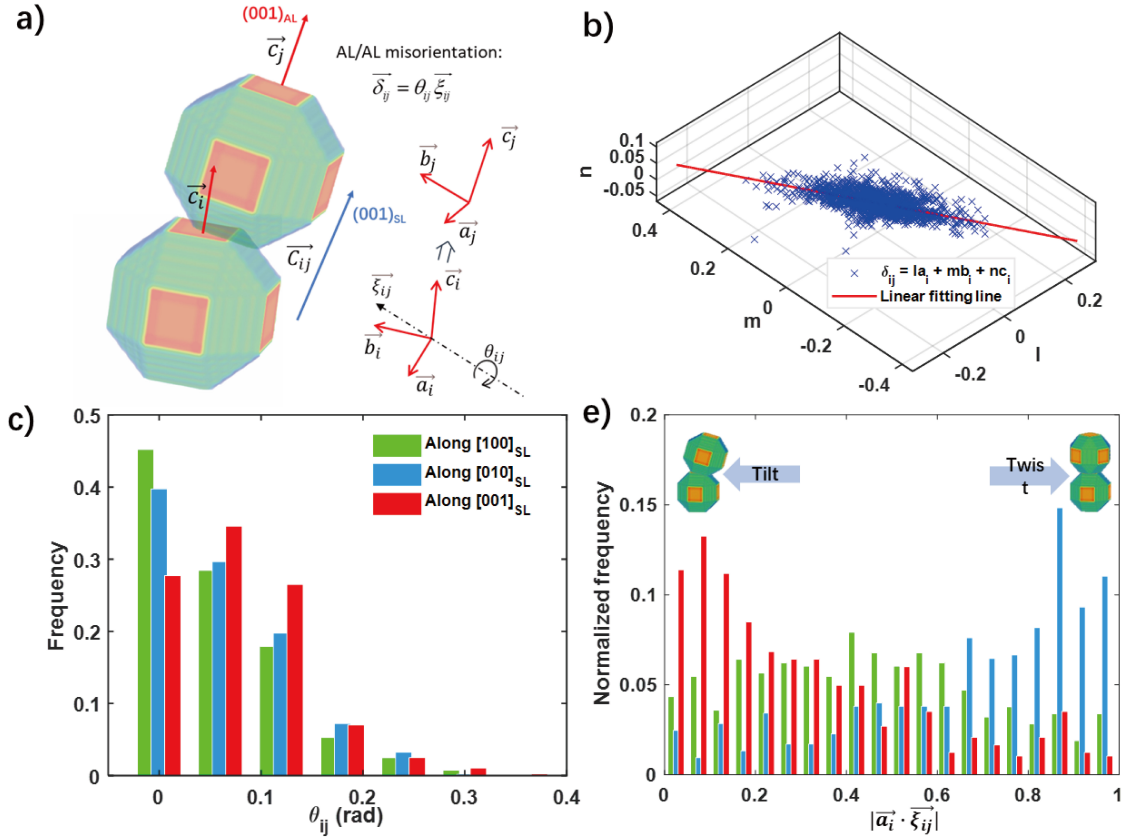


Figure 4.4. Anisotropic orientation disorder. a) Schematic showing the AL misorientation between nearest neighboring QDs. b) Scatter plot and linear regression of $\vec{\delta}_{ij}$ as a linear combination of \vec{a}_i, \vec{b}_i and \vec{c}_i . c) Histograms of magnitudes of misorientation gradient θ_{ij} (rad per SL spacing) along different SL directions. d) Histograms of $|\vec{a}_i \cdot \vec{\xi}_{ij}|$ showing distinct tilt/twist misorientation characteristics along different SL direction.

4.4.2 Anisotropic orientation disorder

To further investigate the orientation disorder, we define a angle-axis form of rotation transformation as $\vec{\delta}_{ij} = \theta_{ij} \vec{\xi}_{ij}$, where $\vec{\xi}_{ij}$ represents the rotation axis against which a single-axis rigid body rotation is assumed to occur between the nearest neighboring QD i and j , as indicated in Fig. 4.4a, and θ_{ij} defines the magnitude of this rotation. θ_{ij} and $\vec{\xi}_{ij}$ are both solved from rotational transformation matrix $T_{ij} = R_j^{AL}/R_i^{AL}$ (see in-detail calculation in SI). The basic assumption here is that the AL orientation remains still within a single QD and thus the smallest orientation change can only be measured between the nearest neighbors. In light of this, θ_{ij} can be also interpreted as the magnitude of the orientation gradient per SL spacing in different directions. For both simplicity and the limitation of our angular resolution, we omit possible

lattice distortion within the neck regions. We then rewrite $\vec{\delta}_{ij}$ as a linear combination of the local AL basis vectors. In Fig. 4.4b, these coefficients can be fitted linearly in 3D, indicating a characteristic rotational axis determined as ${}_i\vec{\xi}_{ij} = [\bar{1}20]$, which explains 89% of the vectorial variance of $\{\vec{\delta}_{ij}\}$ by Principal Component Analysis (PCA). The perpendicularity of ${}_i\vec{\xi}_{ij}$ to the $[001]_{AL}$ explains the slit-like shape and orientation of the AL vector distributions, which itself cannot be used to determine the characteristic rotation axis since the overall distribution might be a superposition of several random sub-distribution clusters. It is not completely understood why the QDs share such a rotation axis but it is worth to note that Abelson *et al.* reported that the QD reorientation occurring during the ligand deprivation of OA-capped QDs follows a rotation axis of $[110]_{AL}$. [2] This is close to our observation and the deviation possibly comes from the combination of this sample's more distorted SL structure and aforementioned shearing effect. However, it is clear that the AL orientation disorder of this sample are more of a consequence of misorientations that exist prior to oriented attachments, as opposed to random misorientation due to atomic dislocations formed during or after the attachment. This observation agrees with previous experimental and simulation studies. [99, 22] Insights can be learned that the misorientation defects are largely kinetics-based and can be potentially minimized by slower ligand exchange process that allows for larger QD reorientation. According to the distribution of θ_{ij} shown in Fig. 4.4b, the orientation gradient is relatively higher along $[001]_{SL}$ direction with an average value of 0.09 rad per SL spacing, compared to 0.07 rad for both $[100]_{SL}$ and $[010]_{SL}$ respectively. This result, again addresses additional forces driving QDs' reorientation in the film normal direction. This is probably tied to the vertical systematic change of SL structure shown in Fig. 4.3d. It also indicates that $[100]_{SL}$ or $[010]_{SL}$ is more likely to be the primary direction of the epitaxial growth of the SL structure, since the least gradient of AL orientation is found in this direction.

For 1D QD nanorod and 2D QD SLs, the orientation difference between two attached neighboring QDs are reported and generally categorized into tilt or twist misorientation. [126, 114, 100] The former features a rotational axis perpendicular to the AL vector aligned with the QDs' attaching direction, while the later features a parallel rotational axis. Here, we show that it is more of a mixing case for a 3D SLs. We measure $|\vec{a}_i \cdot \vec{\xi}_{ij}|$ as the dot product between $\vec{\xi}_{ij}$ and

the pertinent local AL vector to evaluate the tilt/twist mixing level of each QD NN pairs of non-trivial(≥ 0.05 rad) orientation difference. A dot product of zero means complete tilt and one being pure twist. The resulted distributions (Fig. 4.4c) shows distinct misorientation characteristics along different SL directions. For neighbors along $[001]_{SL}$, the distribution is highly skewed toward pure tilt misorientation with an average dot product of 0.23, whereas $[010]_{SL}$ neighbors mostly exhibit twist misorientation with an average dot product of 0.78. This is a direct consequence of the principal rotation axis. Since tilt misorientation is likely to introduce extra normal stress while twist exerts more shear stress, this analysis sets a classification method basis for future investigations on measuring and comparing strain/stress tensor field profiles that resulted from variations of misorientation types.[99, 114, 123, 78]

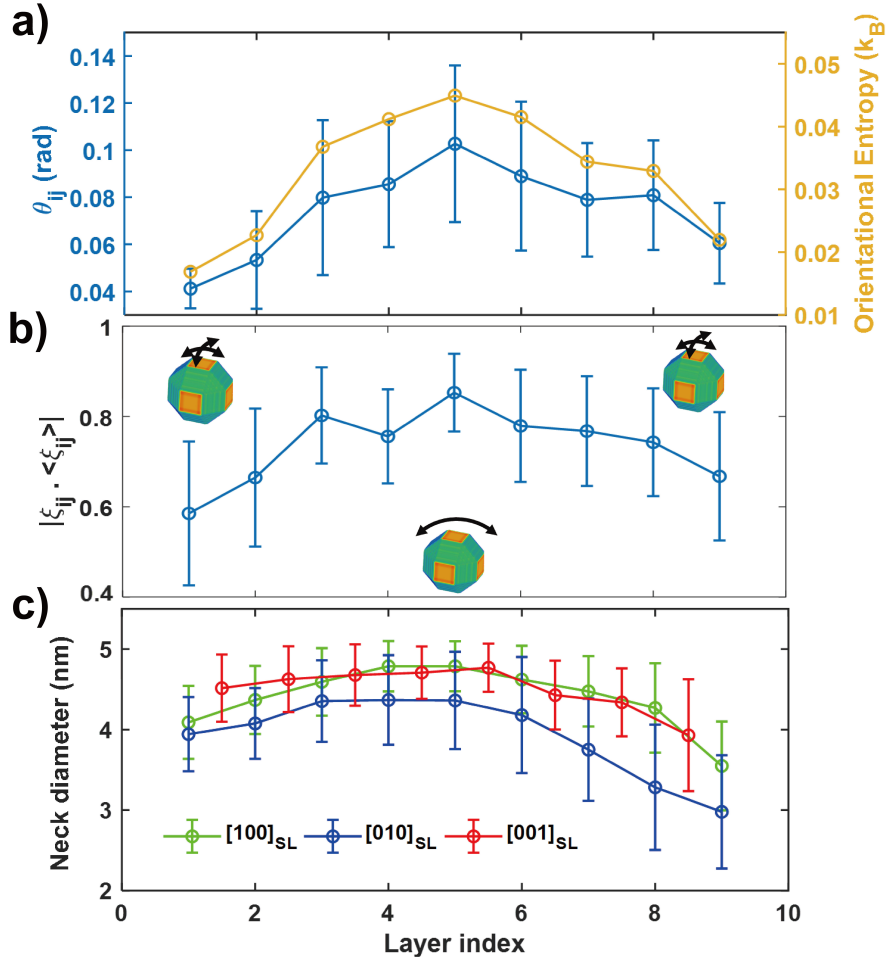


Figure 4.5. Effects of interfaces on orientational entropy and neck disorder. a) Vertical variations of in-layer component of misorientation gradient magnitude θ_{ij} (blue) and orientational entropy (orange) over each $(001)_{SL}$ (C) layers. b) Vertical variations of the alignment between determined common rotational axis ξ_{ij} and local rotation axis, averaged over each C layers. c) Vertical variation of neck diameters.

4.4.3 Effect of interfaces

The effect of the interfaces is seen on multiple aspects of the local structural order including the translate SL variation, AL orientation order and the neck size order. A direct observation on the visualization in Fig. 4.2 indicates that the AL/AL misorientation magnitude (color of the necks), i.e. the stepwise change of orientation between in-layer nearest neighbors are systematically larger in middle layers than interfacial layers. Indeed, the layer-averaged θ_{ij} (shown in the top panel of Fig. 4.5c) tops at the middle layer and decays towards the interfaces. On another aspect, we measure the cosine alignment between the local rotation axes vector and the

determined $\vec{\xi}_{ij}$ to quantify the preservation of characteristic rotation axis in each layer. The NN rotations are highly similar with an alignment of 0.87 in C5 and decays to almost complete misalignment of ~ 0.62 towards either side of the interfaces (note that the average cosine between a randomly distributed vector set with a specific vector of an arbitrary direction is roughly 0.64). In light of both results, the rotation behavior of QDs in the middle layer are relatively mono-directional with a larger magnitude (0.1 rad in average), while orientation changes are more random with a roughly 50% smaller magnitude at the interface, reaching the limit of our angular resolution. Nevertheless, We note that a smaller average magnitude of inter-NN rotation does not necessary lead to a collectively lower orientation entropy compared to a different set of QDs. To address this, we utilize the von Neumann entropy as a generalized form of Shannon entropy to characterize and compare the dispersity of QD orientation in each layer.[26] The von Neumann entropy can be conveniently derived from the diagonal blocks from the $\{R_i^{AL}\}$ PCM in Fig. 4.3c (see detailed calculation in SI).[46, 33] We show in Fig. 4.5c that the orientational entropy drops rapidly from the middle layer C5 towards either side of the interfaces and is very well correlated with θ_{ij} , indicating that the dispersity of orientation in this sample is more dependent on the reorientation magnitude than the randomness of the reorientation direction. The source of such orientational entropy profile is unlikely a result of the SL structure, as indicated by the entropy profile of $\{\hat{R}_i^{AL}\}$, but more likely to be affected by the presence of the interfaces. We also characterize the neck size between each NN QD pairs and observed a continuous decreasing of average neck size starting from C5 towards the gas interface, accounting for a roughly 20% decline considering all SL directions.

4.5 Conclusion

In summary, we conducted structural analysis on a full-tilt electron tomographic reconstruction of a disc-shaped single-grain region from a 3D epitaxially-connected PbSe QD SL film. The 3.1 Å spatial resolution allows for accurate determinations of the 3D SL position together with AL orientation of each of the 633 QDs. We show that the AL orientation variation over the entire sample is not random but suggests a characteristic rotation axis of $[\bar{1}20]_{AL}$ shared by the majority of QD pairs of non-trivial orientation difference. This effect results in a major

contribution from out-of-plane tilting to the overall orientation disorder. We are also able to mathematically describe and statistically validate the AL/SL relationship in which the AL forms the nearest orthogonal basis to the SL. We show that the AL orientation collectively adapts to a small systematic shear distortion of the SL structure without significantly breaking the short-range atomic alignment. This finding addresses the importance of regulating mid- to long-range SL order to minimize orientation disorder within a single grain.

A particular lesson learnt from characterizing this 3D QD SLs sample is that interface in the Langmuir Schaefer method ([more discussion on that in the result](#)) imposes significant effects on suppressing both the SL translational disorder and orientational disorder of the QDs at the interfaces. Furthermore, we learn from the morphology measurements that the attachments between QDs are also 20% narrower at the film-gas interface, compared to the liquid side. Therefore, relying solely on surface or 2D imaging characterizations such as SEM or STEM could result in unrepresentative results that lead to misinterpretations of the 3D sample quality. The ET data, on the other hand, permits determination of 3D structural attributes that are spatially coupled and thus allows extraction of knowledge that are typically inaccessible with other structural characterization techniques. We believe that the experimental and analytical approach presented in this study can be applied to other hard materials of complex structure for studying 3D spatial dependency of atomic to nanoscale structural features within a $\sim 10^2$ nm length scale. With continuous developments in TEM sample preparation techniques, electron microscopy, automated image acquisition, reconstruction algorithms, and big data processing, we expect the throughput of such measurements can be greatly improved to enable sampling in a larger spatial scale as well as extending to sample comparison in the temporal dimension.

4.6 Supporting Information

Synthesis, ultraviolet visible spectroscopy, crystal Stacking, grazing incidence x-ray diffraction analysis, small angle neutron scattering analysis, atomic force microscopy analysis

4.7 Acknowledgments

This project was supported by the U.S. Department of Energy, Office of Basic Energy Sciences, Division of Materials Sciences and Engineering, under Award No. DE-SC0010419, and

the German Federal Office of Science and Technology (BMBF, MEDOS FKZ: 03EK3505I). Thanks to the Alexander von Humboldt Foundation and to the Universität zu Köln alumni fellowship fund. for sabbatical funding for A.J.M.. Thanks to the Jülich Centre for Neutron Science at Heinz Maier-Leibnitz Zentrum in Garching, Germany for Small-Angle Neutron Scattering measurement time. This work benefited from the use of the SasView application, originally developed under NSF award DMR-0520547. SasView contains code developed with funding from the European Union's Horizon 2020 research and innovation programme under the SINE2020 project, grant agreement No 654000

4.8 Conflicts of Interest

There are no conflicts of interest to declare.

Chapter 5

Comparison of Structural Disorder in 2D and 3D PbSe Quantum Dot Superlattice

5.1 Preface

In this chapter, I will compare the structural characterization of 2D and 3D PbSe QD SLs and discuss both the similarities and dissimilarities between the two materials. Quantum coupling between periodic nanostructures may manifest novel mesoscale physical properties such as mini-band formation, which can induce high carrier mobility. Colloidal PbSe quantum dots (QDs) can self-assemble into a 3D epitaxially-connected superlattice (epi-SL), is a promising material system to realize these synergistic physical features. However, these has not yet been observed in PbSe QDs epi-SL. Energy disorder induced by structural disorder hypothesized to be the main cause which leads to localization of carriers within QDs. In this work, we investigated the nature of structural disorder in PbSe QDs epi-SLs by comparing monolayer (2D) sample with multilayer (3D) using high resolution atomic images of a 2D epi-SL and electron tomography of a 3D epi-SL. We observed the presence of periodic epitaxial structural continuity, i.e., crystalline necks, connecting individual PbSe QDs in both samples. Microscopic nonuniformity observed widely across the epi-SL in both 2D and 3D shows significant similarities by means of missing necking between QDs which modifies the size of the QDs, its distance to neighboring QDs as well as its deviation from their lattice positions. Furthermore, number of missing necking also modifies the dimensions of the necks itself. We found 20% of the expected necking to be missing and these correlations are more pronounced in 2D in comparison to 3D due to absence of interlayer necking in 2D sample. These suggest significant energy dispersion may be induced in the epi-SL by absence of necking leading to modification of the energy landscape. Anderson localization may be the underlying mechanism in PbSe QD epi-SLs hence realization of mesoscale features necessitates well controlled necking formation in these materials.

5.2 Introduction

The electronic and photonic properties of quantum dots (QDs) can be controlled by tailoring their shape and size.[75, 82] The electronic structure of QDs differs from that of macroscopic crystals due to confinement of the electron and hole wave functions within the QD, resulting in discrete “atom-like” energy states rather than continuous bands.[9, 7] Spatially and energet-

ically ordered QD superlattices (crystals of QDs) are predicted to exhibit emergent mesoscale phenomena such as electronic mini-bands, topological states, and Bloch oscillations.[7, 132, 113, 81] Many studies have focused on self-assembly and ligand exchange processes in colloidal QD systems. In recent years, researchers have investigated the formation of highly-ordered, epitaxially-fused QD superlattices (epi-SLs).[13] Among colloidal nanocrystals, low electron effective mass and a high dielectric constant, large exciton Bohr radius which leads to strong confinement and wave function overlap between neighboring QDs makes PbSe QDs promising candidates for optoelectronic applications.[30] However, experimental studies on this materials system have not yet shown the expected high carrier mobility, to decisively demonstrate mini-band formation.[4, 1] For instance, recently developed PbSe QD epi-SLs have only shown mobilities on the order of $1 \text{ cm}^2/\text{Vs}$ without the aid of device modifications, such as electrolytic gating, suggesting hopping transport rather than charge delocalization.[8] Several mechanisms have been proposed to explain this inconsistency, including intragrain: charge trapping by surface states, structure-induced energy disorder (variation in QD and neck size) , intergrain: charge scattering at the grain boundaries, and inadequate coupling between the QDs, however, the primary causes have not yet been deciphered. Electrical characterization of epi-SLs is primarily accomplished using field-effect transistors where the channel region is composed of a polycrystalline epi-SL film with a variety of macro- and microscopic defects. Thus, the extracted mobility values are a convolution of inter- and intra-grain charge transport. Here, we investigate the correlation between structural disorder and electronic structure/charge transport within individual epi-SL grains. By studying single epi-SL crystals, we eliminate the ill-defined effects that grain boundaries and other macroscopic defects have on transport in measurements of polycrystalline epi-SLs. In this work, We combine insights from electron tomography (ET) of a 3D PbSe QD epi-SL with atomic-resolution high angle annular dark field (HAADF) images of analogous 2D epi-SLs. We observed significant superlattice disorder and show that it correlates with the number of necks per QD for 2D layers in these comparisons. We hypothesize that structural disorder resulting from QD and neck size inhomogeneity causes energetic disorder within the epi-SL, resulting in carrier localization and relatively low carrier mobilities.

5.3 Experimentals

5.3.1 Materials

All chemicals were used as received unless otherwise noted. Lead oxide (PbO, 99.999%), lead iodide (PbI₂, 99.9985%) and selenium shot (99.999%) were purchased from Alfa Aesar. Oleic acid (OA, technical grade, 90%), diphenylphosphine (DPP, 98%), 1-octadecene (ODE, 90%), anhydrous ethylene glycol (EG, 99.8%), anhydrous acetonitrile (99.99%), anhydrous hexanes (99%), anhydrous toluene (99.8%), 3-mercaptopropyltrimethoxysilane (3-MPTMS, 95%), trimethylaluminum (TMA, 97%) and anhydrous dimethyl sulfoxide (DMSO, 99.9%) were purchased from Sigma Aldrich. Anhydrous 1,2-ethylenediamine (EDA, 98.0%) was purchased from TCI. Trioctylphosphine (TOP, technical grade, 90%) was acquired from Fluka and mixed with selenium shot for 24 hours to form a 1 M TOP-Se stock solution. Nitric acid (TraceMetal grade, Fisher Scientific) was distilled twice before use. 18.2 MΩ water (Milli-Q Gradient) was used for substrate cleaning and atomic layer deposition (ALD). Water for ALD was degassed with three freeze-pump-thaw cycles before use.

5.3.2 Quantum dot synthesis

PbSe QDs were synthesized and purified using standard air-free techniques according to a previously published procedure. Briefly, PbO (1.50 g), OA (5.00 g), and ODE (10.00 g) were mixed and degassed in a three-neck round-bottom flask at room temperature. The mixture was then heated at 120 °C under vacuum to form Pb(OA)₂ and dry the solution. After 1.5 hours, the Pb(OA)₂ solution was heated to 180 °C under argon flow and 9.5 mL of a 1 M solution of TOP-Se containing 200 μL of DPP was rapidly injected into this hot solution. An immediate darkening of the solution was observed, and the QDs were grown for 105 seconds at ~160 °C. The reaction was quenched with a liquid nitrogen bath and injection of 10 mL of anhydrous hexanes. The QDs were purified in an N₂-filled glovebox (<0.5 ppm O₂) by adding 2 mL of toluene and 9 mL of acetonitrile to the reaction solution, collecting the QDs by centrifugation, performing 6-8 cycles of redispersion/precipitation using toluene/acetonitrile (3 mL/24 mL), and then drying and storing the QDs as a powder in the glovebox.

5.3.3 Fabrication of multilayer QD superlattices

Multilayer (3D) epi-SL films consisting of 6-7 QD layers (~ 40 nm thick) were made using a modified version of a published procedure. Briefly, in an N_2 -filled glovebox with < 0.5 ppm O_2 , oleate-capped PbSe QD superlattices were prepared by carefully drop casting $60 \mu\text{L}$ of a 15 mg/mL solution of PbSe QDs dispersed in hexanes onto 7 mL of ethylene glycol in a Teflon well (3.5 cm wide \times 5 cm long \times 1 cm deep) that was cleaned by soaking overnight in 5 M nitric acid and then soaking and rinsing in Millipore water at least ten times. After depositing the QD solution, the well was immediately covered with a glass slide and the hexanes allowed to slowly evaporate in 25 - 30 minutes, resulting in a smooth, dry QD film floating on the EG surface. The slide was then removed and $100 \mu\text{L}$ of a 7.5 M solution of ethylenediamine in acetonitrile was slowly (5 - 10 s) injected into the EG directly underneath a corner of the film. As the EDA solution spread throughout the well, the film visibly darkened, indicating film densification and conversion to the epi-SL. After 30 seconds, the darkened SL film nearest to the EDA injection point was transferred to a solid substrate (SiO_2 -coated Si) by manual stamping using a vacuum wand. Prior to stamping, the SiO_2 -coated Si substrate was cleaned by 15 minutes of sonication in acetone, water, and isopropanol, dried under flowing air, soaked in a 100 mM solution of 3-MPTMS in toluene for 1 hour to functionalize the surface for improved QD adhesion, then rinsed with neat toluene and dried under flowing air. The stamped film was rinsed vigorously with neat acetonitrile and dried under flowing N_2 . Next, the SL film was immediately soaked in a 10 mM solution of PbI_2 in DMSO for 5 minutes to reduce the amount of residual oleate and adsorbed glycoxide, rinsed with copious amounts of DMSO and acetonitrile, and dried under flowing N_2 .

5.3.4 Fabrication of monolayer QD superlattices for STEM experiments

Monolayer (2D) epi-SL films for EELS experiments were made as follows. An aliquot of a 1.75 mg/mL PbSe QD dispersion in toluene was drop cast onto a Pelco SiO_2 support film TEM grid (8 nm thick SiO_2 windows, product 21532-10, Ted Pella) and dried over the course of several minutes. The grid was then immersed for 15 seconds in a 15 mM ammonium thiocyanate (NH_4SCN) solution in acetonitrile, soaked in neat acetonitrile for 10 seconds to remove unbound NH_4SCN , dried, soaked in neat hexanes for 10 seconds to remove residual unbound

oleic acid/oleate, dried again, and finally dipped into neat acetonitrile, quickly removed, and blown dry in a stream of N₂ to prevent solvent droplets from depositing residue onto the grid surface.

5.3.5 Electron Tomography

The sample used for tomography and its analysis previously studied by Chu et. al.[25] A 3D PbSe epi-SL film on a Si substrate was characterized by electron tomography. An $8 \times 6 \times 2 \mu\text{m}$ lamella was cut from the film by focused ion beam (FIB) milling in a FEI Quanta 3D FEG Dual-Beam microscope. The lamella was repositioned, and FIB welded on the tip of a copper post and then FIB milled into a needle shape with an epi-SL diameter of 120 nm. The post was loaded on a STEM tomography holder (Hummingbird Scientific) and images (2048×2048 pixels) were acquired using a double aberration corrected JEOL JEM-ARM 300F TEM operated at 300 keV. The projection tilt-series contained 181 images spanning an overall tilt range of 0-226° with an average tilting increment of 1.4 degrees. The image stack was aligned through common-line and cross-correlation comparison.[21] Tomographic reconstruction was performed with the simultaneous iterative reconstruction technique (SIRT) in the ASTRA toolbox[119, 122] using 200 SIRT iterations. Post-reconstruction processing and 3D image analysis utilized in-house MATLAB and Python scripts.

5.3.6 STEM-HAADF Analysis

Experiments were performed on the monolayer epi-SL samples in a double aberration corrected, monochromated Nion UltraSTEM 100 HERMES microscope[54] equipped with a Nion Iris spectrometer operating at 60 keV and an energy resolution of 100 meV at Oak Ridge National Laboratory. The elastically scattered electrons collected in the HAADF detector provide direct information about the local atomic structure through atomic contrast[17].

5.4 Results and Discussion

Monolayer and multilayer PbSe QDs epi-SL is obtained by one of various controlled ligand exchange processes, including drop-casting and self-assembly[11]. We used STEM-HAADF imaging for characterization of 2D epi-SL drop casted on a TEM grid, and ET for characterization of a 3D epi-SL. Figure 1a shows examples of QDs having one, two, three, and four necks as

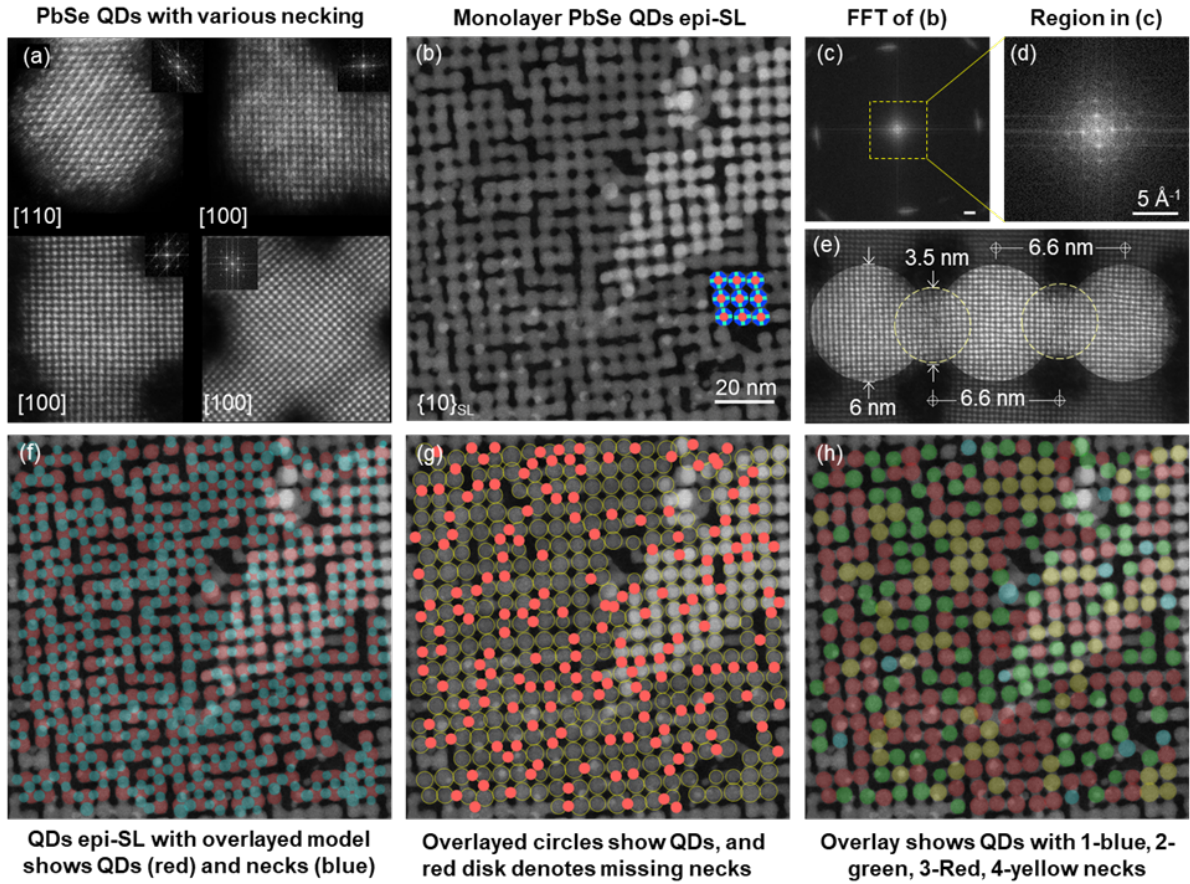


Figure 5.1. Structural analysis of monolayer PbSe QD epi-SLs. (a) STEM-HAADF images of QDs with one, two, three, and four necks. Inset FFT images show the corresponding orientations of the atomic lattice for indicated zone axis. (b) Large area HAADF image of 2D PbSe QDs epi-SL. Overlaid model indicates square lattice symmetry. (c-d) FFT image of HAADF in b indicating the atomic (100) and super lattice (10) symmetry. (e) Optimum QDs with epitaxial necking (encircled with yellow dashed line) is highlighted. (f) Variation of QDs (red) and neck (blue) size in epi-SL presented with overlaid model. (g) QDs (encircled with yellow line) and the missing necks (denoted with red disk) shown. 25% of the necks are missing in the epi-SL. (h) Distribution of the QDs according to their number of necking indicated with color coded overlay showing QDs with one (purple), two (green), three (red), four (yellow) necks.

well as four QDs connected with epitaxial necking forming monolayer epi-SL.¹¹ Long range order in 2D epi-SL is shown in a large area HAADF image in Fig. 1b which presents both monolayer and bilayers (high contrast). We can see the missing QDs and necks across the epi-SL. The overlaid model presents the square lattice structure of the epi-SL confirmed by FFT in Fig. 5.1. Formation of ideal epitaxial connection between QDs is presented in Fig. 5.1. Here, the QD and neck diameter is defined by the outmost atoms at the periphery of the cir-

cle and found to be 6.6nm and 3.5nm respectively. We studied the structural disorder in PbSe QDs epi-SL in Fig. 5.1b by means of QD and neck diameter, inter-QD distance, deviation of QDs from its lattice position and their correlation to number of necking for each QD. To do this, we developed an algorithm (see Fig. S1) to determine the size and position of the QDs and their necks as presented in Fig. 5.1f. In this analysis, we excluded QD at the edges since information about their necking cannot be obtained. Here we show the QDs with red and necks with blue overlay and necks is placed front in overlaid regions. While most of the necks are smaller than QDs, some necks are bigger than QDs. We found significant number of missing necks between QDs forming 25% of the total expected necking as shown in Fig. 5.1g and the missing necks distributed randomly across the epi-SL. We also looked at the distribution of the QDs across the epi-SL according to the number of necking it has as shown in Fig. 5.1h and did not observe meaningful pattern. However, we found significant correlation between number of missing necks on QDs and its size and position. We present these correlations in comparison with multilayer structure in the next section.

We used various imaging techniques to investigate the structural disorder in multilayer PbSe QDs epi-SL. Fig. 5.2a shows SEM image of the surface of the 3D epi-SL which has two crystal plane $(100)_{SL}$ and $(01\bar{1})_{SL}$ separated by a grain boundary. While the extent of necking is not visible in these images, missing QDs in the topmost epi-SL layers is seen. The periodicity and registry between the adjacent layers in epi-SL is presented with HIM and HAADF images in Fig. 5.2b and c. Self-assembly of the PbSe QDs in multilayer epi-SL differs from cubic structure of monolayer and forms distorted primitive cubic cell as depicted by inset models in Fig. 5.2a-c. This difference introduces an offset between the atomic lattice and superlattice (i.e., $(100)_{SL}$ is $\sim 5^\circ$ of from $[001]_{AL}$. [1] We used ET to study the size of the QDs and neck, their position, inter QDs distance, their relation to number of necking in the 3D epi-SL sample shown in Fig. S3a. It consists of three grains as presented in a reconstruction in Fig. 4a which denotes only the positions of the QDs. In this analysis, we excluded edge QDs since we cannot obtain information about its necking. We selected highly ordered single grain region (highlighted in Fig. 5.3a) presented in Fig. 5.3b for the analysis. Then we divided it into three sets of isolated 2D layers defined as $(001)_{SL}$ being the lateral layers (Fig. 5.3c), and $(010)_{SL}$ and $(100)_{SL}$

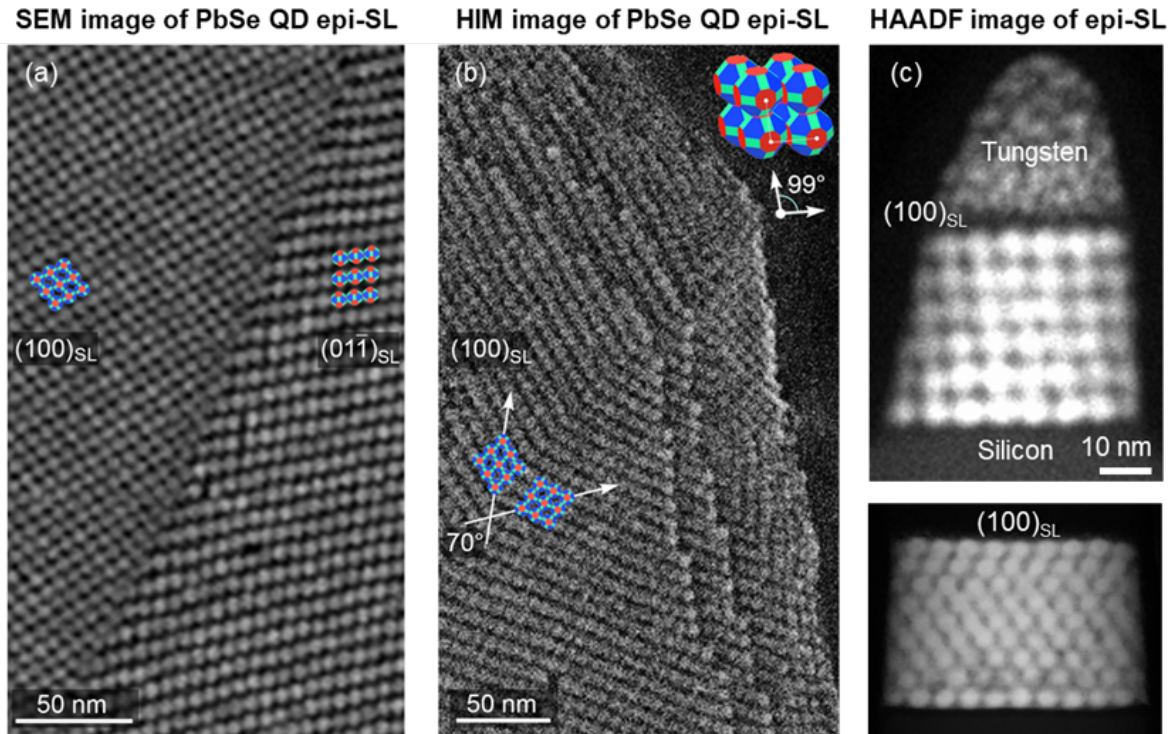


Figure 5.2. Structural analysis of multilayer (3D) PbSe QD epi-SLs. (a) SEM image of a QD epi-SL showing a boundary of two crystal plane orientation. Overlay model shows surface orientation of epi-SL. (b) HIM image shows periodic registry between inter layers in (100) orientation. Overlay model shows the twin boundary angled 70 degrees. Inset 3D model presents the distorted cubic structure of the PbSe QDs epi-SL. (c) HAADF image shows the cross section of the QD epi-SL on APT post.

both being vertical layers in Fig. 5.3d-e (combined) disregarding interlayer necking. We then compare the monolayers in 3D epi-SL with 2D epi-SL presented in Fig. 1b.

Histogram of the QDs and necks' diameter for the three types of monolayers; the 2D epi-SL, lateral and vertical monolayers in 3D epi-SLs, are presented in Fig. 5.4a. It shows broad dispersion of their size both for QDs and necks for all the layers however, there is no significant variation in average QD size and neck size among the layers. We sorted the QDs according to their number of necking with neighboring QDs for all layers and compare them in Fig. 5.4b. The QDs mostly makes two and three necking and again shows similar trend for all. We then investigated the intraplane deviation of the QDs from their expected lattice positions (explained in Fig. SX) as a function of their number of intraplane necking as shown in Fig. 5.4c. We found surprisingly same but intuitive correlation for all layers which shows decrease in deviation by making more necking with neighbor QDs. It should be noted that we also confirmed this rela-

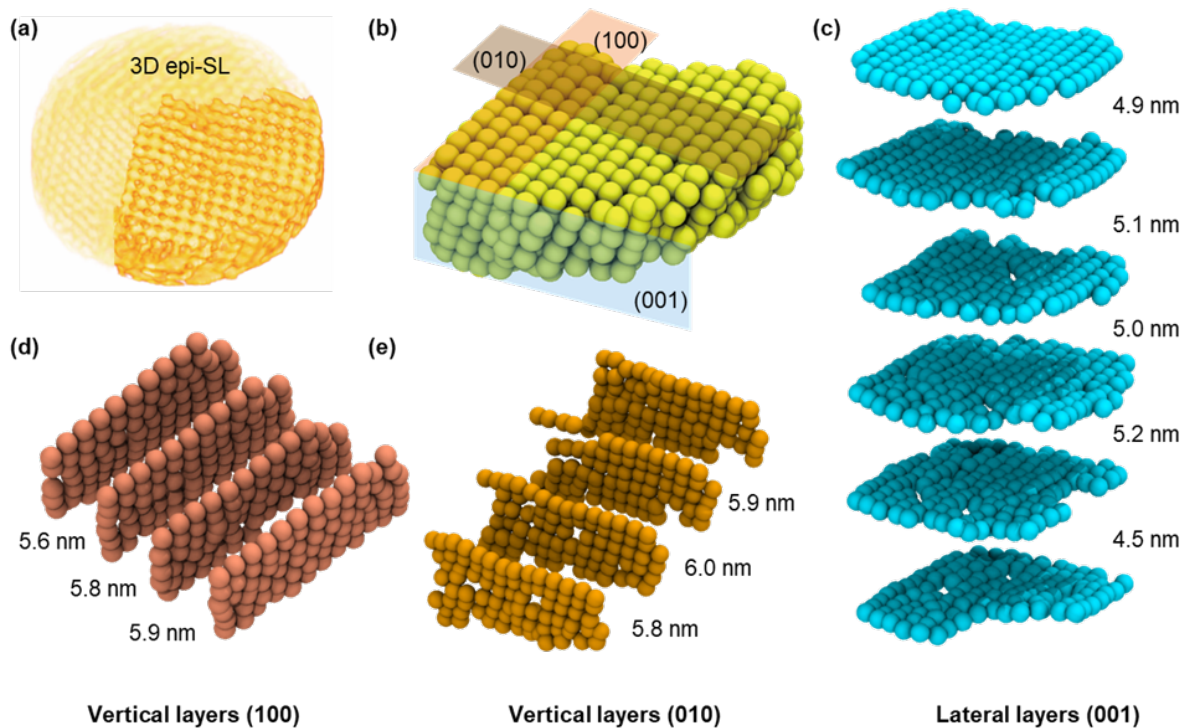


Figure 5.3. (a) Tomography analysis of PbSe QD epi-SL consist of three grains presented with yellow reconstruction (1 nm resolution) and the highly ordered grain presented with green reconstruction in (b). This reconstruction does not present the size dispersion of the QDs, nor the necking, but shows the location of the QDs in the 3D epi-SL as obtained from center-of-mass analysis. 3D sample grouped into three sets of 2D plane defined as (001) being lateral layers in (c) , (010) in (d) and (100) in (e) being vertical layers (grouped) denoted with blue, red, and brown accordingly.

tion by considering QDs with zero, one and two interplane necking separately as shown in Fig. SX. We then examined the interplane distance variation for the layers in 3D epi-SL (explained in Fig. SX) and presented in Fig. 5.4d. Similar to the correlation observed for intraplane, interplanar distance increases by missing necking. This is more significant for lateral layers while vertical layers show a subtle change. This indicates that intraplane necking in lateral layers which corresponds to interplanar necking between vertical layers impacts the structural order more significantly. This can be associated with the directional preference for assembling of the QD during epi-SL formation which may favor growth in parallel with liquid interface rather than vertical into the solution. This difference in divergence is critical for electronic properties considering current conduction along various super lattice directions. The deviation analysis for both intra and inter plane necking clearly indicates that number of necking determines the

QDs position in the super lattice. We then studied the impact of necking on inter QD distance as shown in Fig. 5.4e. All layer present surprisingly same trend, the inter QDs distance increases by making more necking with neighboring QDs. However, the magnitude of the change for inter QD distance is different monolayer in 2D epi-SL is being the most prone to variation while the vertical layers is the least. This can be again explained by the inter plane necking which is absent for monolayer in 2D epi-SL is prone to more deviation by missing necking as seen in fig. 5.4c. Last, we examined the impact of necking on the QDs and neck size in Fig. 5.4f and g. While the diameter of the QDs increases by more necking, neck size is decreasing as presented in fig. 5.4f and g. Considering the fusion process of the QDs via necking in which Pb and Se atoms transfers from QDs to its necking, this correlation is not intuitive. Because the size of the QDs should decrease during fusion process by atoms moving away from the QDs. This relation can be seen better in Fig. 4h which shows the ratio of neck size versus QDs increases by more necking. One plausible explanation would be the transformation of some QDs to neck populating the size of the neighboring QDs by participation of its atoms. This hypothesis is consistent with observation of necks larger than QDs size in Fig. 1f and overlapped region observed between 5nm to 6nm in histogram in fig. 5.4a which shows very large neck formation exceeding size of the QDs and vice versa.

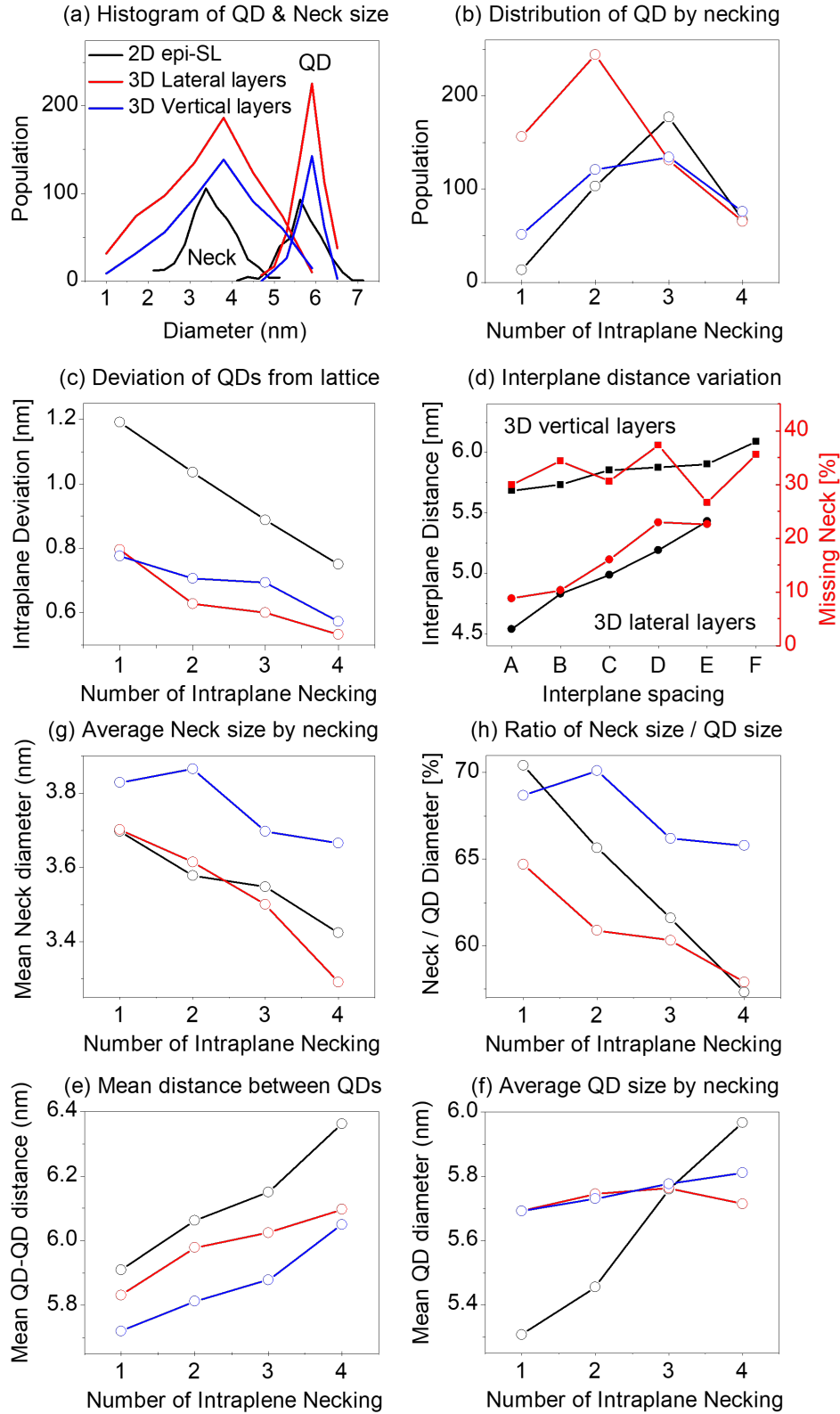


Figure 5.4. Structural analysis of PbSe QD epi-SLs. (a) Histogram of QDs and neck's diameter show similar distribution for all layers. (b) QDs sorted according to their number of intraplane necking shows similar trend. (c) QDs deviate from their lattice points by increase in missing number of necking for all planes. (d) Interplanar distance increases by missing necks for 3D lateral layers while subtle change seen for 3D vertical layers. (e) Inter QDs distance increases by increasing intraplanar necking. (f) While the average QDs size is increasing by necking, the opposite trend is observed for size of the neck in (g). The relative change of neck size vs QDs size as a function of necking shown in (h) indicates inverse relation.

5.5 Conclusion

Comprehensive and comparative analysis of monolayer QD epi-SL with HAADF and multi-layer QDs epi-SL with ET revealed intricate but decisive universal neck-dependence for structural nonuniformity and aperiodicity in PbSe QDs epi-SL. These correlations implies that structural and consequently energy disorder in this material directly and prominently depends on the connectivity between the QDs rather than the variation of the QD diameters and their necks. Surprising structural differences between the lateral and vertical layers may induce distinct energy dispersions in the corresponding superlattice Brillouin zone directions which shapes the landscape of the electronic structure of the PbSe epi-SL.

5.6 Acknowledgement

This work was funded by the UC Office of the President under the UC Laboratory Fees Research Program Collaborative Research and Training Award LFR-17-477148. It was mainly conducted at the Center for Nanophase Materials Sciences, a DOE Office of Science User Facility. It was performed in part at the San Diego Nanotechnology Infrastructure (SDNI) of UCSD, a member of the National Nanotechnology Coordinated Infrastructure, which is supported by the National Science Foundation (Grant ECCS-1542148).

5.7 Supporting Information

Molecular Structure of Materials, Experimental Methods, PDPP-2T Synthesis, UV-Vis-NIR Full Gaussian Fits, PDPP-2T FeCl_3 Absorption Discussion, Fractional Doping Level (Θ) and Isotherm Fitting, Discussion of ΔG° , P3HT Anion Exchange (Assuming one monomer site), Anion Exchange Isotherm Site Size Comparison, Discussion of Θ : Is $\Theta \propto P1$ or $\propto \sum(P1, P2, P3)$?, Anion Exchange Simulations, Extra UV-Vis-NIR Tests, Sheet Resistance IV Curves and Discussion of Conductivity Enhancements, Discussion of Carrier Density, X-ray Photoelectron Spectroscopy.

Chapter 6

Unfinished Work

6.1 Preamble

The content of this chapter are either unpublished data or published studies not strictly related to the topic of this thesis. Some of the unpublished data will serve as foundations for future publications for the current or future graduate students in the Moule lab.

6.2 Electron Tomography Study on the Phase distribution of PCE11-PCBM Organic Bulk Heterojunctions

Organic solar cells (OSCs), which are generally based on bulk heterojunctions (BHJ) between an electron donor and an electron acceptor,[107] have recently achieved power-conversion efficiencies (PCE) over 16%,[45] rendering this 3rd-generation solar-cell technology attractive for commercial exploitation. A significant contribution to this progress resulted from the advancement of new materials. This has led to a large number of novel OSC materials and, in turn, a plethora of donor:acceptor combinations.[134] However, since the device performance is inter-linked in a complex way not only with the properties of the individual components but also with the blends' microstructure and phase morphology (e.g., the length scale of the donor:acceptor phase separation; the donor:acceptor interfacial area; their phase purity; and the formation of bi-continuous percolation paths),[77, 59, 57, 90] identifying high-performing donor:acceptor combinations is still an intricate process nearly uniquely relying on tedious and time-consuming trial-and-error procedures. Such an approach is unsustainable, especially considering the large number of possible materials combinations. Here, we demonstrate that differential scanning calorimetry (DSC), vapor phase infiltration (VPI) and transient absorption spectroscopy (TAS) measurements can be collectively harnessed to fast-screen OSC blends. To illustrate the usefulness of our screening method, we selected poly[(5,6-difluoro-2,1,3-benzothiadiazol-4,7-diyl)-alt-(3,3''-di(2-octyldodecyl)-2,2';5',2'';5''',2''''-quaterthiophen-5,5''''-diyl)] (PCE11)[85] and phenyl-C61-butyric-acid-methyl ester (PCBM) as a model donor:acceptor system. Their chemical structures are displayed in Fig. 6.1a. We scrutinize our methodology both on spin-coated and less-studied wire-bar-coated PCE11:PCBM blend films/devices, with and without process-

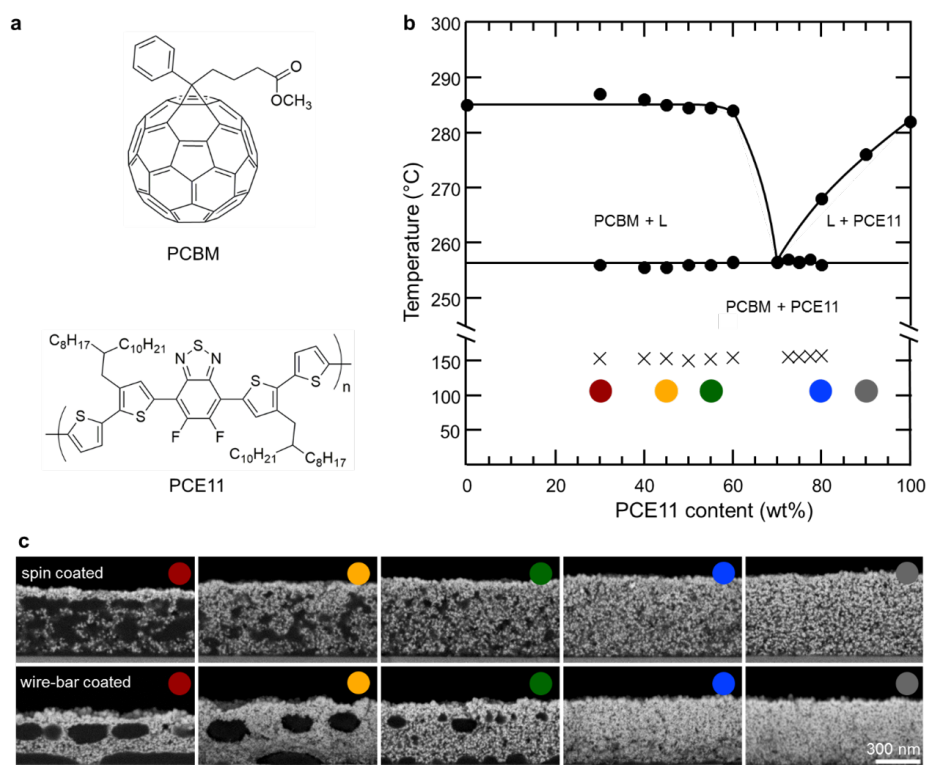


Figure 6.1. Phase behaviour and solid state microstructure of PCE11:PCBM blend films. a, Chemical structures of PCBM and PCE11. b, Non-equilibrium phase diagram of the PCE11:PCBM system deduced from DSC first heating thermograms, obtained at 10°C/min, of high-temperature drop-cast samples. A eutectic behaviour is found with a eutectic composition around 75-80 %wt PCE11 and a eutectic temperature around 252 °C. The black crosses represent the cold-crystallisation temperature, as deduced by a line drawn tangential to the thermograms to intercept the onset of the heat-flow slope variation. c, Cross-section HRSEM BSE micrographs of spin-coated (top row) and wire-bar coated (bottom row) PCE11:PCBM films of different blend compositions, after exposure to 80 cycles of DEZ and water at 60 °C, showing selective deposition of ZnO in the PCE11-rich domains (bright contrast). In contrast, PCBM-rich domains inhibit ZnO deposition, and, thus, are characterized by dark contrast. The selective “staining” of PCE11-rich domains by ZnO in the VPI process effectively maps the phase separation as well as the size- and spatial distribution of the donor- and acceptor-rich domains in PCE11:PCBM blend films. The scale bar for all the micrographs is 300 nm.

ing additives such as nucleating agents, to understand why up-scaling can be a highly difficult task if one cannot obtain rapid feedback. We start our discussion with information that can be obtained from DSC (Fig 6.1), comparing the thermal behavior of films drop-cast at room temperature and 120 °C, respectively, for both the neat materials (PCE11, PCBM) and blends of different compositions. The two sets of thermograms are displayed in Supplementary Fig. 6.1. From these, we conclude that both sample sets feature a very similar eutectic behavior with the

eutectic composition being around 75-80 wt% PCE11 and the eutectic temperature around 252 °C (see Fig. 6.1b for an illustration of the phase diagram plotted based on the thermograms of the high-temperature-cast samples). However, by comparing the individual thermograms of the differently cast films, slight but important differences can be discerned. From these we learn how the samples' processing history affects their solid-state microstructure. For instance, the relative enthalpies of fusion for the fullerene, δH_f relative (PCBM), with respect to the δH_f of neat PCBM films are notably smaller in the high-temperature-cast films than in blends deposited at room temperature (46% and 74%, respectively, e.g. for blends of 30 wt% PCE11; Supplementary Fig. 6.1). Since δH_f is directly correlated with the degree of crystallinity, this implies that in the high-temperature-cast structures, the PCBM regions are more vitrified compared to films cast at room temperature.

Since the phase diagrams established by DSC are deduced for non-equilibrium structures (cf. Refs. [91, 133]), they are not always straight-forward to interpret. Also, they can only be deduced using material obtained from relatively thick films. We, thus, went on to visualize the phase behavior and phase morphology of device-relevant thin films via VPI. We prepared PCE11:PCBM BHJ structures as well as neat PCE11 and PCBM films. In a first set of experiments, we processed these systems via spin-coating from hot solutions (130 °C) preheating the spin-coating chuck and the substrates to 130 °C. To ensure comparison with device performances, all films were prepared to be ~300 nm thick. The films were left to dry overnight in inert atmosphere and then were exposed to gaseous metal-oxide precursors, in this case diethyl zinc (DEZ) and water, followed by in-situ conversion to the metal oxide [96, 94, 95, 79, 80] as outlined in Supplementary Fig. 2.

Cross-section high-resolution scanning electron microscopy (HRSEM) back-scattered electron (BSE) images after exposure of the neat PCE11 and PCBM films to DEZ and water show that the precursor can only diffuse through the polymer phase. Indeed, we find homogenous, rich sub-surface deposition of ZnO within neat PCE11 films, leading to a bright contrast; no ZnO is deposited within PCBM films, resulting in a dark contrast even after prolonged exposure times, in agreement with our previous observations. [96, 94, 95]

In blends, this z-contrast between inorganic ZnO deposits in PCE11-rich domains and do-

mains where the presence of PCBM inhibits ZnO deposition, enables rapidly analyzing the BHJ phase morphology as a function of composition and processing conditions. Fig. 6.1c (top row) shows cross-section HRSEM BSE micrographs of spin-coated PCE11:PCBM films of different compositions. The films with high PCE11 content (i.e., 80-90 wt% PCE11) show homogeneous, sub-surface ZnO deposition (Fig. 6.1c) similar to what is found for neat PCE11 (Supplementary Fig. 2) and in agreement with DSC (Fig. 6.1b), which predicts these blends to be predominantly composed of eutectic morphologies (i.e. finely-phase separated PCE11:PCBM regions) with some PCE11-rich domains. When decreasing the PCE11 content below 80 wt%, we observe the evolution of distinct, seemingly interconnected PCBM-rich domains that increase in size with increasing PCBM content (Fig. 6.1c, top row) as also expected from DSC. We attribute these domains based on classical materials nomenclature to be pro-eutectic PCBM regions.

Based on the phase morphology only, slightly hypo-eutectic films are expected to perform best as active solar cell layers[133] as they feature interconnected, fullerene-rich domains that are of limited size; i.e. they can act as energy sinks for electrons assisting exciton dissociation while also assisting charge extraction. Other structural features, including phase purity of domains, degree of molecular order and crystalline quality, will play important roles in the photovoltaic energy-conversion process. Elucidation of these requires, however, the collective information from a broad combination of experimental tools including grazing-incidence wide-angle X-ray diffraction and soft-X-ray synchrotron methodologies that are not compatible with fast screening. We, thus, selected to carry out transient-absorption spectroscopy (TAS) to obtain rapid information on the PCE11:PCBM thin films in addition to the phase morphology revealed by VPI/DSC. With current ultrafast laser technology, TAS can provide critical information on BHJ blends very rapidly. As importantly, since TAS measures the population dynamics over nanosecond time windows and with sub-picosecond time resolution, it provides insights on the initial charge-generation and recombination processes. Because short-range structural features, including molecular conformation, intermolecular order and packing, molecular mixing and local arrangements (e.g. chain-segment conformation), are important in these dynamics, TAS can provide indirect information on length scales that cannot be accessed by VPI/DSC measure-

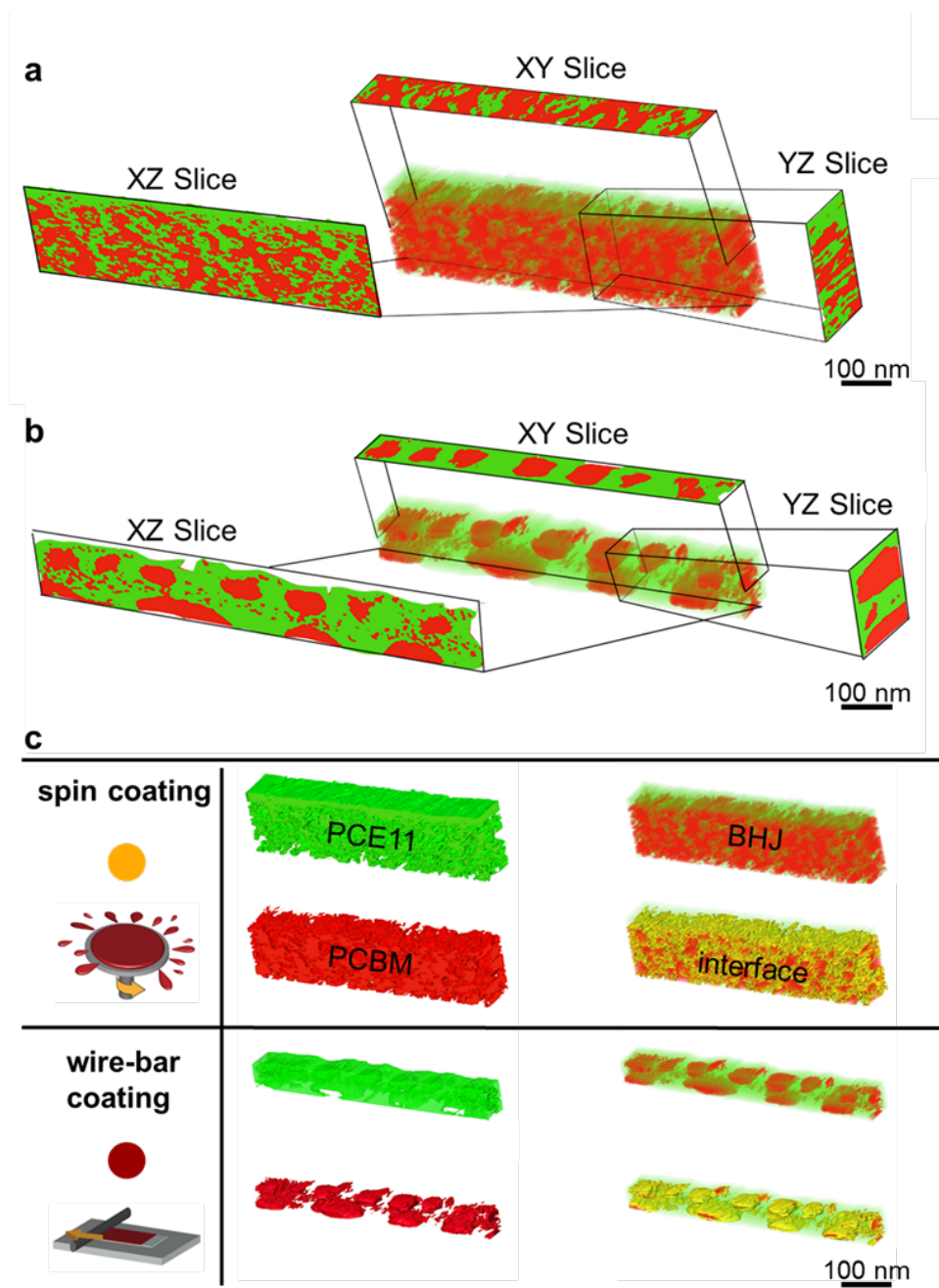


Figure 6.2. Tomographic reconstruction of selected PCE11:PCBM BHJs films from TEM-STEM tilt-series showing the 3D-spatial distribution of PCE11-rich domains (green), PCBM-rich domains (red) and the interface between them (yellow).

ments. TAS hence is complementary to the information revealed by imaging/thermal analysis.

In conclusion, we demonstrated a fast-screening methodology based on a combination of DSC, VPI and TAS. While important structural details such as crystal orientation are not probed

with these methodologies, the spatially mapping of the OSC phase morphology via VPI provides insights into the size, shape, distribution and connectivity of specific domains, resolved through fast, straightforward HRSEM characterization. When combined with information obtained on the general phase behavior and phase purity (or at least degree of order) via DSC, and the indirect correlations on the fine structure of, e.g., the intermixed phases/phase-pure domains provided by the charge-population dynamics from TAS, this data set can be used to identify best-working compositions and deliver understanding why specific deposition methodologies do not lead to well-performing devices and, indeed, large device-to-device variations. Since VPI also can be used on complete device structures (Supplementary Fig. 7), our methodology can in principle also be applied to provide rapid feedback on the origins of device degradation over time, e.g., the burn-in caused by spinodal decomposition¹⁹. It furthermore should help understanding the structure development in OSC blends comprising non-fullerene acceptors. Initial VPI experiments, for instance, show that a contrast between donor and acceptor domains can be realized, however, with the contrast inversed to that in PCE11:PCBM blends—a fact that will not be discussed here. Generally, the advantage of our approach lies in its simplicity and its broad application, allowing obtaining information on a broad spectra of blends. We can compare, for instance, our strategy with grazing-incidence small-angle scattering (GI-SAXS). Here, only the spin-coated films comprising 30 wt% PCE11 show a distinct feature at $\sim 0.012 \text{ \AA}^{-1}$ indicating that these samples have characteristic domain sizes of 52 nm (Supplementary Fig. 8). In all the other cases, a precise domain size cannot be extracted from GI-SAXS, most likely because the phase separation is too fine (e.g. in the samples of high PCE11 content) or too rough (e.g., wire-bar coated films of high PCBM content). Grazing-incidence wide-angle scattering (GI-WAXS) provide important information on the PCE11:PCBM thin-films' texture. We find that in wire-bar coated films, PCE11 molecules feature a bimodal, predominantly edge-on orientation while in spin-coated films show a face on orientation. However, no clear trend is observed that would help identifying optimum compositions. Finally, we like to highlight that VPI provides similar quality information as high-resolution transmission electron microscopy (HRTEM) imaging and tomography, however in a much straight-forward fashion. Fig. 6.2 shows 3D-morphology reconstructions of two samples: a spin-coated film compris-

ing 45 %wt PCE11 (Fig. 6.2a) and a wire-bar coated film with 30 %wt PCE11 (Fig. 6.2b) based on three perpendicular cross-section images that are frames from movies showing the full 3D-morphology reconstruction of the selected sample volume. The images support the insights obtained from the 2D-HRSEM images (Fig 1c) that the 45 %wt PCE11 spin-coated film architecture is based on interconnected donor:acceptor networks, while the wire-bar coated film of 30 %wt PCE11 is composed of coarse, isolated PCBM-rich domains within a PCE11-rich matrix. This picture is supported by the tomography data representing the 3D donor:acceptor interface (Fig. 6.2c). Unambiguously, while very helpful, these are not techniques that can be used for fast screening. In contrast, the VPI/DSC/TAS-screening can be executed relatively fast, using standard lab techniques and using a range of systems, from neat films to blends of different composition/thicknesses, promising wide-applicability, especially to new OSC-blend combinations.

6.3 Three Dimensional Geometric Phase Analysis

6.3.1 Introduction

Geometric phase analysis (GPA) is a quantitative image analysis technique that has been used to process high-resolution TEM and STEM images since it was introduced in 1997[58]. GPA uses diffraction features in the image to identify one or several specific spatial periodicity in the reciprocal space through fast-Fourier-transformation. These information are digitally enhanced, isolated and reconstructed back into real-space to generate Bragg-filtered images which contains partial information of the original image with respect to the spatial frequency of interests, which usually point to specific lattice spacings. GPA is widely used to generate quantitative measurements on local atomic lattice displacement, strain, dislocation and orientation change.[67] To date, most of the GPA measurements have done on 2D images with near-atomic to atomic resolutions. The application of GPA is mathematically valid for processing 3D images, particularly tomography reconstructions of periodic atomic feature. Yet few study have reported 3D GPA mainly due to the challenge of acquiring 3D data set with adequate spatial resolution. In this chapter, I demonstrate the methodology of conducting 3D GPA analysis on a near-atomic resolution electron tomography data set. The interpretation of the quantitative result generated from

the 3D GPA analysis, including displacement, strain and dislocation maps, are important for understanding the root cause of different structural defects in the PbSe QD SLs material.

6.3.2 Methodology

The 3D tomogram volume can be expressed as a Fourier series,

$$I(\vec{r}) = \sum_g H_g \exp\{2\pi i g \cdot \vec{r}\} \quad (6.1)$$

where the H_g refers the coefficient associated to a Bragg Spot of a particular spatial frequency.

The corresponding Fourier transformation can be written as,

$$\hat{I}(\vec{k}) = \sum_g \hat{H}_g(\vec{k} - g) \quad (6.2)$$

We take the inverse Fourier transformation regarding the designated Bragg Spot giving,

$$H_g(\vec{r}) = A_g(r) \exp\{iP_g(\vec{r})\} \quad (6.3)$$

$H_g(\vec{r})$ takes a complex form and $A_g(r)$ is the Bragg magnitude image which are simply the norm of $H_g(\vec{r})$

$$A_g(\vec{r}) = |H_g(\vec{r})| \quad (6.4)$$

$P_g(r)$ is the phase image calculated as,

$$P_g(\vec{r}) = \text{atan} \frac{\text{Im}\{H_g(\vec{r})\}}{\text{Re}\{H_g(\vec{r})\}} \quad (6.5)$$

The Bragg filtered image is the real part of $H_g(\vec{r})$,

$$B_g(\vec{r}) = 2\text{Re}H_g(\vec{r}) \quad (6.6)$$

We calculate the phase difference by subtracting $P_g(r)$ with a perfect phase $2\pi \cdot r$, which yields the phase difference image.

$$P_g^*(\vec{r}) = P_g(\vec{r}) - 2\pi g \cdot \vec{r} \quad (6.7)$$

The local reciprocal lattice vector can then be derived from phase difference,

$$\Delta P_g^*(\vec{r}) = 2\pi g(\vec{r}) \quad (6.8)$$

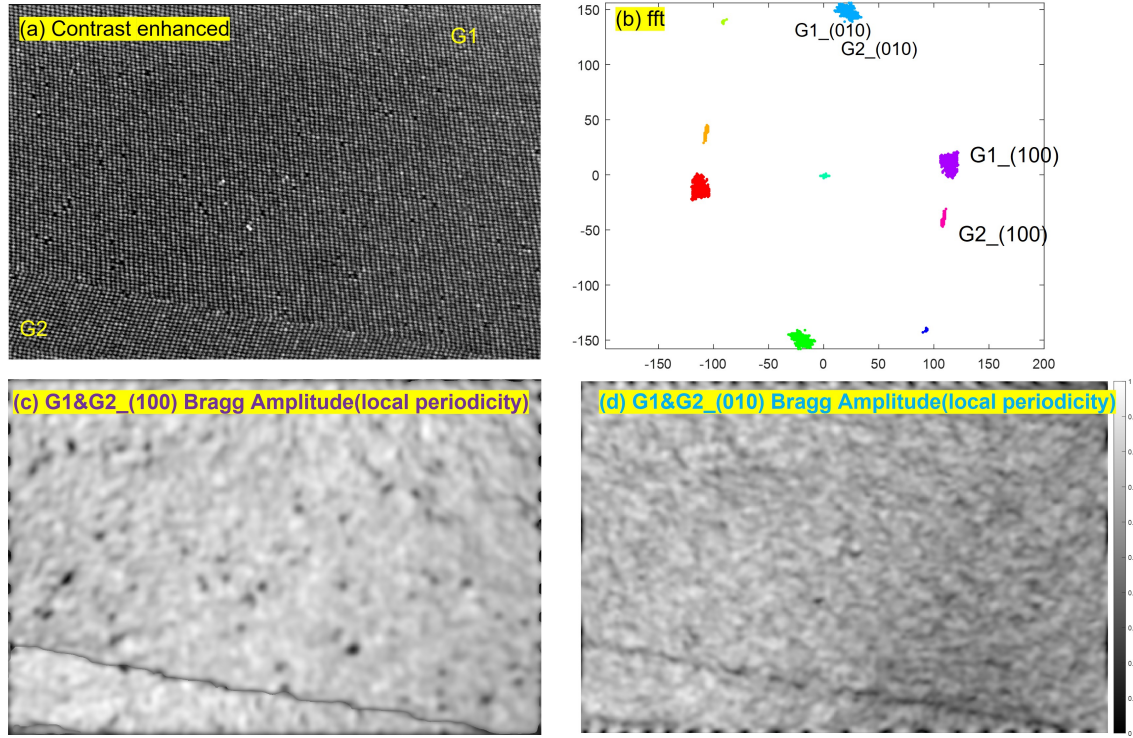


Figure 6.3. Two-dimensional GPA analysis on PbSe epi-SLs. (a) Contrast-enhanced SEM image of the surface of the epi-SLs. (b) FFT of the image with different Bragg spots segmented. (c) The Bragg-filtered image with respect to the $(100)_{SL}$ d-spacing and (d) $(010)_{SL}$ d-spacing

Figure 3 shows the a example of the many decomposed images from GPA analysis with respect to the $[001]_{AL}$. To obtain the 3D displacement field, we need three basis displacement components from 3 designated Bragg Spot identified by the Fourier power spectrum. Then displacement field $u(r)$ is then calculated as

$$\begin{pmatrix} u_x \\ u_y \\ u_z \end{pmatrix} = -\frac{1}{2\pi} \begin{pmatrix} a_{1x} & a_{1y} & a_{1z} \\ a_{2x} & a_{2y} & a_{2z} \\ a_{3x} & a_{3y} & a_{3z} \end{pmatrix} \begin{pmatrix} P_{g1}^* \\ P_{g2}^* \\ P_{g3}^* \end{pmatrix} \quad (6.9)$$

Here \vec{a}_1 , \vec{a}_2 and \vec{a}_3 are real space lattice vectors corresponding to their reciprocal counterparts \vec{g}_1 , \vec{g}_2 and \vec{g}_3 .

$$\begin{pmatrix} a_{1x} & a_{1y} & a_{1z} \\ a_{2x} & a_{2y} & a_{2z} \\ a_{3x} & a_{3y} & a_{3z} \end{pmatrix} = \begin{pmatrix} g_{1x} & g_{1y} & g_{1z} \\ g_{2x} & g_{2y} & g_{2z} \\ g_{3x} & g_{3y} & g_{3z} \end{pmatrix}^{-1} \quad (6.10)$$

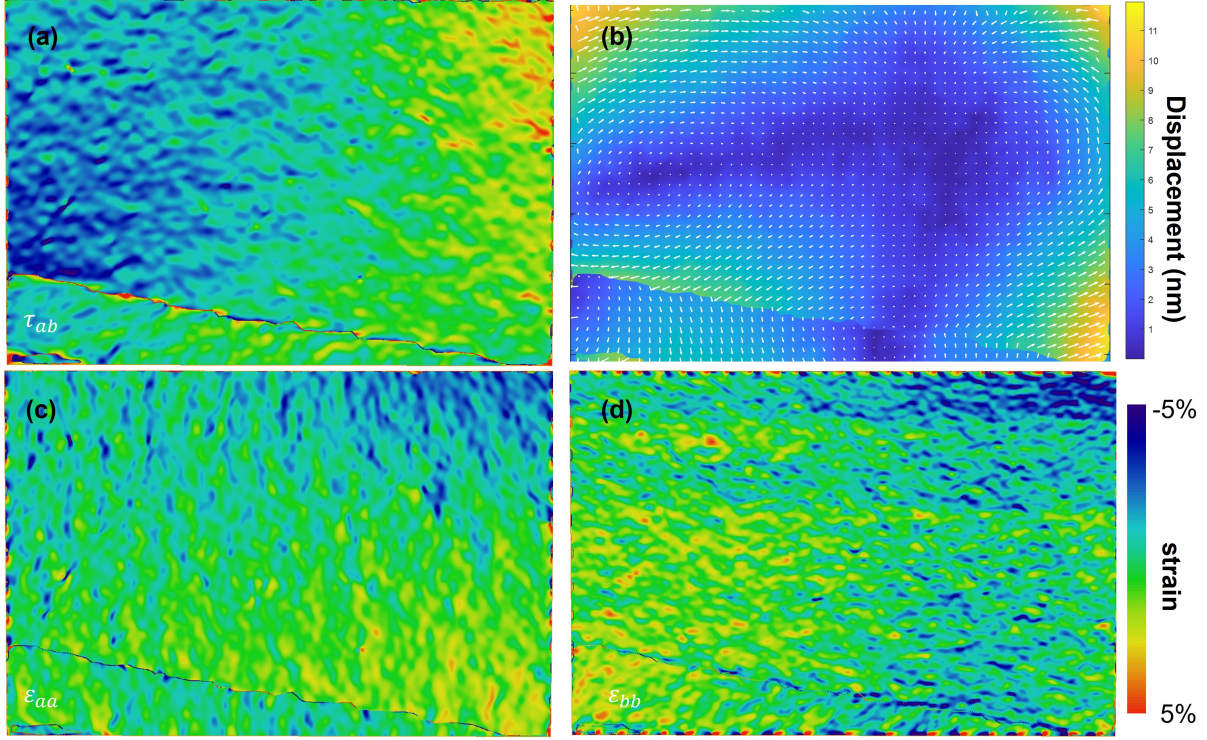


Figure 6.4. Strain and displacement of SLs. (a) Map of shear strain τ_{ab} . (b) The displacement vector field with white arrows representing the direction of the displacement and the underlying color scale represents the magnitude of the local SL displacement. (c) Map of normal strain ε_{aa} and (d) Map of normal strain ε_{bb} .

The total displacement vector field can be derived such that

$$\vec{u}(\vec{r}) = -\frac{1}{2\pi} [P_{g1}(\vec{r})\vec{a}_1 + P_{g2}(\vec{r})\vec{a}_2 + P_{g3}(\vec{r})\vec{a}_3] \quad (6.11)$$

The strain field is then calculated through taking gradient of the displacement field,

$$e = \begin{pmatrix} e_{xx} & e_{xy} & e_{xz} \\ e_{yx} & e_{yy} & e_{yz} \\ e_{zx} & e_{zy} & e_{zz} \end{pmatrix} = \begin{pmatrix} \frac{\partial u_x}{\partial x} & \frac{\partial u_x}{\partial y} & \frac{\partial u_x}{\partial z} \\ \frac{\partial u_y}{\partial x} & \frac{\partial u_y}{\partial y} & \frac{\partial u_y}{\partial z} \\ \frac{\partial u_z}{\partial x} & \frac{\partial u_z}{\partial y} & \frac{\partial u_z}{\partial z} \end{pmatrix} \quad (6.12)$$

$$\varepsilon = \frac{1}{2} \{e + e^T\} \quad (6.13)$$

6.3.3 2D GPA Analysis on Superlattices

The PbSe epi-SLs form cubic-to-triclinic crystal structures in the nanometer length scale. The surface of the 3D SLs is identified either as the $[100]_{SL}$ or $[01\bar{1}]_{SL}$ lattice planes. Therefore, two-dimensional GPA analysis can be applied to SEM images to study the structural disorder

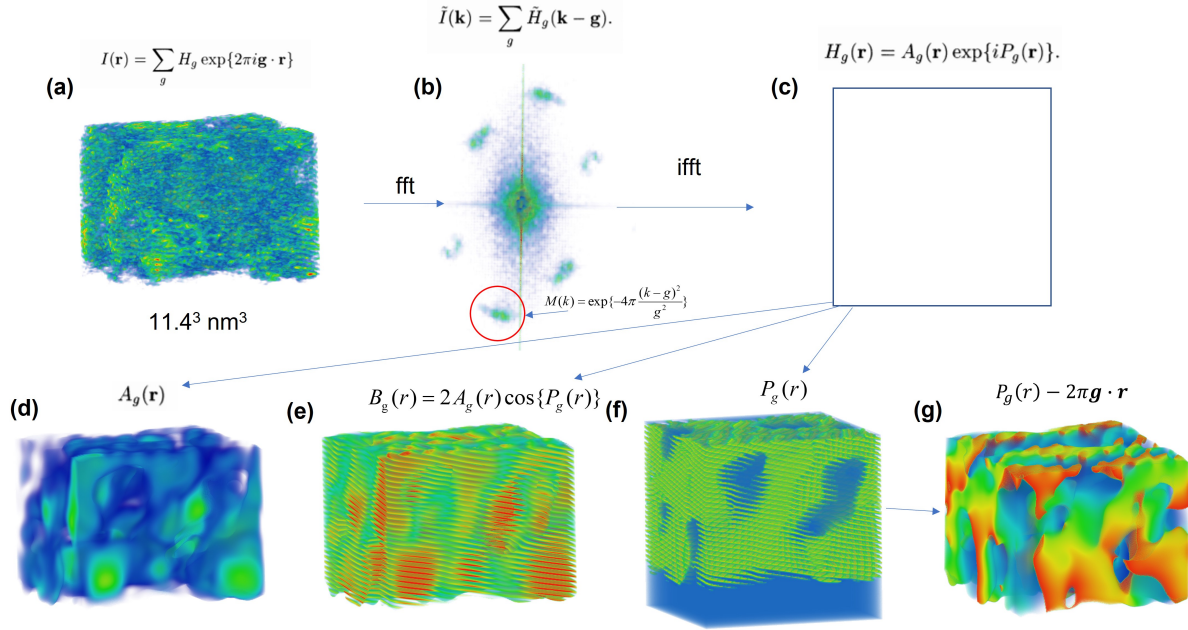


Figure 6.5. 3D GPA processing of a tomogram.

such as break of local periodicity, grain boundary and strain field. Figure 6.4a and b shows an SEM image of the epi-SLs and the relevant diffraction spots are extracted and highlighted in Figure 6.3(b). We select the base Bragg spots corresponding to the $[100]_{SL}$ and $[010]_{SL}$ d-spacing for SLs of $[100]_{SL}$ orientation. Similarly, the essential Bragg spots will be for $[100]_{SL}$ and $[01\bar{1}]_{SL}$. Figure 6.3 (c) and (d) shows the Bragg amplitude images $A_g(\vec{r})$ that indicates the local SL periodicity for the corresponding SL direction. In these images, we can observe a clear darker line marking the grain boundary between the two grains, indicating a break of local SL periodicity. Darker spots in $A_g(\vec{r})$ are also indicators of SL point defects such as missing dots. This can be useful in quantitatively evaluating surface point defect density by sampling a larger area through acquiring and concatenating multiple SEM images. From phase difference images $P_g^*(\vec{r})$, displacement vector fields $\vec{u}(\vec{r})$ can be obtained to produce quantitative assessment of the magnitude and direction of the middle to long range superlattice distortion. Structural disorders such as meandering and SL column tilting can be characterized with this method. Figure 6.4(b) shows the overall SL displacement field for the examined area and clearly indicates the propagation of continuous SL distortion that are likely related to mechanical perturbation during the ligand exchange process. As illustrated in Figure 6.7, the same GPA technique can

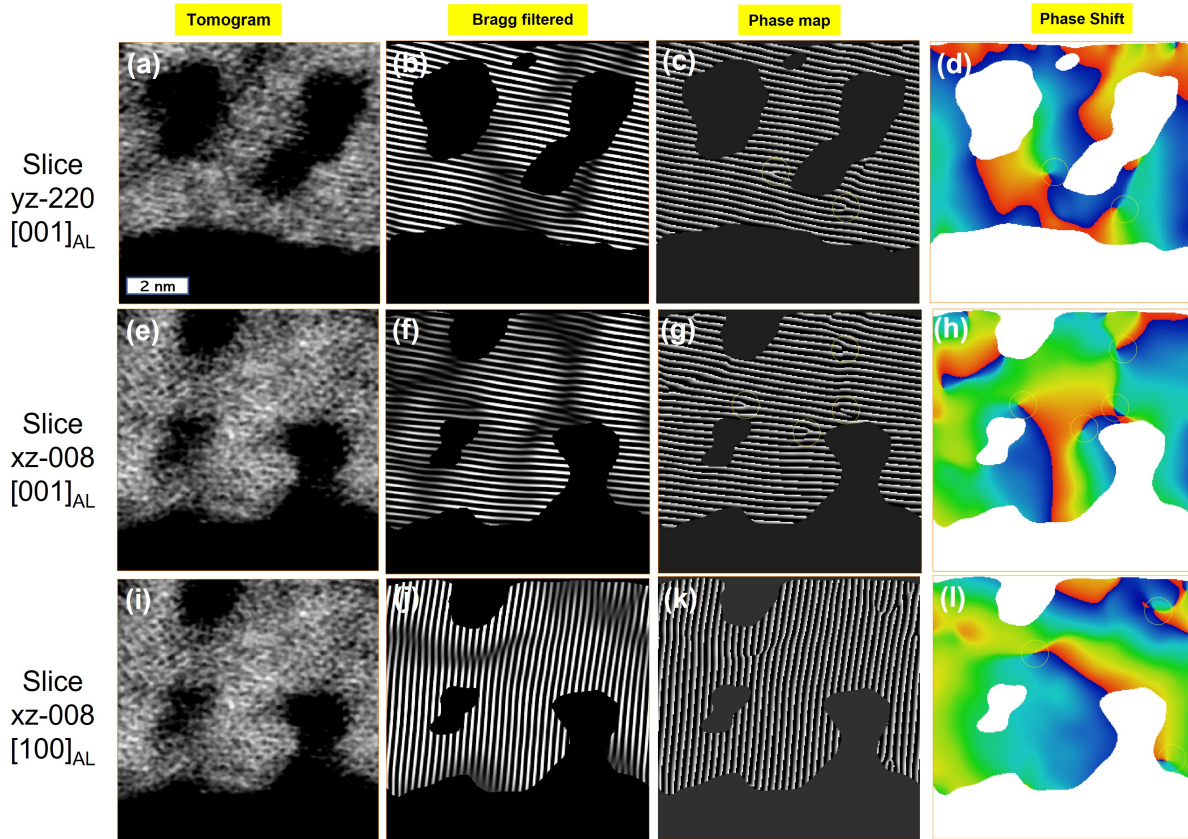


Figure 6.6. Slice view of the tomogram before and after the GPA processing. Panels in the first column are slices of the original tomogram. Panels in the second column are from Bragg-filtered tomogram. The third column includes phase maps and the fourth column includes phase shift maps.

be extended to 3D tomograms containing periodic atomic or mesoscopic features, producing similar auxiliary images(volumes) for quantitative structural analysis, including 3D FFT power spectrum, 3D Bragg Amplitude, 3D Bragg filtered, 3D Phase differences, etc. Depending on the Bragg spot of interest, the corresponding atomic fringes will be highlighted in the tomogram and local distortion of the fringe is also preserved with a precision that is affected by the size of the Gaussian filter applied around the Bragg spot. To better illustrate the result of 3D GPA on a tomograe, we show in Figure 6.6 slices of the original reconstruction compared with post-GPA-processed ones. In this instance, the 001_{AL} Bragg spot is isolated from other diffraction signals. Therefore, the 001_{AL} fringes are highlighted in the Bragg filtered volume, in which the variation of the brightness represents the local intensity of the periodicity of the $[001]_{AL}$ lattice planes. It is obvious that where the lattice plane is deformed, the intensity decreases. The phase

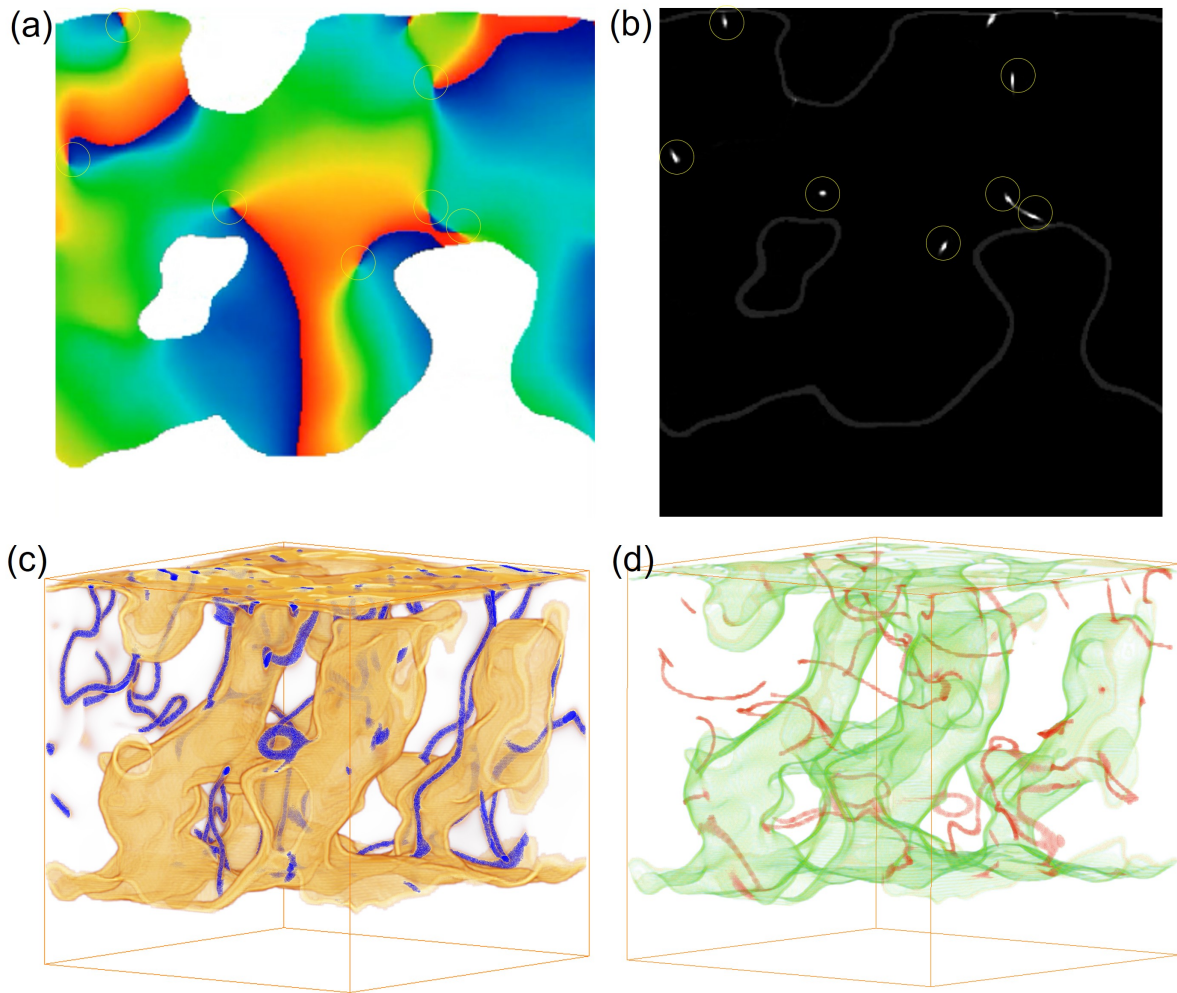


Figure 6.7. Detection of dislocation lines. (a) Phase shift map. (b) Processed with phase variance algorithms. The bright spots are where phase singularities (dislocation cores) are found. (c) 3D map of (001) misfit dislocation line colored in blue and the surface of the bulk material is colored in gold. (d) (010) misfit dislocation line.

map simply shows the extracted lattice planes without the intensity variation, while phase shift is generated by subtracting a reference phase map from the phase image. To investigate atomic defects in the 3D volume, we interpret the half planes in the phase map to be edge/screw dislocation defects in the material. We have marked the dislocation cores in both the phase and the phase shift map in Figure 4. We must always remember that the dislocation core is always migrating while we view the volume slice by slice. It is therefore feasible to detect the dislocation line (trajectory) by identifying the dislocation cores from iterating over all 2D slices. To achieve this, we have utilize the feature of dislocation core in the phase shift map, in which the

cores are surrounded by a full $0-2\pi$ change of phase difference. In another word, the circular line integration around the dislocation core yields 2π . To detect dislocation core, or phase singularity as a more general term, we treat each slice by calculating the phase variance of each pixels.[118] The phase variance is defined as,

$$V = 1 - \left| \frac{1}{N} \sum_g e^{j\theta_k} \right| \quad (6.14)$$

where N is size of the kernel and is usually taken as $3*3$ and θ_k is the phase shift.

In Figure 5, we show that the dislocation cores are found where the phase variance is at local maximum. This calculation can be applied conveniently to the entire volume to trace the dislocation line (DL). In Figure 5(c) and (d), we show the identified DL for $[002]_{AL}$ and $[020]_{AL}$ misfit respectively. One observation is that all DLs start or end at the material surface. This is a reasonable phenomena from the energy perspective. Regarding the orientation of the DLs, the $[002]$ misfit DL tend to be perpendicular to the $[002]_{AL}$ lattice planes and the $[020]$ DL be perpendicular to the $[020]_{AL}$ planes. Although we don't have a specific answer to this observation, it is possibly tied to the oriented attachment mechanism of PbSe QDs.

Appendix A

**Supporting information for “Structural
Characterization of Superlattice Disorder
of PbSe epi-SLs by Electron Tomography”**

Table A.1. Preliminary Profilometer thickness measurements of thin films deposited from same processing conditions and at the time the NR films were made.

Film	Layer	Thickness (nm)
Multilayer film	1st layer	75 ± 4
	2nd layer	39 ± 4
	3rd layer	47 ± 2
	4th layer	32 ± 4
Single Layer P3HT Film	NA	187 ± 8

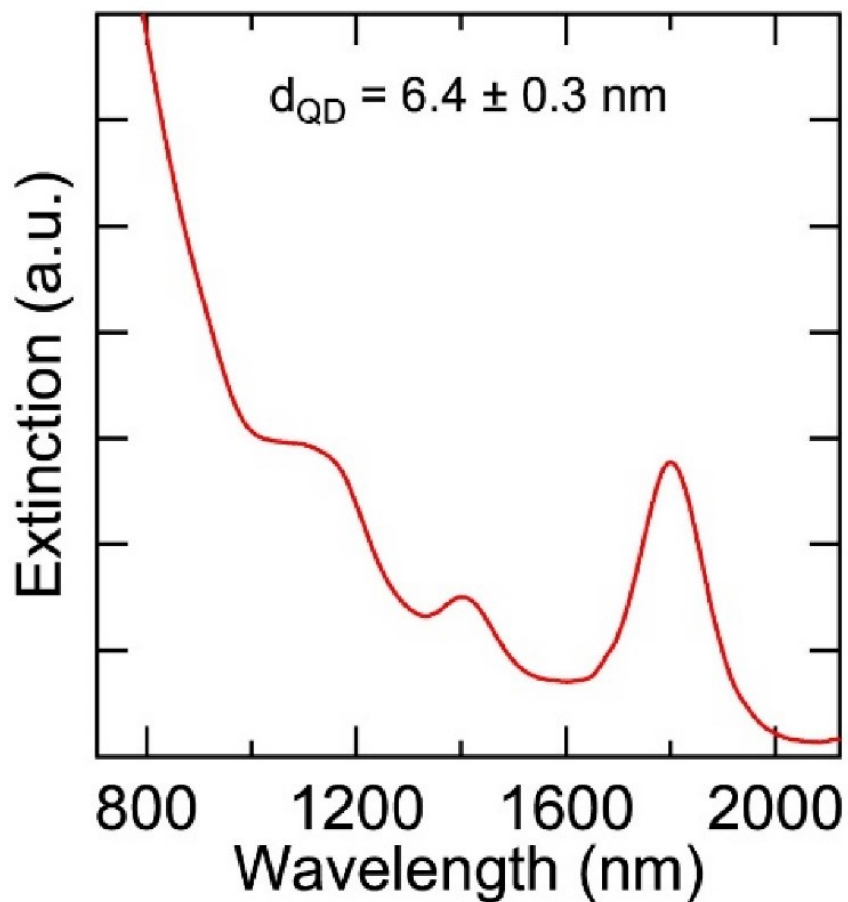


Figure A.1. UV-vis extinction spectrum of colloidal PbSe QDs dispersed in tetrachloroethylene. The average QD diameter (6.4 nm) and standard deviation (0.3 nm) was determined using the empirical relationship by Moreels et al.

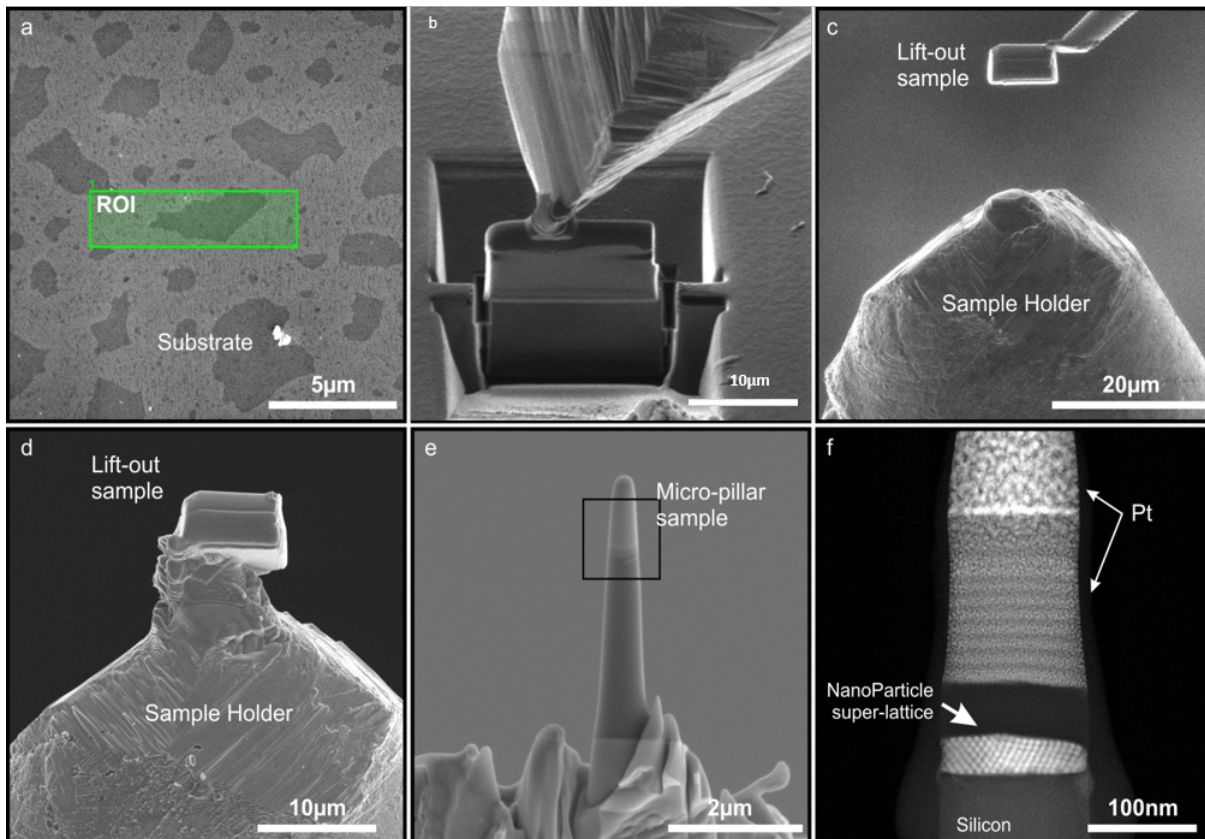


Figure A.2. Steps of FIB tomography needle preparation. (a) The region of interest (ROI) is selected. (b) After carbon and platinum deposition, a wedge is FIB milled and attached to a lift-out probe by ion beam welding. (c) The wedge is transferred to the tip of a sample holder for needle tomography samples. (d-e) The wedge is FIB milled into a needle shape. (f) HAADF-STEM image of the finished needle, with layers labeled.

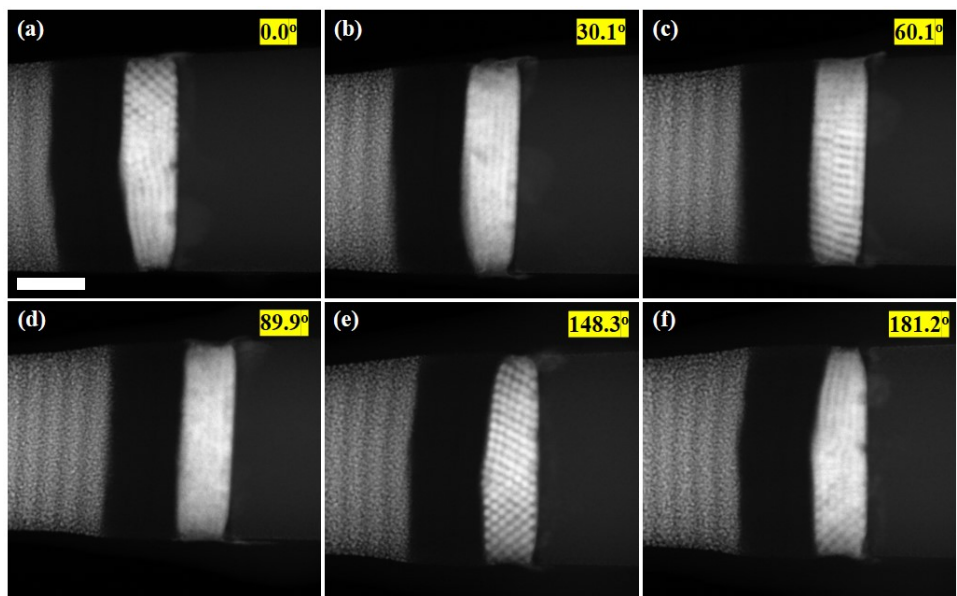


Figure A.3. Six of the 181 images of the HAADF-STEM tilt-series, with tilt angles labeled.

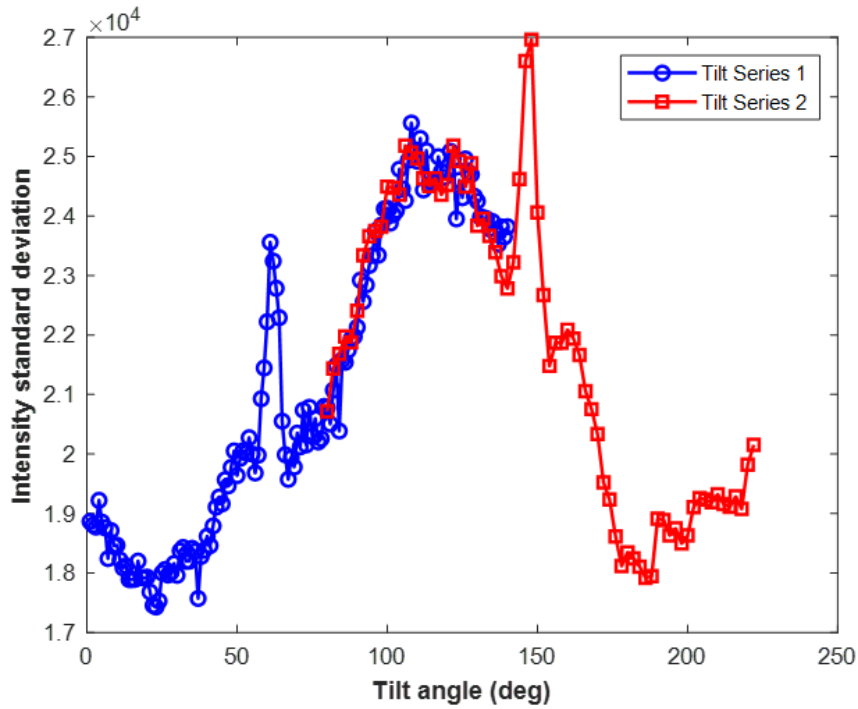


Figure A.4. The entire projection tilt series set is obtained by merging two separately acquired tilt series. Since the ex-situ rotation angle of the holder is not precisely controlled, there is a redundant portion in tilt series 2 that repeats some of the tilt angles that are already sampled in tilt series 1. This overlapped portion is determined by monitoring the standard deviation of the intensity distribution of each image. This value varies as the sample is projected at different tilt angles. The overlapped portion is removed from series 2 and the non-redundant images are attached after series 1 to make the whole tilt series for tomographic reconstruction. The two sharp peaks occur at tilt angles for which the SL axes are inadvertently aligned along the electron beam direction.

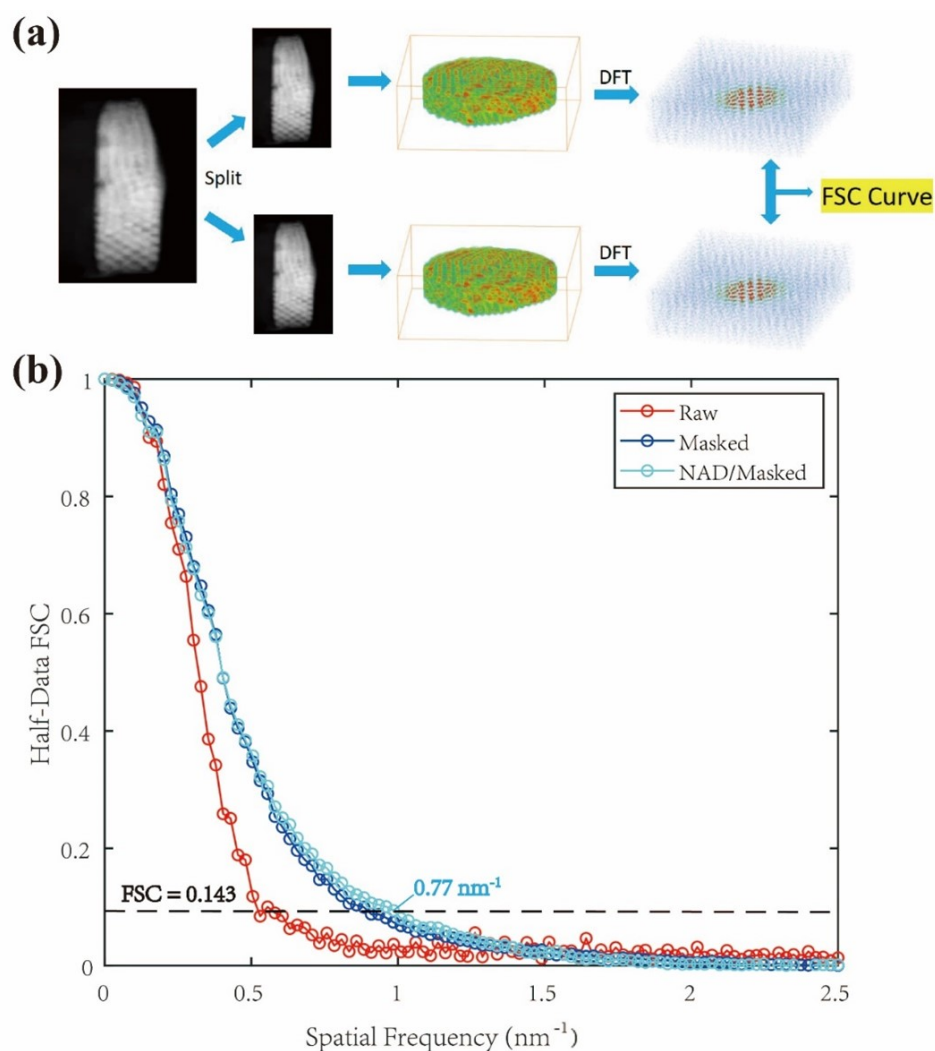


Figure A.5. (a) To conduct Fourier Shell Correlation, the 2D projection images are split into two subsets, with odd-indexed images in one set and even-indexed images in the other. This is to ensure that both subsets are mutually exclusive but still cover the entire tilt angle range. The halves are independently aligned and reconstructed using SIRT and the spatial frequency information is extracted through 3D Discrete Fourier Transformation of the half reconstructions for evaluating correlation.⁴ (b) Fourier Shell Correlation data between the two reconstructed halves as illustrated in Fig. S5a. In the “masked” data, the voxel intensity is set to zero if it is $\geq 2\sigma$ from the mean of the Gaussian-fit intensity distribution of the QDs in the reconstruction. The FSC threshold value is selected to be 0.143.⁶ When the correlation is above the threshold, the orthogonal reconstructions share common structural features that stand out from random noise at the corresponding spatial frequency $f_c = 0.77\text{nm}^{-1}$. Thus the resolution of the half reconstruction is $r_c = 1/f_c = 1.3\text{ nm}$. The other set was reconstructed using the non-linear anisotropic diffusion filter and does not exhibit significant decrease of the resolution. The resolution of the full data set with both odd and even indexed images evaluated to be $r_c = 1/(2f_c) = 0.65\text{ nm}$.

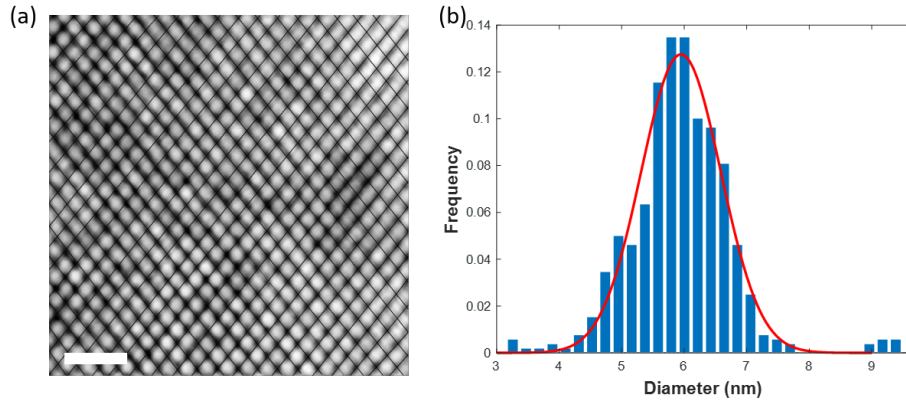


Figure A.6. The diameter of the QDs is determined by analyzing conventional STEM images of the SLs. (a) A program is used to isolate each QD from its connected neighbors and calculate the effective diameter of the dot. The scale bar is 20 nm. (b) The result of QD size distribution from image analysis. The red line is a Gaussian fit to the histogram.

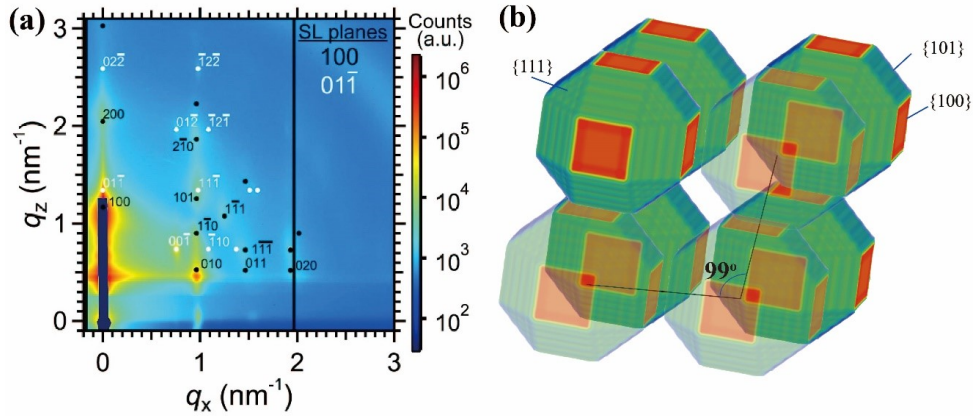


Figure A.7. (a) Grazing incidence small-angle X-ray scattering pattern of the film used in this study, overlaid with calculated diffraction patterns from (100)- and (01 $\bar{1}$)-oriented epi-SL planes (the most prominent SL orientations) with SL unit cell lattice parameters $a = 6.6$ nm and $\alpha = 99^\circ$. (b) Model of the epi-SL showing fusion along PbSe{100}. Additional details of the structure can be found in Ref 6.

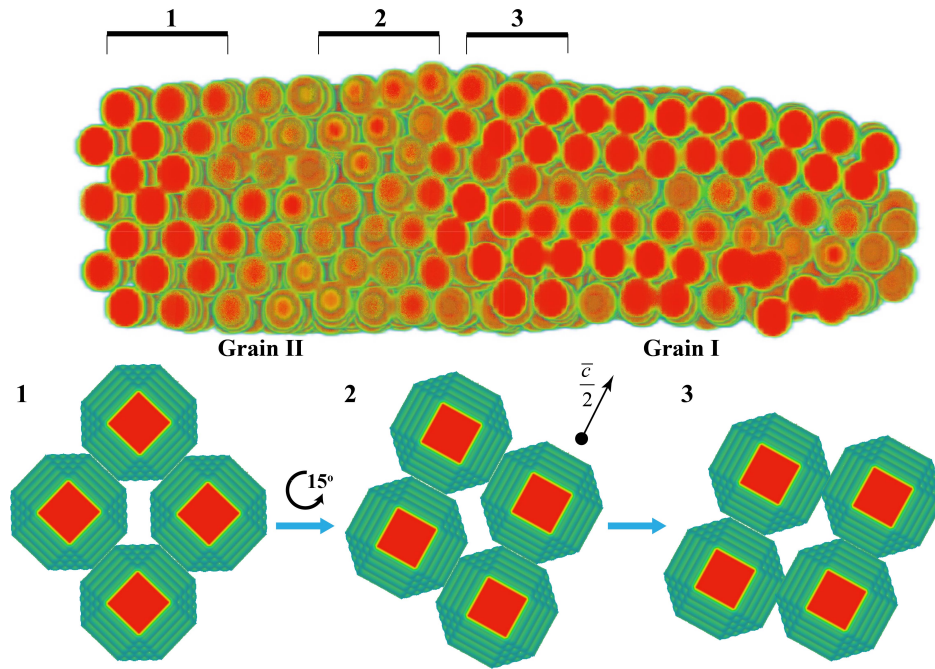


Figure A.8. Proposed mechanism for SL structure transition from grain II to grain I. The SL structure in the far left end (region 1) undergoes a slight tilt of 15 degrees from near-perfect $(011)_{SL}$ orientation as the structure propagates to the right into region 2. A glide of $(100)_{SL}$ plane occurs in between region 2 and 3 that can be effectively considered as if the orientation of SL changes 90 degrees counter-clockwise. Such process may potentially also alter the β angle, explaining our statistics shown in Table 1.

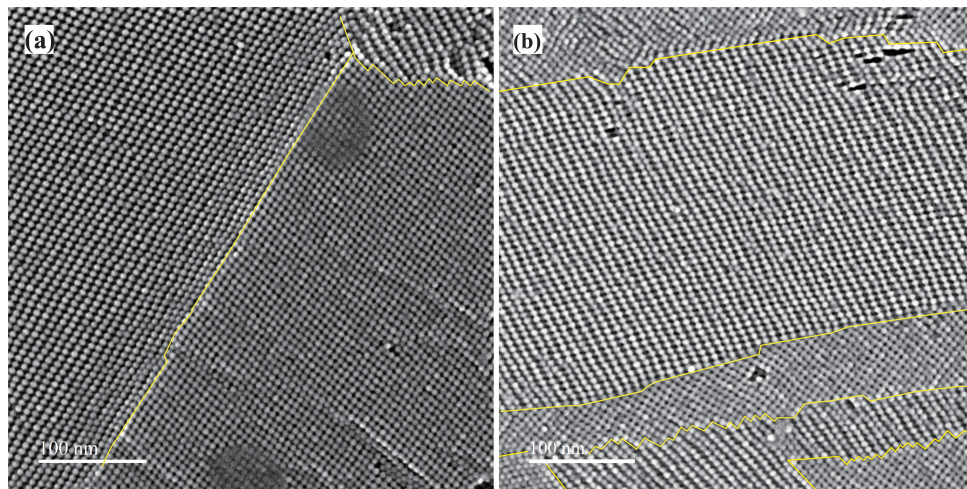


Figure A.9. Plan-view SEM images of grain boundaries of the SL sample, showing the structure of these GBs. (a) A tricrystalline region that is similar to the tomography sample. (b) Corrugated grain boundaries between $(100)_{SL}$ -oriented and $(011)_{SL}$ -oriented grains. Scale bars are 100 nm.

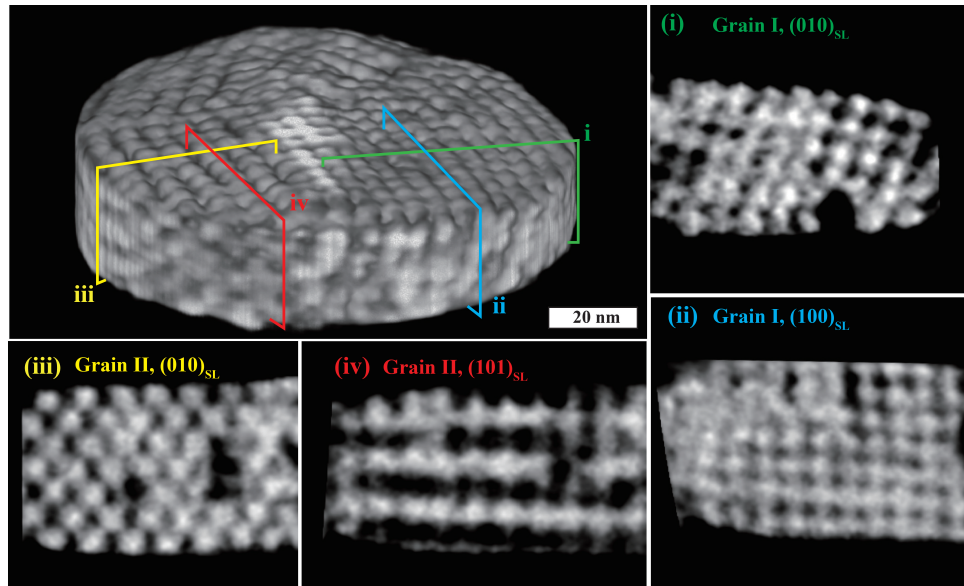


Figure A.10. Regional slices of the tomogram showing arrangements of the QDs and the necks in grain I (i,ii) and II (iii,iv). The bisecting planes are annotated as plane (i-iv) which indicated the position of the respective slices and also represent different lattice planes indexed in the corresponding small panels for different grains. Plane (i) and (iii) are parallel to each other, as well as plane (ii) and (iv). All panels share the same scale bar.

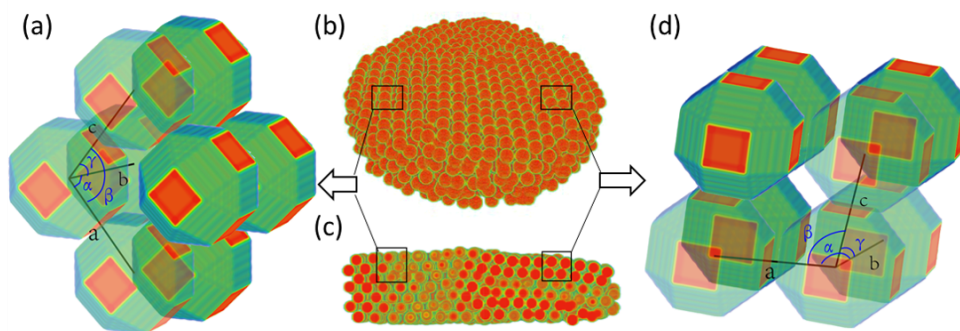


Figure A.11. The epi-SL can be reconstructed with QDs represented by spheres of identical size positioned according to the CoM data. (b) Perspective and (c) cross-sectional views of the sample with the QDs represented by perfect spheres. (a,d) Labeling conventions for assigning lattice parameters to grain I and II, respectively. Red planes correspond to the 100 facets.

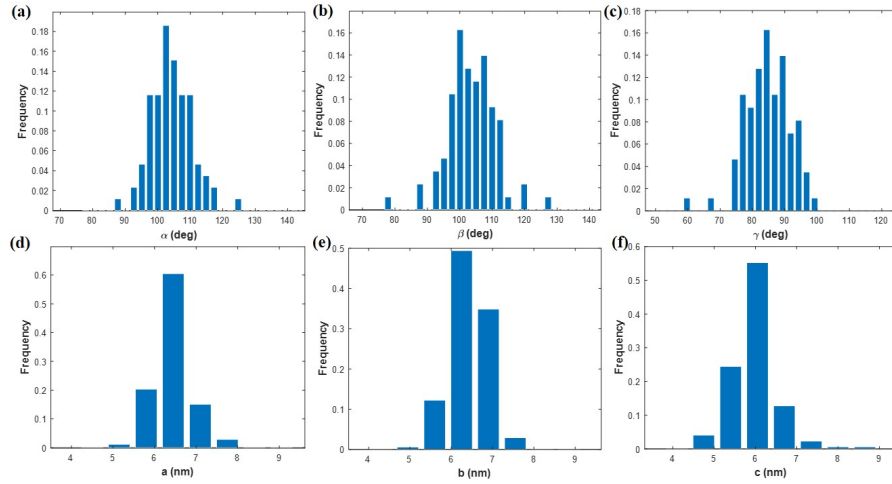


Figure A.12. Histograms of SL lattice parameters in grain I, including (a-c) lattice angles α , β and γ , and (d-f) lattice spacing a, b and c.

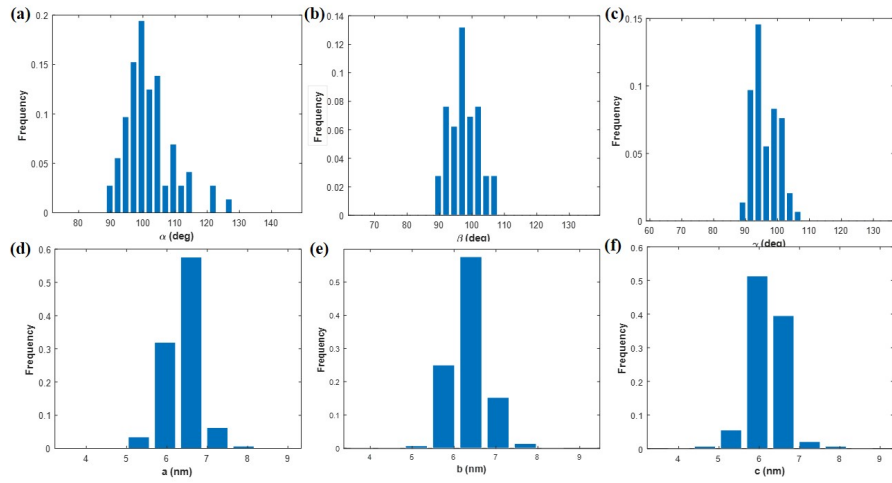


Figure A.13. Histograms of SL lattice parameters in grain II, including (a-c) lattice angles α , β and γ , and (d-f) lattice spacing a, b and c.

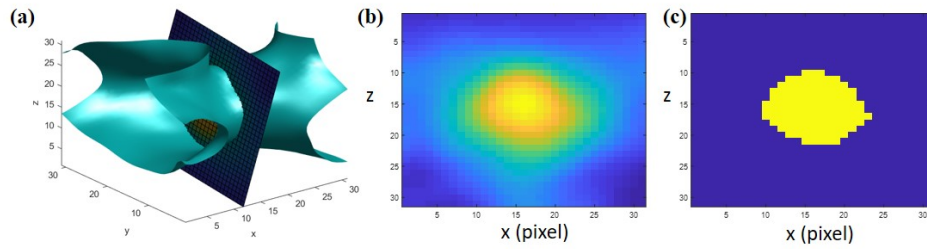


Figure A.14. An illustration of how the neck diameter is determined. In (a), two necked QDs are shown in iso-surface form. A plane is generated such that it is perpendicular to the vector between the centers of mass of the necked QDs. This plane is then allowed to slide along this vector to locate the minimum area of the neck. (b) Image of this plane at the neck minimum. Using a threshold value (the same value for the masking reconstruction in Fig. S5), (b) is reduced to (c) to estimate the neck shape and area. The neck diameter is calculated as the effective diameter of the neck area.

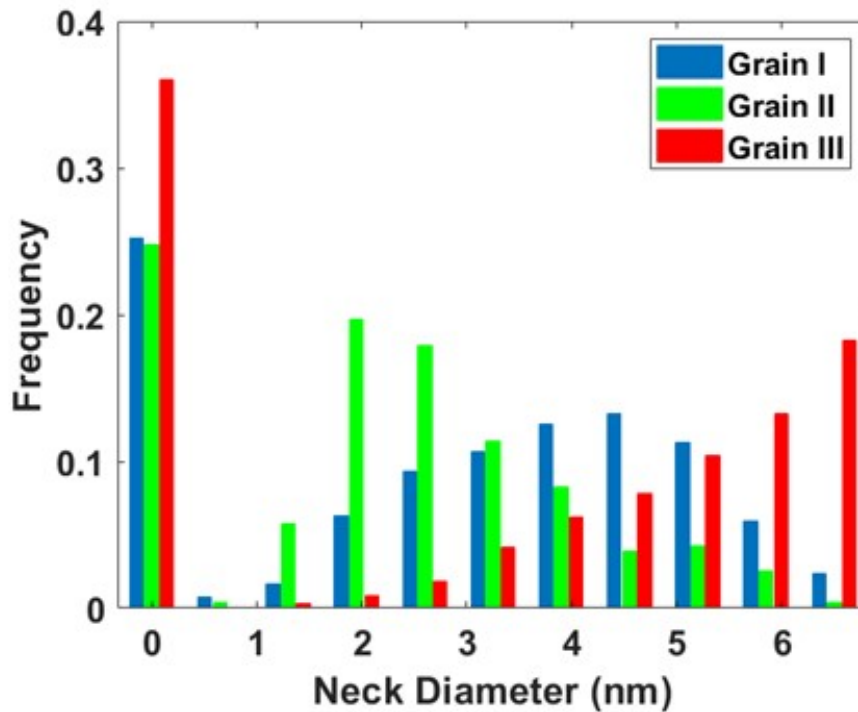


Figure A.15. Histograms of diameters of each individual neck characterized from each of the three grains. Zero diameter represents a “missing neck”.

Neck number heat maps

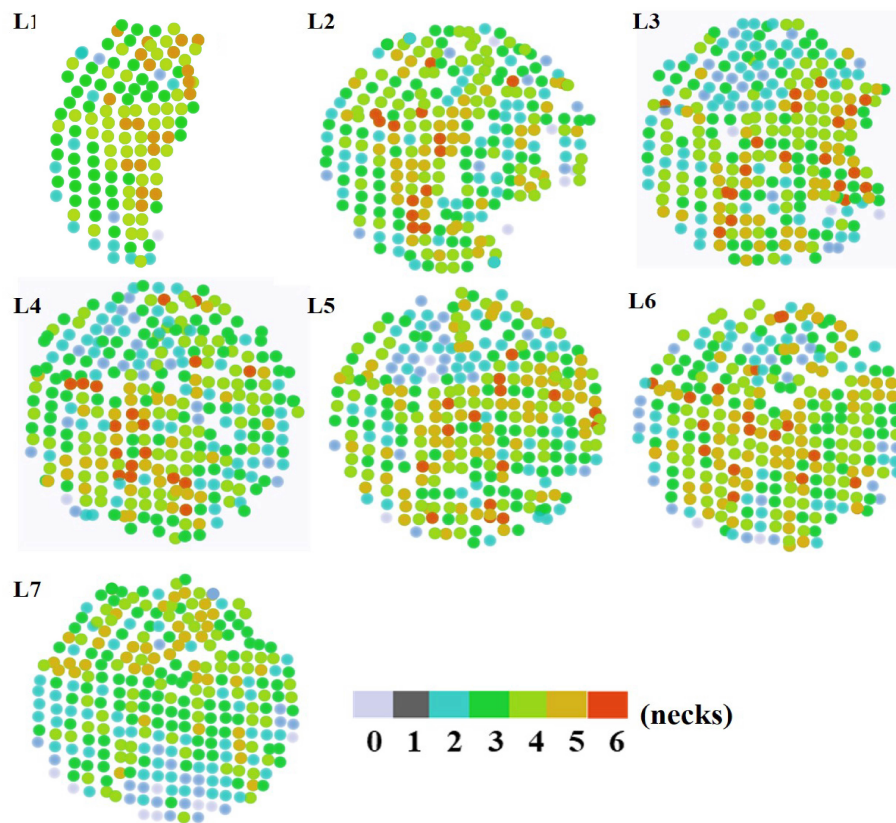


Figure A.16. Heat maps of the neck number for each QD in the sample. Each circle represents a QD in L1-7.

Neck diameter heat maps

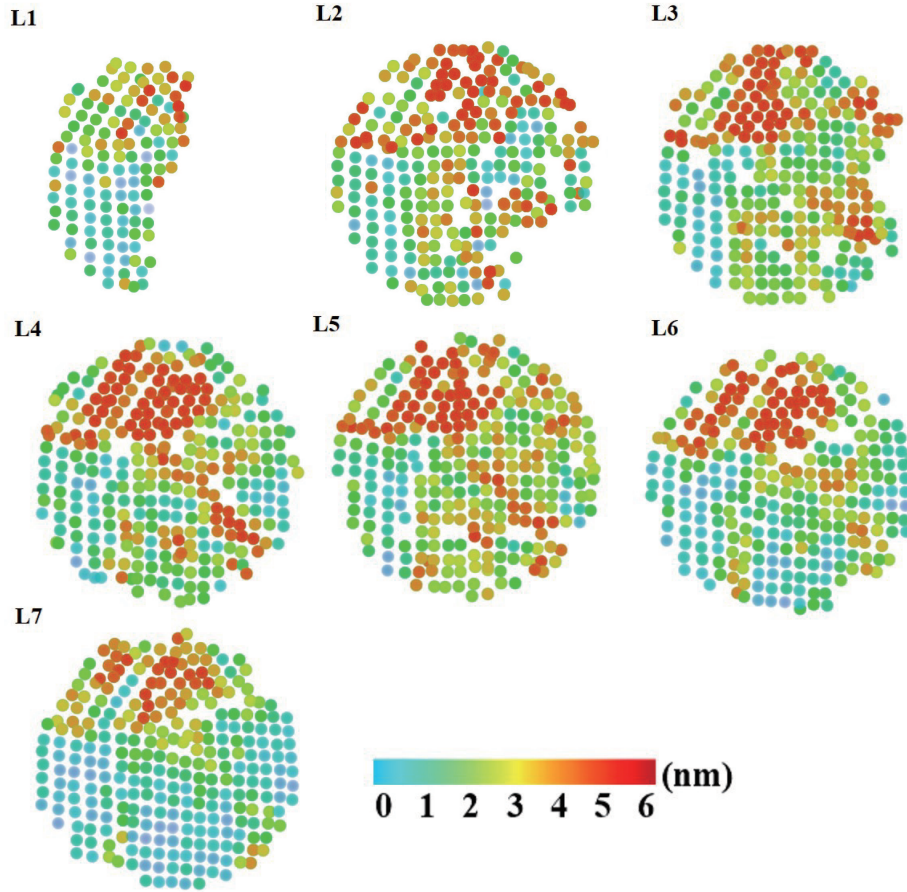


Figure A.17. Heat maps of the average neck diameter for each QD in the sample. Each circle represents a QD in L1-7.

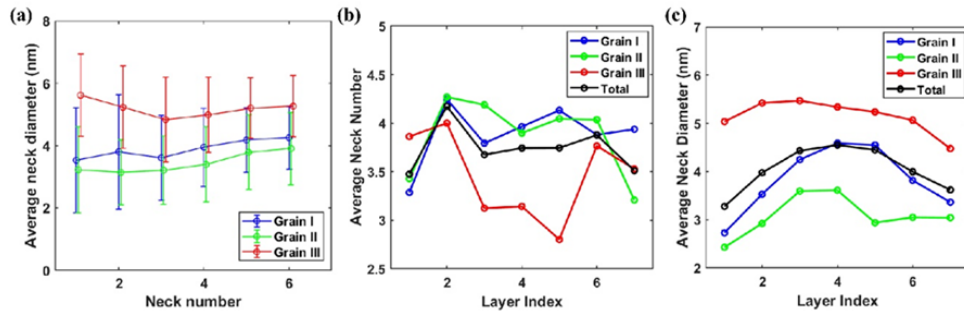


Figure A.18. (a) Average neck diameter as a function of neck number for each QD in grains I, II, and III. Error bars denote one standard deviation. (b) Average neck number for each QD layer in the tomogram. Layer 1 is the top of the epi-SL (QD/gas interface) and Layer 7 is the bottom of the epi-SL (QD/liquid interface). (c) Average neck diameter for each QD layer.

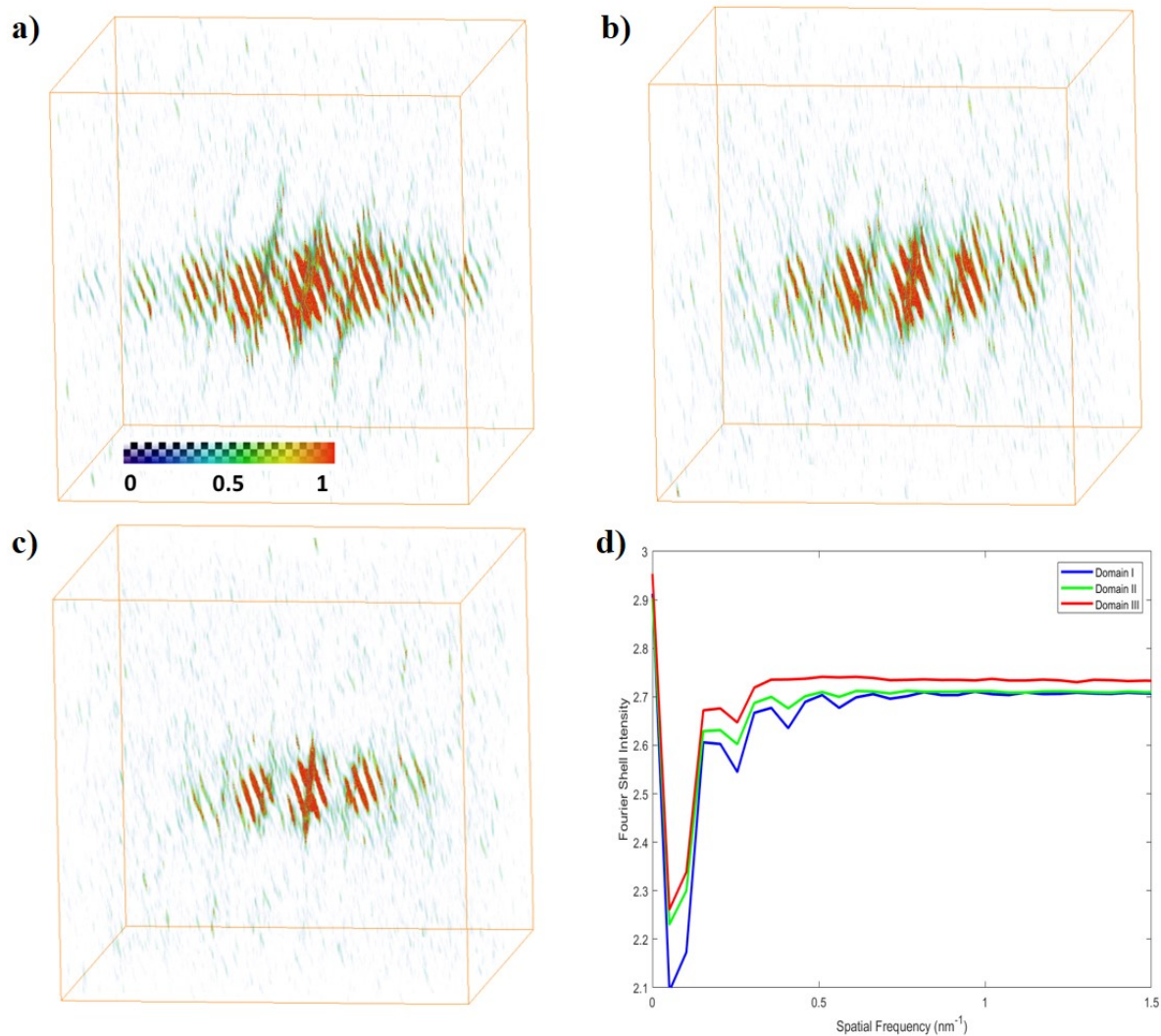


Figure A.19. (a-c) Separate 3D Fourier transformations of (a) grain I, (b) grain II and (c) grain III. (d) Fourier Shell Intensity comparison between the three grains. Both grain I and grain II show structural features at high spatial frequency, while grain III lacks fine feature at sub-QD length scales ($< 6 \text{ nm}$).

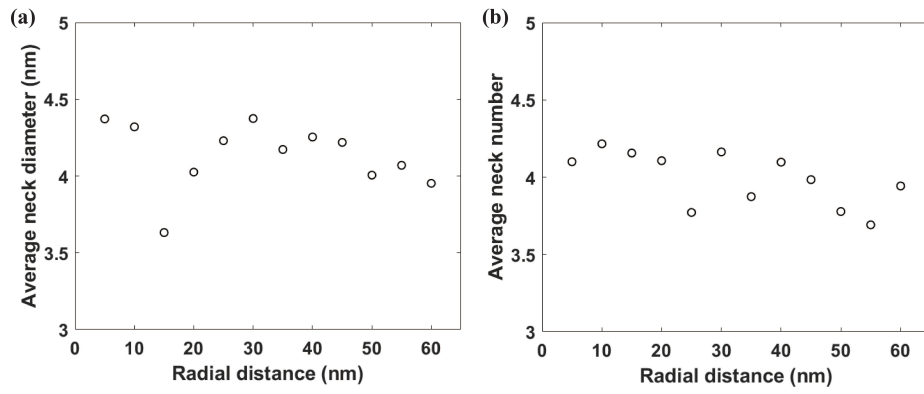


Figure A.20. Radial distribution of (a) average neck diameter and (b) average neck number.

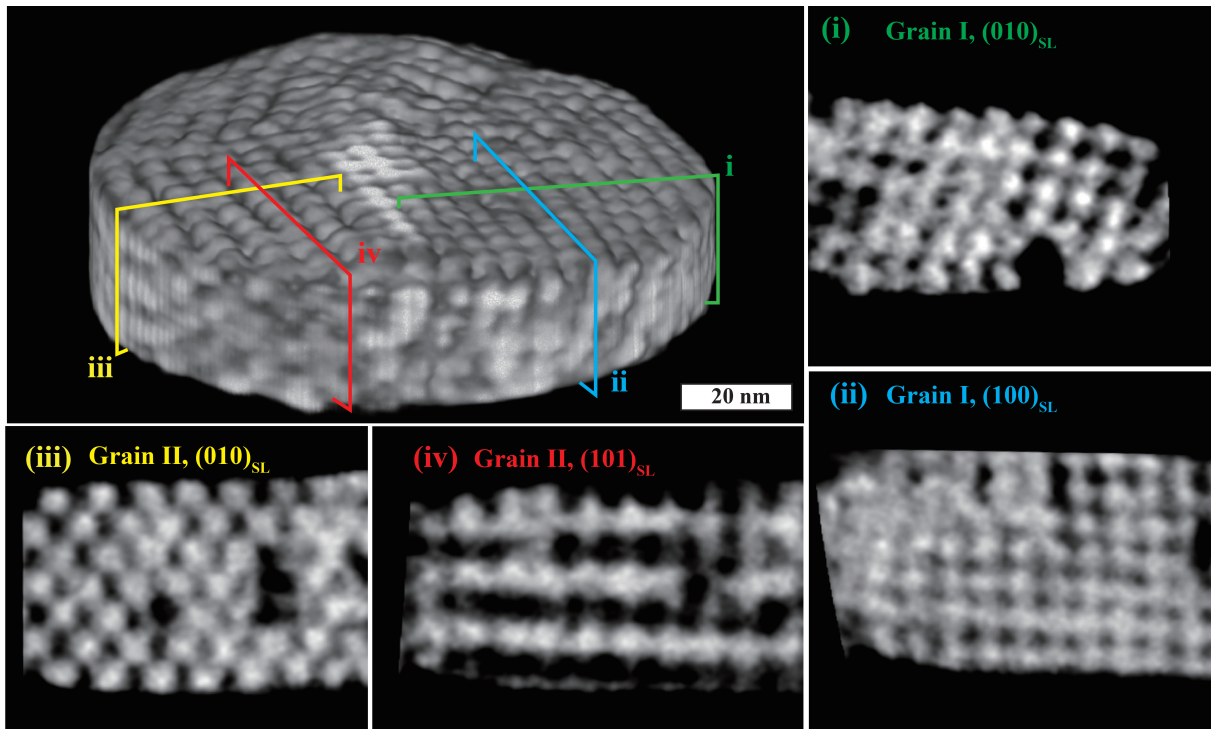


Figure A.21. Radial distribution of (a) average neck diameter and (b) average neck number.

Appendix B

**Supporting information for “Near-Atomic
Electron Tomography Study on the
Orientation Disorder of PbSe epi-SLs”**

B.1 Sample Preparation and Tomography Reconstruction

An area of the epi-SL film suitable for FIB milling was located by SEM and several images of different magnifications were taken with the pre-deposited Au arrays as fiducial markers for later relocating the area of interest. The sample was then coated with 50 nm of carbon using the pulse plasma mode of a Leica ACE200 evaporator and returned to an FEI Quanta 3D FEG DualBeam microscope for FIB milling, lift-out, and final needle sample preparation. Prior to milling, a 200 nm Pt capping layer was deposited onto the carbon-coated sample by EBID, followed by an additional ~ 2000 nm of Pt deposited by ion beam induced deposition (IBID). The carbon layer serves primarily to enhance STEM imaging contrast by separating the epi-SL layer from the high-Z protective Pt capping layer. The area of interest was then FIB milled into a wedge shape ($10\ \mu\text{m} \times 6\ \mu\text{m} \times 2\ \mu\text{m}$), lifted-out with an OmniProbe 400 nanomanipulator, ion welded to the tip of a 1-mm-diameter post for an on-axis rotation tomography sample holder (Fischione Model 2050), and FIB milled again into a ~ 60 nm diameter needle (Fig. S2). Milling was performed in several stages. The wedge was first milled into a pillar shape (1 μm diameter) using a 0.3 nA ion beam at a 30 keV accelerating voltage, then thinned to a ~ 200 nm diameter needle using 50 pA at 16 keV. Finally, a 5 minute ion beam shower (25 pA at 5 keV) was employed to sharpen the needle to ~ 60 nm and remove surface damage. The finished needle contained a disc-shaped epi-SL layer (38 nm tall \times 60 nm in diameter) for tomographic analysis.

We mounted the needle sample on a Fischione Model 2050 single-tilt tomography holder. HAADF images ($4\text{k} \times 4\text{k}$) were then acquired in a JEOL JEM-ARM 300F TEM operated at 300 KeV in STEM mode. The projection stack consisted of 124 images spanning tilt angles over 0 to 193 degrees in roughly 1.5 degree steps. Full-tilt projection image acquisition is conducted because of low tolerance of missing-wedge artifact that potentially introduces smearing of the edge profile in the less-sampled direction, causing artificial attachments between QDs. The image stack is then sequentially aligned based on center-of-mass and common-line approaches.[ref] All 2D and subsequent 3D image processing were conducted in MATLAB unless otherwise noted. The aligned stack was further processed by matching histogram of every two consecutive images to compensate for the brightness instability and then denoised via a Wiener filter for 2 iterations. Tomographic reconstruction was conducted on subsequently using 200 iterations

of simultaneous iterative reconstruction technique (SIRT) in the ASTRA Tool box.[122] The raw reconstruction was downsized so that it consisted of $2048 \times 2048 * 700$ voxels with edge lengths of 0.38 \AA . The downsized reconstruction was smoothed with nonlinear anisotropic diffusion filtering for subsequent structural information measurements. The spatial resolution of this reconstruction was evaluated to be 3.1 \AA by comparing the Fourier power spectra between the actual and the simulated reconstructions.[R]

B.2 Tomogram Analysis

B.2.1 Determination of QD positions and SL vectors

The coordinates of the QDs determines the local superlattice vectors and the collective positions determines the representative super lattice unit cell structure for the examined sample. The QD positions are determined by an Iterative Digital Image Correlation (IDIC) method. First, a cubic subvolume (V_s) containing a representative complete sample QD (usually a volume of $301 \times 301 \times 301$ pixels) is extracted from the entire tomogram V via common volume slicing. A cross-correlation 3D convolution operation is conducted upon the original tomogram using V_s as the convolution kernel. Then 3D local maxima are searched for pooling candidate QD centroids. An Otsu-threshold [ref] cutoff is then applied to screen out unlikely candidate centroids of small correlations and result a centroid set $\{r_c\}$. We then sample a set of subvolumes of the same size as V_s around each centroid in $\{r_c\}$ and calculate the average with equal weights. This is again averaged with previous sample QD V_s to generate a new sample volume V_s^* for the next round of convolution. This process is iterated until the number of QD centroids converges and the mean-square-error cannot be improved further. The entire process usually converges within 15 iterations regardless of the initial QD sample we choose, as indicated in Figure Sxyz. We consider the partial QDs as point defects and exclude them from further analysis because their shape significantly deviate from the regular QDs with an over 50% volumetric loss and their orientation can not be sampled accordingly. Layer C8 shows a particularly larger point defect density of 19.7% compared to other layers (0% \sim 3%) but does not affect the integrity of its adjacent layers.

With the pre-knowledge of cubic-like SL structure, the determination of superlattice vec-

tors begins by pooling the 6 nearest neighbors (NNs) for each QD centroid in the final $\{r_c\}$. Considering not all QDs (peripherals) have 6 $\{100\}_{SL}$ NNs, a cut-off maximum distance of 9 nm is used to ensure the sampling is constrained to $\{100\}_{SL}$ neighbors and a minimum amount of $\{110\}_{SL}$ neighbors. Next, an unsupervised K-MEANS clustering is applied to the NN set to determine the representative $\{100\}_{SL}$ vectors. The average SL unit cell parameters are then calculated with the centroids of the determined clusters.

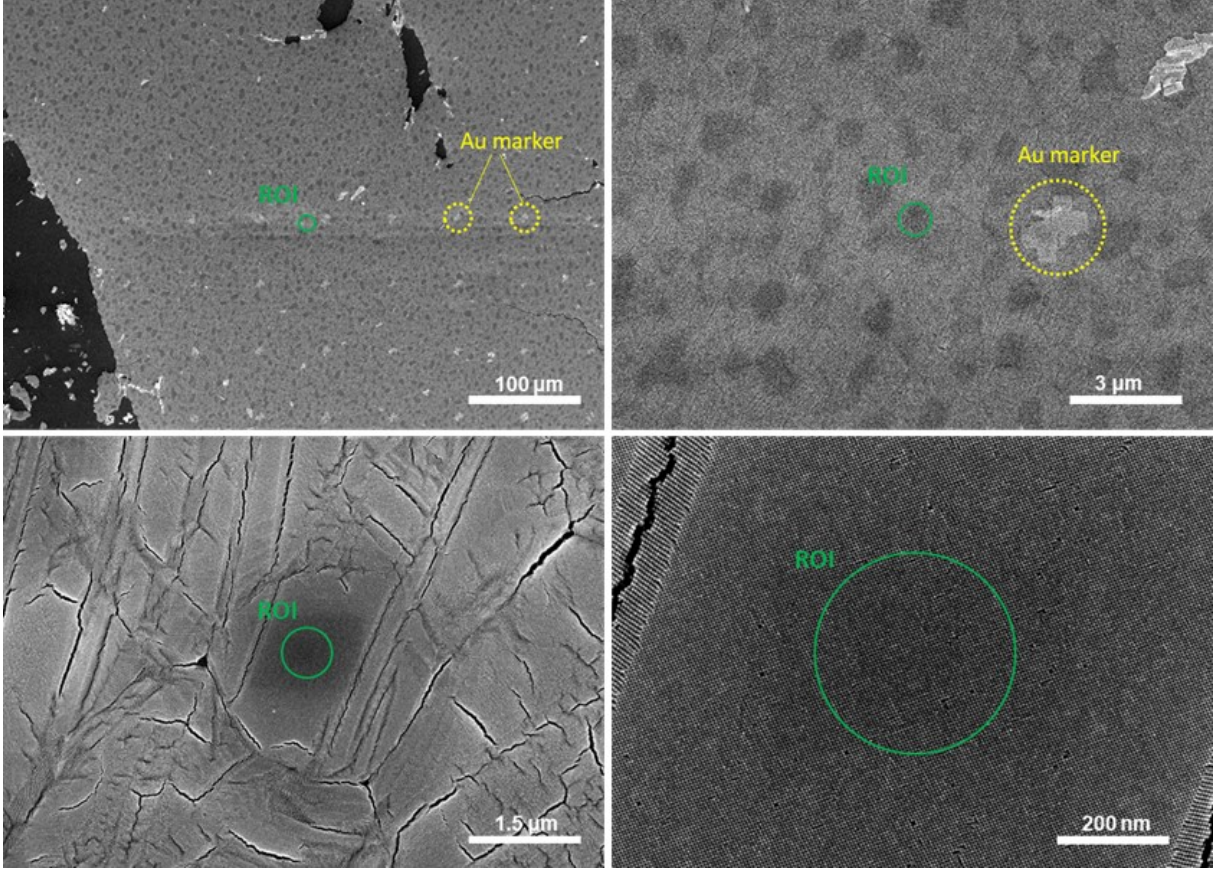


Figure B.1. SEM images of the region of interest (ROI) within a single grain. The Au marker array are deposited onto the substrate before stamping the film. The markers are used to relocate ROI after depositing carbon on top of the film.

B.2.2 Calculating optimal AL orientation from SL basis matrix

First, the SL basis matrix is expressed as

$$R_i^{SL} = \begin{bmatrix} A_x^* & A_y^* & A_z^* \\ B_x^* & B_y^* & B_z^* \\ C_x^* & C_y^* & C_z^* \end{bmatrix}_i \quad (\text{B.1})$$

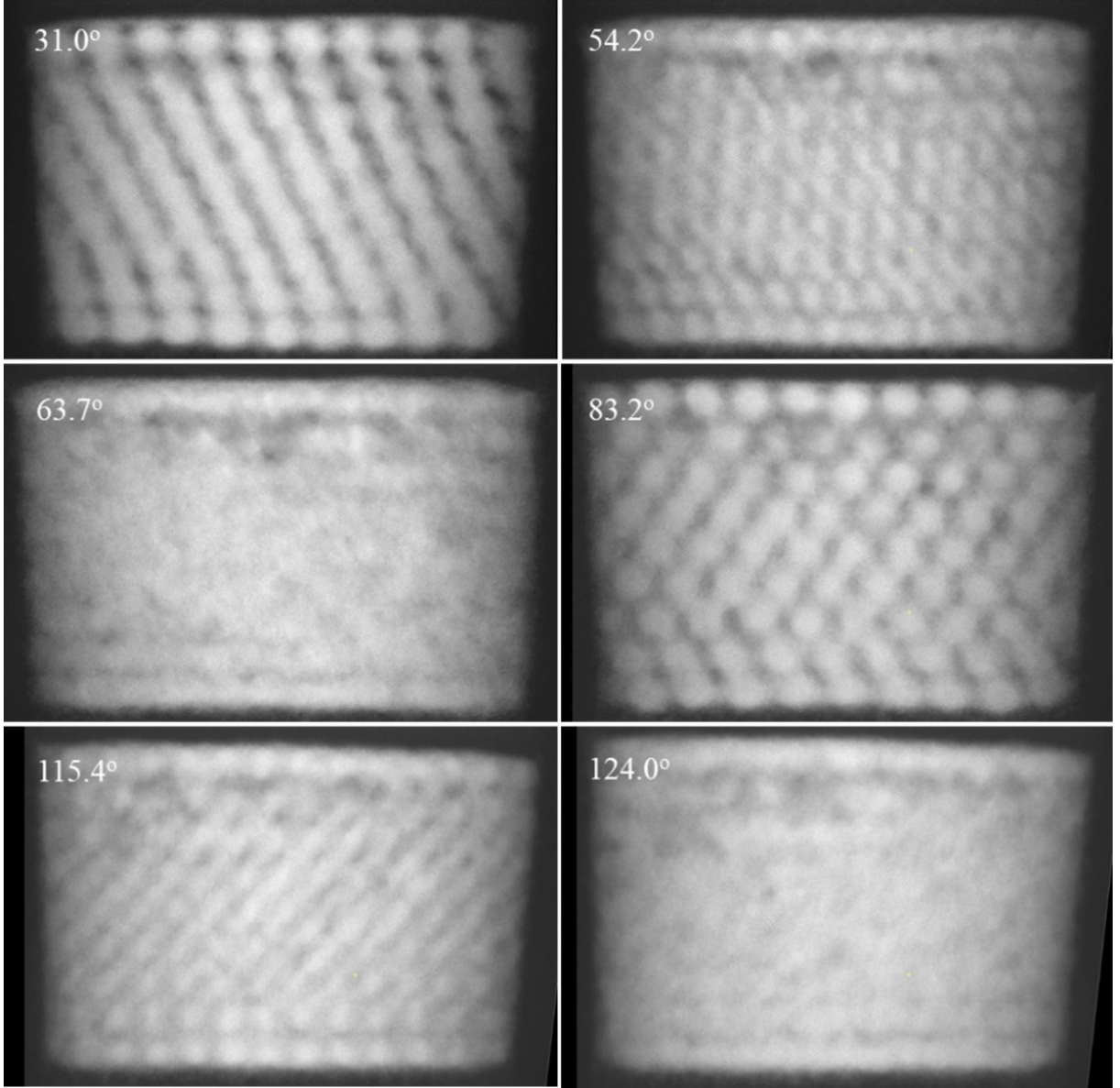


Figure B.2. Selected HAADF projection images from the tilt-series.

where $[A_x^*, A_y^*, A_z^*]$ is the normalized local $[100]_{SL}$ vector $\vec{A}_i/|\vec{A}_i|$ for QD i and similarly for other matrix components.

The corresponding optimal AL orientation assumes an orthonormal 3D basis \hat{R}_i^{AL} that is nearest to R_i^{SL} in terms of $L_{2,2}$ distance.

$$\hat{R}_i^{AL} = \{\operatorname{argmin}_R \|R - R_i^{SL}\| \cap R^T R = I\} \quad (\text{B.2})$$

This is essentially a nonlinear constrained optimization problem, which can be numerically

solved by matrix singular value decomposition (SVD) such that,

$$R_i^{SL} = U\Sigma V^T \quad (\text{B.3})$$

$$\hat{R}_i^{AL} = UV^T \quad (\text{B.4})$$

We solve \hat{R}_i^{AL} for every QD in the sample and obtain the solution set $\{\hat{R}_i^{AL}\}$. This solution assumes the outcome of only minimizing the total 100AL free surfaces. While \hat{R}_i^{AL} can change for different SLs as R_i^{SL} changes locally, a global enforcement of strict mono-crystallinity can be implemented to obtain a different solution set \hat{R}_{mono}^{AL} where all QD adopt the same orientation while simultaneously satisfy the following optimization condition.

$$\hat{R}_i^{AL} = \left\{ \underset{R}{\operatorname{argmin}} \sum_i \|R - R_i^{SL}\| \cap R^T R = I \right\} \quad (\text{B.5})$$

This solution considers the minimization of 100AL free surfaces on the premise of introducing no energetic penalty from atomic misalignment, agreeing better with experimental measurement.

Alternatively, assumptions of bi-crystal or tri-crystal can be made in which orientations are fixed within designated subsets of SLs from the entire sampled. We have compared these solutions with experimental measurement $\{R_i^{AL}\}$ and summarized the results in table S.XYZ. Based on the proposed AL/SL relationship, we also show in SI Fig.S2 a variety of SL cells from cubic to triclinic created from different sets of lattice angles, based on which the AL orientations are calculated to complete each model. This finding may potentially simplify the crystallographic characterization of PbSe SLs samples and inspire designs of new nanocrystal systems.

B.2.3 Experimental Determination of 3D atomic lattice orientation

First, a $301 \times 301 \times 301$ ($\sim 1500 \text{ nm}^3$) cubic subvolume V_0 is extracted from the reconstruction around the center of mass of a specific QD of interest. This size is taken so that it is big enough to include one QD but not too big to include multiple QDs. The volume is then convoluted with a gaussian mask F placed at the center to suppress potential unwanted signals from adjacent QDs. The intensity profile of the filtered volume V is described as following

$$V(\vec{r}) = V_0(\vec{r}) \cdot F(\vec{r}) \quad (\text{B.6})$$

$$F(\vec{r}) = \exp\left(-\frac{\vec{r}^2}{2\sigma^2}\right) \quad (\text{B.7})$$

where σ is usually taken to be the diameter (~ 6 nm) of the QD of interest. We next obtain the reciprocal power volume $\hat{V}(\vec{k})$ following Discrete-Fast-Fourier-Transformation (DFFT) such that

$$\hat{V}(\vec{k}) = \log \left| \iiint V(\vec{r}) \exp(-2\pi i \vec{k} \cdot \vec{r}) d\vec{r} \right| \quad (\text{B.8})$$

The FFT power volume is treated with a band-pass filter to remove information outside of desired spatial frequency ranged within $2 \sim 4 \text{ nm}^{-1}$, in which we shall find the $\{110\}$ and $\{200\}$ PbSe diffraction peaks. The resulted volume is binarized with a threshold equals to 75% of the maximum power. A Density-Based Spatial Clustering of Applications with Noise (DBSCAN) algorithm is applied to the thresholded volume to detect diffraction Bragg spots as voxel clusters and remove noises. Then a Gaussian Mixture Model (GMM) clustering is applied with initial guesses of cluster centroids obtained from the DBSCAN. The resulting fitted GMM model takes the form as

$$P(\vec{k}) = \sum_N \frac{w_i}{2\pi |\Sigma_i|} \exp\left\{-\frac{1}{2}(\vec{k} - \vec{\mu}_i)^T \Sigma_i^{-1} (\vec{k} - \vec{\mu}_i)\right\} \quad (\text{B.9})$$

where N is the number of clusters, w_i is the weight for each cluster and Σ_i is the covariance matrix. The cluster centroids $\vec{\mu}_i$ in the reciprocal space from GMM model are considered as the centroids of the Bragg Spots of Pb lattices resolved from the original reconstruction. The real space lattice vectors are then calculated as

$$\vec{g}_i = \frac{\vec{\mu}_i}{|\vec{\mu}_i|^2} \quad (\text{B.10})$$

The calculated atomic lattices vector \vec{g}_i are classified into $[200]_{AL}(\vec{a})$, $[020]_{AL}(\vec{b})$ and $[002]_{AL}(\vec{c})$ vectors based on their general directions with respect to the reference cartesian axes of the global reconstruction volume.

With the AL vectors characterized, the orientation of a QD in 3D cartesian space can be expressed as

$$R_i^{AL} = \begin{bmatrix} a_x^* & a_y^* & a_z^* \\ b_x^* & b_y^* & b_z^* \\ c_x^* & c_y^* & c_z^* \end{bmatrix}_i \quad (\text{B.11})$$

where $\vec{a}_i^* = (a_x^*, a_y^*, a_z^*)_i$ corresponds to the unit basis vector $[200]_{AL}$ measured from WFFT and similarly for the other AL vectors. Since R_i are numerically derived, the orthogonality of the matrix is not strictly ensured. Therefore, matrix regularization is conducted via finding the closest orthogonal matrix to enforce mutual orthonormality among the basis vectors in R_i^{AL} . The mean error between raw R_i^{AL} and regularized R_i^{AL} is evaluated to be 0.2%.

Another commonly used approach to determine crystal orientation from 2D and 3D TEM/STEM measurements is the Geometric Phase Analysis (GPA) method.[58, 52] GPA is particularly useful for obtaining relative lattice orientation differences in a tensor field form from the vectorial displacement field when there is no need to couple the orientation to other structural feature. However, since our subsequent analyses are heavily relied on correlating AL orientations to other attributes such as positions and SL vectors, we instead use a direct WFFT method.[29]

B.2.4 Characterization of AL orientation transformation

The orientation difference between QD i and QD j are described by a single-axis rigid body rotation transformation vector $\vec{\delta}_{ij}$,

$$\vec{\delta}_{ij} = \varepsilon_{ij} \vec{\xi}_{ij} \quad (\text{B.12})$$

where ε_{ij} is the magnitude of the rotation and $\vec{\xi}_{ij}$ is the unit vector defining the rotation axis, which are calculated as following,

$$T_{ij} \vec{\xi}_{ij} = \vec{\xi}_{ij} \quad (\text{B.13})$$

$$\varepsilon_{ij} = \arccos\left(\frac{\text{trace}(T_{ij}) - 1}{2}\right) \quad (\text{B.14})$$

$$T_{ij} = \frac{R_j^{AL}}{R_i^{AL}} \quad (\text{B.15})$$

T_{ij} is the rotational transformation matrix between orientation R_i^{AL} and R_j^{AL} , and $\vec{\xi}_{ij}$ is obtained through solving the eigen vector for T_{ij} with a corresponding eigenvalue of 1. $\vec{\xi}_{ij}$ can then be rewritten as a linear combination of local AL basis vectors such that

$$\vec{\xi}_{ij} = l \frac{\vec{a}_i^* + \vec{a}_j^*}{|\vec{a}_i^* + \vec{a}_j^*|} + m \frac{\vec{b}_i^* + \vec{b}_j^*}{|\vec{b}_i^* + \vec{b}_j^*|} + n \frac{\vec{c}_i^* + \vec{c}_j^*}{|\vec{c}_i^* + \vec{c}_j^*|} \quad (\text{B.16})$$

The coefficients l, m and n are used to find major rotation axis using linear regression.

B.2.5 Orientation correlation matrix and von Neumann entropy

The Pearson correlation matrix K for the orientation of QDs are constructed such that for each element in K ,

$$K_{ij} = \text{corr}(R_i, R_j) \quad (\text{B.17})$$

The von Neumann entropy of a group of QDs' orientational states is derived such that

$$S_I = -k_B \text{trace}(\rho_I \ln \rho_I) \quad (\text{B.18})$$

$$\rho_I = \frac{K_{II}}{N} \quad (\text{B.19})$$

where I is the group index for a particular layer, K_{II} is the diagonal blocks in the Pearson correlation matrices representing the intra-group correlation submatrices for group I and N is the dimension of K_{II} . Note that here the \ln is a matrix natural logarithmic operator instead of an elementwise operator.

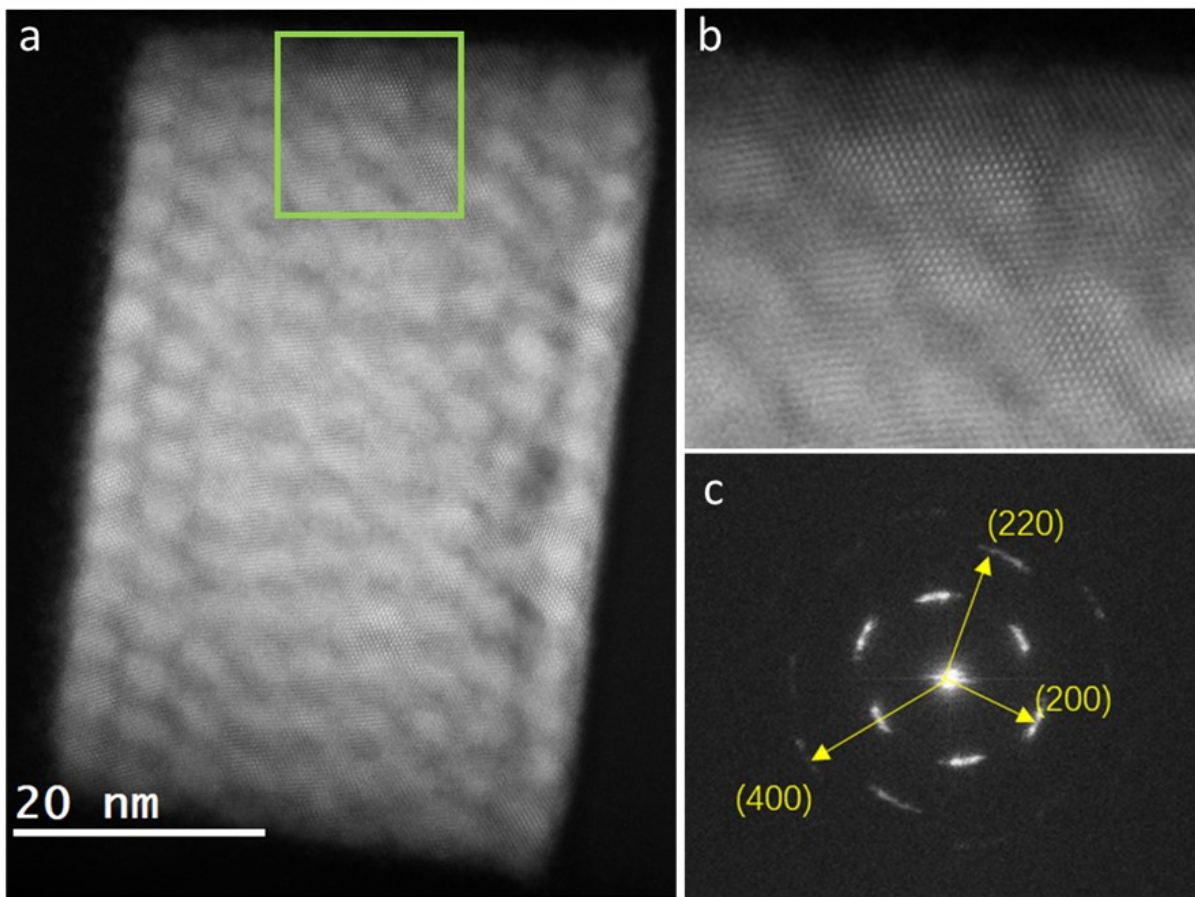


Figure B.3. An exemplary STEM projection image showing atomic details.

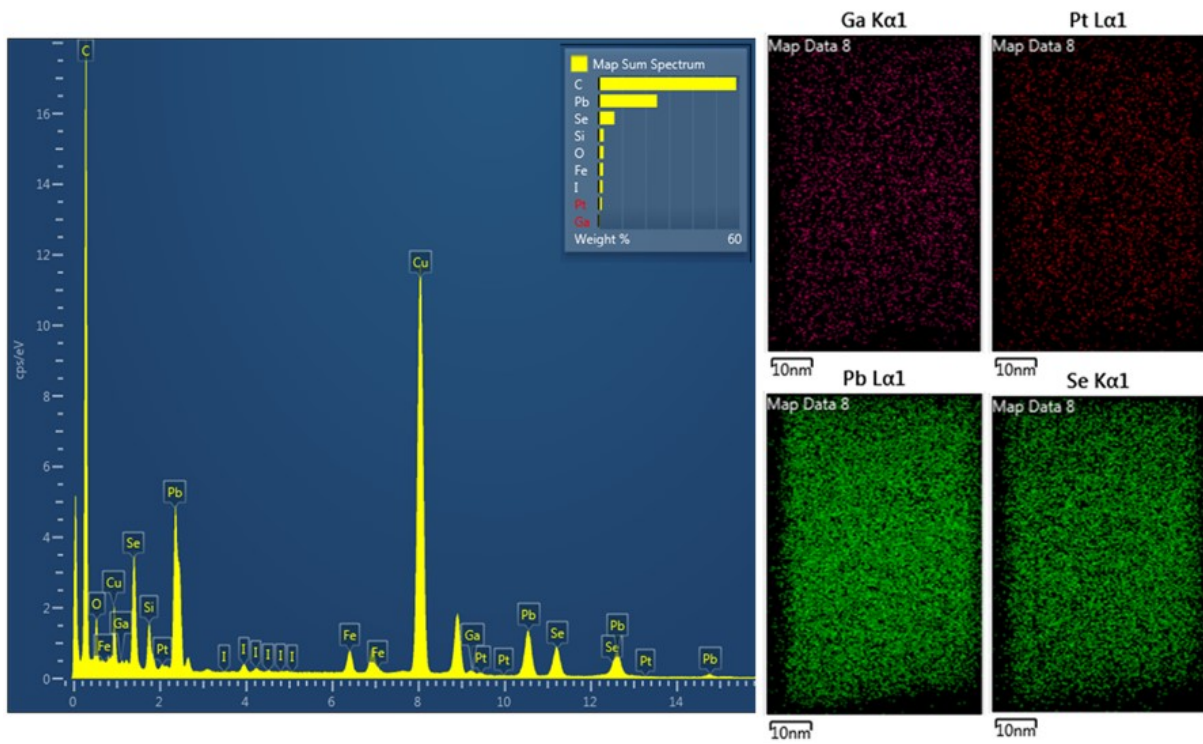


Figure B.4. EDX measurement of PbSe section on the tomography needle.

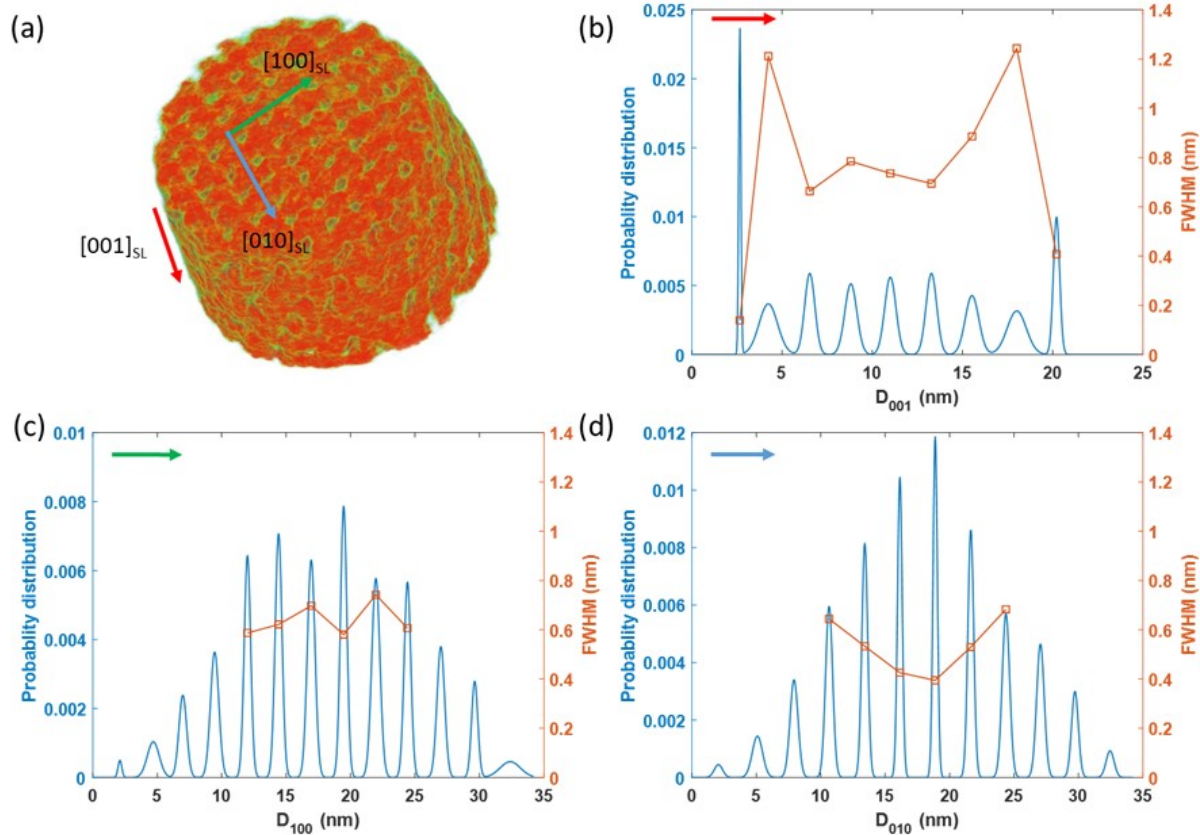


Figure B.5. QD center-of-mass distributions along different SL direction: $[001]_{SL}$ (b), $[010]_{SL}$ (c) and $[100]_{SL}$ (c).

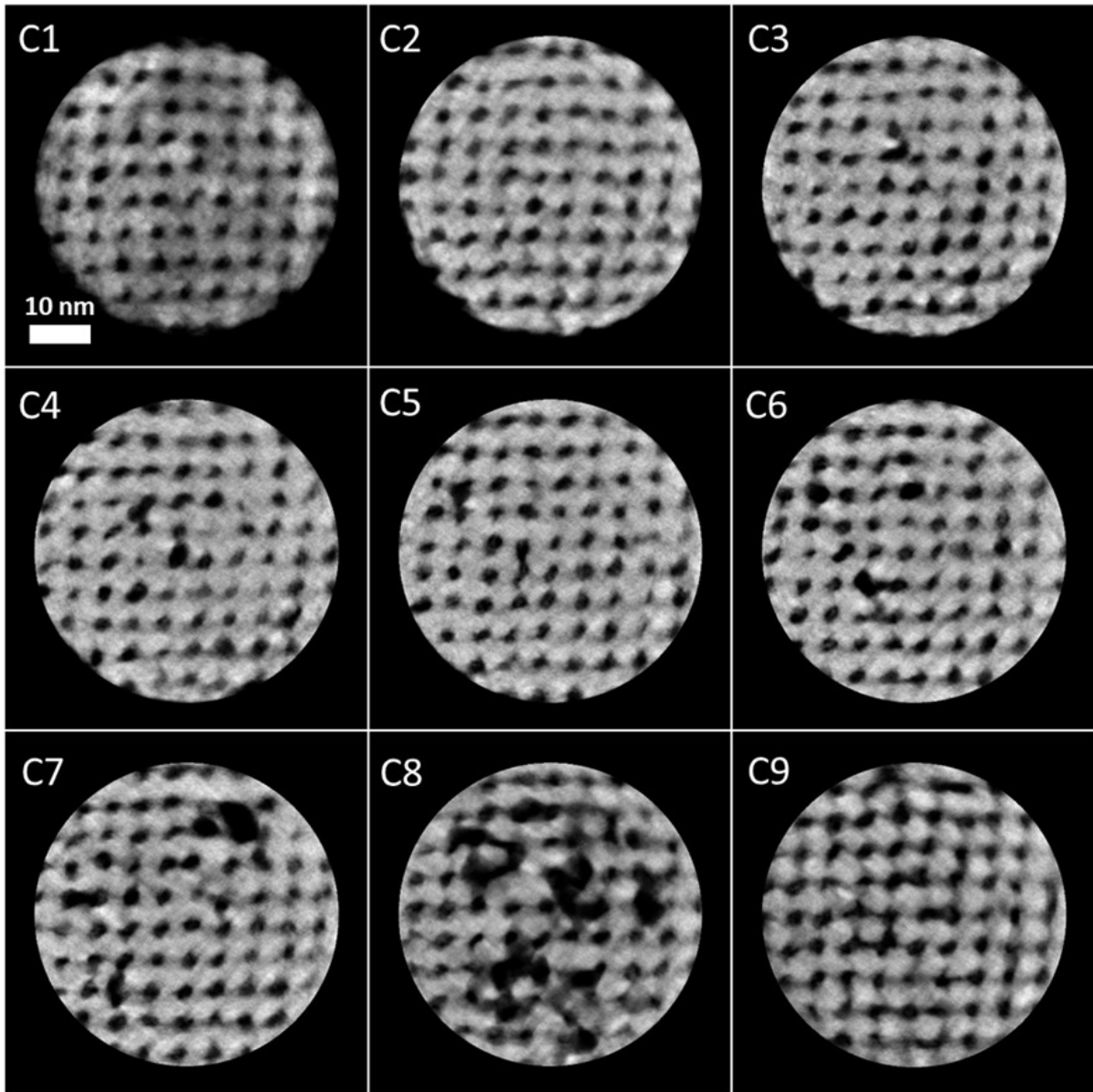


Figure B.6. Slices of $(001)_{SL}$ layers from the raw reconstruction.

B.3 Crystal Stacking

B.4 Grazing Incidence X-ray Diffraction

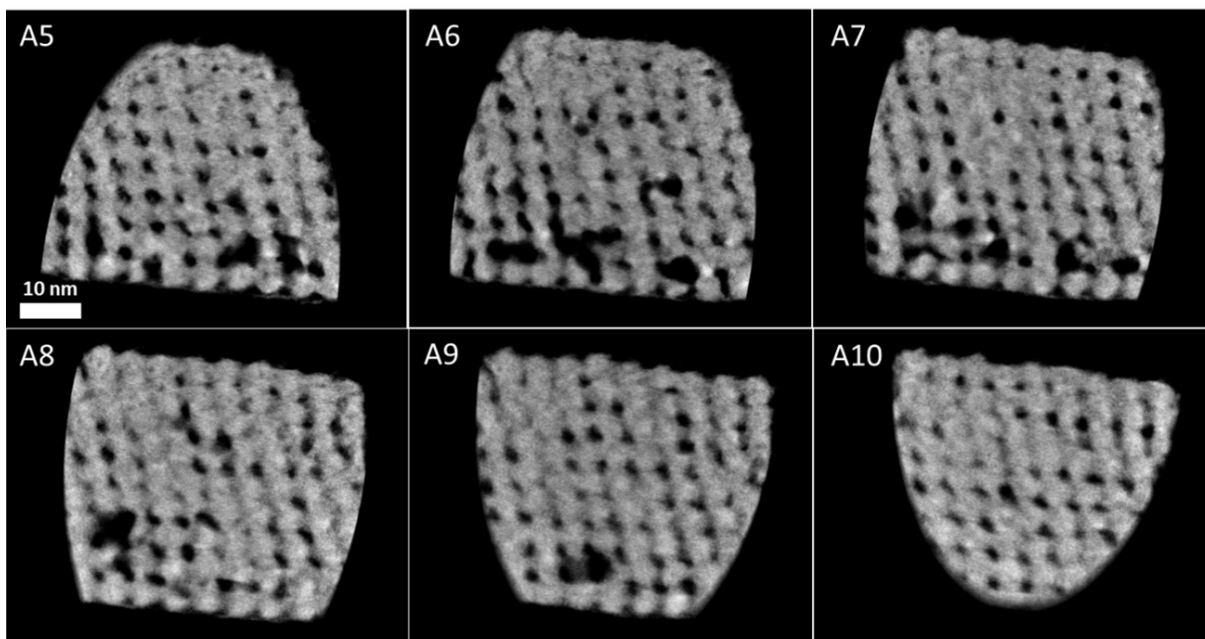


Figure B.7. Slices of $(100)_{SL}$ (A) layers from the raw reconstruction.

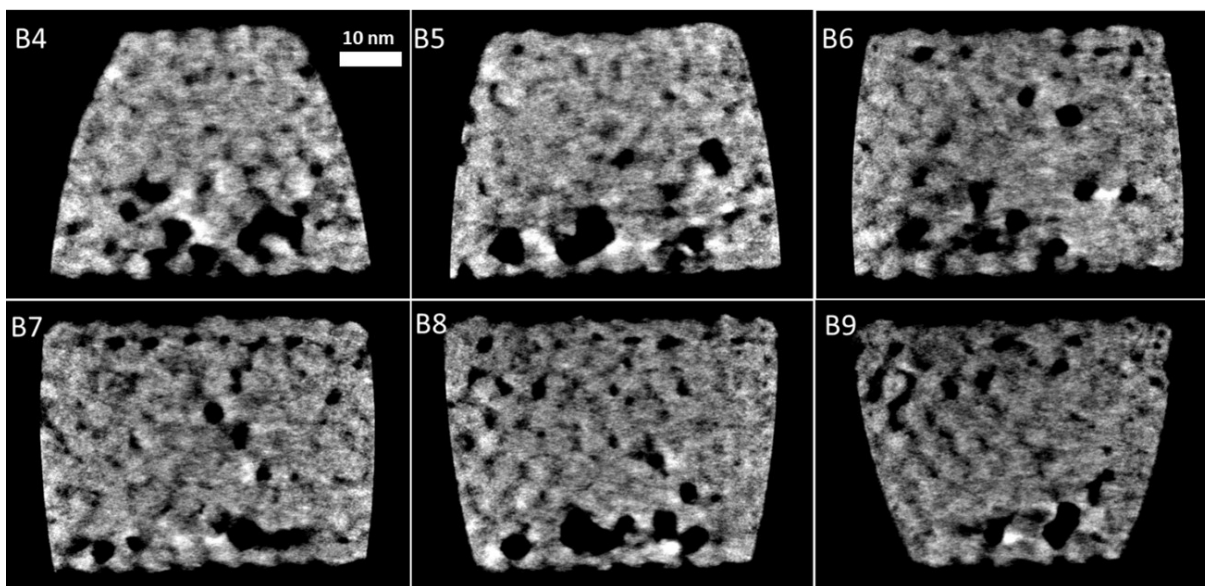


Figure B.8. Slices of $(010)_{SL}$ (B) layers from the raw reconstruction.

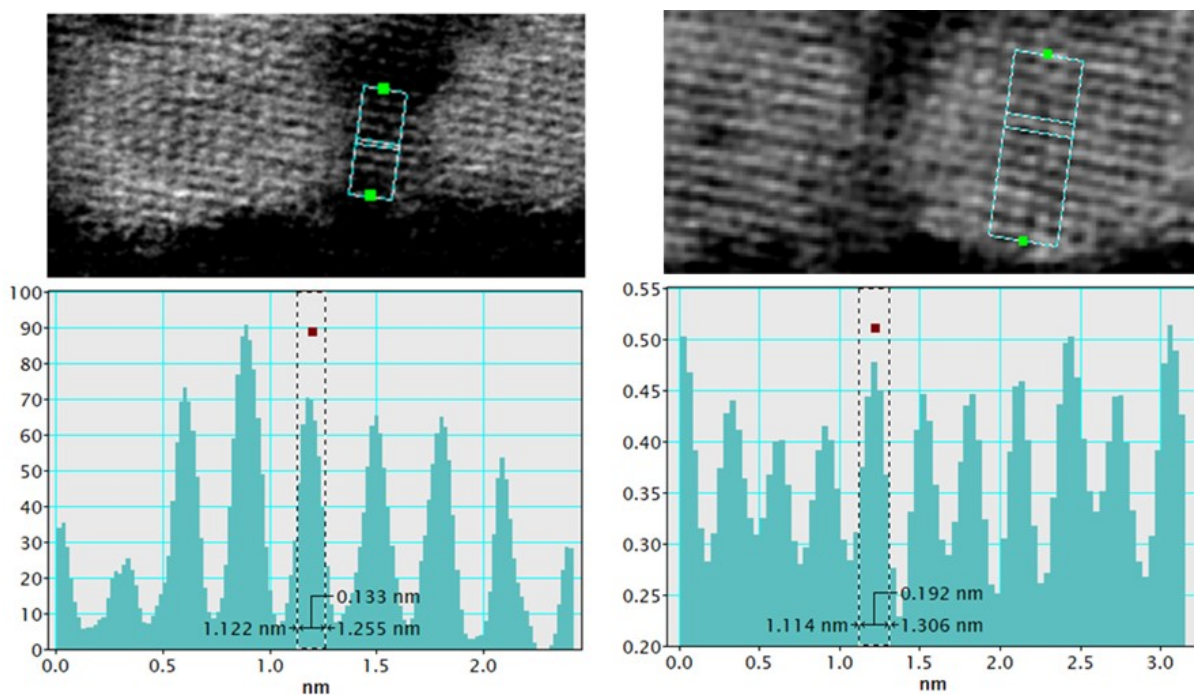


Figure B.9. Local tomographic slices showing 3D atomic details with a resolution of ~ 0.2 nm.

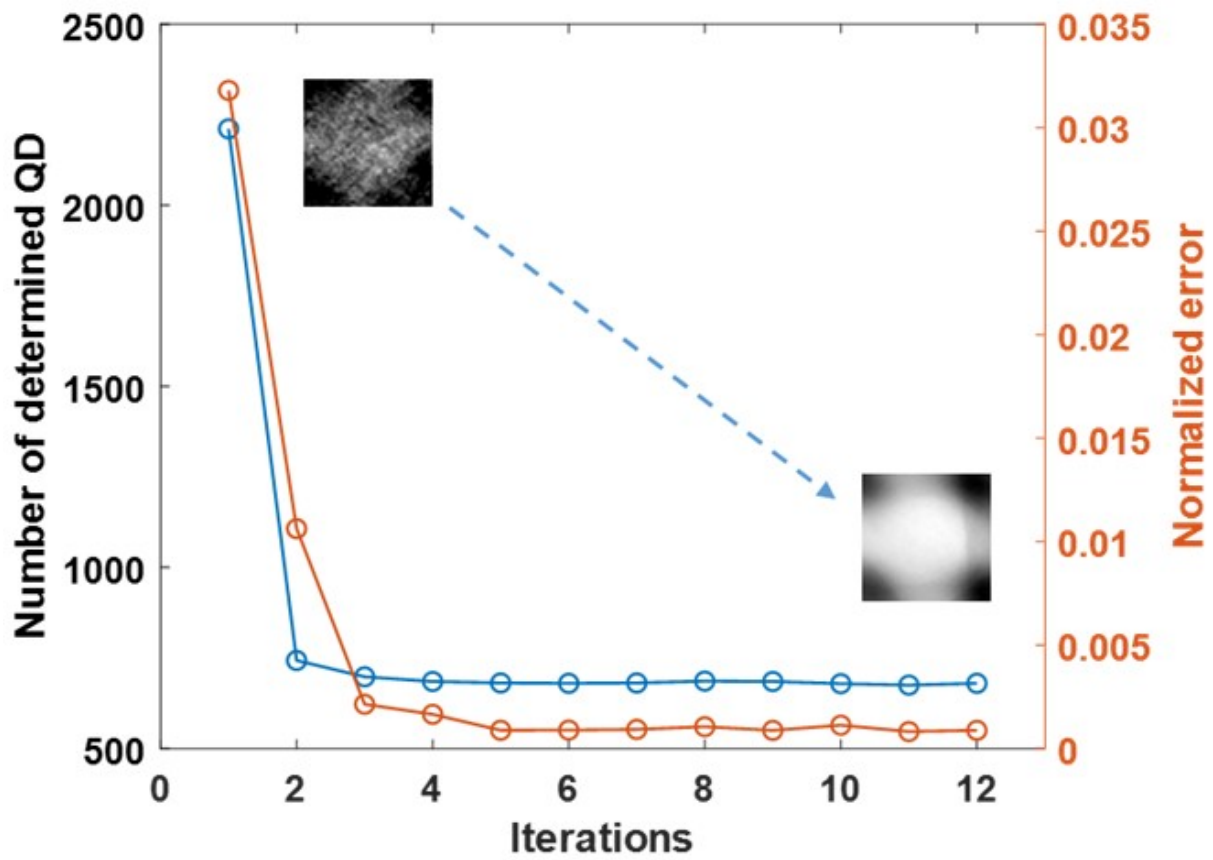


Figure B.10. The iterative process of QD center-of-mass determination.

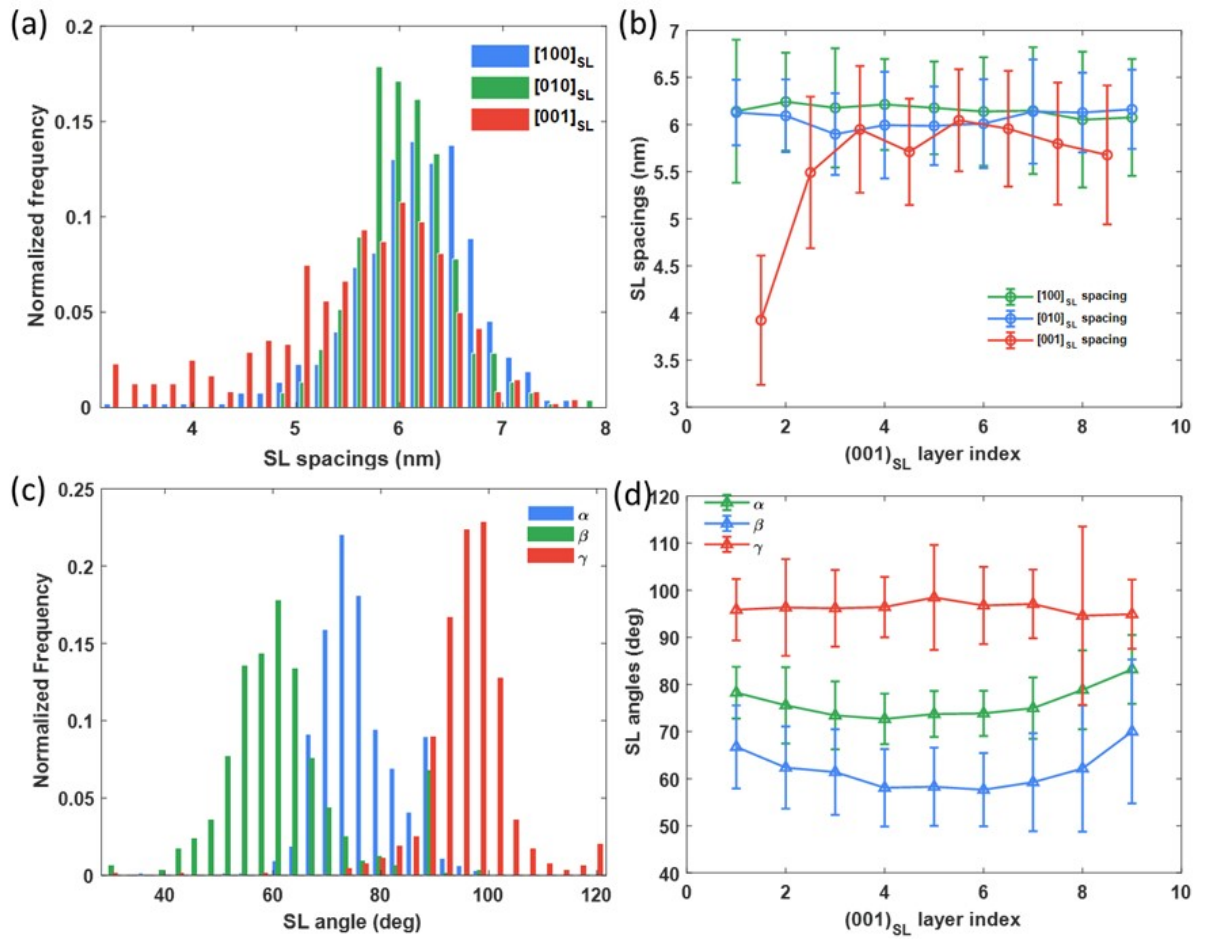


Figure B.11. (a) SL spacings distributions. (b) Mean SL spacings over different $[100]_{SL}$ layers.

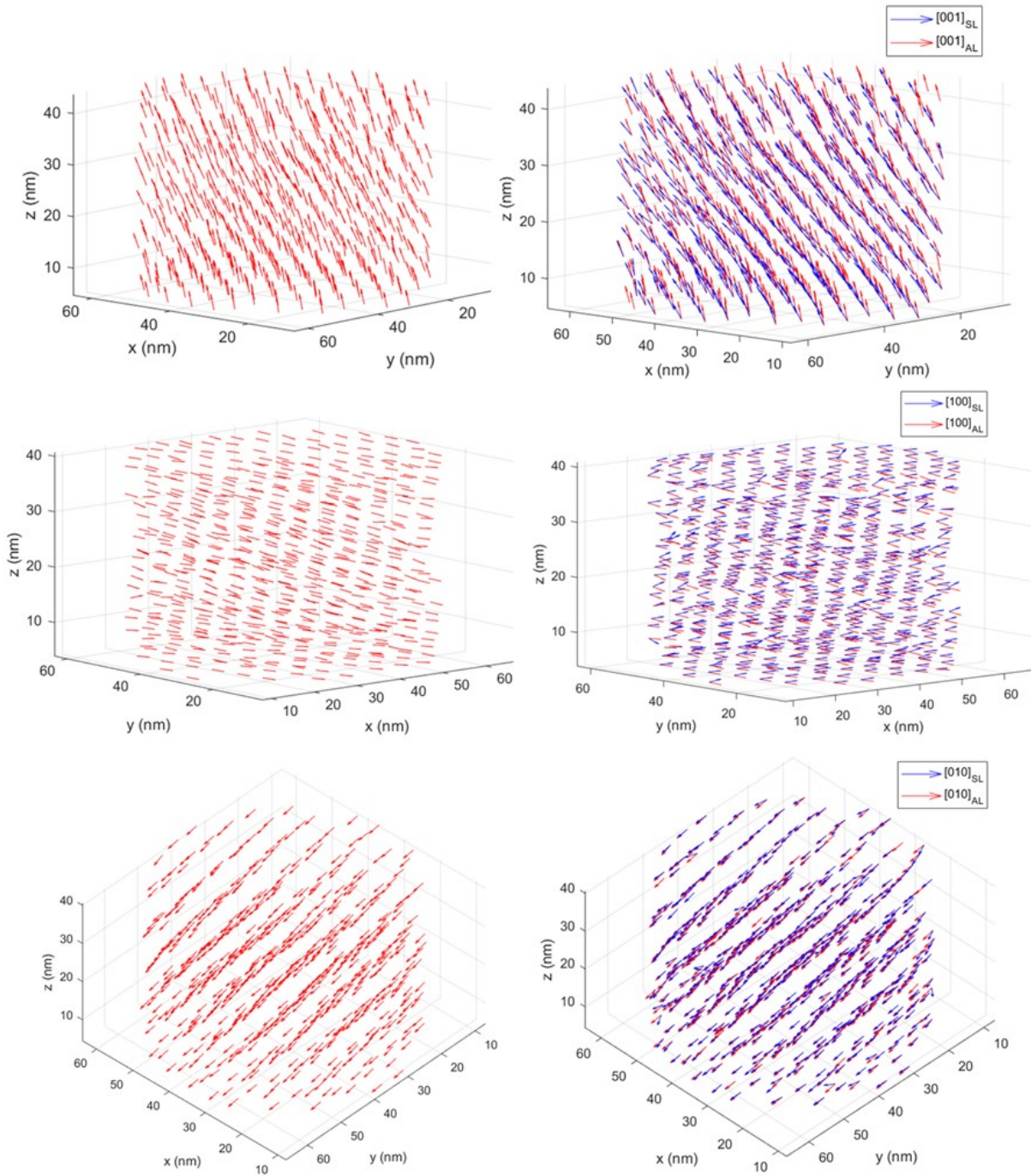


Figure B.12. Vector field maps for the orientation of the QDs. The positions of each arrow represent the actual positions of the QD. The directions of the arrows represent the vector directions of the corresponding atomic lattice and superlattice vectors. Plots in the first column just show the AL vectors while plots in the second column show both AL and SL vectors.

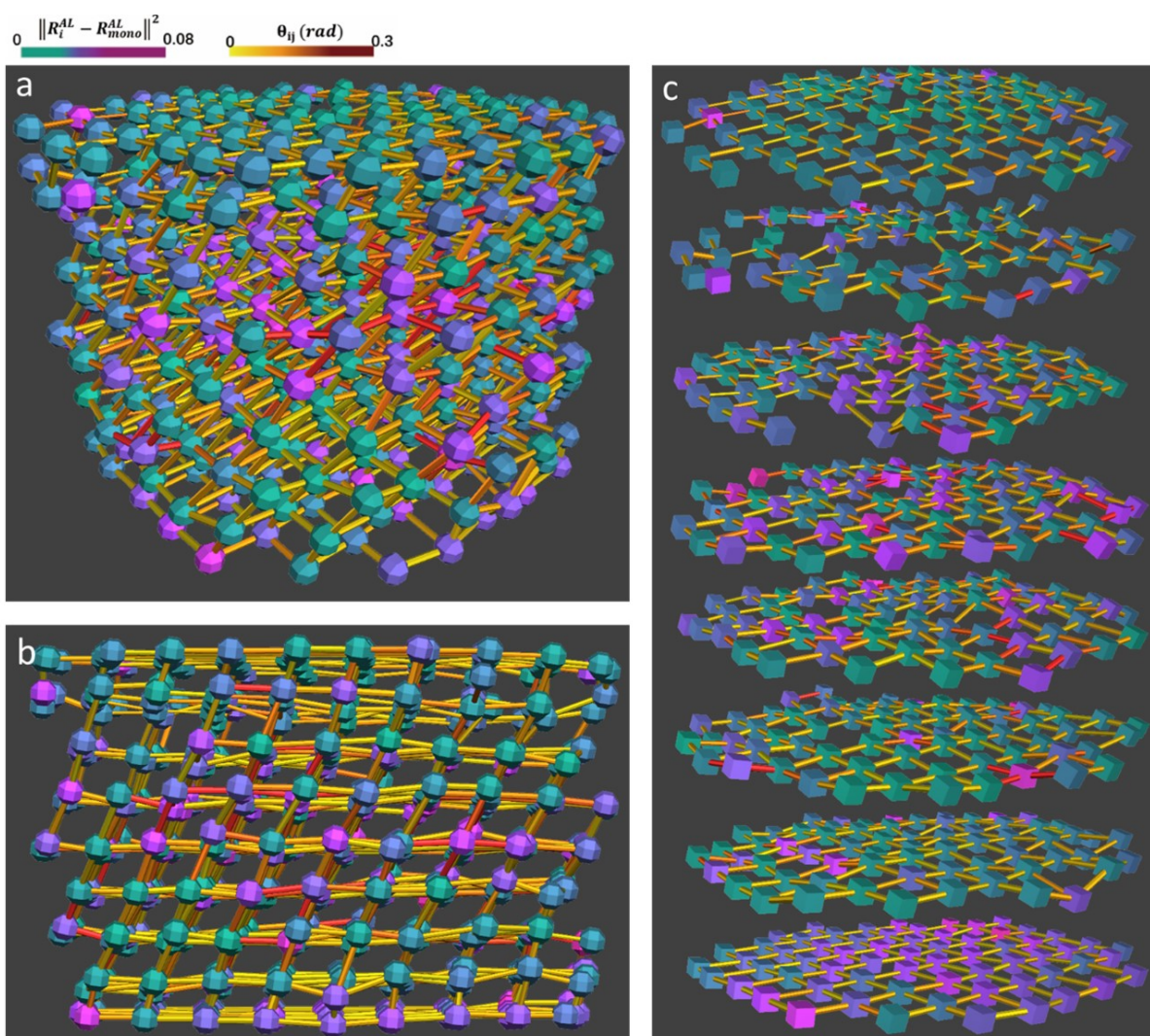


Figure B.13. The glyph-stick visualization of the structural information.

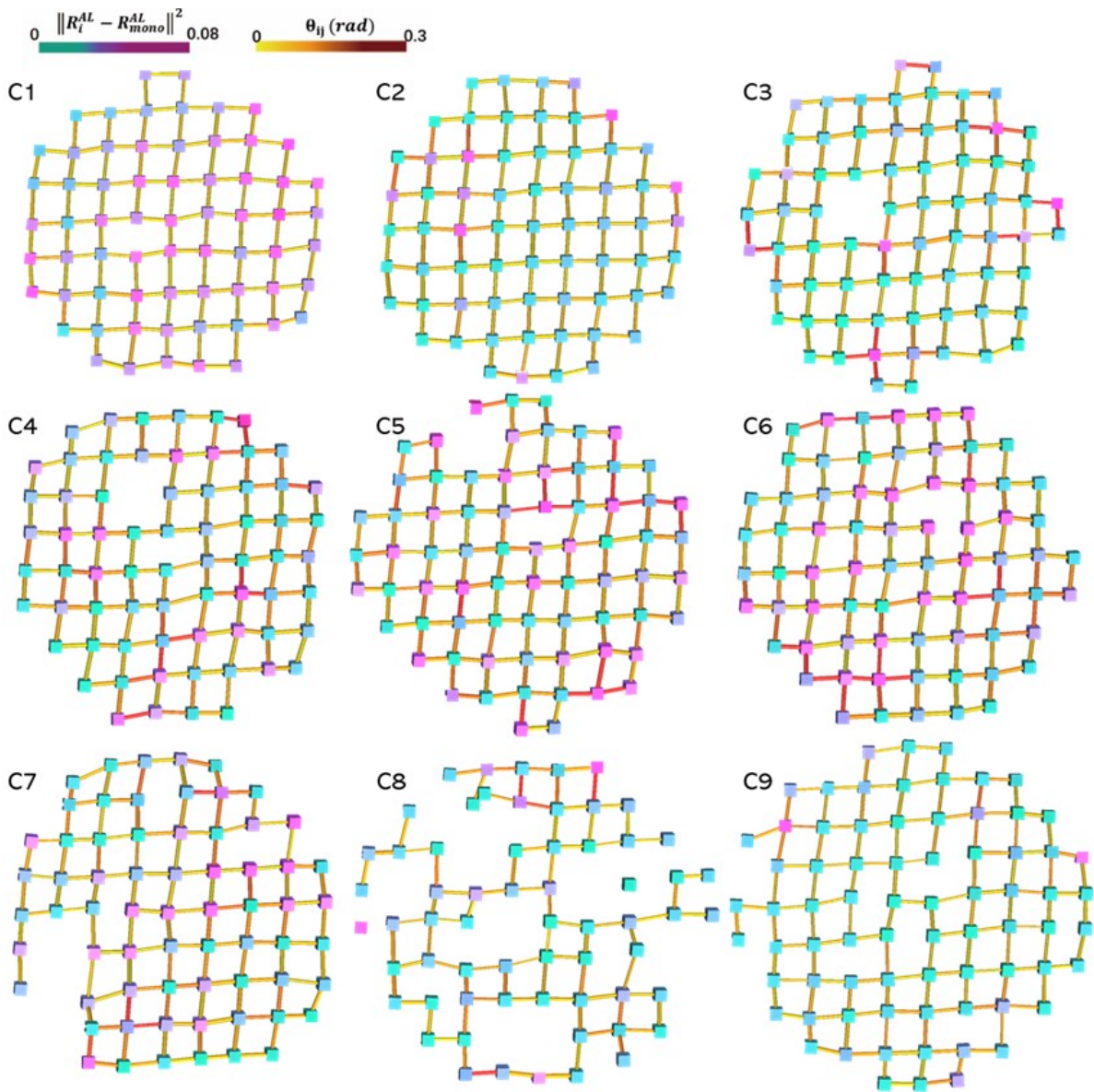


Figure B.14. The glyph-stick visualization of all $(001)_{SL}$ planes (C1-C9).

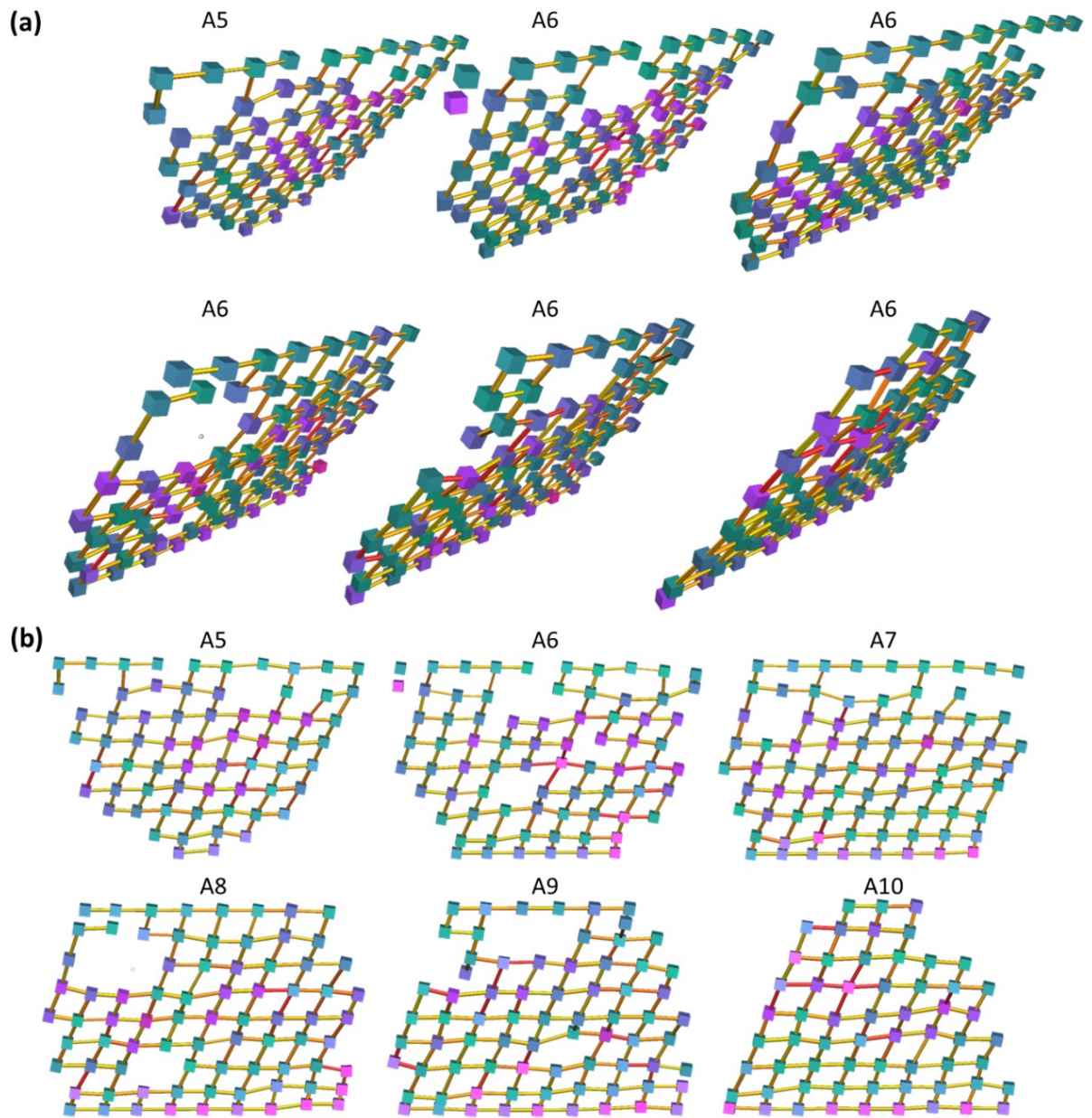


Figure B.15. The glyph-stick visualization of selected $(100)_{SL}$ planes (A5 – B10). (a) perspective side views. (b) orthogonal views.

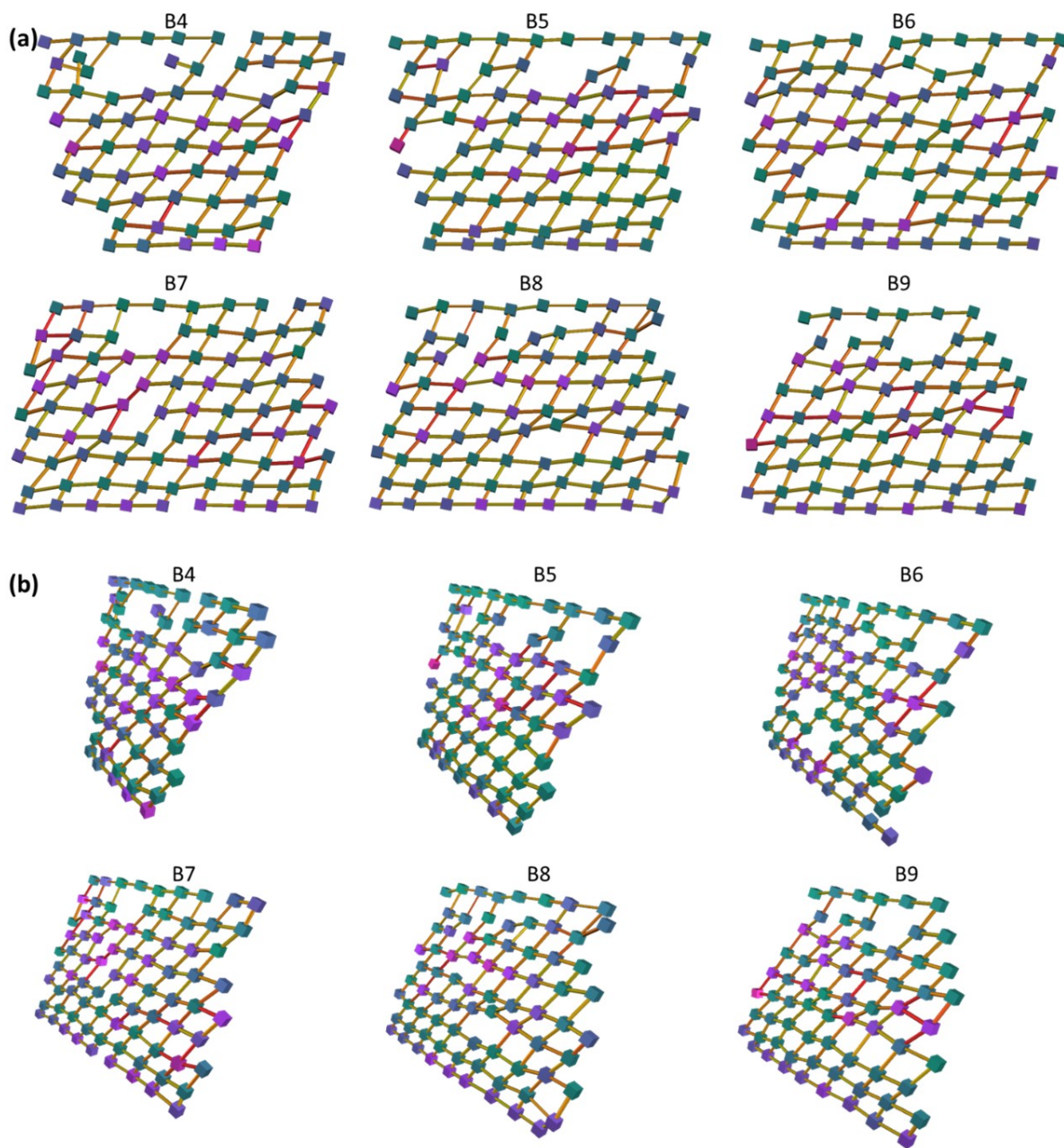


Figure B.16. The glyph-stick visualization of selected $(010)_{SL}$ planes (B5 – B10). (a) orthogonal views. (b) perspective side views.

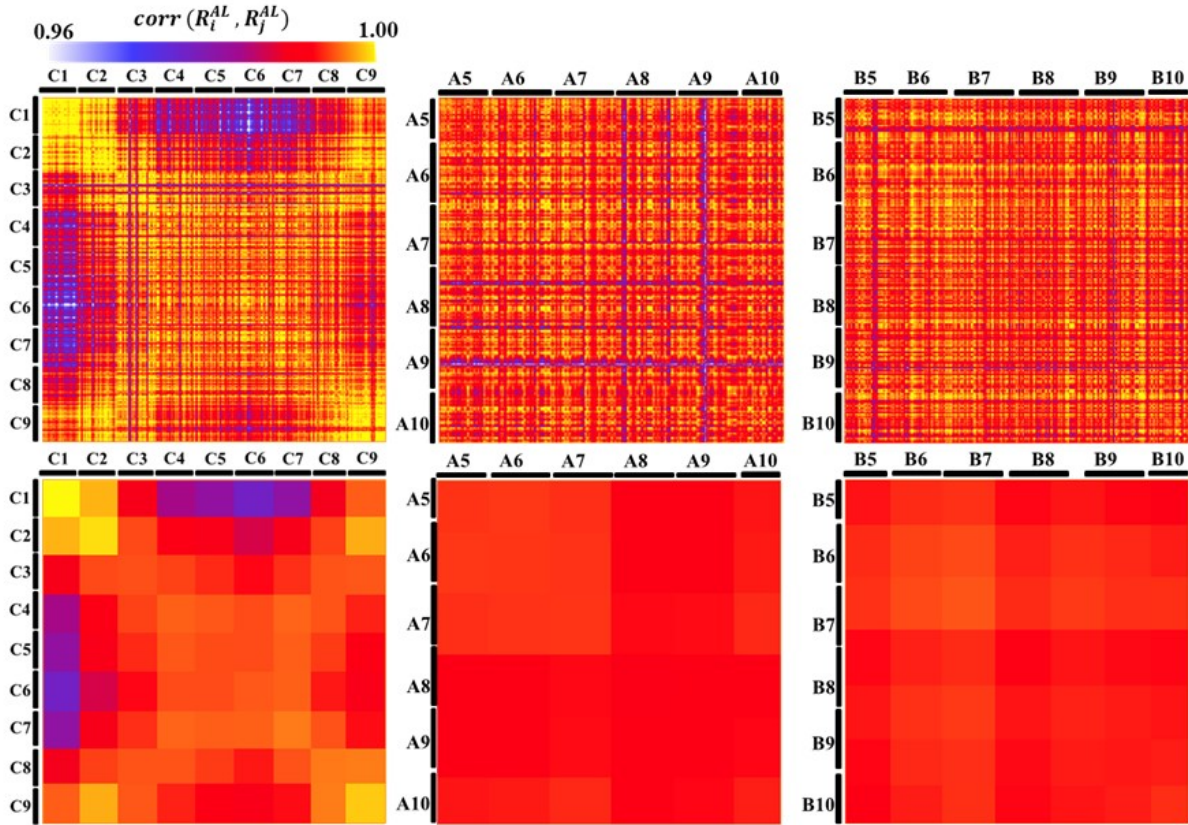


Figure B.17. Pearson cross-correlation matrices for R_i^{AL} grouping by $[001]_{SL}$ (first column), $[100]_{SL}$ (second column) and $[010]_{SL}$ (third column) layers. The first row are raw PCMs and the second rows are block averaged. The elements in the PCMs are the cross-correlation coefficients of the orientation basis matrices $corr(R_i^{AL}, R_j^{AL})$ between a pair of QD i and j . The elements are arranged in groups following ascending $[001]_{SL}$ (C) layer indices. Within each group, the order of QDs is reshuffled to exclude potential unwanted grouping effect from other SL directions. Comparing PCMs of each SL direction, we see that the orientation gradient is unique in $[001]_{SL}$.

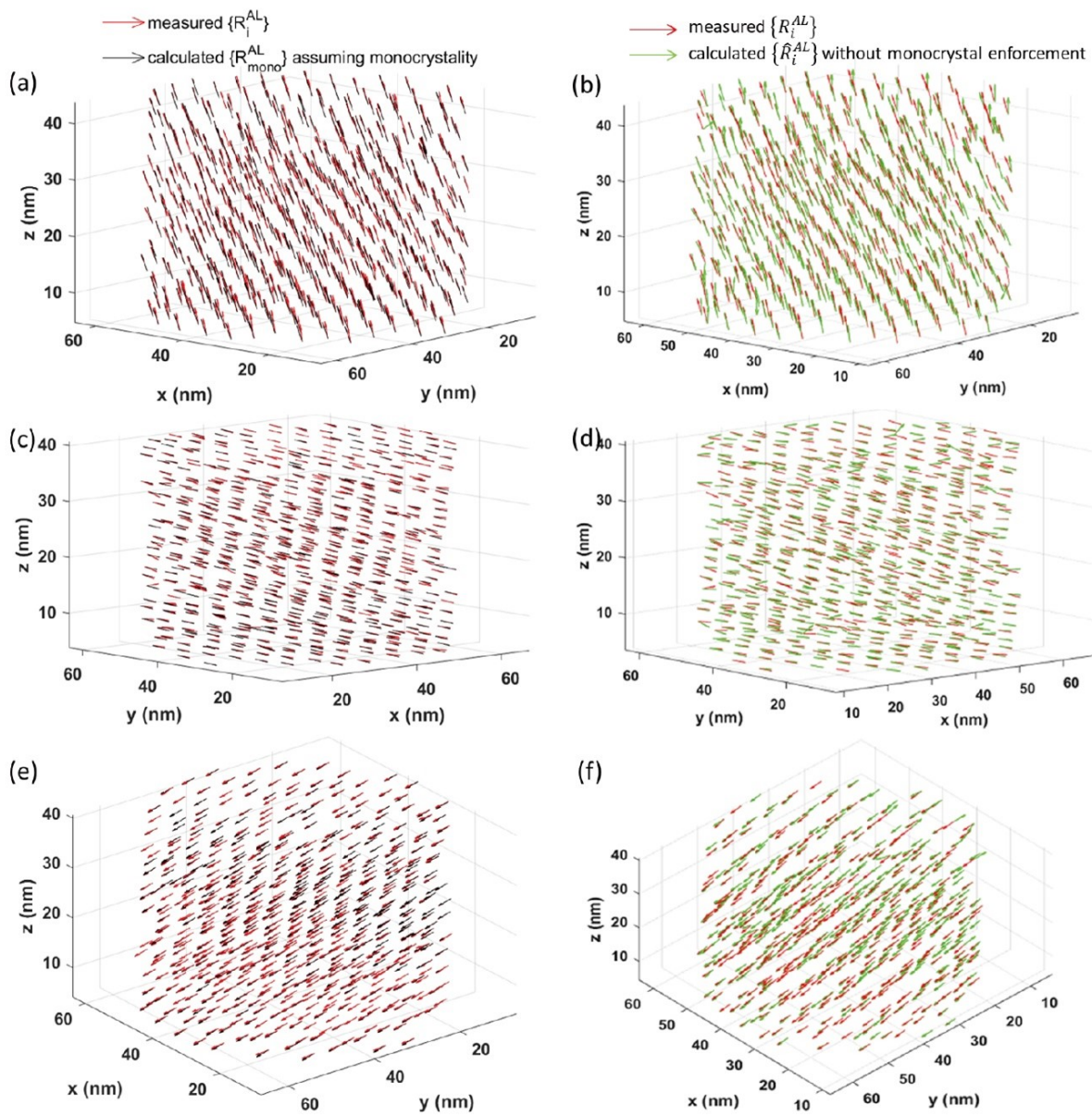


Figure B.18. Vector field of measured AL and calculated AL with/without global monocrystal assumption. (a,b) $[001]_{AL}$, (c,d) $[010]_{AL}$ and (e,f) $[100]_{AL}$.

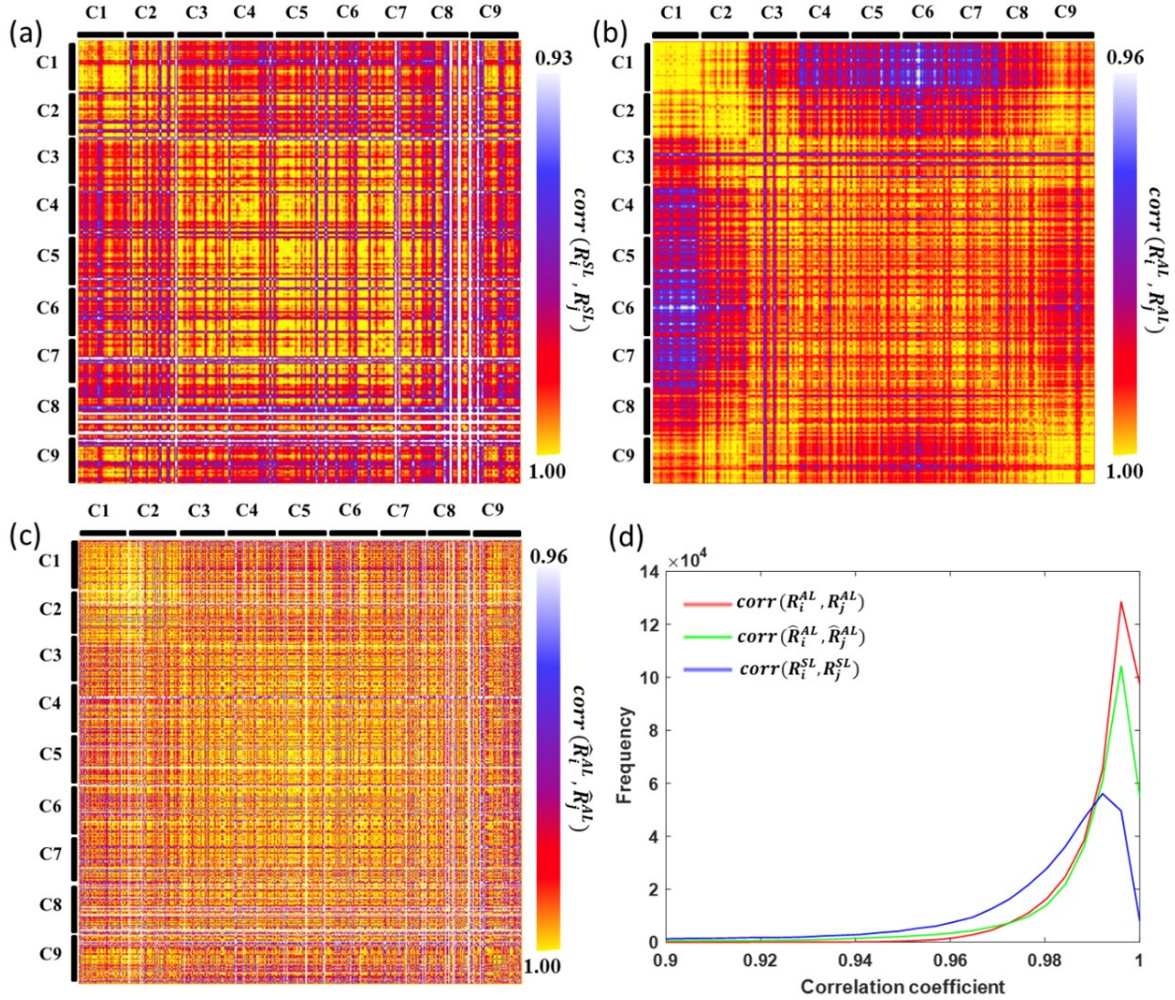


Figure B.19. (a-c) PCMs of R_i^{SL} , R_i^{AL} (experimental) and \hat{R}_i^{AL} (polycrystal prediction). The outliers related with C8 in (a) come from this layer's high density of missing dots. (d) PCM intensity profiles. Three observations can be distilled from the comparisons of the PCMs shown. (1) The R_i^{AL} PCM shares similarity with the R_i^{SL} PCM, indicating that the AL orientation is systematically determined by the SL structure. The differences are that any change in the AL appear to be smoother than change in the SL. (2) The roughness of \hat{R}_i^{AL} PCM indicates the short-range AL coherence is worse than experimental measurements, indicating that AL is inert to local SL randomness and minimization of AL misalignment is preferred for the system. (3) The diagonal block color scale is a qualitative indicator of the orientational entropy of each $[001]_{SL}$ layers.

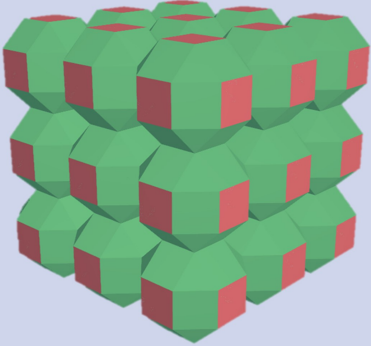
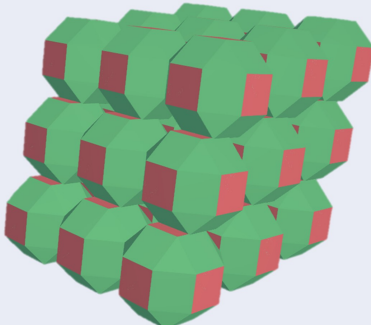
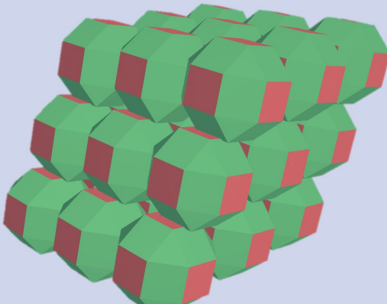
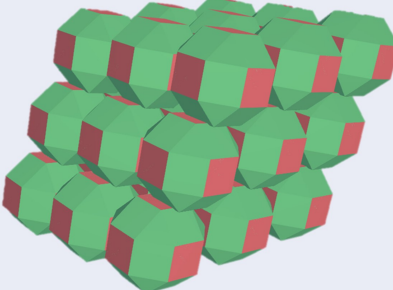
Assumed SL angles $\alpha/\beta/\gamma$	Calculated AL/SL misalignment	Calculated unit cell structure
$\alpha = 90^\circ$ $\beta = 90^\circ$ $\gamma = 90^\circ$	$[100]_{\text{SL}} \angle [100]_{\text{AL}} = 0^\circ$ $[100]_{\text{SL}} \angle [100]_{\text{AL}} = 0^\circ$ $[100]_{\text{SL}} \angle [100]_{\text{AL}} = 0^\circ$	
$\alpha = 70^\circ$ $\beta = 90^\circ$ $\gamma = 90^\circ$	$[100]_{\text{SL}} \angle [100]_{\text{AL}} = 0^\circ$ $[100]_{\text{SL}} \angle [100]_{\text{AL}} = 10.00^\circ$ $[100]_{\text{SL}} \angle [100]_{\text{AL}} = 10.00^\circ$	
$\alpha = 70^\circ$ $\beta = 80^\circ$ $\gamma = 90^\circ$	$[100]_{\text{SL}} \angle [100]_{\text{AL}} = 5.09^\circ$ $[100]_{\text{SL}} \angle [100]_{\text{AL}} = 10.05^\circ$ $[100]_{\text{SL}} \angle [100]_{\text{AL}} = 11.28^\circ$	
$\alpha = 70^\circ$ $\beta = 80^\circ$ $\gamma = 80^\circ$	$[100]_{\text{SL}} \angle [100]_{\text{AL}} = 6.54^\circ$ $[100]_{\text{SL}} \angle [100]_{\text{AL}} = 11.44^\circ$ $[100]_{\text{SL}} \angle [100]_{text{AL}} = 11.44^\circ$	

Figure B.20. Predicted optimal AL/SL configurations based on SL angles.

REFERENCES

- [1] Alex Abelson, Caroline Qian, Trenton Salk, Zhongyue Luan, Kan Fu, Jian-Guo Zheng, Jenna L Wardini, and Matt Law. Collective topo-epitaxy in the self-assembly of a 3d quantum dot superlattice. *Nat. Mater.*, 19(1):49–55, 2020.
- [2] Alex Abelson, Caroline Qian, Trenton Salk, Zhongyue Luan, Kan Fu, Jian-Guo Zheng, Jenna L Wardini, and Matt Law. Collective topo-epitaxy in the self-assembly of a 3d quantum dot superlattice. *Nature materials*, 19(1):49–55, 2020.
- [3] Matthew M Ackerman, Xin Tang, and Philippe Guyot-Sionnest. Fast and sensitive colloidal quantum dot mid-wave infrared photodetectors. *ACS Nano*, 12(7):7264–7271, 2018.
- [4] G Allan and C Delerue. Confinement effects in pbse quantum wells and nanocrystals. *Physical Review B*, 70(24):245321, 2004.
- [5] Davide Altamura, Vaclav Holý, Dritan Siliqi, Indira Chaitanya Lekshmi, Concetta Nobile, Giuseppe Maruccio, P Davide Cozzoli, Lixin Fan, Fabia Gozzo, and Cinzia Giannini. Exploiting gisaxs for the study of a 3d ordered superlattice of self-assembled colloidal iron oxide nanocrystals. *Cryst. Growth Des.*, 12(11):5505–5512, 2012.
- [6] V Arivazhagan, M Manonmani Parvathi, and S Rajesh. Impact of thickness on vacuum deposited pbse thin films. *Vacuum*, 86(8):1092–1096, 2012.
- [7] RC Ashoori. Electrons in artificial atoms. *Nature*, 379(6564):413–419, 1996.
- [8] Daniel M Balazs, Bartosz M Matysiak, Jamo Momand, Artem G Shulga, Maria Ibáñez, Maksym V Kovalenko, Bart J Kooi, and Maria Antonietta Loi. Electron mobility of $24 \text{ cm}^2 \text{ v}^{-1} \text{ s}^{-1}$ in pbse colloidal-quantum-dot superlattices. *Adv. Mater.*, 30(38):1802265, 2018.
- [9] Uri Banin, YunWei Cao, David Katz, and Oded Millo. Identification of atomic-like electronic states in indium arsenide nanocrystal quantum dots. *Nature*, 400(6744):542–544, 1999.

- [10] Alexander V Baranov, Elena V Ushakova, Valery V Golubkov, Aleksandr P Litvin, Peter S Parfenov, Anatoly V Fedorov, and Kevin Berwick. Self-organization of colloidal pbs quantum dots into highly ordered superlattices. *Langmuir*, 31(1):506–513, 2015.
- [11] William J Baumgardner, Kevin Whitham, and Tobias Hanrath. Confined-but-connected quantum solids *via* controlled ligand displacement. *Nano Lett.*, 13(7):3225–3231, 2013.
- [12] E Biermans, L Molina, KJ Batenburg, S Bals, and G Van Tendeloo. Measuring porosity at the nanoscale by quantitative electron tomography. *Nano letters*, 10(12):5014–5019, 2010.
- [13] Michael A Boles, Michael Engel, and Dmitri V Talapin. Self-assembly of colloidal nanocrystals: From intricate structures to functional materials. *Chemical reviews*, 116(18):11220–11289, 2016.
- [14] Mark P Boneschanscher, Wiel H Evers, Jaco J Geuchies, Thomas Altantzis, Bart Goris, Freddy T Rabouw, SAP Van Rossum, Herre SJ van der Zant, Laurent DA Siebbeles, Gustaaf Van Tendeloo, et al. Long-range orientation and atomic attachment of nanocrystals in 2d honeycomb superlattices. *Science*, 344(6190):1377–1380, 2014.
- [15] Mark P Boneschanscher, Wiel H Evers, Weikai Qi, Johannes D Meeldijk, Marjolein Dijkstra, and Daniel Vanmaekelbergh. Electron tomography resolves a novel crystal structure in a binary nanocrystal superlattice. *Nano Lett.*, 13(3):1312–1316, 2013.
- [16] Julian Brunner, Igor A Baburin, Sebastian Sturm, Kristina Kvashnina, André Rossberg, Torsten Pietsch, Sergej Andreev, Elena Sturm, and Helmut Cölfen. Self-assembled magnetite mesocrystalline films: Toward structural evolution from 2d to 3d superlattices. *Advanced Materials Interfaces*, 4(1):1600431, 2017.
- [17] TL Burnett, SA McDonald, A Gholinia, R Geurts, M Janus, T Slater, SJ Haigh, C Ornek, F Almuaili, DL Engelberg, et al. Correlative tomography. *Scientific reports*, 4(1):1–6, 2014.

- [18] Thorsten M Buzug. *Einführung in die Computertomographie: mathematisch-physikalische Grundlagen der Bildrekonstruktion*. Springer-Verlag, 2011.
- [19] Marion Calcagnotto, Dirk Ponge, Eralp Demir, and Dierk Raabe. Orientation gradients and geometrically necessary dislocations in ultrafine grained dual-phase steels studied by 2d and 3d ebsd. *Materials Science and Engineering: A*, 527(10-11):2738–2746, 2010.
- [20] Graham H Carey, Ahmed L Abdelhady, Zhijun Ning, Susanna M Thon, Osman M Bakr, and Edward H Sargent. Colloidal quantum dot solar cells. *Chem. Rev.*, 115(23):12732–12763, 2015.
- [21] Chien-Chun Chen, Chun Zhu, Edward R White, Chin-Yi Chiu, MC Scott, BC Regan, Laurence D Marks, Yu Huang, and Jianwei Miao. Three-dimensional imaging of dislocations in a nanoparticle at atomic resolution. *Nature*, 496(7443):74, 2013.
- [22] Isaiah Y Chen, Jessica Cimada daSilva, Daniel M Balazs, Michelle A Smeaton, Lena F Kourkoutis, Tobias Hanrath, and Paulette Clancy. The role of dimer formation in the nucleation of superlattice transformations and its impact on disorder. *ACS nano*, 14(9):11431–11441, 2020.
- [23] Yujie Chen, Johannes Herrnsdorf, Benoit Guilhabert, Yanfeng Zhang, Ian M Watson, Erdan Gu, Nicolas Laurand, and Martin D Dawson. Colloidal quantum dot random laser. *Opt. Express*, 19(4):2996–3003, 2011.
- [24] Joshua J Choi, Kaifu Bian, William J Baumgardner, Detlef-M Smilgies, and Tobias Hanrath. Interface-induced nucleation, orientational alignment and symmetry transformations in nanocube superlattices. *Nano letters*, 12(9):4791–4798, 2012.
- [25] Xiaolei Chu, Hamed Heidari, Alex Abelson, Davis Unruh, Chase Hansen, Caroline Qian, Gergely Zimanyi, Matt Law, and Adam J Moulé. Structural characterization of a polycrystalline epitaxially-fused colloidal quantum dot superlattice by electron tomography. *Journal of Materials Chemistry A*, 8(35):18254–18265, 2020.

- [26] Eugene YS Chua. Does von neumann entropy correspond to thermodynamic entropy? *Philosophy of Science*, 88(1):145–168, 2021.
- [27] Richard Anthony Crowther, DJ DeRosier, and Aaron Klug. The reconstruction of a three-dimensional structure from projections and its application to electron microscopy. *Proceedings of the Royal Society of London. A. Mathematical and Physical Sciences*, 317(1530):319–340, 1970.
- [28] Xianglu Dai, Huimin Xie, Huaixi Wang, Chuanwei Li, Zhanwei Liu, and Lifu Wu. The geometric phase analysis method based on the local high resolution discrete fourier transform for deformation measurement. *Measurement Science and Technology*, 25(2):025402, 2014.
- [29] Xianglu Dai, Huimin Xie, and Qinghua Wang. Geometric phase analysis based on the windowed fourier transform for the deformation field measurement. *Optics & Laser Technology*, 58:119–127, 2014.
- [30] Richard Dalven. A review of the semiconductor properties of pbte, pbse, pbs and pbo. *Infrared physics*, 9(4):141–184, 1969.
- [31] Cuong Dang, Joonhee Lee, Craig Breen, Jonathan S Steckel, Seth Coe-Sullivan, and Arto Nurmikko. Red, green and blue lasing enabled by single-exciton gain in colloidal quantum dot films. *Nat. Nanotechnol.*, 7(5):335, 2012.
- [32] Jessica Cimada daSilva, Michelle A Smeaton, Tyler A Dunbar, Yuanze Xu, Daniel M Balazs, Lena F Kourkoutis, and Tobias Hanrath. Mechanistic insights into superlattice transformation at a single nanocrystal level using nanobeam electron diffraction. *Nano Letters*, 20(7):5267–5274, 2020.
- [33] Manlio De Domenico and Jacob Biamonte. Spectral entropies as information-theoretic tools for complex network comparison. *Physical Review X*, 6(4):041062, 2016.
- [34] Christophe Jean Delerue and Michel Lannoo. *Nanostructures: Theory and Modeling*. Springer Science & Business Media, 2013.

- [35] Benjamin T Diroll, Nicholas J Greybush, Cherie R Kagan, and Christopher B Murray. Smectic nanorod superlattices assembled on liquid subphases: Structure, orientation, defects, and optical polarization. *Chem. Mater.*, 27(8):2998–3008, 2015.
- [36] Angang Dong, Jun Chen, Patrick M Vora, James M Kikkawa, and Christopher B Murray. Binary nanocrystal superlattice membranes self-assembled at the liquid–air interface. *Nature*, 466(7305):474, 2010.
- [37] Angang Dong, Yucong Jiao, and Delia J Milliron. Electronically coupled nanocrystal superlattice films by in situ ligand exchange at the liquid–air interface. *ACS Nano*, 7(12):10978–10984, 2013.
- [38] Frédéric Dumestre, Bruno Chaudret, Catherine Amiens, Philippe Renaud, and Peter Fejes. Superlattices of iron nanocubes synthesized from $Fe[N(SiMe_3)_2]_2$. *Science*, 303(5659):821–823, 2004.
- [39] Darren Dunphy, Hongyou Fan, Xuefa Li, Jin Wang, and C Jeffrey Brinker. Dynamic investigation of gold nanocrystal assembly using in situ grazing-incidence small-angle x-ray scattering. *Langmuir*, 24(19):10575–10578, 2008.
- [40] Moses Ender, Jochen Joos, Thomas Carraro, and Ellen Ivers-Tiffée. Quantitative characterization of LiFePO₄ cathodes reconstructed by fib/sem tomography. *Journal of the electrochemical society*, 159(7):A972, 2012.
- [41] Viktor A Ermakov, José Maria Clemente da Silva Filho, Luiz Gustavo Bonato, Naga Vishnu Vardhan Mogili, Fabiano Emmanuel Montoro, Fernando Iikawa, Ana Flavia Nogueira, Carlos Lenz Cesar, Ernesto Jimenez-Villar, and Francisco Chagas Marques. Three-dimensional superlattice of pbs quantum dots in flakes. *ACS omega*, 3(2):2027–2032, 2018.
- [42] Wiel H Evers, Heiner Friedrich, Laura Fillion, Marjolein Dijkstra, and Daniel Vanmaekelbergh. Observation of a ternary nanocrystal superlattice and its structural characterization by electron tomography. *Angew. Chem., Int. Ed.*, 48(51):9655–9657, 2009.

- [43] Wiel H Evers, Bart Goris, Sara Bals, Marianna Casavola, Joost De Graaf, Rene Van Roij, Marjolein Dijkstra, and Daniël Vanmaekelbergh. Low-dimensional semiconductor superlattices formed by geometric control over nanocrystal attachment. *Nano Lett.*, 13(6):2317–2323, 2012.
- [44] Wiel H Evers, Juleon M Schins, Michiel Aerts, Aditya Kulkarni, Pierre Capiod, Maxime Berthe, Bruno Grandidier, Christophe Delerue, Herre SJ Van Der Zant, Carlo Van Overbeek, et al. High charge mobility in two-dimensional percolative networks of pbse quantum dots connected by atomic bonds. *Nat. Commun.*, 6:8195, 2015.
- [45] Baobing Fan, Difei Zhang, Meijing Li, Wenkai Zhong, Zhaomiyi Zeng, Lei Ying, Fei Huang, and Yong Cao. Achieving over 16% efficiency for single-junction organic solar cells. *Science China Chemistry*, 62(6):746–752, 2019.
- [46] H. Felipe, A. Viol, D. B. de Araujo, M. G. E. da Luz, F. Palhano-Fontes, H. Onias, E. P. Raposo, and G. M. Viswanathan. The von neumann entropy for the pearson correlation matrix: A test of the entropic brain hypothesis, 2021.
- [47] Heiner Friedrich, Cedric J Gommès, Karin Overgaag, Johannes D Meeldijk, Wiel H Evers, Bart de Nijs, Mark P Boneschanscher, Petra E de Jongh, Arie J Verkleij, Krijn P de Jong, et al. Quantitative structural analysis of binary nanocrystal superlattices by electron tomography. *Nano Lett.*, 9(7):2719–2724, 2009.
- [48] Han Fu, K. V. Reich, and B. I. Shklovskii. Hopping conductivity and insulator-metal transition in films of touching semiconductor nanocrystals. *Phys. Rev. B*, 93:125430, Mar 2016.
- [49] Jaco J Geuchies, Giuseppe Soligno, Ellenor Geraffy, Cedric P Hendrikx, Carlo van Overbeek, Federico Montanarella, Marlou R Slot, Oleg V Konovalov, Andrei V Petukhov, and Daniel Vanmaekelbergh. Unravelling three-dimensional adsorption geometries of pbse nanocrystal monolayers at a liquid-air interface. *Communications Chemistry*, 3(1):1–10, 2020.

- [50] Jaco J Geuchies, Carlo Van Overbeek, Wiel H Evers, Bart Goris, Annick De Backer, Anjan P Gantapara, Freddy T Rabouw, Jan Hilhorst, Joep L Peters, Oleg Kononov, et al. In situ study of the formation mechanism of two-dimensional superlattices from pbse nanocrystals. *Nat. Mater.*, 15(12):1248, 2016.
- [51] Heather Goodwin, Tom C Jellicoe, Nathaniel JLK Davis, and Marcus L Böhm. Multiple exciton generation in quantum dot-based solar cells. *Nanophotonics*, 7(1):111–126, 2018.
- [52] Bart Goris, Sara Bals, Wouter Van den Broek, Enrique Carbó-Argibay, Sergio Gómez-Graña, Luis M Liz-Marzán, and Gustaaf Van Tendeloo. Atomic-scale determination of surface facets in gold nanorods. *Nature materials*, 11(11):930–935, 2012.
- [53] Philippe Guyot-Sionnest. Electrical transport in colloidal quantum dot films. *J. Phys. Chem. Lett.*, 3(9):1169–1175, 2012.
- [54] Jordan A Hachtel, Andrew R Lupini, and Juan Carlos Idrobo. Exploring the capabilities of monochromated electron energy loss spectroscopy in the infrared regime. *Scientific Reports*, 8(1):1–10, 2018.
- [55] Tobias Hanrath, Joshua J Choi, and Detlef-M Smilgies. Structure/processing relationships of highly ordered lead salt nanocrystal superlattices. *ACS Nano*, 3(10):2975–2988, 2009.
- [56] Arjan J. Houtepen, Daan Kockmann, and Daniël Vanmaekelbergh. Reappraisal of variable-range hopping in quantum-dot solids. *Nano Lett.*, 8(10):3516–3520, 2008.
- [57] Ye Huang, Edward J Kramer, Alan J Heeger, and Guillermo C Bazan. Bulk heterojunction solar cells: morphology and performance relationships. *Chemical reviews*, 114(14):7006–7043, 2014.
- [58] MJ Hÿtch, E Snoeck, and R Kilaas. Quantitative measurement of displacement and strain fields from hrem micrographs. *Ultramicroscopy*, 74(3):131–146, 1998.

- [59] Xuechen Jiao, Long Ye, and Harald Ade. Quantitative morphology–performance correlations in organic solar cells: Insights from soft x-ray scattering. *Advanced Energy Materials*, 7(18):1700084, 2017.
- [60] Cherie R Kagan, Efrat Lifshitz, Edward H Sargent, and Dmitri V Talapin. Building devices from colloidal quantum dots. *Science*, 353(6302):aac5523, 2016.
- [61] Cherie R Kagan and Christopher B Murray. Charge transport in strongly coupled quantum dot solids. *Nat. Nanotechnol.*, 10(12):1013, 2015.
- [62] Avinash C Kak and Malcolm Slaney. *Principles of computerized tomographic imaging*. SIAM, 2001.
- [63] Inuk Kang and Frank W Wise. Electronic structure and optical properties of pbs and pbse quantum dots. *J. Opt. Soc. Am. B*, 14(7):1632–1646, 1997.
- [64] Noboru Kawase, Mitsuro Kato, Hideo Nishioka, and Hiroshi Jinnai. Transmission electron microtomography without the “missing wedge” for quantitative structural analysis. *Ultramicroscopy*, 107(1):8–15, 2007.
- [65] Xiaoxing Ke, Sara Bals, Daire Cott, Thomas Hantschel, Hugo Bender, and Gustaaf Van Tendeloo. Three-dimensional analysis of carbon nanotube networks in interconnects by electron tomography without missing wedge artifacts. *Microscopy and Microanalysis*, 16(2):210–217, 2010.
- [66] Thomas F Kelly and Michael K Miller. Atom probe tomography. *Review of scientific instruments*, 78(3):031101, 2007.
- [67] Byung Hyo Kim, Junyoung Heo, Sungin Kim, Cyril F Reboul, Hoje Chun, Dohun Kang, Hyeonhu Bae, Hyejeong Hyun, Jongwoo Lim, Hoonkyung Lee, et al. Critical differences in 3d atomic structure of individual ligand-protected nanocrystals in solution. *Science*, 368(6486):60–67, 2020.

- [68] Sung Jin Kim, Won Jin Kim, Yudhistira Sahoo, Alexander N Cartwright, and Paras N Prasad. Multiple exciton generation and electrical extraction from a pbse quantum dot photoconductor. *Applied Physics Letters*, 92(3):031107, 2008.
- [69] Younghoon Kim, Fanglin Che, Jea Woong Jo, Jongmin Choi, F Pelayo García de Arquer, Oleksandr Voznyy, Bin Sun, Junghwan Kim, Min-Jae Choi, Rafael Quintero-Bermudez, et al. A facet-specific quantum dot passivation strategy for colloid management and efficient infrared photovoltaics. *Adv. Mater.*, page 1805580, 2019.
- [70] Masanari Koguchi, Hiroshi Kakibayashi, Ruriko Tsuneta, Masahiro Yamaoka, Toshiki Niino, Nobuo Tanaka, Kiwamu Kase, and Masaya Iwaki. Three-dimensional stem for observing nanostructures. *Microscopy*, 50(3):235–241, 2001.
- [71] J Konrad, S Zaefferer, and D Raabe. Investigation of orientation gradients around a hard laves particle in a warm-rolled fe3al-based alloy using a 3d ebsd-fib technique. *Acta Materialia*, 54(5):1369–1380, 2006.
- [72] Gerasimos Konstantatos and Edward H Sargent. Colloidal quantum dot photodetectors. *Infrared Phys. Technol.*, 54(3):278–282, 2011.
- [73] DJ Larson, DT Foord, AK Petford-Long, TC Anthony, IM Rozdilsky, A Cerezo, and GWD Smith. Focused ion-beam milling for field-ion specimen preparation:: preliminary investigations. *Ultramicroscopy*, 75(3):147–159, 1998.
- [74] Olga L Lazarenkova and Alexander A Balandin. Miniband formation in a quantum dot crystal. *Journal of Applied Physics*, 89(10):5509–5515, 2001.
- [75] Brus LE. Electron-electron and electron-hole interactions in small semiconductor crystallites: the size dependence of the lowest excited electronic state. *J Chem Phys*, 80:4403–4417, 1984.
- [76] Rowan Leary, Zineb Saghi, Paul A Midgley, and Daniel J Holland. Compressed sensing electron tomography. *Ultramicroscopy*, 131:70–91, 2013.

- [77] Hansol Lee, Chaneui Park, Dong Hun Sin, Jong Hwan Park, and Kilwon Cho. Recent advances in morphology optimization for organic photovoltaics. *Advanced Materials*, 30(34):1800453, 2018.
- [78] Jisoo Lee, Jiwoong Yang, Soon Gu Kwon, and Taeghwan Hyeon. Nonclassical nucleation and growth of inorganic nanoparticles. *Nature Reviews Materials*, 1(8):1–16, 2016.
- [79] Collen Z Leng and Mark D Losego. Vapor phase infiltration (vpi) for transforming polymers into organic–inorganic hybrid materials: a critical review of current progress and future challenges. *Materials Horizons*, 4(5):747–771, 2017.
- [80] Collen Z Leng and Mark D Losego. A physiochemical processing kinetics model for the vapor phase infiltration of polymers: measuring the energetics of precursor-polymer sorption, diffusion, and reaction. *Physical Chemistry Chemical Physics*, 20(33):21506–21514, 2018.
- [81] Karl Leo, Peter Haring Bolivar, Frank Brüggemann, Ralf Schwedler, and Klaus Köhler. Observation of bloch oscillations in a semiconductor superlattice. *Solid State Communications*, 84(10):943–946, 1992.
- [82] K Liu, JD Cruzan, and RJ Saykally. Water clusters. *Science*, 271(5251):929–933, 1996.
- [83] Yao Liu, Markelle Gibbs, James Puthussery, Steven Gaik, Rachelle Ihly, Hugh W Hillhouse, and Matt Law. Dependence of carrier mobility on nanocrystal size and ligand length in pbse nanocrystal solids. *Nano Lett.*, 10(5):1960–1969, 2010.
- [84] Yao Liu, Jason Tolentino, Markelle Gibbs, Rachelle Ihly, Craig L Perkins, Yu Liu, Nathan Crawford, John C Hemminger, and Matt Law. Pbse quantum dot field-effect transistors with air-stable electron mobilities above $7 \text{ cm}^2\text{v}^{-1}\text{s}^{-1}$. *Nano Lett.*, 13(4):1578–1587, 2013.
- [85] Yuhang Liu, Jingbo Zhao, Zhengke Li, Cheng Mu, Wei Ma, Huawei Hu, Kui Jiang, Haoran Lin, Harald Ade, and He Yan. Aggregation and morphology control enables

- multiple cases of high-efficiency polymer solar cells. *Nature communications*, 5(1):1–8, 2014.
- [86] David N Mastrorarde. Dual-axis tomography: an approach with alignment methods that preserve resolution. *Journal of structural biology*, 120(3):343–352, 1997.
- [87] Arthur RC McCray, Benjamin H Savitzky, Kevin Whitham, Tobias Hanrath, and Lena F Kourkoutis. Orientational disorder in epitaxially connected quantum dot solids. *ACS nano*, 13(10):11460–11468, 2019.
- [88] Hamed Heidari Mezerji, Wouter Van den Broek, and Sara Bals. A practical method to determine the effective resolution in incoherent experimental electron tomography. *Ultramicroscopy*, 111(5):330–336, 2011.
- [89] Iwan Moreels, Karel Lambert, Dries Smeets, David De Muynck, Tom Nollet, José C Martins, Frank Vanhaecke, Andre Vantomme, Christophe Delerue, Guy Allan, et al. Size-dependent optical properties of colloidal pbs quantum dots. *ACS Nano*, 3(10):3023–3030, 2009.
- [90] Subhrangsu Mukherjee, Xuechen Jiao, and Harald Ade. Charge creation and recombination in multi-length scale polymer: Fullerene bhj solar cell morphologies. *Advanced Energy Materials*, 6(18):1600699, 2016.
- [91] Christian Müller, Toby AM Ferenczi, Mariano Campoy-Quiles, Jarvist M Frost, Donal DC Bradley, Paul Smith, Natalie Stingelin-Stutzmann, and Jenny Nelson. Binary organic photovoltaic blends: a simple rationale for optimum compositions. *Advanced Materials*, 20(18):3510–3515, 2008.
- [92] AC Neville and S Caveney. Scarabaeid beetle exocuticle as an optical analogue of cholesteric liquid crystals. *Biological Reviews*, 44(4):531–562, 1969.
- [93] Arthur J Nozik, Matthew C Beard, Joseph M Luther, Matt Law, Randy J Ellingson, and Justin C Johnson. Semiconductor quantum dots and quantum dot arrays and applications

- of multiple exciton generation to third-generation photovoltaic solar cells. *Chemical reviews*, 110(11):6873–6890, 2010.
- [94] Stas Obuchovsky, Hadar Frankenstein, Jane Vinokur, Anna K Hailey, Yueh-Lin Loo, and Gitti L Frey. Mechanism of metal oxide deposition from atomic layer deposition inside nonreactive polymer matrices: effects of polymer crystallinity and temperature. *Chemistry of Materials*, 28(8):2668–2676, 2016.
- [95] Stas Obuchovsky, Matan Levin, Artem Levitsky, and Gitti L Frey. Morphology visualization of p3ht: Fullerene blends by using subsurface atomic layer deposition. *Organic Electronics*, 49:234–241, 2017.
- [96] Stas Obuchovsky, Basel Shamieh, Igal Deckman, Guy Ankonina, and Gitti L Frey. Harnessing ald to directly map the morphology of organic photovoltaic bulk heterojunctions. *Solar Energy Materials and Solar Cells*, 143:280–283, 2015.
- [97] Soong Ju Oh, Zhuqing Wang, Nathaniel E Berry, Ji-Hyuk Choi, Tianshuo Zhao, E Ashley Gauling, Taejong Paik, Yuming Lai, Christopher B Murray, and Cherie R Kagan. Engineering charge injection and charge transport for high performance pbse nanocrystal thin film devices and circuits. *Nano Lett.*, 14(11):6210–6216, 2014.
- [98] T Ohkubo, H Sepehri-Amin, TT Sasaki, and K Hono. Multi-scale characterization by fib-sem/tem/3dap. *Microscopy*, 63(suppl_1):i6–i7, 2014.
- [99] Justin C Ondry and A Paul Alivisatos. Application of dislocation theory to minimize defects in artificial solids built with nanocrystal building blocks. *Accounts of chemical research*, 54(6):1419–1429, 2021.
- [100] Justin C Ondry, Matthew R Hauwiller, and A Paul Alivisatos. Dynamics and removal pathway of edge dislocations in imperfectly attached pbte nanocrystal pairs: toward design rules for oriented attachment. *ACS nano*, 12(4):3178–3189, 2018.
- [101] Andras G Pattantyus-Abraham, Illan J Kramer, Aaron R Barkhouse, Xihua Wang, Gerasimos Konstantatos, Ratan Debnath, Larissa Levina, Ines Raabe, Mohammad K

- Nazeeruddin, Michael Gratzel, and Edward Sargent. Depleted-heterojunction colloidal quantum dot solar cells. *ACS Nano*, 4(6):3374–3380, 2010.
- [102] Joep L Peters, Thomas Altantzis, Ivan Lobato, Maryam Alimoradi Jazi, Carlo Van Overbeek, Sara Bals, Daniel Vanmaekelbergh, and Sophia Buhbut Sinai. Mono- and multilayer silicene-type honeycomb lattices by oriented attachment of pbse nanocrystals: Synthesis, structural characterization, and analysis of the disorder. *Chem. Mater.*, 30(14):4831–4837, 2018.
- [103] Hadi Pirgazi. On the alignment of 3d ebsd data collected by serial sectioning technique. *Materials Characterization*, 152:223–229, 2019.
- [104] Luman Qu, Márton Vörös, and Gergely T Zimanyi. Metal-insulator transition in nanoparticle solids: Insights from kinetic monte carlo simulations. *Sci. Rep.*, 7(1):7071, 2017.
- [105] Gabriele Rainò, Michael A Becker, Maryna I Bodnarchuk, Rainer F Mahrt, Maksym V Kovalenko, and Thilo Stöferle. Superfluorescence from lead halide perovskite quantum dot superlattices. *Nature*, 563(7733):671–675, 2018.
- [106] Brent A Ridley, Babak Nivi, and Joseph M Jacobson. All-inorganic field effect transistors fabricated by printing. *Science*, 286(5440):746–749, 1999.
- [107] Matthias A Ruderer and Peter Müller-Buschbaum. Morphology of polymer-based bulk heterojunction films for organic photovoltaics. *Soft Matter*, 7(12):5482–5493, 2011.
- [108] Zineb Saghi and Paul A Midgley. Electron tomography in the (s) tem: from nanoscale morphological analysis to 3d atomic imaging. *Annual Review of Materials Research*, 42:59–79, 2012.
- [109] CS Suchand Sandeep, Jon Mikel Azpiroz, Wiel H Evers, Simon C Boehme, Iwan Moreels, Sachin Kinge, Laurens DA Siebbeles, Ivan Infante, and Arjan J Houtepen. Epitaxially connected pbse quantum-dot films: Controlled neck formation and optoelectronic properties. *ACS Nano*, 8(11):11499–11511, 2014.
- [110] Edward H Sargent. Colloidal quantum dot solar cells. *Nat. Photonics*, 6(3):133, 2012.

- [111] Benjamin H Savitzky, Robert Hovden, Kevin Whitham, Jun Yang, Frank Wise, Tobias Hanrath, and Lena F Kourkoutis. Propagation of structural disorder in epitaxially connected quantum dot solids from atomic to micron scale. *Nano Lett.*, 16(9):5714–5718, 2016.
- [112] Benjamin H Savitzky, Kevin Whitham, Kaifu Bian, Robert Hovden, Tobias Hanrath, and Lena F Kourkoutis. Three-dimensional arrangement and connectivity of lead-chalcogenide nanoparticle assemblies for next generation photovoltaics. *Microsc. Microanal.*, 20(S3):542–543, 2014.
- [113] Yozo Shimada, Tetsuya Matsuno, and Kazuhiko Hirakawa. Terahertz emission due to miniband transport in gaas/algaas superlattices. *Japanese Journal of Applied Physics*, 40(4S):3009, 2001.
- [114] Michelle A Smeaton, Ismail El Baggari, Daniel M Balazs, Tobias Hanrath, and Lena F Kourkoutis. Mapping defect relaxation in quantum dot solids upon in situ heating. *ACS nano*, 15(1):719–726, 2021.
- [115] Danielle K Smith, Brian Goodfellow, Detlef-M Smilgies, and Brian A Korgel. Self-assembled simple hexagonal ab₂ binary nanocrystal superlattices: Sem, gisaxs, and defects. *J. Am. Chem. Soc.*, 131(9):3281–3290, 2009.
- [116] Daniela Stoeckel, Christian Kubel, Kristof Hormann, Alexandra Holtzel, Bernd M Smarsly, and Ulrich Tallarek. Morphological analysis of disordered macroporous–mesoporous solids based on physical reconstruction by nanoscale tomography. *Langmuir*, 30(30):9022–9027, 2014.
- [117] C Jackson Stolle, Taylor B Harvey, Douglas R Pernik, Jarett I Hibbert, Jiang Du, Dong Joon Rhee, Vahid A Akhavan, Richard D Schaller, and Brian A Korgel. Multi-exciton solar cells of cuinse₂ nanocrystals. *The journal of physical chemistry letters*, 5(2):304–309, 2014.
- [118] Naoki Tomii, Masatoshi Yamazaki, Tatsuhiko Arafune, Haruo Honjo, Nitaro Shibata, and Ichiro Sakuma. Detection algorithm of phase singularity using phase variance analysis

- for epicardial optical mapping data. *IEEE Transactions on Biomedical Engineering*, 63(9):1795–1803, 2015.
- [119] Jeannot Trampert and Jean-Jacques Leveque. Simultaneous iterative reconstruction technique: Physical interpretation based on the generalized least squares solution. *J. Geophys. Res.: Solid Earth*, 95(B8):12553–12559, 1990.
- [120] Benjamin E Treml, Benjamin H Savitzky, Ali M Tirmzi, Jessica Cimada DaSilva, Lena F Kourkoutis, and Tobias Hanrath. Successive ionic layer absorption and reaction for postassembly control over inorganic interdot bonds in long-range ordered nanocrystal films. *ACS Appl. Mater. Interfaces*, 9(15):13500–13507, 2017.
- [121] Davis Unruh, Chase Hansen, Alberto Camjanyi, Joel Bobadilla, Marcelo Rozenberg, and Gergely T Zimanyi. Persistent coulomb blockade across the metal-insulator transition in nanoparticle solids. *arXiv.org, e-Print Arch., Condens. Matter*, 2019.
- [122] Wim van Aarle, Willem Jan Palenstijn, Jan De Beenhouwer, Thomas Altantzis, Sara Bals, K Joost Batenburg, and Jan Sijbers. The astra toolbox: A platform for advanced algorithm development in electron tomography. *Ultramicroscopy*, 157:35–47, 2015.
- [123] Marijn A Van Huis, Lucas T Kunneman, Karin Overgaag, Qiang Xu, Gregory Pandraud, Henny W Zandbergen, and Daniël Vanmaekelbergh. Low-temperature nanocrystal unification through rotations and relaxations probed by in situ transmission electron microscopy. *Nano letters*, 8(11):3959–3963, 2008.
- [124] Carlo Van Overbeek, Joep L Peters, Susan AP Van Rossum, Marc Smits, Marijn A Van Huis, and Daniel Vanmaekelbergh. Interfacial self-assembly and oriented attachment in the family of pbx (x= s, se, te) nanocrystals. *J. Phys. Chem. C*, 122(23):12464–12473, 2018.
- [125] Willem Walravens, Jonathan De Roo, Emile Drijvers, Stephanie Ten Brinck, Eduardo Solano, Jolien Dendooven, Christophe Detavernier, Ivan Infante, and Zeger Hens. Chemically triggered formation of two-dimensional epitaxial quantum dot superlattices. *ACS Nano*, 10(7):6861–6870, 2016.

- [126] Willem Walravens, Eduardo Solano, Filip Geenen, Jolien Dendooven, Oleg Gorobtsov, Athmane Tadjine, Nayyera Mahmoud, Patrick Peiwen Ding, Jacob PC Ruff, Andrej Singer, et al. Setting carriers free, healing faulty interfaces promotes delocalization and transport in nanocrystal solids. *ACS nano*, 13(11):12774–12786, 2019.
- [127] Junfeng Wang, Zongzheng Zhou, Wei Zhang, Timothy M Garoni, and Youjin Deng. Bond and site percolation in three dimensions. *Phys. Rev. E*, 87(5):052107, 2013.
- [128] Robert Y Wang, Joseph P Feser, Jong-Soo Lee, Dmitri V Talapin, Rachel Segalman, and Arun Majumdar. Enhanced thermopower in pbse nanocrystal quantum dot superlattices. *Nano letters*, 8(8):2283–2288, 2008.
- [129] Yu Wang, Xinxing Peng, Alex Abelson, Penghao Xiao, Caroline Qian, Lei Yu, Colin Ophus, Peter Ercius, Lin-Wang Wang, Matt Law, et al. Dynamic deformability of individual pbse nanocrystals during superlattice phase transitions. *Sci. Adv.*, 5(6):eaaw5623, 2019.
- [130] Mark C Weidman, Detlef-M Smilgies, and William A Tisdale. Kinetics of the self-assembly of nanocrystal superlattices measured by real-time in situ x-ray scattering. *Nat. Mater.*, 15(7):775, 2016.
- [131] Kevin Whitham and Tobias Hanrath. Formation of epitaxially connected quantum dot solids: Nucleation and coherent phase transition. *J. Phys. Chem. Lett.*, 8(12):2623–2628, 2017.
- [132] Kevin Whitham, Jun Yang, Benjamin H Savitzky, Lena F Kourkoutis, Frank Wise, and Tobias Hanrath. Charge transport and localization in atomically coherent quantum dot solids. *Nat. Mater.*, 15(5):557, 2016.
- [133] Pascal Wolfer, Paul E Schwenn, Ajay K Pandey, Yuan Fang, Natalie Stingelin, Paul L Burn, and Paul Meredith. Identifying the optimum composition in organic solar cells comprising non-fullerene electron acceptors. *Journal of Materials Chemistry A*, 1(19):5989–5995, 2013.

- [134] Rongming Xue, Jingwen Zhang, Yaowen Li, and Yongfang Li. Organic solar cell materials toward commercialization. *Small*, 14(41):1801793, 2018.
- [135] Dong Yu, Congjun Wang, Brian L. Wehrenberg, and Philippe Guyot-Sionnest. Variable range hopping conduction in semiconductor nanocrystal solids. *Phys. Rev. Lett.*, 92:216802, May 2004.
- [136] Bingsen Zhang and Dang Sheng Su. Electron tomography: Three-dimensional imaging of real crystal structures at atomic resolution. *Angewandte Chemie International Edition*, 52(33):8504–8506, 2013.
- [137] Haibo Zhang, Akio Takaoka, and Kyoichi Miyauchi. A 360° – tilt specimen holder for electron tomography in an ultrahigh – voltage electron microscope. *Review of scientific instruments*, 69(11) : 4008 – 4009, 1998.
- [138] Man Zhao, Defang Ding, Fangxu Yang, Dawei Wang, Jiawei Lv, Wenping Hu, Chenguang Lu, and Zhiyong Tang. Ligand effects on electronic and optoelectronic properties of two-dimensional pbs necking percolative superlattices. *Nano Res.*, 10(4):1249–1257, 2017.
- [139] Man Zhao, Fangxu Yang, Chao Liang, Dawei Wang, Defang Ding, Jiawei Lv, Jianqi Zhang, Wenping Hu, Chenguang Lu, and Zhiyong Tang. High hole mobility in long-range ordered 2d lead sulfide nanocrystal monolayer films. *Adv. Funct. Mater.*, 26(28):5182–5188, 2016.